

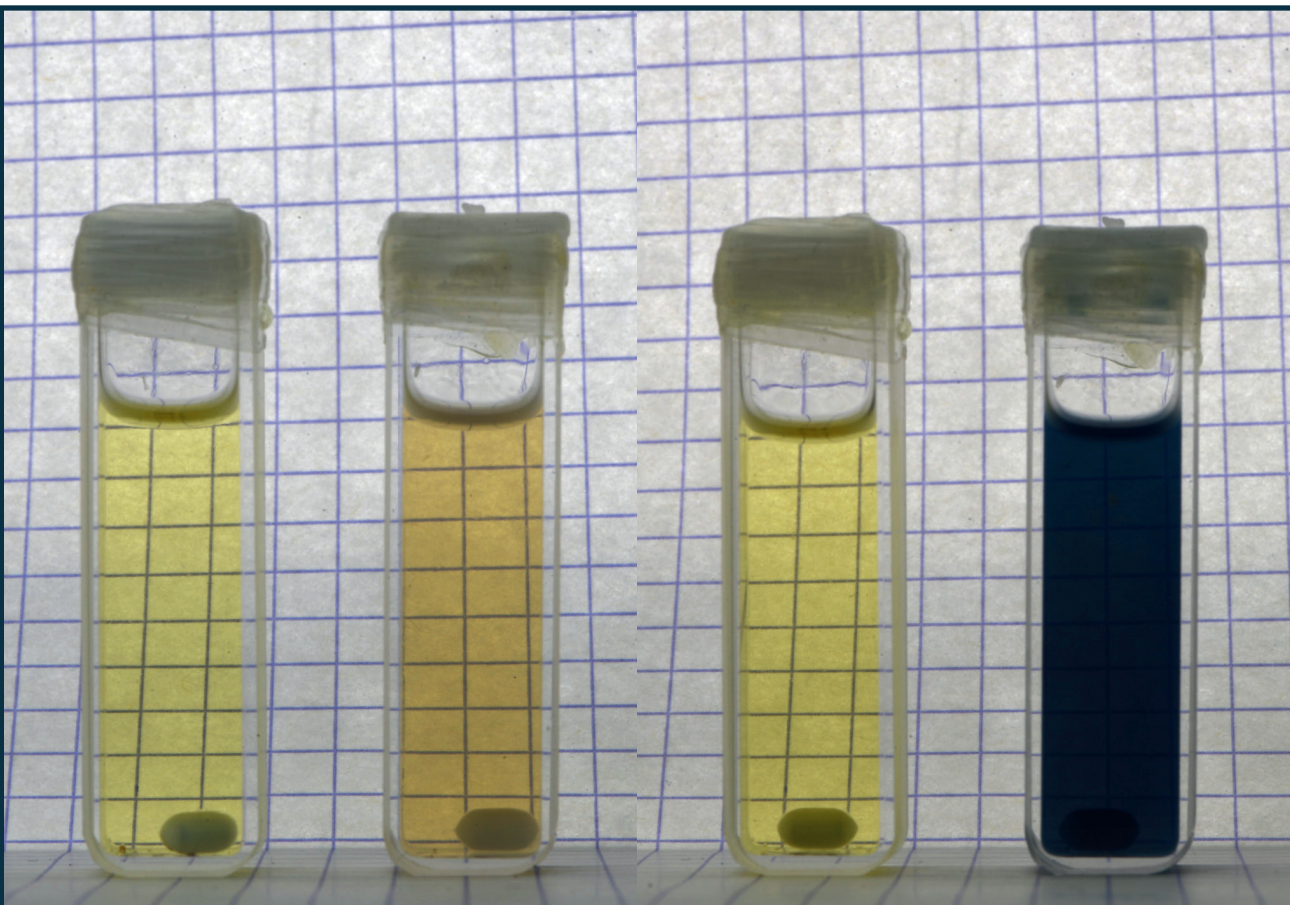


RIGA TECHNICAL
UNIVERSITY

Raivis Eglītis

**PHOTOCHROMIC MATERIALS BASED ON ULTRA
SMALL TITANIUM DIOXIDE NANOPARTICLES**

Doctoral Thesis



RTU Press
Riga 2023

RIGA TECHNICAL UNIVERSITY
Faculty of Materials Science and Applied Chemistry
Institute of Materials and Surface Engineering

Raivis Eglītis

Doctoral Student of the Study Programme “Materials Science”

**Photochromic materials based on ultra small
titanium dioxide nanoparticles**

Doctoral Thesis

Scientific supervisor
Professor Dr. sc. ing.
ANDRIS ŠUTKA

Riga 2023

Eglītis, R. Photochromic Materials Based on Ultra small Titanium Dioxide Nanoparticles. Doctoral Thesis. Riga: RTU Press, 2023. 142 p.

Published in accordance with the decision of the Promotion Council “RTU P-02” of 16 September 2022, Minutes No. 04030-9.2.2/10.

This work has been supported by the European Social Fund within the Project No 8.2.2.0/20/I/008 “Strengthening of PhD students and academic personnel of Riga Technical University and BA School of Business and Finance in the strategic fields of specialization” of the Specific Objective 8.2.2 “To Strengthen Academic Staff of Higher Education Institutions in Strategic Specialization Areas” of the Operational Programme “Growth and Employment”



NATIONAL
DEVELOPMENT
PLAN 2020



EUROPEAN UNION
European Social
Fund

INVESTING IN YOUR FUTURE

This publication was supported by Riga Technical University's Doctoral Grant programme

DOCTORAL THESIS PROPOSED TO RIGA TECHNICAL UNIVERSITY FOR THE PROMOTION TO THE SCIENTIFIC DEGREE OF DOCTOR OF SCIENCE

To be granted the scientific degree of Doctor of Science (Ph. D.), the present Doctoral Thesis has been submitted for the defence at the open meeting of RTU Promotion Council on 2 March 2023 at 10.30 at the Faculty of Materials Science and Applied Chemistry of Riga Technical University, 3 Paula Valdena Street, Room 272.

OFFICIAL REVIEWERS

Dr. chem. Donāts Erts
University of Latvia, Latvia

Dr. phys. Anatolijs Šarakovskis,
University of Latvia, Latvia

PhD. Gemma García Mandayo,
Centro de Estudios e Investigaciones Técnicas de Gipuzkoa, Spain

DECLARATION OF ACADEMIC INTEGRITY

I hereby declare that the Doctoral Thesis submitted for the review to Riga Technical University for the promotion to the scientific degree of Doctor of Science (Ph. D.) is my own. I confirm that this Doctoral Thesis had not been submitted to any other university for the promotion to a scientific degree.

Name Surname (signature)

Date:

The Doctoral Thesis has been written in English. It consists of an Introduction, 3 chapters, Conclusions, 79 figures, 8 tables; the total number of pages is 142. The Bibliography contains 376 titles.

ACKNOWLEDGEMENTS

I would like to express my thanks to all the people who helped both directly and indirectly in the creation of this thesis. Especially, I would like to express my gratitude to my scientific supervisor, professor Andris Šutka, who helped me both with guidance and encouragement. I also want to express my thanks to professor Roman Viter, who helped me with the initial photochromic data dissemination. Furthermore, all of my colleagues in both the institute of materials and surface engineering as well as the institute of technical physics also deserve my thanks as they were gracious in taking time out of their busy days in order to listen to my problems and gave suggestions that oftentimes led to a positive outcome. Out of all of them I want to mention by name: Astrīda Bērziņa, Linards Lapčinskis and Anzelms Zukuls.

I also want to express my deepest gratitude to my partner Vivita Priedniece, who helped me not to lose track of the important things and motivated me when I needed it most. With her we have gone through all the different levels of higher education: bachelors, masters and now – doctoral studies. Her unwavering support was and is most appreciated. She, together with our cat Tomass as well as my mother Zaīga Eglīte helped to get through all the ups and downs the writing of this work provided.

Content

List of abbreviations.....	7
1 Literature overview.....	13
1.1 Chromic materials and their working principles.....	13
1.2 Titanium dioxide nanoparticle properties and synthesis.....	36
1.3 Controlling the optical properties of titanium dioxide by means of defect chemistry.....	46
1.4 Modification of titanium dioxide photochromic properties by heterostructure formation and other means.....	54
1.5 Summary.....	58
2 Methodic section.....	60
2.1 Reagents used.....	60
2.2 Synthesis of TiO ₂ and doped TiO ₂ nanoparticles.....	62
2.3 Coating preparation.....	64
2.4 Scientific equipment used for the characterization of the materials and their photochromic performance.....	65
2.5 X-ray diffraction.....	66
2.6 Rietveld refinement.....	66
2.7 Raman spectroscopy.....	66
2.8 Scanning and transmission electron microscopy.....	67
2.9 Selected Area Electron Diffraction.....	67
2.10 Diffuse reflectance spectroscopy.....	67
2.11 X-ray photoelectron spectroscopy.....	69
2.12 Electron paramagnetic resonance spectroscopy.....	69
2.13 Thermogravimetry.....	69
2.14 Electric resistance measurements for the determination of photoinduced charge carriers.....	70
2.15 Determination of Photochromic properties and charge carrier concentration using UV-Vis spectroscopy.....	71
2.16 Photochromic gel preparation.....	73
3 Results and Discussions.....	75
3.1 Photochromic properties of titanium dioxide.....	75
3.2 The electrical properties of titanium dioxide thin films under UV illumination and in the presence of hole scavenger vapors.....	83
3.3 Photoelectron accumulation in titanium dioxide films under UV irradiation while submersed in a hole scavenger.....	89

3.4	The influence of Nb ⁵⁺ dopant on photochromic response of titanium dioxide	91
3.5	Photochromic TiO ₂ polymer gels	107
3.6	Conclusions	120
3.7	Secinājumi	122
4	References	123

LIST OF ABBREVIATIONS

HVAC	heating, ventilation, and cooling
MOF	metal organic framework
COF	covalent organic framework
MIT	metal-insulator transition
TTiPr	titanium tetra isopropoxide
TEOT	tetra ethyl orto titanite
TBOT	tetra butyl orto titanite
TiCl ₄	titanium tetrachloride
TiF ₄	titanium tetrafluoride
SPR	surface plasmon resonance
4-DDBSA	4-dodecylbenzene sulphonic acid
EtOH	ethanol
MeOH	methanol
<i>i</i> PrOH	isopropanol
<i>n</i> PrOH	<i>n</i> -propanol
<i>n</i> BuOH	<i>n</i> -butanol
<i>n</i> AmOH	<i>n</i> -pentanol
<i>n</i> HexOH	<i>n</i> -hexanol
MEOA	monoethanolamine
DEOA	diethanolamine
TEOA	triethanolamine
AcacH	acetylacetone
Acac	acetylacetonate ligand
(<i>n</i> BuO) ₄ Ti	tetra (<i>n</i> -butoxy) titanate
TiO ₂	titanium dioxide
CaH ₂	calcium hydride
Nb(OEt) ₅	niobium penta ethoxide
TMO	transition metal oxide
DMF	<i>N,N</i> -dimethylformamide
PEGDA	polyethylene glycol diacrylate
TCO	transparent conducting oxide
ITO	tin doped Indium oxide

ANNOTATION

Nowadays, global warming is causing a slow, but sure increase in the average annual temperature. This causes more countries to experience more and more extremely hot days. To be able to ensure comfortable working and living conditions in buildings, HVAC systems need to be used. However, these systems are power hungry and can account for around a third of the electrical energy consumption of buildings, especially office buildings. To reduce their usage, we need to reduce the amount of incoming light and with it – heat.

A slowly emerging technology are smart windows that can modulate the incoming light by dynamically changing their optical transmittance. The main technology behind smart windows are electrochromic materials, which change the optical properties when an electric field is applied. However, these require the usage of electricity and other constituents to ensure any autonomous action. Photochromic materials can act fully autonomously by changing their transmittance in response to incoming light.

The Thesis explores the photochromic properties of titanium dioxide nanoparticles in different environments. Furthermore, the modification of the nanoparticles with the introduction of a dopant cation and the influence on the photochromic properties is examined. Lastly, the electric properties of the nanoparticles were also examined. It was seen that the environment in which the nanoparticles are dispersed as well as the modification of the nanoparticles has a profound effect on the photochromic properties and can change not only the photodarkening kinetics but also the recovery kinetics. Furthermore, the incorporation of the nanoparticles into organic gels was achieved while retaining high transparency and the photochromic properties of the nanoparticles. Finally, it was shown that the photochromic process was accompanied by changes in the electric properties of the nanoparticles which were used to determine the amount of photoaccumulated electron carriers in the nanoparticles.

ANOTĀCIJA

Mūsdienās klimata pārmaiņas izraisa lēnu, bet ievērojamu gada vidējās gaisa temperatūras pieaugumu, tāpēc daudzās valstīs arvien vairāk novērojamas ekstremāli karstas dienas. Lai nodrošinātu komfortablus darba un dzīves apstākļus arī šādās situācijās, jāizmanto apsildīšanas, ventilācijas un gaisa kondicionēšanas sistēmas. Taču šādas sistēmas ir ar augstu enerģijas patēriņu un var veidot līdz trešdaļai no kopējā elektroenerģijas patēriņa ēkās, īpaši biroju ēkās. Lai samazinātu to izmantošanu, nepieciešams samazināt ienākošās gaismas un tās radītā siltuma daudzumu.

Tehnoloģija, kas lēnām attīstās, ir viedie logi, kas var modulēt ienākošo gaismu, dinamiski mainot tās optisko caurlaidību. Galvenā viedo logu tehnoloģija ir elektrochromie materiāli, kas maina optiskās īpašības, kad uz tiem iedarbojas elektriskais lauks. Taču tiem nepieciešama elektroenerģijas, kā arī citu sastāvdaļu (elektrodi, elektrolīts) izmantošana, lai nodrošinātu jebkādu autonomu darbību. Turklāt fotochromie materiāli var darboties pilnīgi autonomi, mainot savu caurlaidību ienākošās gaismas ietekmē.

Promocijas darba gaitā pētītas titāna dioksīda nanodaļiņu fotochromās īpašības dažādās vidēs. Darbā aplūkota arī nanodaļiņu pārveide, izmantojot katjonu dopēšanu un tā ietekmi uz fotochromām īpašībām. Papildus pētītas un sniegtas arī nanodaļiņu elektriskās īpašības. Izpētes rezultātā novērots, ka vide, kurā nanodaļiņas ir izkliedētas, un nanodaļiņu dopēšana rada ievērojamu ietekmi uz fotochromām īpašībām un var mainīt ne tikai fotoaptumšošanās kinētiku, bet arī atkrāsošanās kinētiku. Papildus īstenota nanodaļiņu iekļaušana organiskajos gēlos, saglabājot augstu gaismas caurlaidību un nanodaļiņu fotochromās īpašības. Visbeidzot, novērots arī tas, ka fotochromo procesu papildina izmaiņas nanodaļiņu elektriskajās īpašībās un to var izmantot, lai noteiktu fotoakumulēto elektronu nesēju daudzumu nanodaļiņās.

INTRODUCTION

Chromism is a material's change in color in response to an external stimulus. Chromic materials have become a staple of modern life in different ways – be it color changing thermometers, self-tinting glasses, or even smart windows. Out of the different types of chromism, photochromism stands out as being one of the most significant because of its passive nature and a wide range of applications. Furthermore, its combinations with other chromism types make it an important characteristic for any material.

In most cases the photochromic material used is organic. This means that its lifetime is limited. Conversely, although inorganic photochromic materials are also widely known, their usage is limited due to their (in most cases) relatively slow chromism. Furthermore, most of the inorganic photochromic materials are either classified as toxic, expensive, or scarce. Currently titanium dioxide does not have any of these drawbacks. However, its photochromic capabilities are not as well pronounced and are overshadowed by other materials, such as tungsten oxide. Although a material is usually looked at on its own, in most cases it is but a part of a larger system, meaning that its capabilities should be examined with respect to other components. Furthermore, it should be possible to offset the drawbacks of titanium dioxide with different methods, making it a more viable candidate for wide scale usage in photochromic applications. The term “ultra-small” refers to the fact that the size of nanoparticles are smaller than 10 nm. Furthermore, since photochromism is a surface process for nanoparticles, the usage of smaller nanoparticles leads to higher photodarkening and recovery speeds than for larger nanoparticles.

Aim of the Thesis

To synthesize ultra-small TiO₂ nanoparticles with high absorption and study their photochromic properties and incorporate them into a gel matrix.

Main tasks

- To study the influence of the surrounding medium on the photochromic properties of TiO₂ nanoparticles.
- To synthesize doped TiO₂ nanoparticles with a high amount of acceptor dopants (such as Nb⁵⁺).
- To study the photochromic properties of the synthesized doped TiO₂ nanoparticles.
- To incorporate TiO₂ nanoparticles into a polymer matrix while retaining high transparency to prepare photochromic gels capable of a high degree of light modulation.

Scientific significance

The influence of the hole scavenger as well as the dopant influence on the photochromic properties of TiO₂ are shown, indicating the possibility of severely influencing the photochromic properties. Furthermore, as of the performing this research, no transparent photochromic gels based on TiO₂ have been reported in literature.

Practical significance

Photochromic materials can be used to form smart windows that are capable of solar light modulation. This has the significance of providing a relatively inexpensive alternative to current smart window technologies employing mostly tungsten oxide or organic chromic materials. The incorporation of the photochromic nanoparticles in polymer gels would provide the

possibility of producing photochromic gel films based on stable inorganic photochromic materials.

Defendable theses

1. The photochromic properties of titanium dioxide are strongly related to its surrounding medium, given that photochromism is limited by the hole scavenging happening on the surface of the photochromic material.
2. The effect of photochromism on titanium dioxide is detectable not only by optical means but also by changes in the electric properties of the nanoparticles, as photochromism is accompanied by the photoaccumulation of electrons, which can change the electric properties of the material.
3. Doping of titanium dioxide with acceptor dopants has a strong positive influence on the photochromic properties of the material and increases the photodarkening rate.
4. It is possible to incorporate titanium dioxide into a transparent gel matrix while retaining the transmittance if the nanoparticles are small enough. This allows to obtain photochromic gels that are transparent in the un-darkened state.

APROBATION OF THE RESEARCH

Publications:

1. Eglītis, R., Šutka, A. Photochromic TiO₂/PEGDA organogels. *Photochem Photobiol Sci*, 2022. DOI: 10.1007/s43630-022-00183-6
2. Šutka, A., Eglītis, R., Kuzma, A., Smits, K., Zukuls, A., Prades, J.D., Fàbrega, C. Photodoping-Inspired Room-Temperature Gas Sensing by Anatase TiO₂ Quantum Dots. *ACS Applied Nano Materials*, 2021, 4, (3), pp. 2522–2527 DOI: 10.1021/acsnm.0c03089
3. Eglītis, R., Joost, U., Zukuls, A., Rubenis, K., Ignatāns, R., Avotiņa, L., Baumann, L., Šmits, Krišjānis., Hirsimäki, M., Käämbre, T., Šutka, A. Strong, Rapid, and Reversible Photochromic Response of Nb Doped TiO₂ Nanocrystal Colloids in Hole Scavenging Media, *ACS Applied Materials & Interfaces*, 2020, 12 (51), 57609–57618. DOI: 10.1021/acsmi.0c17902
4. Eglītis, R., Zukuls, A., Viter, R., Šutka, A. Kinetics of TiO₂ photochromic response in different hole scavenging solvents *Photochemical and Photobiological Sciences*, 2020, 19 (8), pp. 1072–1077

Patents:

1. Latvian patent: P-19-57 Andris Šutka, Anzelms Zukuls, Raivis Eglītis. Method for the enhancement of electrical conductivity of degenerated oxide semiconductors. Accepted 05.04.2022.
2. Latvian patent: P-19-86 Andris Šutka, Kaspars Mālnieks, Raivis Eglītis. Photoactive device for the selective detection of alcohols. Accepted 03.05.2022.

Presentations at conferences:

1. R. Eglītis, A. Šutka, Photochromism of titanium dioxide in various forms. 5th International conference of Applied Surface Science 25.04.2022 – 28.04.2022.
2. R. Eglītis, Photochromic TiO₂/PEGDA organogels. 62nd RTU conference “Materials Science and Applied Chemistry” 22.10.2021.
3. R. Eglītis, A. Šutka, An adaptive smart window device based on the photochromic effect and capable of electricity generation. 61st RTU conference “Materials Science and Applied Chemistry” 23.10.2020.
4. R. Eglītis, A. Šutka, A. Zukuls, Synthesis and photochromic properties of Nb-doped TiO₂ colloidal nanoparticles. 16th Zsigmondy Colloquium “Soft Colloids” 09.03.2020 – 11.03.2020.
5. R. Eglītis, A. Šutka, Photochromic properties of TiO₂. 60th RTU conference “Materials Science and Applied Chemistry” 24.10.2019.
6. R. Eglītis, A. Šutka, A. Zukuls, R. Viter, A Study of the TiO₂ photochromic response kinetics in different solvents. 6th Nano Today conference 16.06.2019 – 19.06.2019.

1 LITERATURE OVERVIEW

HVAC systems are consuming around a third of all of the electricity used in office buildings, in countries, that have a weighted average temperature above 15-20 °C (Fig. 1.1). Using blinds to block infra-red radiation (heat) increases the usage of artificial lighting as it also blocks visible light. Alternative to blinds is the usage of tinted films of reflective coatings. A downside to reflective coatings is no option for modulation of optical properties. In cloudy days it is needed to let more daylight in the building. The most advanced option is to use smart windows, that would modulate both visible and infrared light transmittance in response to external stimulus.¹ The smart window devices allow reduction of both electrical energy required for internal (room) cooling and for lighting (Fig. 1.1).² The change in light transmittance and absorption (in essence colour) as a response to a stimulus is called chromism and will be discussed next.

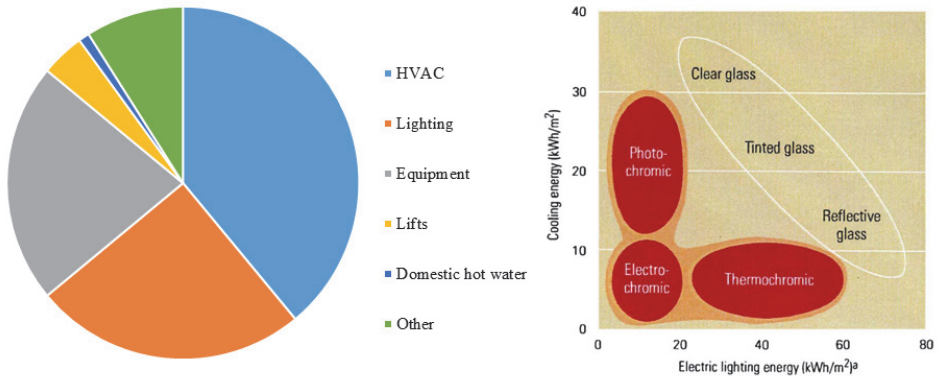


Fig. 1.1 Left) Typical office building energy consumption in Australia 2017. Data from the Australian Government Department of the Environment and Energy; **Right)** Chromic material comparison with conventional windows²

1.1 Chromic materials and their working principles

Chromism is materials ability to change its optical transmittance in response an external stimulus.³ These materials have been studied for over a century³ and there are several different kinds of chromic materials available commercially today (Fig. 1.2). Chromism is usually divided into subcategories, depending on the stimulus necessary for chromism to take place. These main categories are:

- Electrochromism
- Thermo-chromism
- Gasochromism
- Solvatochromism
- Photochromism

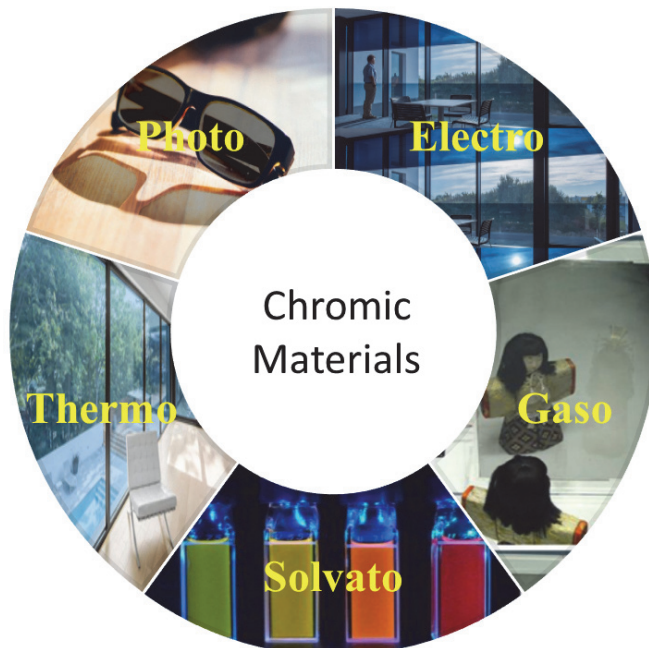


Fig. 1.2. Different types of chromic materials.

Chromic materials also can be divided according to whether they are inorganic, organic, or a mixture of both (i.e. hybrid). These can have different mechanism for chromism to manifest and result in different use cases with certain advantages or disadvantages, when compared to other chromic materials (Table 1).

Table 1.

Overview of the most common chromism types.

Chromism	Material	Mechanism	Advantages	Disadvantages	Uses
Electro	Inorganic	Redox reactions facilitated via electron injection/subtraction. This changes the crystalline structure of the material, resulting in chromism; ⁴ Transition metal oxides undergo reduction and cation intercalation, resulting in chromism. ⁵	User controllable chromism; ⁶ Can be combined with other electrochromic materials to increase the chromic effect.	A need for an electrolyte as well as TCO electrodes; Slow (with the exception of WO ₃) ⁵ chromism change. ⁷	Smart windows. ⁸
	Organic	Redox reactions facilitated via electron injection/subtraction. ⁹	Fast switching, electrochromic performance can be fine-tuned by group substitution. ⁹	Poor cycle lifetime and efficiency. ¹⁰	Auto-tinting rear-view mirrors. ⁹
Thermo	Inorganic	Crystalline phase change accompanied by a metal-to-insulator transition at a set temperature. ¹¹	Passive with chromism being expressed mainly in the NIR wavelength range. ¹²	Low visible light transmittance, hysteresis and stability problems. ¹³	Smart windows. ¹⁴
	Organic	Temperature induced conformation changes in the chromophore. ¹⁵	Ability to change the thermochromism temperature over a wide range. ¹⁶	No possibility of controlling the chromism.	Colorimetric thermometers; Adaptive camouflage and smart textiles. ¹⁷
	Hybrid	Transmittance change via ligand geometry change or spin crossover. ¹⁸	Capable of high temperature thermochromism up to 235 °C. ¹⁹	Prone to hysteresis and poor stability.	Colorimetric thermometers; Adaptive camouflage. ¹⁷
Gas	Inorganic	Reduction of the chromic material via exposure to reducing	Fast chromism over a wide wavelength	Require noble metal catalyst and the use of	Smart windows; colorimetric

		gases over a catalyst. ²⁰	range; Good stability. ²¹	flammable gases. ²¹	gas detection. ²⁰
	Organic	Reduction of the chromic material via hydrogen spillover from a catalyst. ²²	Fast chromism over a wide wavelength range. ²²	Require noble metal catalyst and the use of flammable gases, poor stability ²²	Smart windows, colorimetric gas detection. ²⁰
Solvato	Organic	Solvent-dependent internal charge transfer. ²³	High stability, purely dependent on solvent polarity. ²³	Can only be used in a solution.	Colorimetric water detection in organic solvents. ²⁴
	Hybrid	Solvent-dependent internal charge transfer. ²⁵	High stability, purely dependent on solvent polarity. ²⁵	Can only be used for solvents with small molecules. ²⁵	Colorimetric water detection in organic solvents. ²⁴
Photo	Inorganic	Photoreduction of the PC material in the presence of a hole scavenger. ²⁶	Passive chromism within a wide wavelength range. ²⁶	Slow and requires a hole scavenger to be present. ²⁷	Smart windows and photochromic eyewear. ²⁸
	Organic	Chemical bond formation/breakage when exposed to light. ²⁹	Fast and reversible chromism, possibility to tailor the transmittance change by using different functional groups. ⁹⁷	Lower stability when compared to inorganic PC materials. Chromism exhibited mainly in the visible wavelength range. ³⁰	photochromic eyewear and dyes. ²⁸
	Hybrid	Metal cation accelerated isomerization or charge transfer. ³¹	Fast and reversible chromism, possibility to tailor the transmittance change by using different functional groups. ³¹	Lower stability when compared to inorganic PC materials. Depending on the chromophore, can only exhibit chromism in the visible wavelength range. ³⁰	photochromic eyewear and dyes. ²⁸

Each of these will be discussed in more detail in the following chapters. There are also several other more obscure types of chromism (carsolchromism, piezochromism). These will be discussed very briefly at the end of the chapter. The prevalence of each of the different types of chromism is dependent on the field of materials science. In the case of smart windows, the main topics of research are: electrochromism, photochromism and thermochromism,² while in other fields (such as the textile industry) photochromism and thermochromism is more prevalent.³

Electrochromic materials. Electrochromism is the materials property to exhibit colour change when applying electric voltage. For optical modulation, they usually need to be incorporated into an electrochromic device, consisting of 5 layers: ion storage layer, electrolyte and electrochromic material film, sandwiched between two transparent conductor layers (as seen in Fig. 1.3).³²

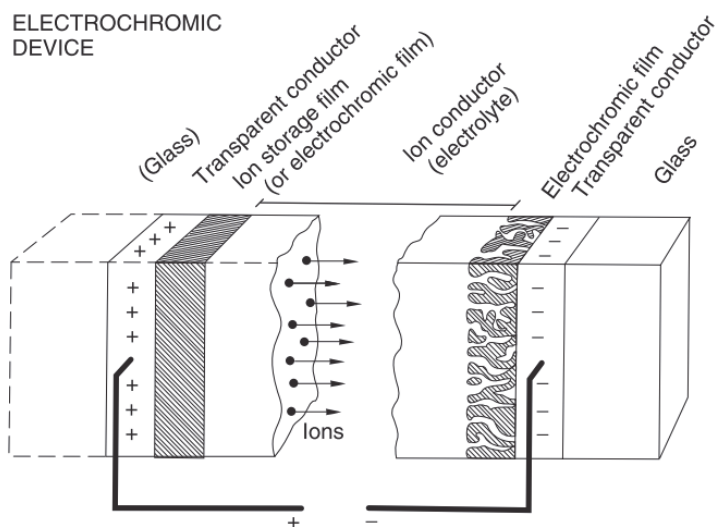
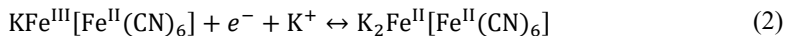
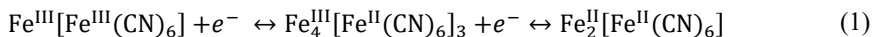


Fig. 1.3. Electrochromic device schematic.³²

There are many different types of electrochromic materials, ranging from organic complexes to inorganic oxides and complexes. In all cases, the electrochromism happens, because of reduction via electron or ion insertion. Usually, the reduced compound is the colored state, while the oxidized form is either colorless or coloured only slightly and with a different absorption spectrum. There are several main categories of electrochromic materials, each with their own specificities.

Prussian Blue is the main hexacyanide, that exhibits electrochromism with maximum absorbance ranging between 650-720 nm. The fact, that Prussian Blue exhibits this behaviour was first noted as early as 1704.³³ There are two main forms of Prussian blue: insoluble, with the formula $\text{Fe}^{\text{III}}_4[\text{Fe}^{\text{II}}(\text{CN})_6]_3$, and soluble, with the formula $\text{MFe}^{\text{III}}[\text{Fe}^{\text{II}}(\text{CN})_6]$ (M being an alkali metal cation).³⁴ In either case, this can be switched between a colored blue state and a transparent colorless state (equation (1) and (2)). This can also be further oxidized to a Prussian yellow $\text{Fe}^{\text{III}}[\text{Fe}^{\text{III}}(\text{CN})_6]$ state according to the equation (1).⁹



This is a stable of electrochromics, as this material is easy to synthesize and to produce thin films of it. Despite it being known for decades, even as recently as last year, research revealing the electrochromic mechanism has been published.³⁵ This is mainly due to the fact, that, PB has a fairly complex crystalline structure (shown in Fig. 1.4).

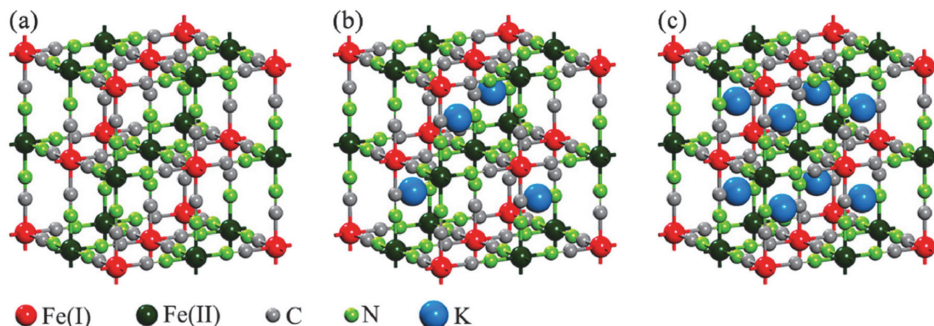


Fig. 1.4. Crystalline structure of **a)** Prussian yellow, **b)** Prussian Blue and **c)** Prussian White.³⁵

A downside to using Prussian Blue, that has kept it from being widely used commercially is their bleached state stability as it can trap water and hinder the electrochromic reactions in PB.³⁶ The stability of PB can be increased by combining it with graphene.³⁷

Viologens: these aromatic organic molecules are derivatives of 4,4'-bipyridinium salts (generalized chemical structure can be seen in Fig. 1.5), that are switched between a colored bication and a cationic radical. These compounds are often also called paraquats (PQ) due to the first commercialized 4,4'-bipyridinium electrochrome – methyl viologen.⁹ They undergo redox reactions induced via the injection or removal of electrons.

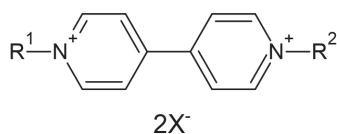


Fig. 1.5. Generalized chemical structure of viologen. R^1 and R^2 – different alkyl and aryl groups.

These viologen compounds have the added benefit, that the anions can be switched or even made from a polymer backbone, allowing to incorporate viologens chemically into gels or polymer films. Furthermore, the reduced form of PQ is one of the most stable radicals and can be made as air stable salts.³⁸ From the 3 different forms of viologen, the dication is usually colorless, while the reduced radical cation has a vibrant color. The fully reduced form usually has only a very weak color (i.e. low light absorption).³⁹ The color of the radical cation is strongly dependent on the anion, solvent and the R^1 and R^2 groups.⁹

A lot of work has been done both in terms of viologen synthesis as well as electrochromic viologen material development.¹⁰ There has been both research for the synthesis of asymmetric viologens,⁴⁰ viologen ionic gels⁴¹ and even viologen incorporating co-polymers⁴². However, these materials have a reduced solubility in most solvents. Furthermore, electrochromic devices have a poor cycle lifetime as well as poor efficiency.¹⁰

Conjugated electrochromic polymers are polymer materials with π -electron systems, capable of absorption change under an applied voltage. One such material is the well-known conductive polymer PEDOT.⁴³ The color contrast of PEDOT, however, is not satisfactory for any practical applications. The color contrast can be increased by co-polymerizing with viologens (tying into the previous electrochrome group).³⁹ Similarly, other polythiophenes can be used as electrochromes (an array of different polythiophenes can be seen in Fig. 1.6)⁴⁴ as well as heterocyclic polymers other than polythiophenes (for example phenylamines).⁹

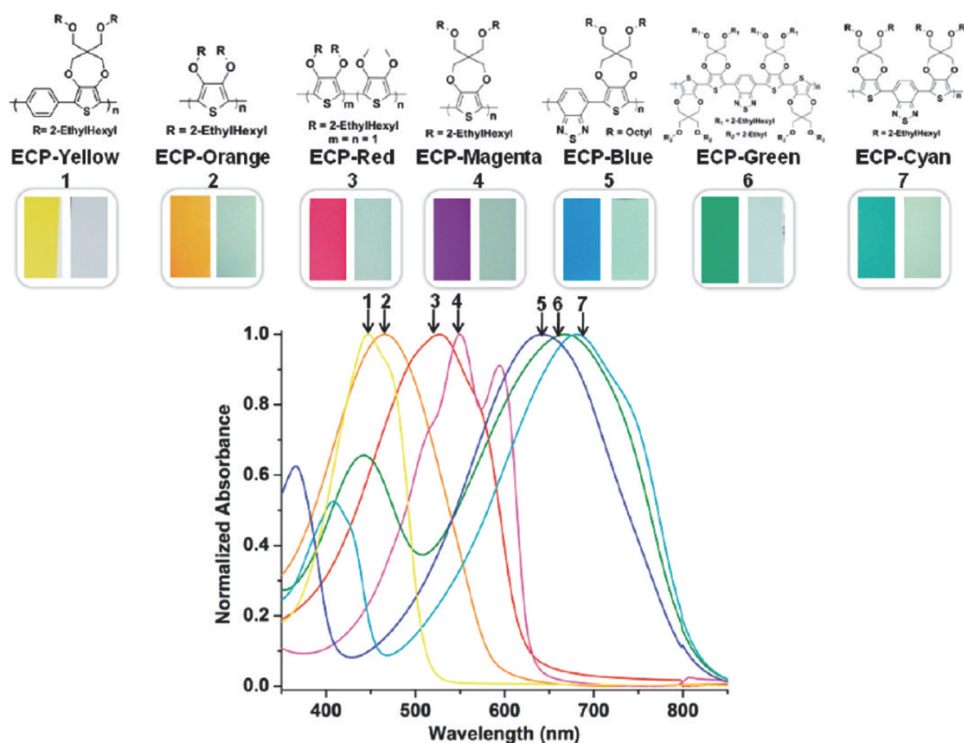


Fig. 1.6. Colour of different polythiophenes.⁴⁴

A drawback to these polymers is, that depending on the electrolyte used, these can require post-modification in order to avoid delamination or dissolving.⁴⁵ Furthermore, the color switching speed (kinetics) for polymers is slower than for other types of electrochromic materials.⁴⁶

Electrochromic metal oxides. Most electrochromic materials are metal oxides, all of these being transition metal oxides. This is because transition metal ions have unoccupied *d* orbitals. These orbitals are influenced by the surrounding anions, resulting in splitting of these orbitals. Light to be absorbed by electrons moving between these splitted orbitals.⁴ These can be further divided into categories (Fig. 1.7), depending on whether the oxide colours under oxidation or

reduction: cathodic coloration happens under reduction accompanied with ion insertion and anodic coloration happens under oxidation and ion extraction. It is also of note, that vanadium oxides are intermediate, meaning that they can act both ways.⁴⁷ That being said, the model electrochromic oxide is tungsten oxide, that has been studied for more than 50 years.⁴⁸ Also, of interest are NiO, IrO_x, V₂O₅ as well as MoO₃.³³

ELECTROCHROMIC OXIDES:

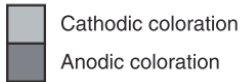
																															
H																	He														
Li	Be															B	C	N	O	F	Ne										
Na	Mg															Al	Si	P	S	Cl	Ar										
K	Ca	Sc	Ti	V	Cr	Mn	Fe	Co	Ni	Cu	Zn	Ga	Ge	As	Se	Br	Kr														
Rb	Sr	Y	Zr	Nb	Mo	Tc	Ru	Rh	Pd	Ag	Cd	In	Sn	Sb	Te	I	Xe														
Cs	Ba	La	Hf	Ta	W	Re	Os	Ir	Pt	Au	Hg	Tl	Pb	Bi	Po	At	Rn														
Fr	Ra	Ac																													

Fig. 1.7. Electrochromic metal oxide table⁹

The most widely used electrochromic oxide is WO₃, because it has one of the highest intensity color changes (i.e. one of the greatest absorptions).⁴⁹ It is a metal oxide that can color both when it is in an amorphous state as well as in a crystalline state with the hexagonal WO₃ polymorph being the best suited for electrochromic thin films.⁵⁰ The coloration is cathodic, meaning that it occurs upon electron injection into the material.⁵¹ This results in the reduction of W⁶⁺ to W⁵⁺. To preserve charge neutrality of the material, small cations (typically H⁺ protons, Li⁺ and Na⁺ cations) adsorb and intercalate into the crystalline lattice.⁵² This is made possible by the relatively open crystalline structure of the different WO₃ polymorphs, especially hexagonal WO₃. This results in the formation of tungsten bronze, with the formula A_xW_{1-x}O₃ (A being a proton H⁺ or alkali cation).⁵³ It should also be noted, that the coloration rate can be increased by increasing the surface area of the thin film, as mesoporous WO₃ thin films have much higher withing rates compared to dense films.⁵⁴

The electrochromic performance, i.e. coloration rate and total transmittance change of WO₃ can be improved by creating heterostructures with other oxides such as WO₃-TiO₂⁵⁵, WO₃-MoO₃⁵⁶ or WO_{3-x}-NbO_x.⁶ For example, the enhancement of the lifetime under electrochemical cycling has been observed due to the stabilization of a disordered structure of WO₃ by TiO₂.^{57, 58} The WO₃ deterioration occurs during the cycling which results in reduced capacity for lithium accumulation.⁵⁹ Mixed oxide is WO_{3-x}-NbO_x exhibit independent NIR and VIS modulation (shown in Fig. 1.8).⁶ Here, WO₃ nanoparticles were dispersed in amorphous NbO_x. At a high applied voltage (4 V), the thin film is transparent. However, when the voltage is lowered to 2.3 V, WO_{3-x} is charged and adsorbs NIR radiation, while at 1.5 V NbO_x is reduced at starts to adsorb vis light.⁶

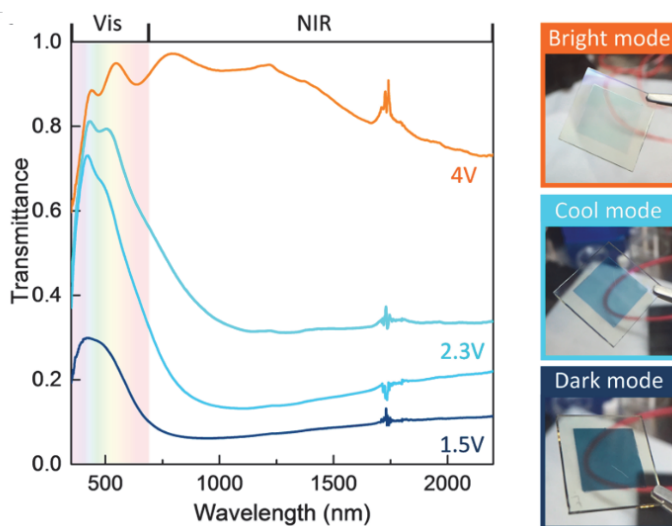


Fig. 1.8. $\text{WO}_3\text{-NbO}_x$ dual mode electrochromism.⁶

One of the most popular anodic electrochromic materials is NiO. NiO is a large band gap semiconductor with a band gap of 3.6 eV.⁶⁰ As an anodic electrochromic material, coloration happens, when electrons are extracted from it, leading to oxidation of Ni^{2+} to Ni^{3+} .⁶¹ Furthermore, there is also evidence, that further oxidation of Ni^{3+} to Ni^{4+} also happens.⁶² This is of note, because it can be used in an electrochromic device as a good counter electrode to cathodic electrochromic materials, such as WO_3 . For successful electrochromism of NiO hydroxyl groups need to be adsorbed on the surface. To account for the change in the charge of Ni^{2+} to Ni^{3+} , the hydroxyl groups will desorb either hydrogen cations or water molecules, depending on the type of electrolyte.⁶⁰ NiO can also be modified via doping by such metals as Al, Si, Zr, Nb and Ta. These have the effect of lowering the absorbance of the bleached state of the thin films.³² These higher valence dopants have the effect of donating excess electrons and thus filling any electron holes present in the NiO lattice. This leads to increased transmittance of the bleached state.⁶³

The main drawback of the vast majority of inorganic electrochromic materials (except for tungsten oxide)⁵ is their relatively slow switching speed of tens of minutes to achieve a photodarkened state. This has been attributed to low electrical conductivity as well as slow ionic transport.⁷ The main drawback to all electrochromic materials is the requirement of additional component such as counter electrodes and an electrolyte as well as the need for electrical current to induce the change in the transmittance.

Usage of electrochromic materials. Electrochromic materials are used in such applications as smart windows, electronic paper and displays, anti-glare mirrors and even eyewear. Viologens were the first electrochromic materials, used in anti-glare rearview car mirrors as early as the late 1970s⁹ while TMO based electrochromic materials were and still are the main materials used in energy-efficient fenestration i.e. smart windows.⁸ The polymer based electrochromic materials have been used to produce thin segmented displays⁶⁴ and are available commercially. Electrochromic eyewear has been researched on and off for as long as smart

windows and are basically miniature versions, that use polymer based electrochromes instead of TMOs, because for their increased flexibility.⁶⁵

Thermochromism. The materials colour change accompanying temperature changes is called thermochromism. This is usually accompanied either by a chemical structure change (for organic thermochromic molecules) or a polymorphic change (inorganic thermochromic materials) as well as a change in accessible d-d transitions, that change the resulting absorption.¹¹ There are also metal complexes, that can exhibit thermochromism such as Ni (II)-isopropylamine complexes.⁶⁶

The staple inorganic thermochromic materials are vanadium (IV) oxide polymorphs. Vanadium itself is a relatively abundant material, being widely used metallurgy to produce impact resistance steel.⁶⁷ VO₂ is a costly transition metal oxide that is subjected to a polymorphic change between a monoclinic and tetragonal rutile phase at around 68 °C.¹² This phase change results in a metal-insulator transition with the metal phase being present above the transition temperature. This in turn, results in a change in the NIR light transmittance, while keeping visible light transmittance relatively unchanged. The change in NIR light transmittance can be very substantial, reaching values of up to 70% at 2500 nm. The MIT temperature can be changed, by varying the synthesis conditions. As shown by *Abdollahi* and his colleagues, by changing the hydrothermal synthesis time and reactants can change the phase composition and, in turn, vary the phase transition temperature can be varied from 68 °C to 5 °C.¹² This can also be modified by layering with TiO₂ or doping with W⁶⁺⁶⁸ or Nb⁵⁺⁶⁹ to increase the transmittance change in the infrared spectral region (see Fig. 1.9).⁷⁰ Further of note is that, these coatings have a change in reflectance due to the metallic nature of the VO₂ rutile phase, not just transmittance.¹³

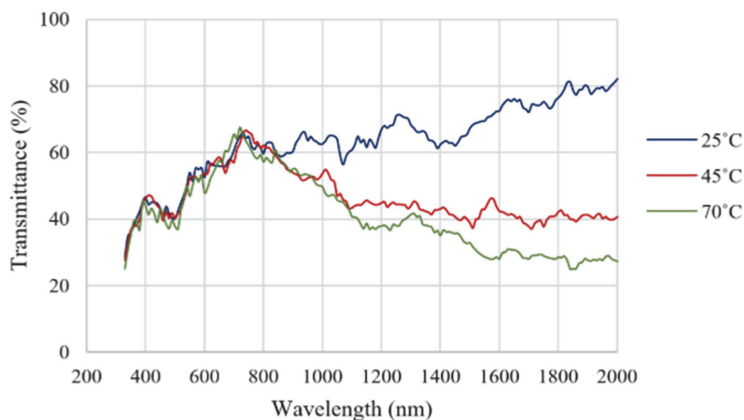


Fig. 1.9. Transmittance of TiO₂ @ W-VO₂ thin films at different temperatures.⁷⁰

VO₂ has several mayor drawbacks. Transmittance in the visible region is poor, with transmittance values <60%. Also, since thermochromism expresses via a crystalline phase change, hysteresis is present within in the heating/cooling cycle, that can vary the MIT temperature by 12-20 °C.¹³ The stability of the thermochromic coatings also is not very good, with VO₂ slowly being oxidized to V₂O₅. This drawback is further enhanced, when the MIT temperature is changed either through doping or synthesis conditions. Toxicity is also of a

concern. Although not fully known, for V^{4+} , the both other form of vanadium (V^{5+} and V^{3+}) are categorized as toxic.⁷¹

Organic thermochromic materials typically express their temperature dependence via structural deformation. An example of this is the reversible thermochromism shown by polydiacetylene/melamine cocrystals (Fig. 1.10).¹⁵ This is achieved via conformation changes in the polydiacetylene. The presence and neat stacking of melamine allowed the conformational changes to be reversible and as such attributed to the reversibility of the materials thermochromism. A similar effect can also be achieved by substituting melamine with inorganic complexes, such as zinc-aluminum double hydroxides.¹⁸ By varying the side chain length of the polydiacetylene the color transition temperature can be varied from 50-90 °C, while a similar polydiacetylene composite with ZnO nanoparticle, exhibited a reversible thermochromic transition, whose transition temperature could be varied from 10-90 °C.¹⁶

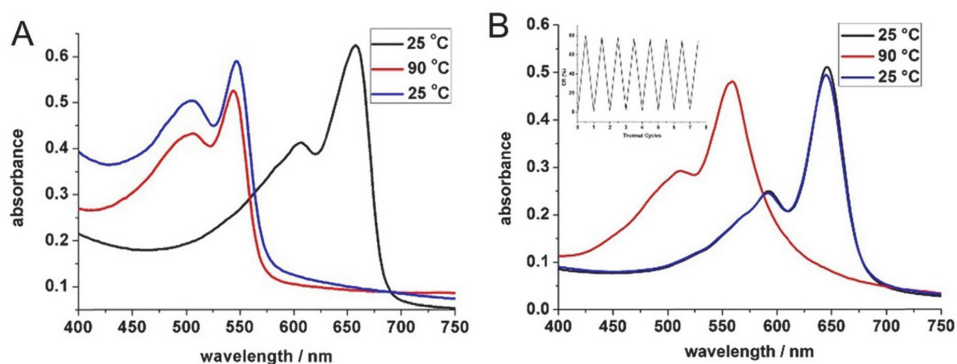


Fig. 1.10. Absorbance spectra before heating, after heating and again after cooling for samples of polydiacetylene and melamine cocrystals.¹⁵

Metal complexes can also exhibit thermochromism.¹¹ For example, $[\text{NH}_2(\text{C}_2\text{H}_5)_2]\text{CuCl}_4$ exhibits a reversible colour change from deep green to yellow at 38 °C.⁷² The transition in these complexes is either due to a phenomenon called spin crossover or the change in the ligand geometry.⁷² Spin crossover is a phenomenon, in which the spin of the metal ions electron is switched from a high-spin state to a low-spin state and vice versa. This is mainly seen in Fe (II) complexes, but can also happen in other transition metal complexes as well.⁷³ Ni (II) complexes have been shown to exhibit reversible thermochromism over a wide temperature interval, ranging from 90 °C all the way up to 235 °C and has been attributed to structural changes in the complex.¹⁹

A downside to thermochromic materials is the inability of decoupling the switching of visible and infrared light. Furthermore, these materials possess no options of controlling the thermochromic effect itself, without actively changing the temperature of the material.

Usage of thermochromic materials. Thermochromic materials are used to visualize temperature, in for example, colorimetric thermometers. More recently, however, thermochromic pigments have been researched to implement in adaptive camouflage, to switch between desert and forest camo¹⁷ and clothing in general. There has also been research into implementing thermochromic pigments in cosmetics, that, combined with heating, could allow change in the applied product on the fly.⁷⁴ By far the most widely studied field for thermochromic material application are smart windows.¹⁴ Recently, research articles have also

been published, examining the combination of thermochromism with passive radiative cooling – a material property used in space to cool spacecraft electronics.⁷⁵

Gasochromism is the materials possibility of changing its color, when exposed to a certain gas. Here again, one of the hallmark materials is WO_3 , while the most used gas is hydrogen.²⁰ However, additional gasochromic materials include different kinds of metal oxides (VO_x ⁷⁶, MO_x such as Pd-doped TiO_2 ⁷⁷, MoO_3 ⁷⁸, $(\text{MoO}_3)_{1-x}(\text{V}_2\text{O}_5)_x$ ⁷⁹, silver/nickel ammonium phosphomolybdate⁸⁰, $(\text{Ti-V-Ta})\text{O}_x$ ⁸¹, $\text{Ni}(\text{OH})_2$ ⁸², peroxopolytungstic acid⁸³, as well as metal alloys (Mg-Ni²¹). When talking about gases, outside of hydrogen, such gases as VOCs (ethanol⁸¹ and cyclehexane⁸⁴), NO_2 ⁸⁵, H_2S ⁸⁰, NH_3 ⁸⁶, CO and Cl_2 ⁸², have been used in gasochromic experiments. In most cases, catalytic metal nanoparticles, such as Pd⁷⁷, Pt⁸⁴ or Au⁷⁸ need to be added for H_2 spillover and for the gasochromism to take place.

For WO_3 and hydrogen, hydrogen intercalates into the crystalline lattice of WO_3 and also reduce W^{6+} to W^{5+} , producing tungsten bronze H_xWO_3 .²¹ However, this, by just exposing WO_3 to hydrogen gas, happens only at elevated temperatures (upwards of 400 °C). More than 50 years ago, it was shown, that, in order to have this happening at room temperature, additional components are needed in order to split the hydrogen molecules into hydrogen ions.⁸⁷ This can be done by adding a thin layer of platinum and can further be enhanced by adsorbing water into the WO_3 .²¹ This concept has already been implemented in a relatively large scale (0.6 x 1.1 m) window, with a thin film of WO_3 and Pt on top (Fig. 1.11).

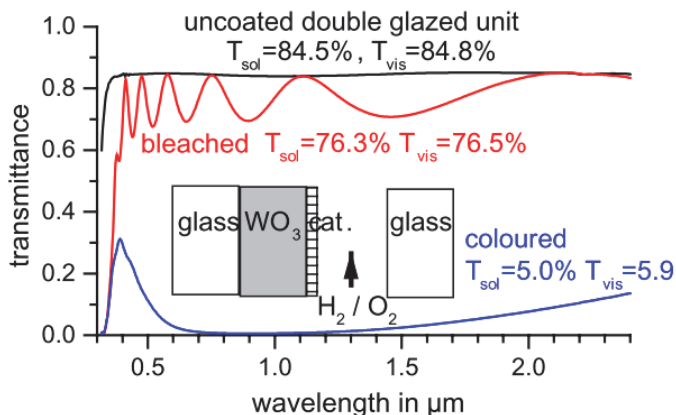


Fig. 1.11. Gasochromic WO_3 layer with a thin layer of Pt on top sandwiched between two panes of glass.²¹

Several organic gasochromic materials and composites have been reported. These materials express their gasochromic properties, when catalyst (such as Pt) nanoparticles are dispersed in the material. When this kind of composite is exposed to hydrogen, the Pt nanoparticle dissociate hydrogen molecules into atoms. The atomic hydrogen then migrates to the polymer matrix as per the hydrogen spillover effect⁸⁸ and facilitates the reduction of the matrix, causing a change in color. *Chih-Wei Hu et al* has reported on the gasochromic properties of electrochromic PANI:PSS films in conjunction with Pt NPs.²² Hydrogen facilitated reduction of PANI fragments from the emeraldine salt form to the reduced leucoemeraldine form, causing a change in colour (Fig. 1.12). This composition resulted in a maximum transmittance change of 63%

for a 410 nm thin film, when exposed to a 4% H₂/Air mixture. Later, the same group also reported on the usage of another electrochromic material as a gasochromic one – Prussian blue. They managed to switch Prussian blue to Prussian white upon exposure to a 4% H₂/Air mixture.⁸⁹ This also had a much higher cycling stability (over 200 cycles as compared to just 7) and higher maximum transmittance change, when compared to the PANI:PSS system. This also had the benefit of being more cost effective (even compared to WO₃ films).⁸⁹

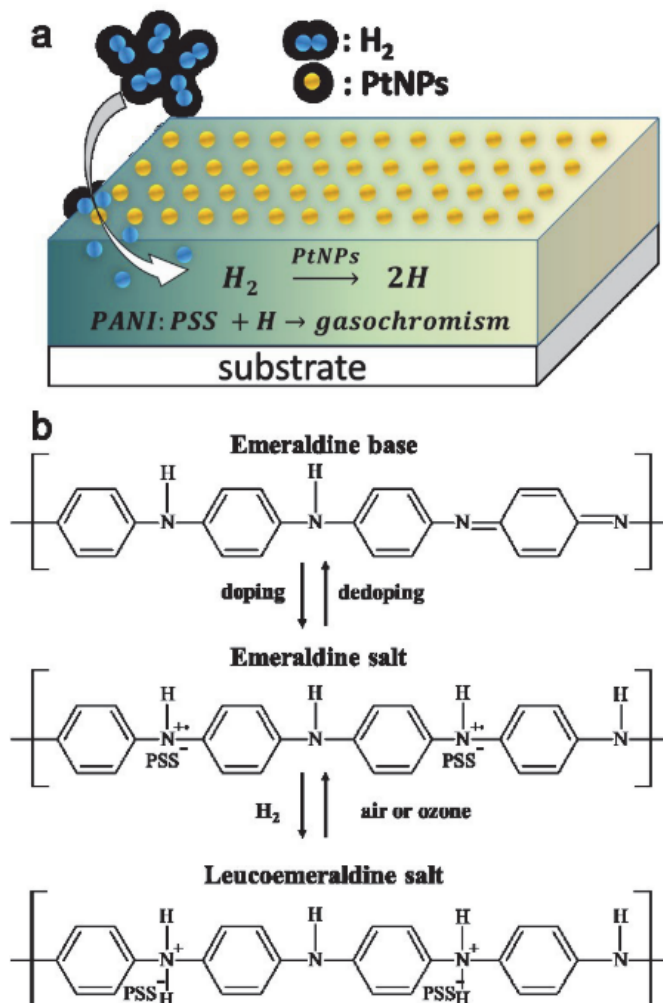


Fig. 1.12. a) Schematic illustration of the gasochromic behaviour of the PANI:PSS/PtNPS thin film on exposure to H₂; b) the proposed redox mechanism.²²

The usage of hydrogen in gasochromism, although showing good results, has the inherent flaw of using an extremely flammable gas, that has the nasty property of being able to permeate a lot of different materials. That being said, research has shown that gasochromic material based smart windows can consume less electricity than similar electrochromic windows.⁹⁰ An alternative to hydrogen would be to use more benign gases, such as ethanol

vapors, though current coloration efficiency is severely lacking, when compared to WO_3/H_2 systems.⁹¹

Usage of gasochromic materials. Gasochromic materials are lot less studied when compared to electrochromic materials, with the main applications being smart windows⁹⁰ and colorimetric gas detection (mainly hydrogen).²⁰ Hydrogen gas detection is especially important, as it allows to easily detect leaks in gas lines⁹² that can easily lead to dangerous situations if left undiscovered.

Solvatochromism is the materials capability of exhibiting an either bathochromic (red shift) or hypsochromic shift (blue shift) in its absorption peak, when dispersed in different solvents. The most popular such dye is Reichardt's dye⁹³ (Fig. 1.13 a), that is classified as being a class I solvatochromic compound exhibiting negative solvatochromic behaviour meaning a hypsochromic shift in response to increasing polarity. A classic example of a class II solvatochromic compound, that also exhibits a positive solvatochromic behavior is Effenberger's dye (Fig. 1.13 b).⁹⁴ Reichardt's dye is also the basis for the $E_T(30)$ solvent polarity scale.⁹⁵

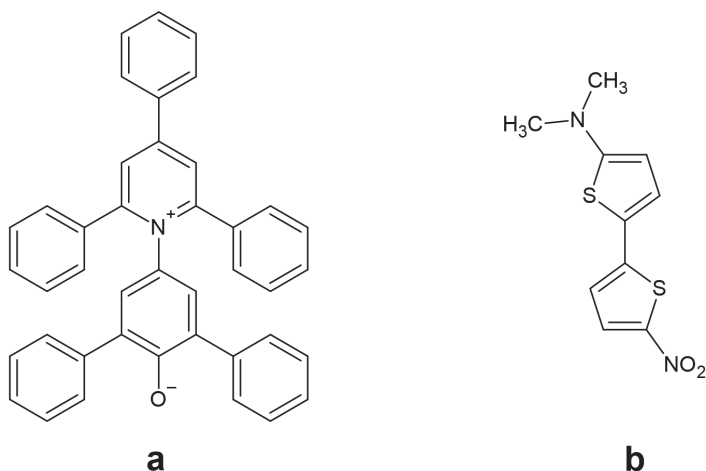


Fig. 1.13. Reichardt's dye (a) and Effenberger's dye (b).

In all cases, a solvatochromic probe molecule consists of electron donor and acceptor moieties, connected by an unsaturated bridge.⁹⁶ Class I molecules are in a charged zwitterionic state as their ground state while class II molecules are neutral.⁹⁷ Solvatochromism is possible, because of a solvent-dependent internal charge transfer. This charge transfer is dependent on the polarity of the solvent (an example can be seen in Fig. 1.14), hence the solvatochromic effect.²³

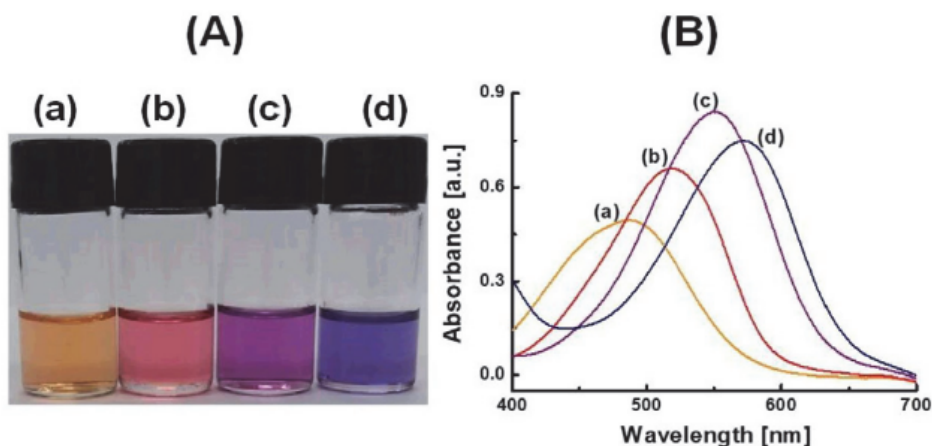


Fig. 1.14. Solutions (A) and UV-vis spectra (B) of a diazo solvatochromic compound in (a) methanol; (b) toluene; (c) dimethoxyethane; (d) acetophenone.⁹⁷

There is also a type of organic molecules called merocyanines, that can exhibit both positive and negative solvatochromism (called inverted solvatochromism), depending on the polarity of the solvent in low-polarity solvents.²³ To explain this phenomenon and solvatochromism in general, several theories have been presented. The main being the cyanine-limit model⁹⁸ and the complementary generalized reversal model.²³

The generalized reversal model postulates, that all pyridinium phenolate betaine dyes (to which Reichardt's dye belongs to) can possess solvatochromism inversion, given a wide enough solvent polarity interval. However, often enough this interval is wider than what is physically possible, and as such, these inversions are deemed "imaginary".²³

Extensive work was been done by *Letrun, et.al.*⁹⁶ in the transition between states in pyridinium and pyrylium phenolates, in order to understand better the structural impact on the solvatochromic behaviour. They have shown that these kinds of compounds also exhibit a twisting around the C-C bond connecting both rings, that impacts the polarity of the compound.

Solvatochromism isn't exclusively reserved for only organic molecules. On the contrary – solvatochromism has also been reported for Tungsten²⁵ and Zinc-MOFs⁹⁹ and even for carbon quantum dots.¹⁰⁰ *Lee, et.al.* reported on the chromic properties of $\{[Zn_2(Htpim)(3,4\text{-pydc})_2] \cdot 4DMF \cdot 4H_2O\}_n$ MOF, showing that it possesses solvatochromic behaviour, changing color from pale to dark yellow, when immersing in different organic solvents. This also resulted in a change in the crystalline structure (as evidenced by XRD).⁹⁹ *Pramanik, Biswas and Kumbhakar* reported on the solvatochromism of carbon quantum dots, obtained from *Aegle marmelos*. These were shown to possess solvatochromic photoluminescence in the presence of organic solvents.¹⁰⁰ Phenylene-(poly)ethynylene has been used by *Guan, et.al.* is another example of a solvatochromic material, that has been used to sense water traces in a whole list of different organic solvents.²⁴ *Ascherl, et.al.* have also studied COFs capable of solvatochromism (Fig. 1.15). While the authors classify the colour change as solvatochromism, these materials are capable of colour change when just exposed to the solvent vapors, akin to gasochromism.¹⁰¹

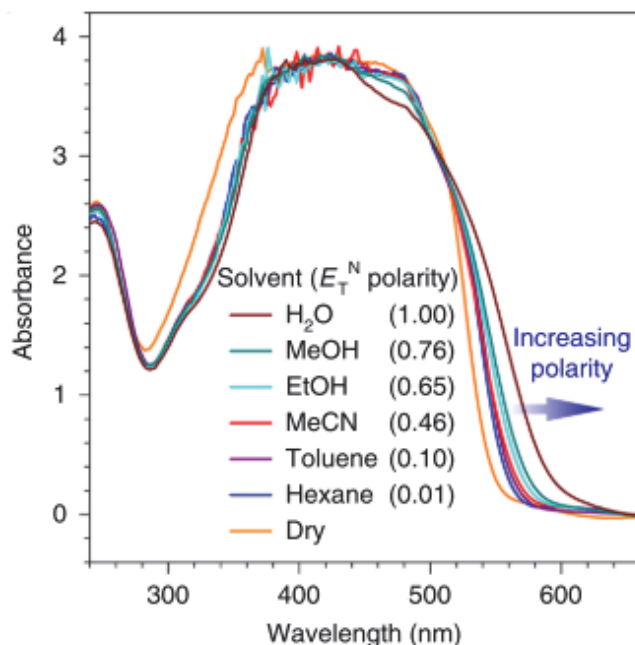


Fig. 1.15. Pyrene thieno-thiophene COF solvatochromism.¹⁰¹ Reproduced under the terms of the Creative Commons CC BY license.

Lastly, there has also been research into combining both solvatochromism with electrochromism, producing different reduced state colors in different solvents. Zhang, *et.al.* have done research into producing an array of aryl ketones.¹⁰² The color can be changed by modifying the phenyl rings with different substituents.

Usage of solvatochromic materials. Solvatochromic materials, however, are not suitable for smart window application due to low influence on total transmittance of the system. Solvatochromic materials can easily be used as colorimetric indicators for titration, as they are for the most part, pH independent. This can be a boon or a bane, depending on the circumstance.¹⁰³ They can also be used for solvent identification. However, to achieve this, a lot of additional information would be necessary (spectral deconvolution, database comparison, etc.). Solvatochromic materials have been studied for their possible usage in textiles, being able to change color when wet, for example.¹⁰⁴ There have also been studies on colorimetric cyanide detection¹⁰⁵ as well as to detect moisture in organic solvents.²⁴

Photochromism. The property to change a materials transmittance under irradiation of a certain kind of light (usually UV light) called photochromism. As it is with thermochromism, photochromism is a passive property, meaning that no other components are required (normally) for photochromism to take place (except for light). This is a contrast to all the other types of chromism (electrochromism, solvatochromism and gasochromism) and allows one to prepare wholly passive thin films that modulate the transmitted light automatically.⁶⁹ However, the caveat to this is that they cannot be controlled. In the literature review different kinds of photochromic materials will be categorized by their nature: organic, inorganic as well as hybrid materials (also including organometallic compounds).

Organic photochromic materials are aromatic compounds capable of going through reversible chemical reactions when exposed to light. For organic photochromophores, there are several categories: type T or P, positive and negative photochromism as well as unimolecular and bimolecular photochromism.²⁹ Type T and P photochromism distinguishes between whether the back reaction is driven by light (P) or temperature (T). Positive photochromism occurs when form A (initial form of the compound) adsorbs light at a shorter wavelength than the form B (resulting form) of the compound. The opposite is true for negative photochromism, while unimolecular and bimolecular photochromism is self-explanatory. An overview of the most popular organic photochromic dye types together with structures of both forms (A and B, colourless and coloured) can be seen in Fig. 1.16). Most organic photochromophores undergo some sort of cyclization reaction (ring closing), with the exception being azobenzene and its derivatives as well as Biindenylidene with its derivatives. Azobenzene undergoes a *cis-trans* photoisomerization reaction, while biindenylidene becomes a biradical.

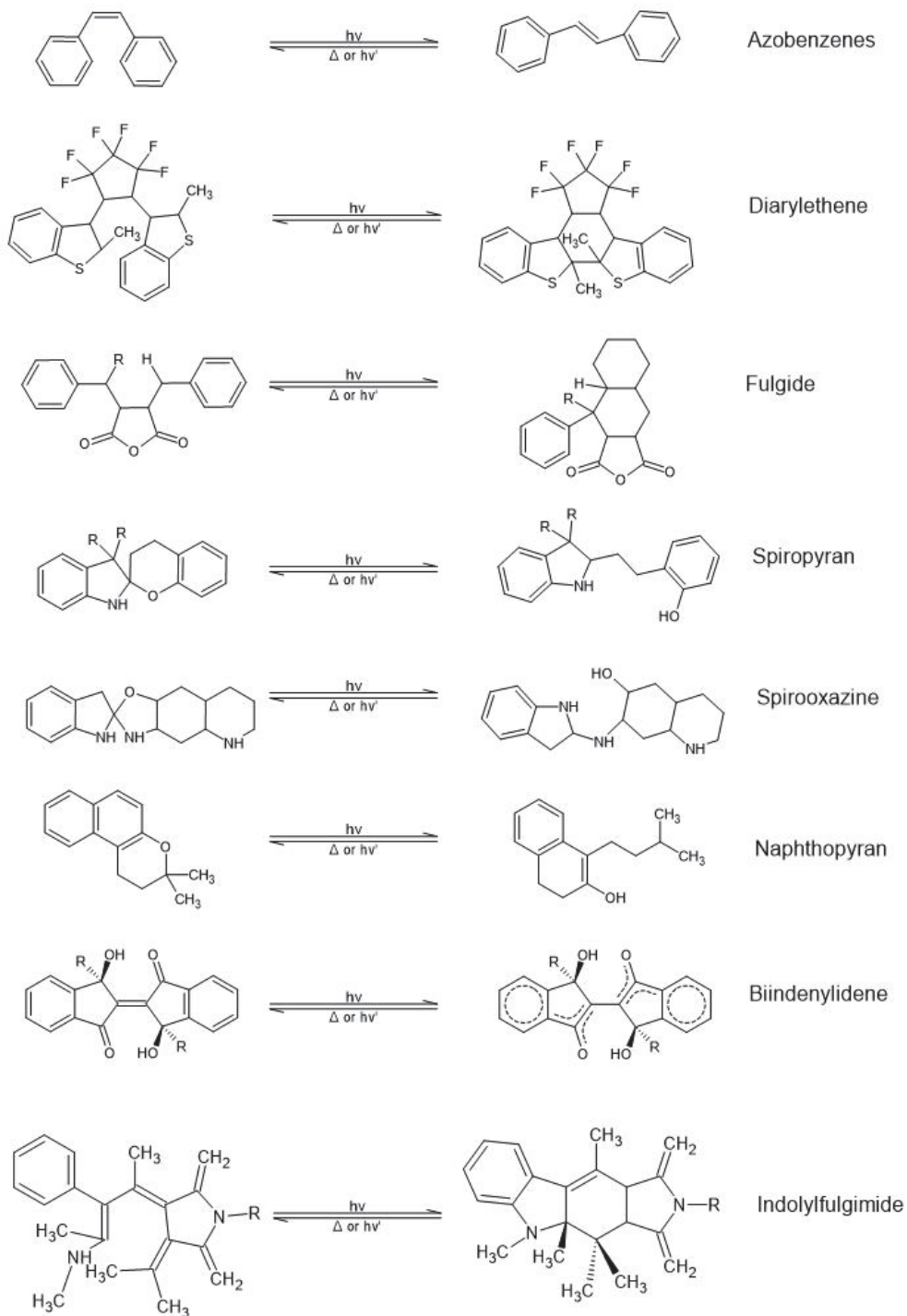


Fig. 1.16. Different types of organic photochromic molecules and their relevant photochemical reactions¹⁰⁶⁻¹⁰⁹

Some of the photochromic organic compounds exhibit photochromic behaviour only in a crystalline solid state and when there is sufficient room around each molecule to move. This can be achieved either by adding large functional groups or by integrating (placing) the photochromic molecule into a cyclodextrin molecule, that would act as spacers. Such compounds are for instance *N*-3,5-Dihalosalicylideneanilines, that become photochromic in the solid state, when adding a *tert*-butyl group to the 4-position of the aniline ring.¹¹⁰ Another example, is 2-hydroxy-5-methyl-isophtalaldehyde, that became photochromic, when complexed with β -cyclodextrin.¹¹¹

Silver halide photochromism. The first commercially available photochromic materials consisted of borosilicate glass with Cu^+ and silver halide dispersed in the glass. This composite, when irradiated by UV light, exhibited the photoreduction of silver ions, resulting in silver nanoparticle formation via equation (3):²⁸



The silver nanoparticles absorb light, causing the glass to darken. When the composite is kept in the dark, the nanoparticles again dissolve. Here, the properties of the photochromic glass are influenced by the choice of silver halide as well as the heat treatment of the glass itself. Furthermore, the size of the silver nanoparticles needs to be controlled with a range of 5-30 nm being considered optimum to avoid light scattering.¹¹²

Hybrid organic-inorganic photochromic materials. There are multiple different kinds of hybrid photochromic materials: nanoparticles with additional organic surface ligands, organic photochromic molecules in inorganic matrices or organometallic complexes. The complexes are different kinds of transition metal ions with arene ligands.²⁹ Most recently, cobalt, nickel and zinc complexes with viologen ligands have been reported.¹¹³ For these materials electron transfer happens between the ligand and metal ion. For example, it has been shown that the formation of a Ag^+ -azobenzene complex can accelerate the isomerization of the azobenzene unit, accelerating the photochromism of the ligand.³¹

Nanoparticle ligand hybrids function with the ligand being photochromic, in which case the nanoparticles help to enhance the photochromism. An example of this are naphthopyran-Ag nanoparticle composites, that exhibited increased photochromic behavior when compared to the naphthopyran alone.¹¹⁴ Another option is that the ligands act as dyes that either sensitize the nanoparticle to visible light or act as hole scavengers to increase the photochromic effect of the nanoparticles, for example different composites TiO_2 with Ru(III) complexes.¹¹⁵

Photochromic organic molecules can also be dispersed into amorphous materials (such as amorphous SiO_2), to keep the molecules in a dispersed state.¹⁰⁶ The usage of ormocers as the matrix allows also for the possibility of further enhancing the photochromic performance of the chromophores through π - π conjugation.

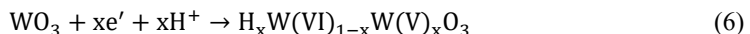
The downside of most photochromic materials is their slow chromic response, when compared to other types of chromics, especially electrochromic materials. Furthermore, organic photochromic materials are relatively unstable. Similarly, to thermochromic materials, there is also no clear way of influencing the photochromic process of a ready-made material.

Transition metal oxide photochromic materials are studied more extensively than organic photochromic materials, due to their better stability,³⁰ as well as due to their lower cost when

compared to other inorganic photochromic materials, such as metal halides of rare earth metal compounds. Despite this, TMO photochromic materials aren't widely used for photochromic applications, because they don't meet the requirements of sustainability and environmental safety or performance.

The most widely known TMO photochromic materials are nickel oxide (NiO),¹¹⁶ tungsten oxide (WO₃),¹¹⁷⁻¹²³ molybdenum oxide (MoO₃),^{122,124-126} vanadium oxide (V₂O₅),¹²⁷ niobium oxide (Nb₂O₅),¹²⁸ and titanium oxide (TiO₂).^{115,129,130} Composites have also been examined, such as, rGO-TiO₂-WO₃.¹³¹ The photochromic properties of TiO₂, along with a whole host of other notable transition metal oxides (Nb₂O₅, CeO₂, Ta₂O₅, V₂O₅, Pr₂O₃ and Bi₂O₃) were reported a century ago (1921), by *Carl Renz*¹³² while WO₃ photochromism was first reported in 1973 by *S. K. Deb*.¹²³ Out of these, W and V are considered scarce elements¹³³ while Ni is associated with health risks.¹³⁴ On the other hand, ZnO, that is also photochromic and is environmentally friendly.¹³⁵ However, ZnO is unstable and prone to photocorrosion¹³⁶ and recrystallization under ambient atmosphere conditions.¹³⁷ It is not studied as a photochromic material by itself and is relegated mostly to combination with other TMOs, such as MoO₃.¹³⁸

In most cases, the base mechanism of photochromism for transition metal oxides is the same. The coloration is governed by a redox process due to optically excited electron-hole pairs.²⁶ Tungsten oxide, being an exemplary material, has received a broad interest, and several theories pertaining to its photochromism have been proposed, such as F-center¹²³ and small polaron theories.¹³⁹ For the photochromism to take place, the film of WO₃ needs to be made mainly out of *h*-WO₃ and have at least some amount of oxygen vacancies present. When WO₃ is irradiated with UV light, electron-hole pairs are formed (4). The holes react with adsorbed water (5) creating protons that intercalate into the WO₃ lattice while electrons reduce W⁶⁺ to W⁵⁺ (6), causing coloration to appear.¹⁴⁰



To enhance the photochromic response of different transition metal oxides, band gap engineering is one of the key methods to employ. One of the simplest interpretations is, that by introducing new energy levels in the band gap, that can accommodate photoexcited electrons, visible light photochromism could be achieved. This can be achieved by different doping strategies. For instance, by reducing WO₃¹⁴¹ or MoO₃¹⁴² electrochromically to their respective bronzes (K_xWO₃ and Li_xMoO₃), a photochromic response to visible light ($\lambda \geq 500$ nm) was achieved. It has also been shown that doping can both increase the speed of colouration as well as the intensity of it. For example, Cu-doped WO₃ has been shown to exhibit an increased photochromic intensity in the visible wavelength range, while also having a decreased intensity in the NIR wavelength range.¹⁴³ A downside to this is, that it can also increase the recovery time dramatically. For instance, by doping ZnO with gallium, the resulting recovery time from the coloured to the bleached state was increased to several months.¹⁴⁴

The photochromic properties of metal oxides can be observed in several different ways (Fig. 1.17). The easiest is by simply dispersing the nanoparticles in a hole scavenging solvent.²⁷

If this is not possible or desired, another possibility is to prepare heterostructures, either TiO₂-semiconductor or TiO₂-metal¹²⁹ as these do not require an additional hole scavenger to be present for photochromism to take place. These can be prepared also in thin film form. Ordinary TiO₂ nanoparticle thin films still need to be immersed in a hole scavenging liquid to undergo photochromism. There are also studies showing that anatase nanocrystals with clearly defined crystalline facets have the possibility of increased charge carrier separation.¹⁴⁵ This is due to the fact, that electrons and holes tend to migrate to different crystalline facets. Finally, there is also the possibility of preparing gels of TiO₂ nanoparticles, in which the nanoparticles are dispersed in a polymer matrix that is also saturated with a hole scavenger. This allows for these composites to act the same way as colloids, but without the drawback of a colloid (evaporation and potential leakage) while also avoiding the problems arising from simple TiO₂ thin films.

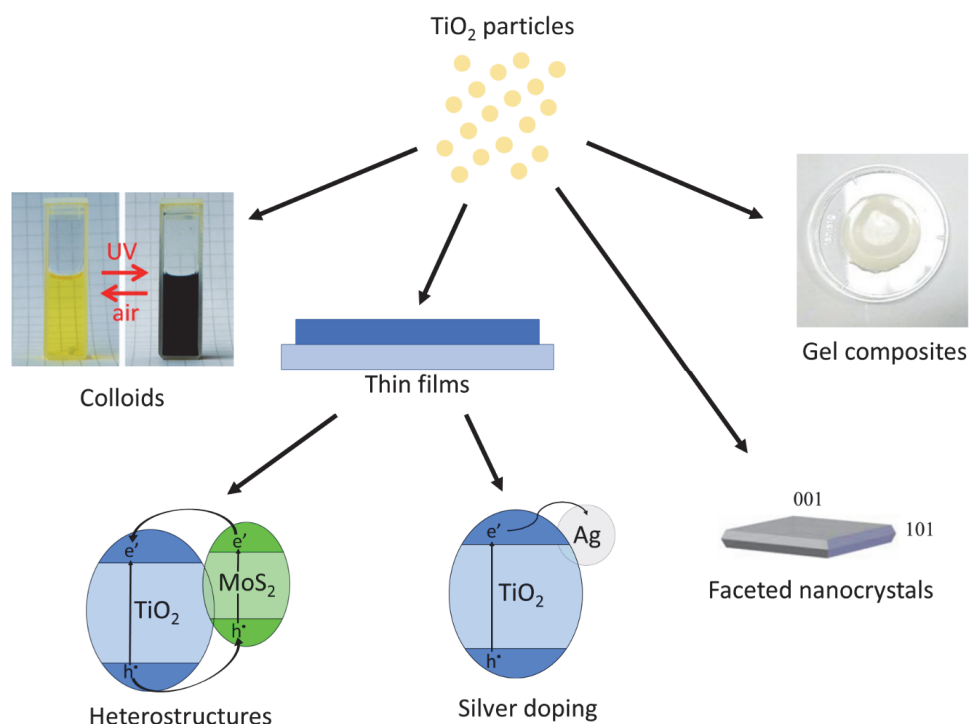
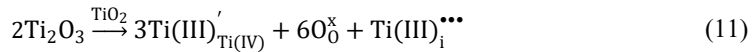
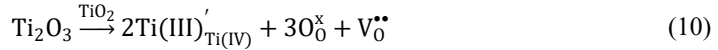
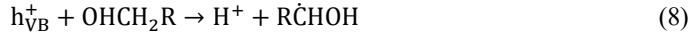


Fig. 1.17. Ways how TiO₂ (and subsequently other TMO) nanoparticles can be implemented for photochromic applications: colloids,¹⁴⁶ thin films, faceted nanocrystals¹⁴⁷ and gel composites.¹⁴⁸

In all the different forms the mechanism underlying photochromism is the same. When these materials are irradiated with light, that has an energy higher than the band gap of the TMO (3.2 eV in the case of un-doped TiO₂), electrons are excited in the valance band. These land in the conduction band, leaving behind a hole (equation (7)). On the one hand, if this process is happening in an aerobic environment and/or in water, oxygen and water will interact with the electrons and holes respectively, producing ROS. On the other, if photoexcitation is happening in an anaerobic environment and in the absence of water, the electrons and the holes are left unaffected and eventually recombine. However, if photoexcitation is done in an anaerobic

environment and in the presence of a hole scavenger, such as alcohols,¹⁴⁹ the holes are filled, with the hole scavengers donating electrons to the TiO₂ valence band (equation (8)). This process results in the oxidation of the hole scavenger¹⁵⁰ and leaves behind an excess of electrons trapped in the conduction band. A part of these electrons will become trapped by reducing Ti⁴⁺ to Ti³⁺ (equation (9)) in the TiO₂ crystalline lattice. This effectively dopes TiO₂ with Ti₂O₃ and can result in the formation of oxygen vacancies (equation (10)) or the formation of titanium interstitials (equation (11)).^{151,152} Because of this, this process is called photodoping.



The defect introduced into the TiO₂ lattice from the photodoping process, introduce additional electron donor and acceptor levels in the TiO₂ lattice. Ti³⁺ introduces shallow electron donor levels in the TiO₂ band gap approx. 1.25 eV below the conduction band minimum,¹⁵³ while oxygen vacancies introduce electron acceptor levels in the TiO₂ bandgap between 0.75 eV and 1.18 eV below the conduction band minimum (Fig. 1.18).^{152,154} These levels allow to the absorption of visible light by the TiO₂ material, which can be seen as a color change of the material from white to blue. Because of apparent color change when the material is irradiated with light, this is also called photochromism.

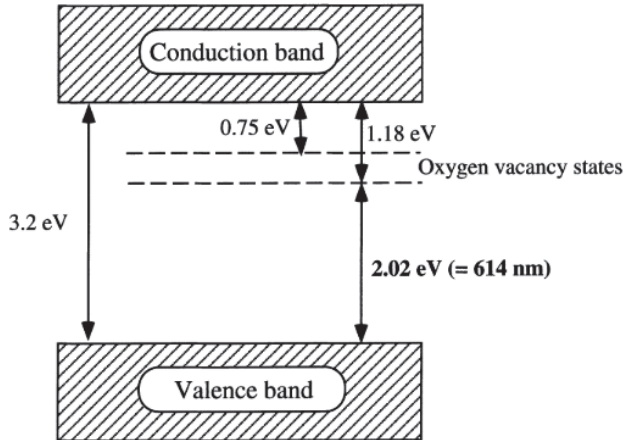


Fig. 1.18. A band structure model for anatase TiO₂ with oxygen vacancies.¹⁵²

The accumulated electrons in the conduction band for the most part, stay in the conduction band with only a small part of them partaking in the Ti³⁺ and V_O formation. Most of them stay delocalized. With so many electrons several new phenomena can be observed. The first is localized surface plasmon resonance, that allows for the absorption of infrared light¹⁵⁵ and populate a new electronic state slightly below (~0.1 eV) below the conduction band minimum.¹⁵⁶ The second phenomena, that can be observed, is the apparent widening of the

optical band gap of the TiO₂. This stems from the fact, that, all states closest to the conduction band minimum are filled. To then excite additional electrons, a higher energy is needed to reach the unoccupied higher energy levels in the conduction band (Fig. 1.19). This phenomena was first reported by *E. Burstein* in 1954¹⁵⁷ in InSb and has since been known as the *Burstein-Moss* shift.¹⁵⁸ This is a common property of degenerate semiconductors, that behave more like metals than semiconductors, but is not exclusive to them.

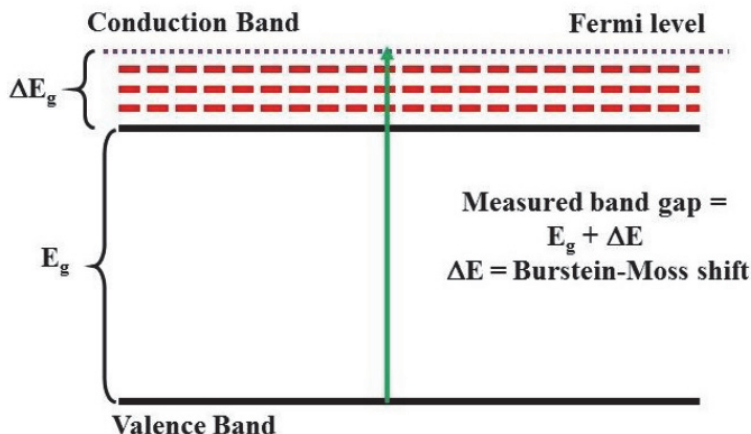
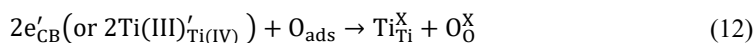


Fig. 1.19. Burstein-Moss shift in degenerate semiconductor.¹⁵⁸

The photochromic process of TiO₂ is reversible. The accumulated electrons modulating the optical properties can be removed (equation (12)) by introducing the oxygen in the photochromic system.



Usage of photochromic materials. Photochromic materials, being the second largest family of chromic materials (after electrochromic materials), have slightly overlapping applications with electrochromic materials. As mentioned before, the most widely known application for photochromism was and still is self-tinting glasses or eyewear. While first, silver halides were used for these materials initially, they were replaced by organic photochromic compounds dispersed in polycarbonate.²⁸ Silver halides have also been used for photography and holography imaging, but in that case silver halides were used without the addition of copper salts. This resulted in the photochromism to be irreversible.¹⁵⁹ Other applications for photochromic materials are smart windows, light sensitive varnishes, and dyes for clothing, as well as colorimetric UV sensors (Fig. 1.20 a-f).

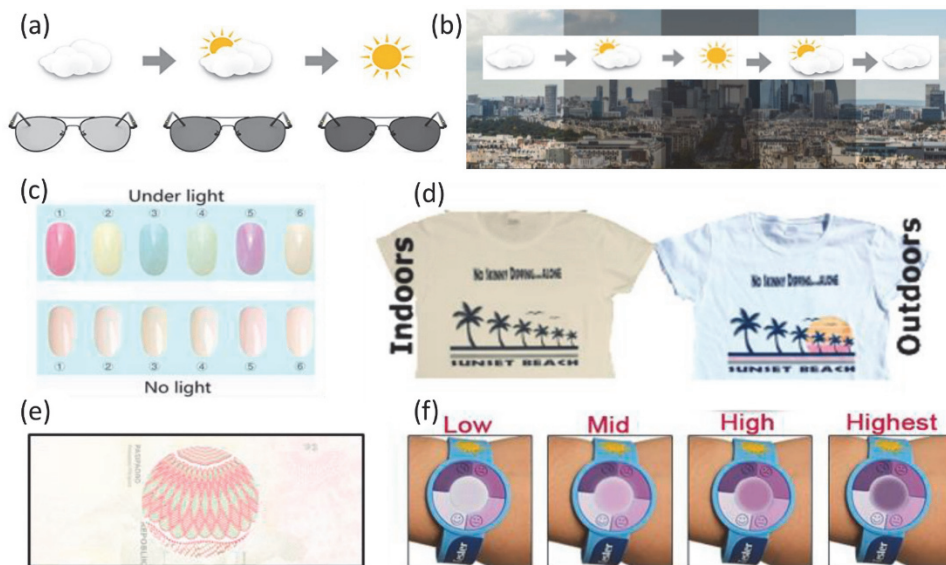


Fig. 1.20. a) Photochromic lenses; b) smart windows; c) light sensitive varnish; d&e) light sensitive dye for clothing and f) colorimetric UV sensor.²⁸

That being said, photochromic materials also have been used as optoelectronic materials for data storage¹⁶⁰ and as colorimetric oxygen sensors.¹⁶¹ These applications are interesting because they use the photochromic materials indirectly with the color being caused by another component of the system. For colorimetric oxygen sensors, they can either be made to lose color, when exposed to oxygen or gain color, when exposed to oxygen, with using the same photochromic material. The difference stems from the co-constituents of the sensor material. For instance, TiO_2 can be used normally to achieve positive photochromism. However, when it is combined with methylene blue in an anaerobic matrix, can achieve negative photochromism, bleaching under UV irradiation.¹⁶¹ Another interesting application of photochromic materials is anti-counterfeiting technologies.¹⁶² In the case of organic photochromics, where the coloration-discoloration is induced by light with different wavelengths, this could be further developed into erasable printer ink, which could be used for sensitive documents or simply to allow the re-use of printer paper.¹⁶³

1.2 Titanium dioxide nanoparticle properties and synthesis

TiO_2 is a well-known and broadly researched wide-band gap semiconductor. It possesses a combination of different desirable properties: non-toxicity, biocompatibility, as well as optical and electrical properties.¹⁶⁴ As it is able to absorb UVA light, it has been researched for usage in such fields as photocatalysis¹⁶⁵, photovoltaics¹⁶⁶, photoelectrochemistry¹⁶⁷ as well as photochromics.¹⁶⁸

TiO_2 exist in a variety of different crystalline modifications, all of which are comprised of TiO_6 octahedral units (Fig. 1.21). Out of these the main crystalline phases are rutile, anatase and brookite (Fig. 1.21.a,b,d) with TiO_2 bronze (Fig. 1.21.c) being less known and the rest being high pressure phases (Fig. 1.21.e-f). Out of the main three the most thermodynamically stable

phase is rutile, with both anatase and brookite exhibiting a phase change to rutile when calcinated at temperatures above 500 °C.^{169,170} Despite this, anatase is the main TiO₂ crystalline phase studied, thanks to its longer charge-carrier lifetime and mobility as well as its wider band gap of 3.2 eV¹⁷¹ when compared to rutile 3.0 eV and brookite 3.1 eV.¹⁷² Another cause of the popularity of anatase when compared to rutile and brookite, its increased thermodynamic stability in ultrafine nanoparticle form (below 11 nm) as well as its ease of synthesis.¹⁷³

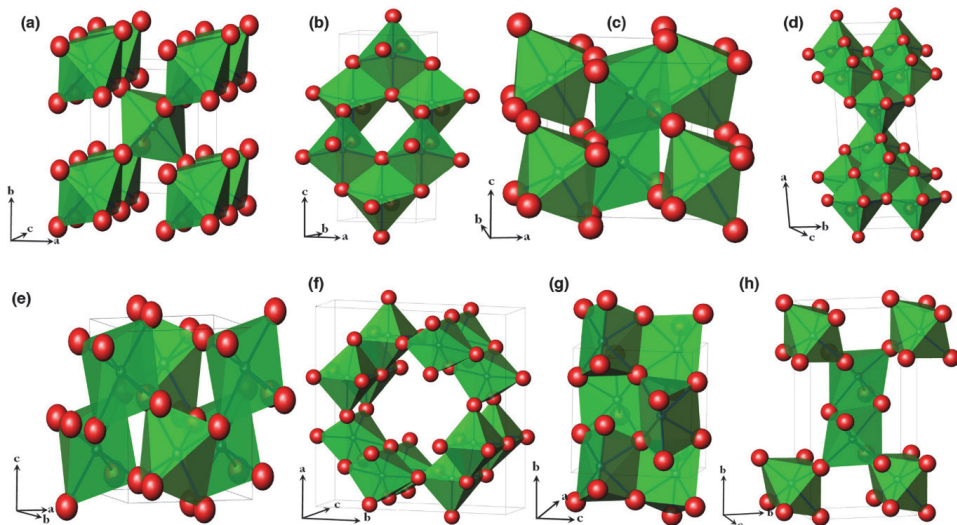


Fig. 1.21. Crystal structures of **a)** rutile; **b)** anatase; **c)** bronze; **d)** brookite; **e)** columbite; **f)** hollandite; **g)** baddeleyite and **h)** ramsdellite phases¹⁷⁴

As with other transition metal oxides, there exists a whole range of different TiO₂ nanostructures, the simplest of which being nanoparticles (Fig. 1.22.A). These also vary in size and shape quite wildly from simple spheres ellipsoids (Fig. 1.22.B) or can have defined crystalline facets, resulting in such complex structures as bipyramids (Fig. 1.22.C). A further refinement of this are nanorods, that can vary in their aspect ratio. They can also be made hollow, producing nanotubes (Fig. 1.22.D) and if the aspect ratio is sufficiently large enough, they can become nanowires (Fig. 1.22.F). For larger nanostructures, hollow nanospheres i.e. nanocups can also be formulated (Fig. 1.22.E). The highest order of nanostructures are for example opal type structures (Fig. 1.22.G) as well as dendritic structures (Fig. 1.22.H&I).

The obtained structures are dependent not only the synthesis method used, but also on the precursors used, and can vary wildly even when just one synthesis method is used. Further processing, such as the combination of multiple synthesis methods, can be used to obtain complex nanostructures (such as the dendrites mentioned earlier).

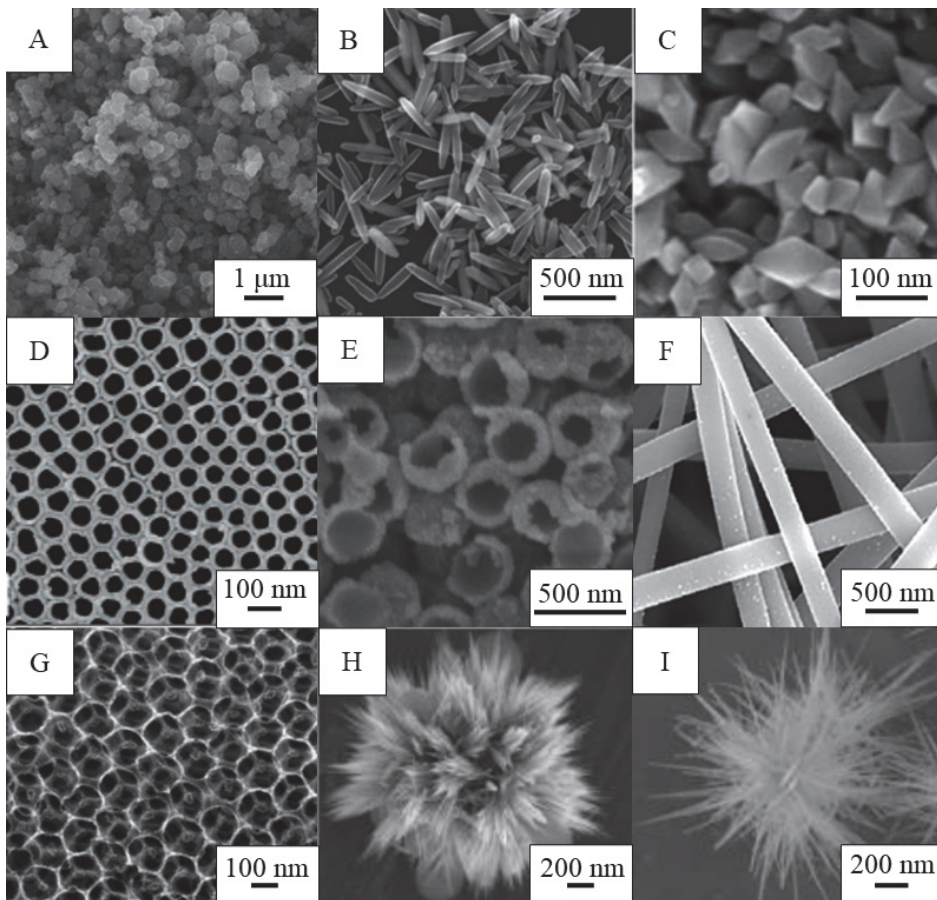


Fig. 1.22. Different types of TiO₂ nanostructures: **A)** nanoparticles;¹⁷⁵ **B)** nanorods;¹⁷⁶ **C)** octahedral bipyramids;¹⁷⁷ **D)** nanotubes;¹⁷⁸ **E)** nanocups¹⁷⁹ **F)** nanofibers¹⁸⁰; **G)** TiO₂ opal nanostructure;¹⁸¹ **H & I)** dendritic nanostructures¹⁸²

The synthesis methods used, are typically divided into physical and chemical synthesis methods and into top-down or bottom-up approaches. Additionally, some synthesis methods can also be classified as biological, stemming from the fact that they use microorganisms to produce the nanoparticle, both anatase and rutile.¹⁸³ Overview of the most common synthesis methods used can be seen in Table 2.

Table 2.Different synthesis methods of TiO₂ nanostructures.

Synthesis method	Precursor used	Controllable parameters	Advantages	Disadvantages
Sol-gel method	TTiPr; TBOT, TEOT, TiCl ₄ , TiF ₄	Precursor concentration; pH; Temperature; Time.	High chemical uniformity, low processing temperature. ¹⁶⁴	Uses expensive and moisture sensitive chemicals. Gel structure formation can be time consuming. ¹¹⁵
Hydrothermal/solvothermal synthesis	TTiPr; TBOT, TEOT, TiCl ₄ , TiF ₄	Precursor concentration; Pressure; Temperature; Time.	High purity of products. ¹⁸⁴	Long synthesis time (even over 24 hours). ¹⁸⁵
Spray pyrolysis	TTiPr; TBOT, TEOT, TiOSO ₄ , Ti(acac) _x (nBuO) _y	Precursor concentration; Substrate temperature and distance to nozzle; Carrier gas flow rate.	Rapid nanoparticle and film growth over a large substrate area. ¹⁶⁴	High substrate temperature, can result in uneven coatings (if used for thin films), a lot of waste material. ¹⁸⁶
Chemical vapor deposition	TTiPr; TBOT, TEOT, TiCl ₄	Precursor concentration; Substrate temperature; Carrier gas concentration.	Allows to prepare both nanoparticles and thin films with a wide range of thicknesses and crystallite polymorphs. ¹⁸⁷	Requires vacuum systems and high temperatures ¹⁸⁸ Uneven film growth if chamber geometry is off. ¹⁸⁸

Most physical methods are top-down, meaning, that the nanostructures are obtained from larger structures. On the other hand, most chemical methods are bottom-up, allowing the preparation of nanostructures from individual atoms. Next, an overview of some of the most common synthesis methods, is given.

Sol-gel synthesis. Sol-gel synthesis method is a wet chemical process, in which metal alkoxides or halogens are hydrolyzed under controlled conditions yield colloids with a nanoparticle size between 1-1000 nm (sols), that can then be aged in order to produce an interpenetrating solid/liquid network (gel).^{189,190} The accessibility of sol-gel synthesis approach lays in its simplicity due to ease of use and do not require any expensive equipment. The usage of the sol-gel method allows for easy preparation of inorganic as well as hybrid organic-inorganic nanomaterials, because of low processing temperatures.¹⁶⁴ Because most of the precursor chemicals are liquids or are used in solutions, the obtained sols and gels are highly homogenic in terms of chemical composition. The downside is that most chemicals used are

expensive and unstable in air or moisture, which makes handling more difficult. Furthermore, if gels with specific structures are required, the gelation can become time consuming, requiring several days or week for gel formation.¹¹⁵

If individual nanoparticles are necessary and to avoid any potential Oswald ripening or sedimentation, the stability of the sol can be increased by protecting the nanoparticles either by purely electrostatic repulsion via pH adjustment,¹⁸⁹ or by using surfactants to achieve steric repulsion between the nanoparticles.^{191,192} If gels are necessary, on the other hand, the stability can be disrupted allowing for interpenetrating nanoparticle/liquid networks to form.¹⁹³ These gels can be further processed (dried, cured, etc.) to obtain either dense ceramics or aerogels (Fig. 1.23).

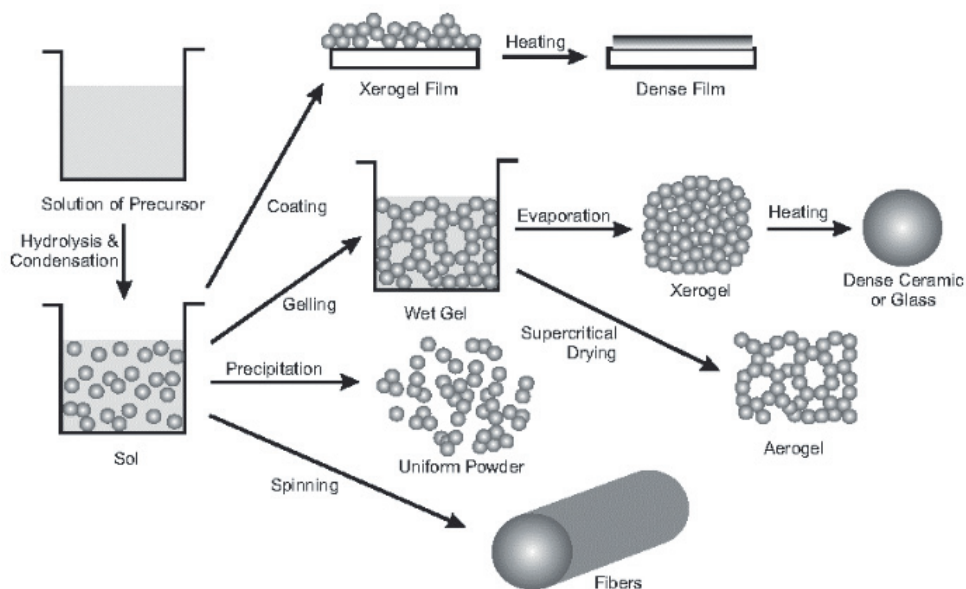


Fig. 1.23. Possible morphologies when using sol-gel technique.¹⁶⁴ Reproduced under the terms of the Creative Commons CC BY license.

The possible sol-gel reactions are determined from the amount of alkoxy groups or halogenide anions available for hydrolysis per metal atom. If the amount is greater than 1 (and in most cases it is), after initial hydrolysis (Fig. 1.24) polymerization and polycondensation occurs.¹⁹⁴ If the amount of these groups/anions 2, linear chains are formed and with an amount of 3 and higher, complex fractal structures can be obtained.¹⁹⁴

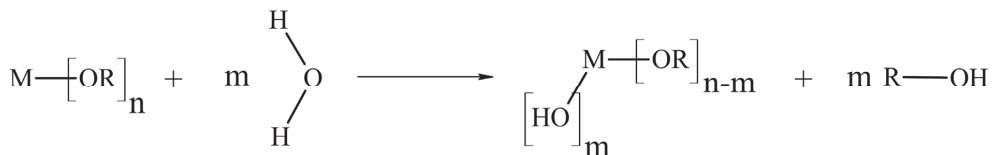


Fig. 1.24. Metal alkoxide hydrolysis reaction. n and m denote the amount of alcohol and water molecules respectively¹⁹⁴

There is also a type of sols, named hydrosols, that consist mainly of water. In these, the pH needs to be very acidic (no higher than 2) for crystallization to occur. Since water is in such high excess, the metal precursors are hydrolyzed very rapidly, producing ultrafine nanoparticles that agglomerate. The added strong acid breaks down these agglomerates, resulting in nanoparticles in the size range of 15-100 nm¹⁹⁵ that are stable and usable without any surfactants (aqueous sol-gel method).¹⁹⁶ To some extent the water can also be swapped for alcohol.¹⁹⁷ These sols can result in the formation of very fine (3-6 nm) anatase nanoparticles.¹⁹⁸

As precursors of TiO₂, the most widely used are TTiPr and TiCl₄¹⁹⁹ as well as TiF₄²⁰⁰, while other alkoxides such as TBOT²⁰¹ or TEOT are being used to a lesser extent. The longer alkoxy chains attached to the main Ti⁴⁺ cation stabilize the molecule, making alkoxides more stable towards hydrolysis when compared to chlorides or fluorides. More stable precursors can allow to slow down the hydrolysis, resulting smaller nanoparticles.²⁰² There have also been reports on anatase nanoparticles, that have been made without the presence of water, using just alcohol and acetic acid (non-aqueous sol-gel method).²⁰³ Doping via hydrolysis also been realized resulting in the usage of such dopants as V⁴⁺, Cr³⁺, Ag⁺ as well as Au³⁺, Ln³⁺ and La³⁺,²⁰⁴ Gd³⁺, Y³⁺ Al³⁺ ²⁰⁵ among others.

Most of the transition metal alkoxides while being susceptible to hydrolysis also can undergo alkoxolation and oxolation which allows for the formation of metal oxides,¹⁹⁴ and is the synthesis method used in this work for the preparation of the TiO₂ nanoparticles. First, a metal cation attracts the electron pair of a water molecules oxygen, forming a complex, after which, slitting of the water molecule and subsequent hydrolysis occurs.¹⁹⁴ If the cation is a part of an alkoxide, this results in the formation of a metal hydroxide and the relevant alcohol. Besides this, there are also other reaction that can occur: alkoxolation and oxolation. Alkoxolation is a nucleophilic substitution, between a M-OH and M-OR, that results in the formation of a M-O-M bond, and another molecule of alcohol (Fig. 1.25).

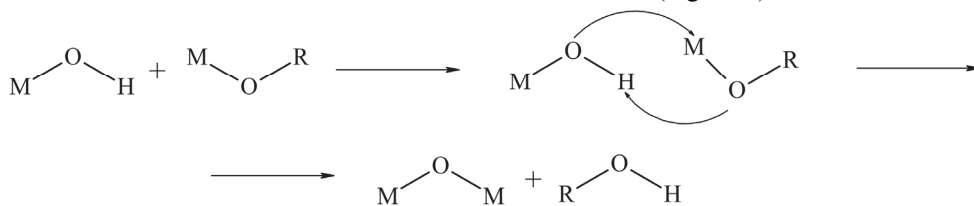


Fig. 1.25 Alkoxolation reaction^{189,194}

In the case of oxolation, two hydrolyzed metal cations react with each other, and form a M-O-M bond, as it is in alkoxolation. However, here, since both reactants are hydrolyzed, the by product is a water molecule. These three reactions are governed by such criteria as temperature, pH, the relative electronegativity of the metal ion as well as the nucleophilic strength of the alkoxide group (these two can be combined into simply hydrolysis rate) and the amount of water present per molecule of alkoxide. In terms of hydrolysis rate, titanium precursors are more stable (have a slower hydrolysis rate) if they have longer alkoxide chains with halogenides being the most unstable.²⁰⁶ The hydrolysis rate can be further reduced, when using chelating agents, such as acac, which can lower the hydrolysis rate several times.²⁰⁷ A change in pH can impact the resulting crystalline phase of the TiO₂ nanoparticles. *Kotsyubynsky et al.* showed that for the hydrolysis of TiCl₄ if, the pH<1, rutile is typically formed.²⁰⁸ If the

pH is between 2 and 3, mixed phase TiO₂ can be obtained. Higher pH values favor the formation of anatase up to pH=8. Above pH=8, brookite is obtained.

Temperature has a substantial impact on the hydrolysis rate of the precursors as well as on the condensation rate and growth of the nanoparticles. For example, *Leyva-Porras et al.* prepared TiO₂ nanoparticles at two different temperatures (25 °C and 80 °C) with the same reaction time of 3 h.²⁰⁹ The result was that nanoparticles prepared at the lower temperature hardly showed any XRD crystalline peaks and were basically amorphous. On the contrary, synthesis at the higher temperature allowed to obtain highly crystalline anatase nanoparticles with an average size of 4.3-4.6 nm.

By choosing the right parameters (temperature, precursor, pH) structures ranging from linear and branched polymers, all the way to crystalline nanoparticles can be obtained. Metal alkoxide hydrolysis can also be used to synthesize not only pristine²¹⁰, but also doped TiO₂ nanoparticles, for example V-doped TiO₂.²¹¹

Solvothermal/hydrothermal methods. The hydrothermal and solvothermal methods use increased pressure (1-100 MPa) and temperature (100-1000 °C) to produce a wide variety of different nanostructures, from simple nanoparticles²¹² to complex nanostructures²¹³ as well as doped nanoparticles²¹⁴ and structures.²¹⁵ The increased temperature and pressure allows for the increased solubility of different reactants as well as lowers the viscosity of the solvent. This facilitates fast diffusion and allows for the synthesis of pure single crystals as well as monodisperse nanoparticles.¹⁸⁴ Furthermore, it allows for the synthesis of complex materials such as zeolites,²¹⁶ MOFs or COFs.²¹⁷ The usage of surfactants also allows for the synthesis of metal oxide nanorods, nanosheets or 3D structures.¹⁸⁵ These materials do not require any form of post-treatment, such as calcination. A downside to these synthesis methods is the need for pressure vessels (autoclaves, Fig. 1.26) that limit the synthesis volume and resulting yield. Furthermore, hydrothermal and solvothermal syntheses are often long, with synthesis times of upwards of 12-24 hours being common for nanostructure fabrication.¹⁸⁵

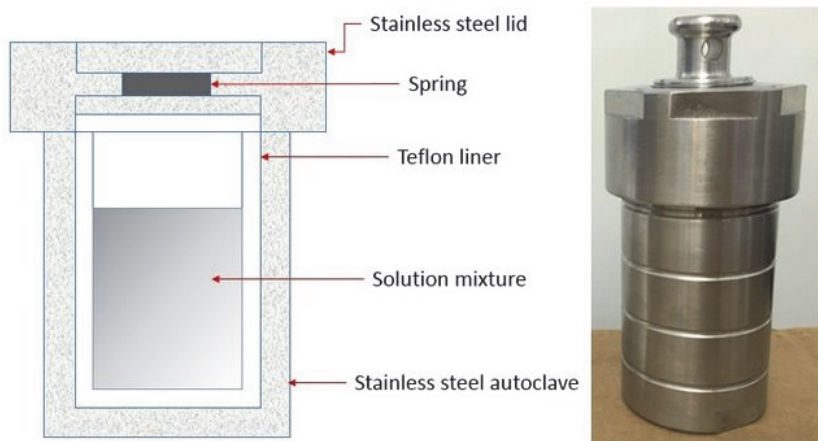


Fig. 1.26. Schematic and photograph of an autoclave used in solvothermal/hydrothermal synthesis.²¹⁸

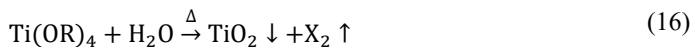
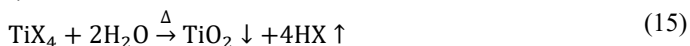
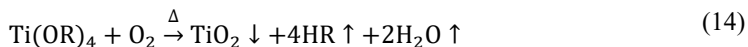
In hydrothermal synthesis of TiO₂, aqueous solutions of Ti precursors are sealed in Teflon lined steel autoclaves, which allows for the use of temperatures higher than the boiling point of water. The solvothermal method differs in the sense, that water is replaced by an organic solvent.

Water can still be used purely as a hydrolyzing agent,²¹² or completely non-aqueous conditions can be used.²¹⁹ In all cases, TiO₂ forms by first forming titanic acid intermediate, that is recrystallized in the elevated temperatures and pressures.²²⁰ The solvent used, can have a noticeable impact of the resulting nanoparticle structure and morphology. *Huang et al.* compared the usage of different alcohols as solvents for the solvothermal synthesis of TiO₂.²²¹ Due to the lower initial viscosity of ethanol smaller nanoparticles and with higher crystallinity are forming resulting in increased surface area and higher charge carrier separation efficiency. When comparing hydrothermally prepared TiO₂ nanoparticle samples with sol-gel samples, prepared from the same starting solution, it was found that hydrothermal samples exhibited larger surface areas as well as a higher anatase content, when compared to the sol-gel samples.²²²

For both hydrothermal and solvothermal methods, the synthesis parameters that can be controlled are temperature and pressure, as well as time and precursor concentration. In most laboratory autoclaves pressure is generated autogenously and as such is directly linked to the temperature. Temperature is responsible for the initiation of the reaction and for the change in diffusivity of the reactants.²²³ At low temperature (< 60 °C) reaction will not take a place or will be very slow.²²⁴ Pressure can be also partially controlled by the fill factor (how much of the autoclave is filled with the synthesis solution).²²⁵ However, at some special cases the fill factor, ranging from 20% up to 90% (at 180 °C) has been reported to have very little effect on the resulting product.²²⁶

The reaction time dictates the general size and crystallinity of the synthesized nanomaterial. If the reaction time is too short, the precursors can be not fully hydrolyzed and can result in the product being amorphous instead of crystalline. However, a too long reaction time, would lead to the growth of larger nanoparticles.²²⁴ This can be detrimental if very fine nanoparticles are required, but can be beneficial if the goal is single crystal growth.

Chemical Vapor Deposition. In chemical Vapor deposition (CVD) precursor vapors (metal alkoxides or metal salts), deposits on the substrate forming different TiO₂ nanostructures, mainly thin films with thicknesses ranging from a few nanometers²²⁷ to several microns¹⁸⁷. The precursor vapors (prepared by heating or by bubbling gas through it) are driven towards the substrate using an inert carrier gas, while oxidation is facilitated by supplying oxygen or water vapor to the gas/vapor mixture. The substrate is heated to facilitate the chemical reactions (13)-(16)¹⁸⁸ and deposition on the substrate surface as opposed to the walls of the reactor (example reactor setup can be seen in Fig. 1.27). CVD can be carried out at varying pressures ranging from atmospheric pressure down to a few Torr. CVD carried out at a reduced pressure (vacuum) is called low-pressure CVD or LPCVD.



The gas flow rate, temperature, pressure as well as even the geometry of the chamber can influence the film growth of the material.²²⁸ For a hot-wall LPCVD reactor (Fig. 1.27) the gas flow rate directly influences the growth rate of the film, with higher growth rates for higher gas flow rates being reported. Lower gas flow rate allow for finer control on the resulting film thickness. However, at low gas flow rates, the films can grow unevenly, with the five-fold difference in growth rate over substrates the leading edge and trailing edge.¹⁸⁸ The temperature also, has a direct influence on the resulting growth rate. However, the effect of a low temperature and can cause the film growth rate to become independent on gas flow rate. The same goes for the pressure of the precursor vapor. A too high vapor pressure can cause the film growth rate to become diffusion limited and independent on the gas flow rate.¹⁸⁸ The chamber geometry is a complex subject, with the gas inlet/outlet positions as well as the position and orientation of the substrate influencing the resulting film.

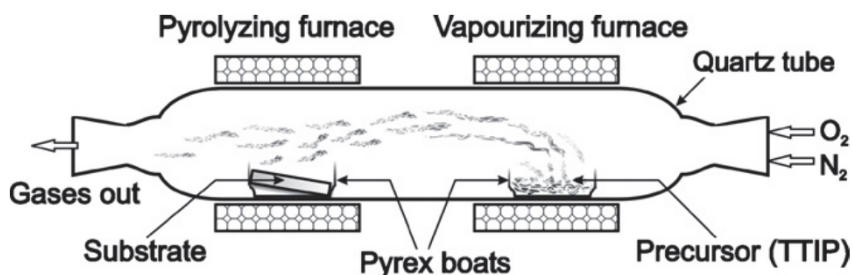


Fig. 1.27. CVD reactor setup²²⁹

There are different variations in of CVD method. One example is mist CVD in which the precursor solution is vaporized using ultrasound. This vapor is then mixed with a carried gas and passed over the substrate at an elevated temperature. This has been used to prepare oriented anatase TiO₂ thin films²³⁰ as well as thin films with no preferred orientation of both anatase²³⁰ and brookite.²³¹ Another variation is laser CVD, in which, a laser beam is used to heat the substrate instead of traditional induction heating, allowing the usage of temperatures upwards of 1000 °C, that, can be used to prepare both anatase and rutile films.²³² Recently, there has been researched published on area-selective CVD possible using a microplasma printer. This has the potential of allowing to produce patterned films directly via CVD, without the need for mask usage.²³³

Spray pyrolysis. In this method, metal precursor (alkoxides or halides, most commonly titanium tetra-isopropoxide) solutions are sprayed out in a fine mist on a heated substrate to produce films (setup shown in Fig. 1.28) or in air flow, in order to prepare fine nanopowders.¹⁶⁴ The main parameters to control during spray pyrolysis are substrate temperature, nozzle-substrate distance, precursor concentration and carrier gas flow rate. Out of these the substrate temperature is arguably the main aspect, with droplet drying, precursor decomposition, crystallization and grain growth all depending on this parameter.¹⁸⁶

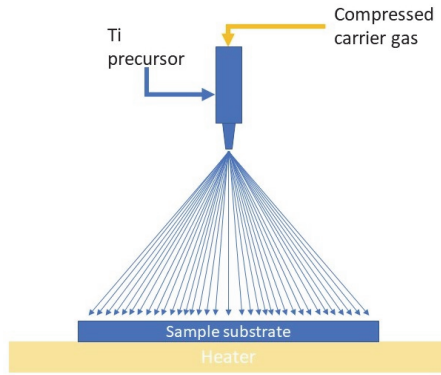
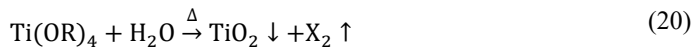
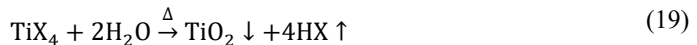
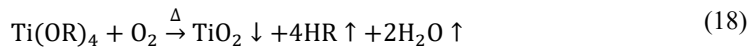


Fig. 1.28. Spray pyrolysis setup schematic. Figure was inspired by *A. Möllmann et al.*²³⁴

The substrate temperature has a direct influence on both the resulting thickness and morphology of the obtained film. Higher thicknesses as well as larger grains are obtained at higher temperatures as compared to lower. For example, an increase in substrate temperature from 250 °C to 450 °C can result in a film thickness increase from 110 to 240 nm as well as a grain size increase from 20 to 50 nm.²³⁵ However, if the substrate temperature is low, the resulting film will be amorphous, and further heat-treatment will be necessary in order to produce crystalline films. If the substrate temperature is very low, the incoming precursor solution aerosol can overwhelm the evaporative rate. This results in wetting of the substrate.²³⁴ Another parameter is the metal precursor, its concentration and carrier gas flow rate. Higher precursor concentration lead to an increase in resulting film thickness as well as increased grain size.²³⁶ A higher carrier gas flow rate can help reduce the droplet size, by resulting in a higher shear force being exerted on the precursor solution in the spray nozzle.²³⁷ However, an increase in carrier gas flow rate also results in a higher film thickness, as in total, a higher amount of the precursor solution will be deposited on substrate. It has also been shown that the usage of either a precursor more stable against hydrolysis as well as switching out compressed air for O₂ can promote anatase formation.²³⁸ The chemical reactions taking place during spray pyrolysis are similar to those taking place in CVD, and, depending on the precursor (halogenide or alkoxide) and solvent (water or organic solvent), are described by equations (17)-(20).



One key parameter that influences the formed nanoparticle size in spray pyrolysis, is the size of the droplets formed. To help decrease this size, and in turn reduce the nanoparticle size, assisted spray pyrolysis methods have been developed. These include ultrasonic spray pyrolysis²³⁹ and electrostatic spray deposition.²⁴⁰ The USP an ultrasonic processor is used to nebulize the precursor solution, similarly to mist CVD. The main difference is that the spraying

is done in the same manner as in tradition spray pyrolysis. In contrast, ESD uses an electric field to further break up the droplets.

1.3 Controlling the optical properties of titanium dioxide by means of defect chemistry

The main drawback of anatase TiO₂ is its wide band gap of 3.2 eV and the low quantum yield primarily determined by the fast recombination of the photogenerated charge carriers.²⁴¹ This means that to photoexcite the TiO₂, UVA light is necessary. To narrow the band gap, doping can be implemented. Doping is the process of introducing either atoms of different elements (both cations as well as anions) with the same (isovalent doping) or different valence (aliovalent doping) or the same elements as the host, but with a different valence (Ti³⁺ in a TiO₂ lattice). There are also other ways how to classify defects: either by their origin (intrinsic or extrinsic) or by their dimensions (point, line, or plane defects). Intrinsic defects are self-defects, present in most crystalline solids because of the fact, that the presence of some amount in the crystalline lattice is a more thermodynamically favorable state than having no defects at all and thus there will always be an equilibrium population of defects in the crystalline lattice.²⁴² Extrinsic defects on the other hand are different ions introduced into the host lattice. These can be either intentional (doping) or un-intentional (impurities). This introduces donor and/or acceptor levels into the band gap of TiO₂ (Fig. 1.29). If the dopant has a higher valence, it is called an acceptor dopant, that introduces levels near to the conduction band. If, however, the dopant has a lower valence, then it is called a donor dopant and it introduces electron donor levels near to the valence band. Doping also has the effect of distorting the crystalline lattice, as all dopants will have a different size than the host materials ions. When comparing anatase to rutile, it has been shown, that anatase favors longer charge carrier lifetimes by surface hole trapping. In rutile, on the other hand, dopants favor recombination and result in much lower charge carrier lifetimes.²⁴³

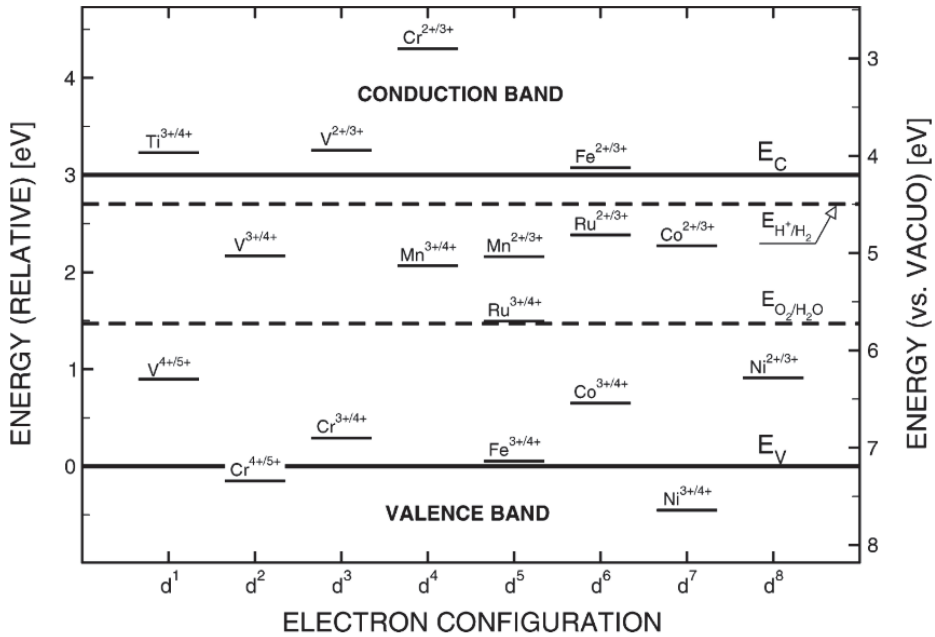


Fig. 1.29. Electronic structure of TiO₂, including different dopant levels.²⁴⁴

The most common type of defects are point defects such as vacancies (empty cation or anion lattice site) or interstitials with ions occupying space between sites within a lattice. Extrinsic defects are alien cations and anions in the lattice i.e., dopants. Dopants substitute the host cation or occupy interstitial position in the lattice. Representation of all these types of defects in TiO₂ can be seen in Fig. 1.30). There is also the possibility of anti-site defects where cations occupy anions sites in lattice and vice-versa. Point defects can build up the more complex defects such as Frenkel and Schottky defects, as well as F-centers. A Frenkel defect consists of a vacancy and interstitial ion pair. A Schottky defect is a cation vacancy together with an anion vacancy. A F-center in its simplest form is an anion vacancy with a trapped electron inside of it.²⁴²

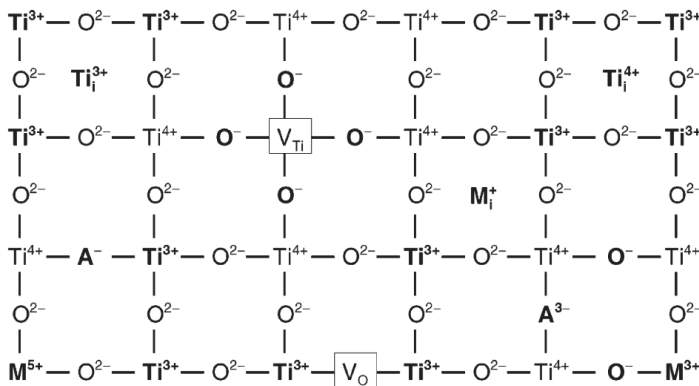


Fig. 1.30. Schematic representation of the defected lattice of TiO₂.²⁴⁴

As crystals tend to be electrically neutral, the introduction of crystalline defects is usually accompanied by electronic defects as well. The introduction of aliovalent dopant can cause

formation of delocalized charge carriers or can induce formation of other type of point defects. For example, Ga³⁺ donor dopant in ZnO lattice can trigger the formation of Zn²⁺ vacancies, oxygen interstitial and delocalized electrons.¹⁴⁴

To describe electric charges and lattice positions of point defect species in crystalline materials, the *Kröger-Vink* notation is used (notation legend in Table 3). The most notable difference between this notation and others is the subscript notation of the lattice space the defect is occupying. The superscript notes the charge by using • for positive charge, ' for negative charge and X for zero charge.

Table 3.

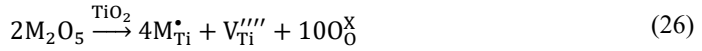
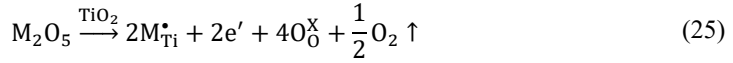
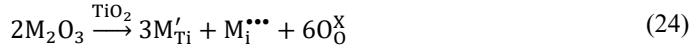
Kröger-Vink notation legend.²⁴⁵

Type of defect	Symbol	Effective charge
Cation in a cation lattice space	M _M	0
Anion in an anion lattice space	A _A	0
Cationic vacancy	V _M	0
Anionic vacancy	V _A	0
Cationic interstitial	M _i	0
Anionic (oxygen) interstitial	A _i	0
Electrically neutral filled cationic lattice space	M _M ^X	0
Electrically neutral filled anionic lattice space	A _A ^X	0
Charged cationic vacancy	V _M [•] or V _M ^{••}	+1 or +2
Charged anionic vacancy	V _M ['] or V _M ^{'''}	-1 or -4
Charged cationic interstitial	M _i [•] or M _i ^{••••}	+1 or +4
Charged anionic interstitial	A _i ['] or A _i ^{'''}	-1 or -2
Electron	e'	-1
Hole	h•	+1

Intrinsic defects in TiO₂ include oxygen vacancies and interstitials as well as Ti vacancies and interstitials. Out of these oxygen interstitials are the most common, followed by Ti interstitials. These are formed when the TiO₂ material is sintered in vacuum, for example, and are compensated as per equations (21) and (22).



The extrinsic doping is done with aliovalent dopants, secondary defects will be created to preserve charge neutrality of the material. If the dopant used in of a lower valence than the host (cations with a valence up to IV in the case of TiO₂) then they are called acceptor dopants and can introduce either oxygen vacancies (23) or cation interstitials (24) in the crystalline lattice. Conversely, if the dopant cation is of a higher valence than the host cation (valence above IV in the case of TiO₂) then they are called donor dopants. These introduce either free electrons (25) or cation vacancies (26) in the crystalline lattice.



Whichever scenario actually happens is dependent on the oxygen partial pressure, with higher pressures favoring scenarios (24) and (26) and lower pressures favoring scenarios (23) and (25).²⁴⁴ This has an effect on the catalytical, optical and electrical properties of TiO_2 .²⁴⁶⁻²⁴⁸ Dopants influence not only the band gap of TiO_2 , but also the photogenerated charge carrier recombination rate. This is important for both photocatalysis as well as photochromism as both are enhanced when recombination is hindered. Depending on the dopant ion, it can act as either a carrier trap or can prevent the trapping of the generated charge carriers.¹⁴⁵ This can also have an impact on both the photodarkening of the material, as well as on the recovery, as more strongly bonded electrons will cause photodarkening to recover slower. Conversely, dopant that mitigate electron trapping, can hamper the photodarkening, while speeding up recovery.

Cation doping is usually achieved by introducing dopant ions into the synthesis reaction of TiO_2 . A way to introduce dopants of the same element (Ti^{3+} or even Ti^{2+}), is to either reduce the ions via ion bombardment,²⁴⁹ sintering in a reductive environment²⁵⁰ or via photodoping.²⁷ In order to study the dopant influence on recombination kinetics as well as the photocatalytic reactivity, TiO_2 has been doped with a plethora different dopants (Fig. 1.31). In a survey comparing 19 different metal dopants, it was shown, that dopants such as Fe^{3+} , Mo^{5+} , Ru^{3+} , Os^{3+} , Re^{5+} , V^{4+} and Rh^{3+} had a positive influence on the photocatalytic properties of TiO_2 , mainly on photooxidation.²⁵¹ These dopants were shown to act as electron traps. Dopants Fe^{3+} , Ru^{3+} and V^{4+} also substantially increased the lifetime of electrons/holes from 200 μs to as long as 50 ms.²⁵¹ This substantial increase in the charge carrier lifetime. An increased charge carrier lifetime can allow for a larger number of charges to migrate to the nanoparticle surface and take part in hole scavenging. This would increase the photochromic performance of the material.

H																	He	
Li	Be											B	C	N	O	F	Ne	
Na	Mg											Al	Si	P	S	Cl	Ar	
K	Ca	Sc	Ti	V	Cr	Mn	Fe	Co	Ni	Cu	Zn	Ga	Ge	As	Se	Br	Kr	
Rb	Sr	Y	Zr	Nb	Mo	Tc	Ru	Rh	Pd	Ag	Cd	In	Sn	Sb	Te	I	Xe	
Cs	Ba	La	Hf	Ta	W	Re	Os	Ir	Pt	Au	Hg	Tl	Pb	Bi	Po	At	Rn	
Fr	Ra	Ac	Rf	Db	Sg	Bh	Hs	Mt	Ds	Rg	Cn	Nh	Fl	Mc	Lv	Ts	Og	
			Ce	Pr	Nd	Pm	Sm	Eu	Gd	Tb	Dy	Ho	Er	Tm	Yb	Lu		
			Th	Pa	U	Np	Pu	Am	Cm	Bk	Cf	Es	Fm	Md	No	Lr		

Fig. 1.31. Periodic table, showing different elements, used to dope TiO₂.^{251–255}

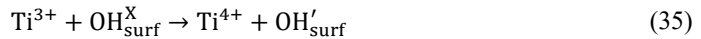
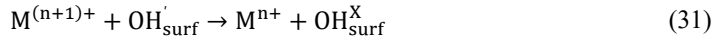
Doping is usually carried out by adding the desired metal precursor (alkoxide or salt) to the synthesis mixture of the TiO₂ material, with either sol-gel or hydrothermal (solvothormal) methods being the most common used to achieve this. This is due to the fact, that with precursor solutions a homogeneous mixture can be easily made, allowing for better dopant uniformity in the resulting nanomaterial. The amount of the metal ions incorporated into the TiO₂ is not always the same as the amount of dopant added to the synthesis. The ratio between these two is called the doping efficiency and depends on the dopant used as well as the synthesis method. In general, a higher doping efficiency can be achieved if the host and dopant ions are of a similar size (generally a size difference of no more than 10% will favor higher doping efficiencies). Ti⁴⁺ has an crystal ionic radius of 74.5 pm.²⁵⁶ This would mean that cation dopants with radii within the range of 67-82 pm could be easily incorporated into the TiO₂ lattice. This includes Al³⁺ (67.5 pm), Ti³⁺ (81 pm), V³⁺ (78 pm), V⁴⁺ (72 pm) and V⁵⁺ (68 pm), Cr³⁺ (75.5 pm), Cr⁴⁺ (69 pm) and many others. Apart from rare-earth and alkaline metals, this range encompasses all cationic metal dopants. Furthermore, isovalent dopants should also show better doping efficiencies as they do not require any additional defects to form to preserve charge neutrality. If the doping efficiency is low, then more dopant precursor is necessary to achieve the same dopant content, than when the efficiency is high. Furthermore, there is also the possibility, that the dopant might not be incorporated into the TiO₂ crystalline lattice. This can result in the formation of secondary phases. This is usually unwanted and as such, should be avoided.

Doping, as discussed previously, can introduce additional electron donor and acceptor levels inside the band gap of TiO₂ and can also introduce electron and hole traps into the crystalline lattice, that can slow down the charge recombination kinetics.²⁵⁷ The induced charges can be trapped on the dopant ions (electrons as per equation (27) and holes as per equation (28)). Holes can also be trapped on surface OH groups (equation (29)).²⁵¹





After the charges have been trapped, depending on the dopant, they can still migrate between neighboring traps according to equation (30) and (31). Charges can also transfer from the traps to the surface and can subsequently be scavenged by the respective (electron and hole) scavengers (equations (32) and (33)). Eventually, the remaining holes and electrons can recombine as per equation (34) while any trapped electrons or holes return their traps to their original valence as per equations (35)-(39) and subsequently recombine.²⁵¹



For a dopant to substantially increase the photochromic properties of TiO_2 , it should act either as an effective electron trap or an effective hole trap. Depending on the electron structure of the dopant, it can result in the production of either shallow or deep trap sites (Fig. 1.32) with deep trap sites being the most favorable for photochromism. This is because electrons in these sites are more stable and have a much higher lifetime than compared to electrons in the conduction band or the shallow trap sites.

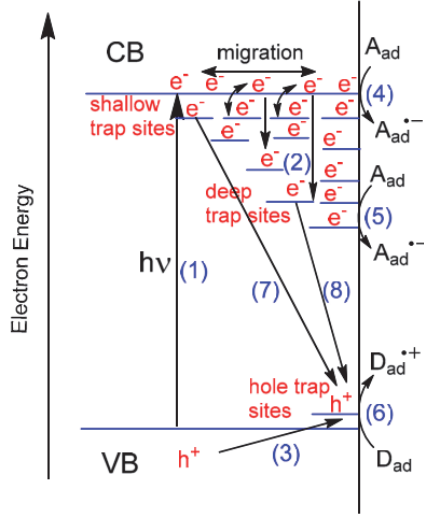
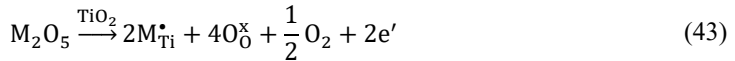
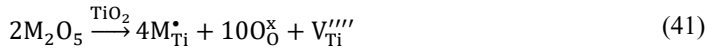
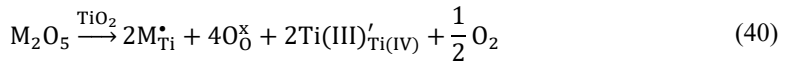
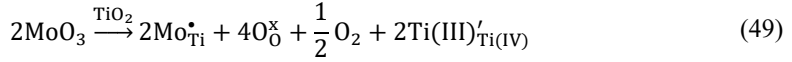
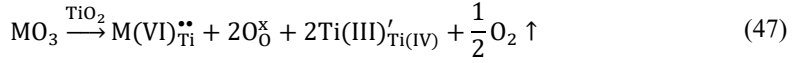
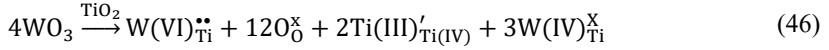
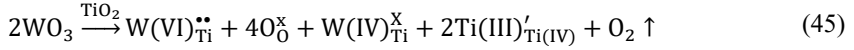
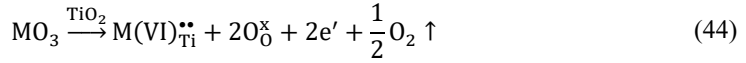


Fig. 1.32. Schematic model of the band structure of anatase TiO₂.²⁵⁸ Reproduced under the terms of the Creative Commons CC BY license.

When the electrons are excited (Fig. 1.32 (1)) both the electrons and holes can be trapped (Fig. 1.32 (2) and (3)). From these traps they can escape either by redox reactions with electrons acceptors ((Fig. 1.32 (4) and (5)) or donors (Fig. 1.32 (6)) or they can recombine between themselves ((Fig. 1.32 (7) and (8)) with hole scavenging inhibiting the recombination.²⁵⁸ This increases the charge carrier lifetime and thus allows for more holes to be potentially scavenged. Possible dopants include pentavalent cations, such as V⁵⁺, Ta⁵⁺ and Nb⁵⁺, as well as hexavalent dopants like W⁶⁺ or Mo⁶⁺. When introduced into the TiO₂ lattice, the pentavalent dopants can substitute Ti⁴⁺ and produce M⁵⁺-Ti³⁺ defect pairs (equation (40)), while also shifting the Fermi level and the conduction band minimum.²⁵⁹ The introduction of a pentavalent cation can also be compensated by titanium vacancies (equation (41)), oxygen vacancies (equation (42)) or simply by delocalized electrons (equation (43)).



Hexavalent cation dopants can also substitute Ti⁴⁺, but in this case, additional defects need to form to compensate the introduction of cations of such a high valence. This includes the formation of more complex defect mixtures, as W⁶⁺ (equation (44)) has been shown to partially reduce to W⁴⁺ when incorporated in the TiO₂ lattice (equation (45)) while also producing Ti³⁺ (equation (46))²⁶⁰ and Mo⁶⁺ (equation (47) and (48)) undergoes a slight reduction to Mo⁵⁺ and produces Ti³⁺ as a way of charge compensation (equation (49)).²⁶¹



Even if different cations have the same valence, they have different electron shell structures and as such act as electron traps. If the core of the cation is less screened than it will attract electrons more when compared to a core that is more screened (has more filled energy levels). This also has the benefit of delocalizing the excited electrons. To this extent, V^{5+} should have the highest electron trapping capability, followed by Nb^{5+} and Ta^{5+} . In a similar fashion Mo^{6+} should have a higher electron trapping capability than W^{6+} . Nb^{5+} incorporation has been shown suppresses the formation of oxygen vacancies²⁶² as well as increases the charge recombination rate²⁶³ the latter being indicative of electron trapping.²⁵⁸

When the material is irradiated with photons that have an energy beyond the band gap, metal oxide nanoparticles can undergo light-driven multi-charge accumulation that accompanies photochromism. This process, also called photodoping, can influence the defect structure, by allowing the photogenerated electrons to interact with the dopant cations.²⁶⁴ Furthermore, the level of accumulated free charges can be controlled by the level of doping, ultimately delivering a tool to continuously tune the optical and electrical properties of the metal oxide nanoparticles.²⁶⁵ When doped with acceptor dopants, the photogenerated charge can be reduced, thus changing the defect structure of the doped oxide. This process has also been linked to a decrease in the depletion layer²⁶⁶ and to the enhancement of conductivity after photodoping.²⁶⁷

Anion doping. TiO_2 has been doped by different anions. During the anion doping the lattice oxygen has been substituted with N, F and C.²⁴¹ Typically, anion doping is a lot more difficult, due to the fact, that during the synthesis procedure oxide formation is favored. Nevertheless, there have been a multitude of different instances in which anatase TiO_2 has been doped with different anions.²⁴¹ Anion dopants bring with them either excess amount of holes (in case of N^{3-}) or an excess amount of electrons (F^{-268} , I^{-269} , Br^{-270} , Cl^{-271}). These can be compensated either by O_i or V_{Ti} in case of excess holes or V_{O} and Ti_i in case of excess electrons. Similarly, to cation dopants, anion dopants as well introduce additional energy levels in the band structure of anatase and can promote visible light absorption. Anion dopants can be introduced by either during synthesis by the addition of the anion containing salts (halogenides, sulfides) or organic precursors,²⁴¹ or acids²⁷⁰. Another option has been the post-treatment sintering of the nanoparticles in the dopant gas as has been done with nitrogen doping²⁷² or treatment by the corresponding ions acid.²⁷³ Anion dopants are more commonly incorporated in the surface O sites of the anatase lattice, especially if doping are done in post-treatment.²⁷³

Carbon can substitute O in the crystalline lattice of TiO₂, as confirmed by XPS showing Ti-C bonds in the samples, and hence can be counted as an anion dopant.²⁷⁴ The introduction of carbon has produced thin films containing not only Ti⁴⁺, but also Ti³⁺ and even Ti²⁺,²⁷⁵ as well as having a band gap as narrow as just 1.78 eV²⁷⁶ due to the mixing of C 2p and O 2p bands.²⁷⁷ This results in a mid-gap band that can sit at around 1.6 eV.²⁷⁸ Carbon doping has also been reported to increase the photocurrent density of TiO₂ photoanodes not only under UV irradiation, but also in visible light, making them prime candidates for use in DSSCs.²⁷⁹ N-doped TiO₂ can also create deep levels in the optical band gap through the mixing of N 2p and O 2p bands, determined by deep-level optical spectroscopy.²⁸⁰ This in turn leads to visible light photocatalytic activity²⁸¹ as well as increased photocurrent density,²⁸² although the values presented are significantly lower, than, for example, Nb-doped TiO₂.²⁴⁶

Halogenide doped TiO₂ has been carried out by the addition of different ammonium halogenides. F-doping of TiO₂ has been shown to have a positive effect on anatase TiO₂, producing F⁻Ti³⁺ pairs for charge compensation,²⁷³ while too much fluorine has been shown to promote the formation of rutile instead of anatase due to degradation of the oxygen sub-lattice.²⁸³ The necessity for charge compensation with secondary defects is why co-doping of fluorine together with nitrogen, has shown an increase in the resulting doping efficiency as this removes the need for Ti³⁺ defect formation.²⁸⁴ Iodide doping has been carried out by doping TiO₂ with iodic acid, which resulted by the introduction of different valence iodine ions (namely I⁵⁺ and I⁻)²⁸⁵ showing the inherent difficulty of anionic doping. A similar effect was achieved when the dopant was introduced via an ammonium salt (NH₄I). This also resulted in the presence of both I⁵⁺ and I⁻, although the iodide anion was in a much higher quantity (in a I⁵⁺:I⁻ ratio of 1:3) than in the aforementioned doping route.²⁶⁹ Similar difficulties can arise when trying to dope TiO₂ with sulfur. When synthesized via calcification together with elemental sulfur powder in an Ar atmosphere, the result was TiO₂ nanoparticles, that has been doped with sulfur as both S²⁻ as well as S⁴⁺.²⁸⁶ However, only S²⁻ was observed if the sulfur precursor was H₂S in the doping procedure.²⁸⁷ If the calcination is done in air, the result is doping with S⁶⁺, since sulfur can easily be oxidized, before incorporation into the TiO₂ lattice.²⁸⁸ This shows an inherent side effect when trying to dope TiO₂ with anions other than fluoride. Since oxygen is more electronegative, it tends to stay in its anion form and can oxidize other ions, including dopant anions. An exception to this is fluorine since it is the only element with a higher electronegativity than oxygen. Hence, it cannot be oxidized to form fluorine cations.²⁸⁹

1.4 Modification of titanium dioxide photochromic properties by heterostructure formation and other means

There is also the possibility of enhancing the photochromic properties of TiO₂ via heterostructure formation.²⁹⁰ This can increase the charge carrier separation and hence lead to a higher number of photoaccumulated electrons, leading to more intense visible and infrared light modulation. Furthermore, doping and heterostructure formation could, in theory, lead to self-sustainable photochromic nanoparticles, that no longer require an additional hole scavenger to be present for photochromism to take place and would recover when not exposed to light with the required photon energy (UVA light for TiO₂). This would present many possibilities

for the subsequent implementation of the photochromic nanoparticles and would allow them to behave the same, irrelevant of the matrix material.

An additional, but inherently difficult way to enhance the photochromic properties of TiO₂ and potentially dismiss the necessity for an external hole scavenger, is the preparation of heterostructures, either with another semiconductor such as ZnS or with a metal such as Ag. In the case of semiconductors, the idea to improve electron accumulation in TiO₂ is to combine it with such a material, whose band gap is skewed in such a way, that favors electron accumulation in the anatase conduction band, while accumulating holes in the accompanying semiconductor. This also has the possibility (if the accompanying semiconductor has a band gap narrow enough of absorbing visible light) of becoming photoactive under visible light irradiation.²⁹¹ This can be achieved by creating heterostructures of TiO₂ with chalcogenides, such as ZnS, CdS, MoS₂²⁹² as well as other oxides such as Bi₂O₃, V₂O₅²⁹³, BiOX (X=I,Cl,Br)²⁹⁴, CuO²⁹⁵, Cu₂O²⁹⁶ and others. There are 3 types of heterostructures possible, classified by the relative position of the semiconductor bandgaps (Fig. 1.33). In a type I heterostructure, the valence and conduction band edges of the first semiconductor lie within the band gap of the second semiconductor. This funnels both holes and electrons to the second semiconductor, increasing the charge carrier recombination rate. Examples of this include MoS₂ as well as BiOI and Fe₂O₃²⁹⁷. Type II heterostructures have both the valence and conduction bands staggered and favor the migration of electrons from the first semiconductor to the second, and holes from the second to the first. This is also the most widely studied type of heterostructures with many of the aforementioned examples falling into this category. Type III heterostructures, are even more staggered, and are the type of choice for Z-schemes, a form of heterostructure where there is a metal nanoparticle between the two semiconductors.²⁹¹

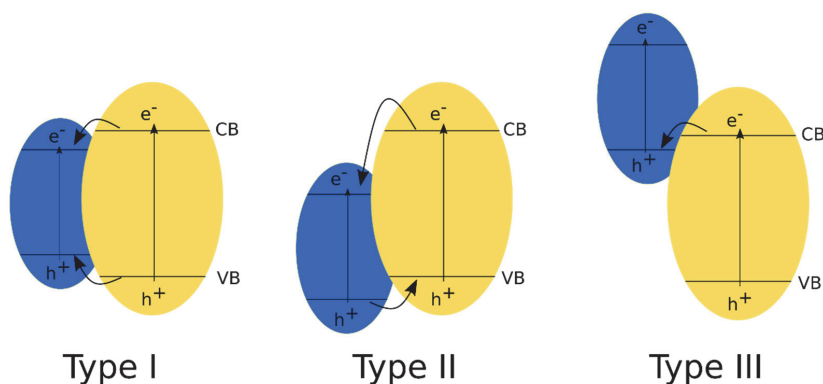


Fig. 1.33. Different types of heterostructure band gap alignments.²⁹⁸

Semiconductor/metal heterostructures made with TiO₂ typically use metals such as silver²⁹⁰, gold²⁹⁹, platinum³⁰⁰ or copper³⁰¹, with silver being the most popular for photochromism. A semiconductor/metal heterostructure hinders the electron/hole recombination through the sequestration of the photoelectrons from the conduction band of the semiconductor to the surface of the metallic nanoparticles (Fig. 1.34).³⁰² This charge carrier transport to the metal nanoparticles is favored by the increased electronegativity of the metal. This accumulation of electrons in the metal nanoparticles leads to surface plasmon resonance. This is the phenomenon of electrons collectively oscillating. This oscillation is induced by light irradiation if the light

wavelength is in accordance with the free electrons.³⁰³ If the amount of accumulated electrons is sufficient, visible light can be absorbed, enhancing the materials photochromic properties.

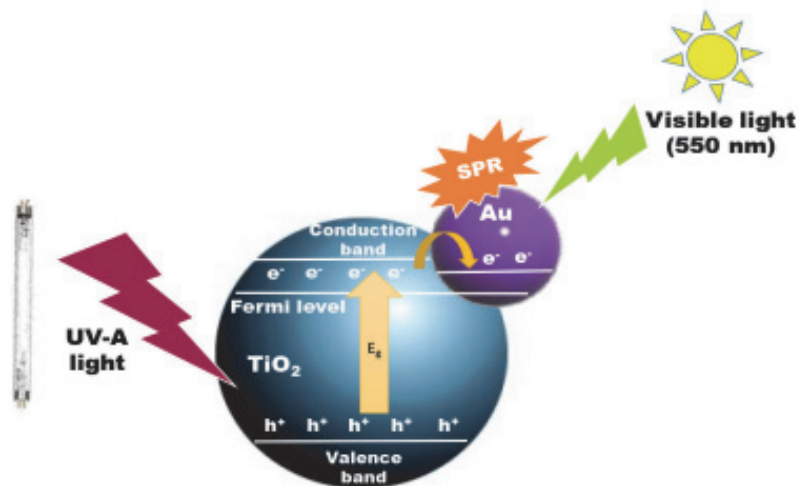


Fig. 1.34. Schematic diagram Ag/TiO₂ heterochromic system and charge transfer.²⁹¹

Reproduced under the terms of the Creative Commons CC BY license.

The loading of TiO₂ films with silver has also had the effect of giving the films multicolor photochromism (Fig. 1.35), as the films changed color with respect to what colour light was used for irradiation ranging from 350 – 700 nm.³⁰⁴ The color stems from the size change of silver nanoparticles upon irradiation with different wavelength light, which changes the SPR absorption wavelength. These films also exhibited a memory effect, being shown to remember an irradiated pattern even after bleaching and subsequent repeated UV irradiation. This is due to the oxidation of the silver nanoparticles and the removal of Ag⁺ ions if the film is irradiated in water.²⁹⁰

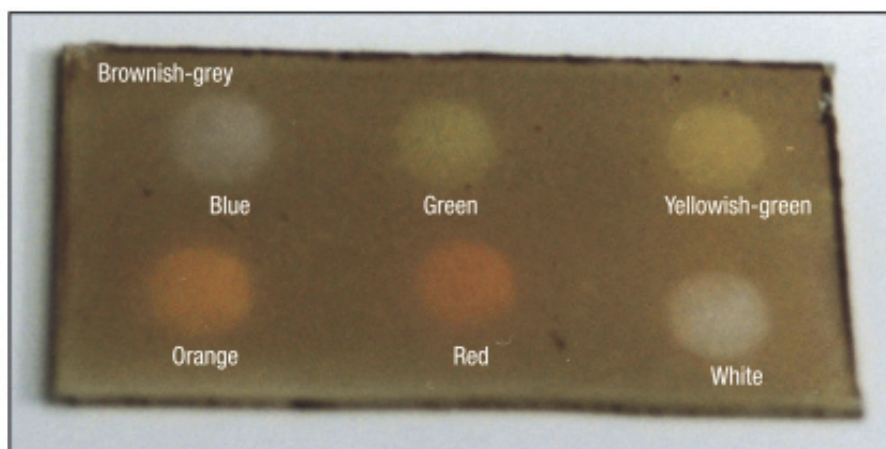


Fig. 1.35. Multicolored Ag-TiO₂ photochromism.³⁰⁴

Facets (001) of TiO₂ have a tendency to attract excited holes, while (101) facets attract excited electrons.³⁰⁵ However, there are still contradictions to this theory, as others have shown

according to DFT calculations, that (001) and (110) facets trap electrons strongly, while (101) repel electrons.³⁰⁶ Irrelevant of this, there has been research showing, that depending on which facets are dominant, a shift in both the valence and conduction bands can be observed, resulting in the band gap shifting both in size as well as relative to vacuum.³⁰⁷ The combination of lattice defects (oxygen vacancies), as well as dominant (001) facets, has resulted in the preparation of anatase TiO₂ with a deep blue color (Fig. 1.36).³⁰⁸

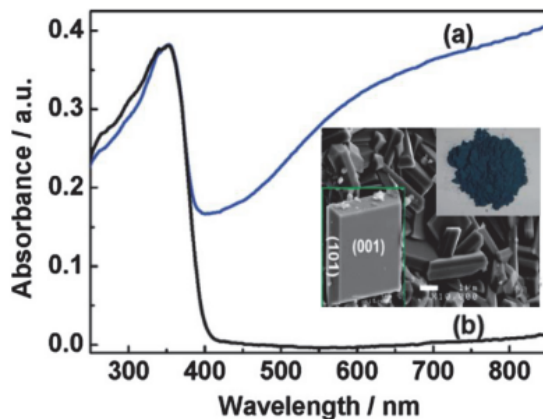


Fig. 1.36. Absorption spectra of (a) oxygen deficient anatase nanosheets with dominant (001) facets and (b) anatase nanosheets without the oxygen vacancies.³⁰⁷

Most of the heterostructures synthesized, however, have been researched for their photocatalytic properties as this is by far a more widely researched topic (especially for semiconductor-semiconductor heterostructure). However, several notions can be taken from photocatalysis and using it to predict the possible photochromic properties. For one, an increased charge carrier lifetime will result in a higher probability of hole scavenging and as such, a higher rate of electron accumulation and photodoping. This results in faster photochromism. Furthermore, if the material is an active photocatalyst under visible light, then, most likely, the material will also be photochromic under anaerobic circumstances, under visible light. Visible light response can be useable for specific application.

Similarly, as the hole scavenging process is happening on the surface of the nanoparticles (especially for plain TiO₂ or doped TiO₂), the nanoparticles size should be as small as possible, to ensure the highest possible surface area. This is also crucial, because, if the nanoparticles are too large, scattering can occur, reducing the transmittance in the uncolored state. To ensure the best photochromic capability, the nanoparticles need to be dispersed in a hole scavenging medium. This hole scavenging medium can be either a solvent, but can also be a polymer, for instance PVA. The most potent hole scavengers are those, whose molecules contain -OH groups.³⁰⁹⁻³¹¹ However, the influence of hole scavengers on the photochromic performance of TiO₂ colloids has not been widely researched. In fact, only one theoretical publication on this topic has been published.¹⁴⁹ This study concluded that more complex alcohols such as glycerol would be better suited as hole scavengers, than simple alcohols due to their capability of scavenging several holes per molecule. This leads to one of my goals in this work – to get an understanding of what hole scavengers would be best suited for the preparation of TiO₂ colloids in terms of photochromic performance.

For most applications, however, a nanoparticle colloid is unsuited as it can leak or evaporate, causing pressure build up in closed systems, creating a burst risk. If the nanoparticles are incorporated in a polymer matrix, such as PVA, the resulting photochromic composite shows low transmittance change as well as low kinetics, requiring several hours to photodarken by just 20%, while also recovering slowly.³¹²⁻³¹⁵ A middle ground for this would be polymer gels containing the photochromic TiO₂ nanoparticles as well as a hole scavenging solvent. The gel could retain the absorbed hole scavenger and allow for it to be readily available for photodoping. However, most gels reported in literature, are opaque and prepared from relatively large TiO₂ nanoparticles.^{148,316}

1.5 Summary

Chromism, being a materials property of changing color in response to an external stimulus, has been widely researched and found usage in a lot of different applications. Out of these, the main three are electrochromism, photochromism and thermochromism, with electrochromism being the most widely researched, especially in for the potential applications of smart windows. Electrochromic materials controllable but do require external controls in the form of power supply and electrodes. On the contrary, photochromic and thermochromic materials are fully autonomous by their nature with responses to light and temperature, respectively.

Depending on the specific goal, out of these two, photochromic would be best suited for thermal radiation control as they would limit the incoming light proactively, while thermochromic materials can limit the incoming light after a certain temperature is reached. Another thing to consider is that thermochromic materials have a set temperature at which thermochromism occurs, while photochromic materials usually change gradually.

When comparing inorganic and organic photochromic materials, inorganic have several major advantages. First, they are more stable, since inorganic photochromic materials are transition metal oxides, that are classified as semiconductors. They are stable to both a wide range of temperatures as well as radiation energies. Second, the photochromic effect changes the transmittance in a wide spectral range, not just in the visible, but also in the infrared range. This is important for controlling thermal radiation. Third, most organic photochromic materials require either a light of a different wavelength or heat to recover, while inorganic materials simply require exposure to air. Of course, there are also downsides. The major downside being the requirement for a hole scavenger to be present for inorganic photochromic materials to function. The potential to circumvent this, is the deployment of semiconductor/semiconductor or semiconductor/metal heterostructures, that can work without the need for a hole scavenger. Another disadvantage (that can also be a possible advantage), is that these inorganic photochromic materials require UV light to function. This is an advantage because that means that they will not darken under artificial lighting. However, this also means that the optical properties can be modulated only by a small portion of UV in sunlight.

Out of the different transition metal oxides, titanium dioxide is a good candidate for photochromism, as it is a very robust semiconductor oxide, that is already extensively studied in photocatalysis. An additional consideration is that TiO₂ is an abundant material, making its usage a favorable alternative to current flagship inorganic photochromic materials such as WO₃ or MoO₃. To enhance the performance of TiO₂, the introduction of cation impurities can be employed in the form of doping, with 5+ and 6+ cation dopant having the best impact on the

photochromic performance. These introduce electron traps and acceptor levels in the band gap, that can help and increase charge carrier lifetime, allowing more time for hole scavenging and thus, increasing the photochromic response.

The simplest method to promote photochromism is dispersing the photochromic nanoparticles in a hole scavenging solvent (i.e. a solvent containing electron donor groups, such as alcohol). This method can be a great way to study the photochromic performance of nanoparticles or the influence of different hole scavengers on them. However, for practical applications, these colloids can prove difficult to be used, as all solvents are prone to evaporation and leakage. The former, if happening in an enclosed container, can lead to pressure build-up, that can rupture the container and lead to leakage.

If the photochromic material is formed into a thin film, then they need to be made into heterostructures, because, since hole scavenging is a surface process, the deeper layers of the film would not be exposed to hole scavengers and would not undergo photochromism. So far, the most widely studied are TiO₂/Ag heterostructures, that can be used in thin film form.

The last possibility of photochromic nanoparticle usage is in gel form. This would allow the nanoparticles to be dispersed in the matrix, increasing the resulting surface area when compared to thin films. Furthermore, if the matrix is saturated with a hole scavenger, it would be better retained when comparing to colloidal suspensions. Furthermore, with the correct matrix material, the gel matrix itself can be made into the hole scavenger, thus reducing the number of components, and further reducing potentials for evaporation. However, so far, most such composites have either low photochromic performance or are opaque, which makes them unsuitable for applications where transparency is required, such as smart windows.

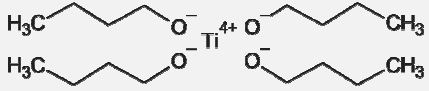

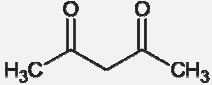
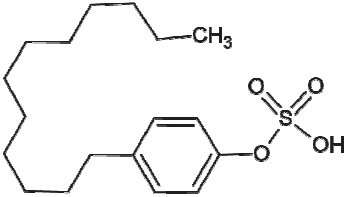
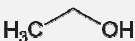
2 METHODIC SECTION


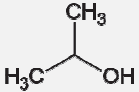


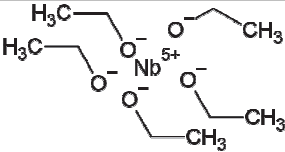


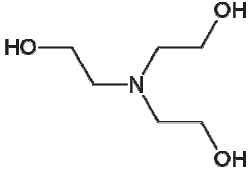
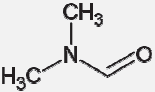
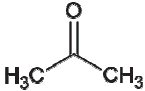
In this section, an overview of the nanoparticle synthesis and film preparation methods is given. Following this, an overview and a brief description of the analysis methods used is shown.

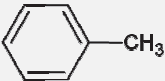
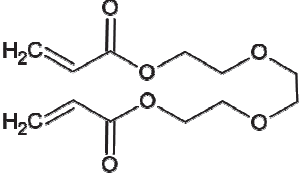
2.1 Reagents used

Information on the reagents used in the preparation of all of the samples can be seen in Table 4. The reagents were used without any further purification, with the exception of *n*-BuOH, which was dried by dispersing CaH₂ in the solvent and kept with CaH₂ in order to kept it dry.

Table 4.

Reagent table			
Chemical name (supplier)	Chemical formula	Assay	Usage
Tetrabutyl orthotitanate (Sigma-Aldrich)		97%	For nanoparticle synthesis, Ti precursor
<i>n</i> -Butanol (Sigma-Aldrich)		≥99.5%	Primary solvent for synthesis and most colloids
2,4-pentanediol (Sigma-Aldrich)		≥99%	Ligand used for controlling nanoparticle growth
4-dodecylbenzene sulphonic acid (Sigma-Aldrich)		≥95.0%	Surfactant
Deionized water (produced in-house)	H ₂ O	-	Used in the synthesis for hydrolysis
Methanol (Merck KGaA)	H ₃ C—OH	≥99.9%	Washing of the nanoparticles and used for electrical resistance tests
Ethanol		98.6%	Colloid preparation

			and used for electrical resistance tests
<i>n</i> -Propanol (Sigma-Aldrich)		≥99.9%	Colloid preparation and used for electrical resistance tests
<i>i</i> -Propanol (Sigma-Aldrich)		≥99.5%	Colloid preparation and used for electrical resistance tests
<i>n</i> -Pentanol (Sigma-Aldrich)		≥99.0%	Colloid preparation and used for electrical resistance tests
<i>n</i> -Hexanol (Merck KGaA)		≥98.0%	Colloid preparation and used for electrical resistance tests
Niobium ethoxide (Sigma-Aldrich)		99.95%	Nb precursor
Calcium hydride (Sigma-Aldrich)	CaH ₂	95%	For <i>n</i> -butanol drying
Ethanolamine (Sigma-Aldrich)		≥99.0%	Colloid preparation
Diethanolamine (-)		-	Colloid preparation
Triethanolamine (Sigma-Aldrich)		98%	Colloid preparation
<i>N,N</i> -dimethylformamide (Sigma-Aldrich)		≥99.8%	Colloid preparation
Acetone (Sigma-Aldrich)		≥99.5%	Used for electrical resistance tests

Toluene (Sigma-Aldrich)		≥99.5%	Used for electrical resistance tests
PEGDA-250 (Sigma-Aldrich)		-	Polymer backbone used for gel preparation

2.2 Synthesis of TiO₂ and doped TiO₂ nanoparticles

TiO₂ nanocrystals were synthesized by using a method, first described by *Scolan and Sanchez*.³¹⁷ It was further developed by *Joost, et.al.*¹⁴⁶ and was as follows (schematic representation can be seen in Fig. 2.1.): in a double necked flask under N₂ flow, 12.4 mL of *n*-BuOH (previously dried by adding CaH₂ to it) was added through a syringe and 0.22 μm filter. Prior to the synthesis procedure, *n*-BuOH was dried by adding 10% w/v of CaH₂ to the solvent and stirring it overnight in a closed flask. The CaH₂ and Ca(OH)₂ nanoparticles were allowed to sediment to avoid larger contaminants to the synthesis. The syringe filter filtered out the smaller nanoparticles. The necessary amount of AcacH (8.368 mL) was added to the butanol. Then the Ti(*n*BuO)₄ (9.05 mL) was added dropwise. This caused a yellowish solution to form, indicating the formation of a Ti(*n*BuO)_{4-x}(acac)_x complex.³¹⁸ After this, the solution was brought to reflux and a mixture of 4-DDBSA (1.76 g) and DI water (4.865 g) was added dropwise to the solution. This was then left to react overnight (around 17 hours). After this, solution was left to cool to room temperature for several hours, during which, a yellow precipitate formed. This was then separated via centrifugation (2000 g, 1 hour). Following this, the sediment was redispersed in MeOH and centrifuged once more (2000 g, 1 hour). Again, the sediment was separated via decantation and redispersed in a fresh batch of MeOH once more. This was followed by yet another centrifugation (this time at 4000 g for 1 hour). After this, the nanoparticle sediment (white to slightly yellowish) was decanted and redispersed in either pristine *n*-BuOH or DMF, or any other solvent, used in this work (EtOH, *n*-PrOH, *i*-PrOH, *n*-Pentanol or *n*-Hexanol). Subsequently, the nanoparticles can also be covered by a small amount of MeOH and kept in a slurry form for later use. This procedure is also shown as a diagram in Fig. 2.2.

To produce doped TiO₂ nanoparticles (synthesis schematic Fig. 2.3), the necessary amount of precursor (dependent on the doping amount), AcacH and *n*-BuOH (both dependent on the dopant precursor amount with a molar ration between dopant precursor: AcacH of 1:4 and precursor: solvent of 1:10) was mixed in a separate flask under N₂ flow and transferred dropwise into the Ti precursor mixture using the N₂ flow to transfer to the Ti precursor/AcacH/*n*-BuOH solution. This was allowed to mix for 15 min before bringing the solution to reflux conditions and adding the 4-DDBSA/DI water mixture. After 17 h reflux, the solution was cooled to 40 °C and transferred into a 50 mL Teflon lined stainless steel autoclave and solvothermally treated for 24 hours at a temperature of 150 °C. Cooling of the autoclave was done slowly in the oven over the timespan of 6 h. After this, the purification procedure is

the same as in the case of un-doped TiO₂. After purification the nanoparticles are immediately redispersed in pristine *n*-BuOH or DMF.

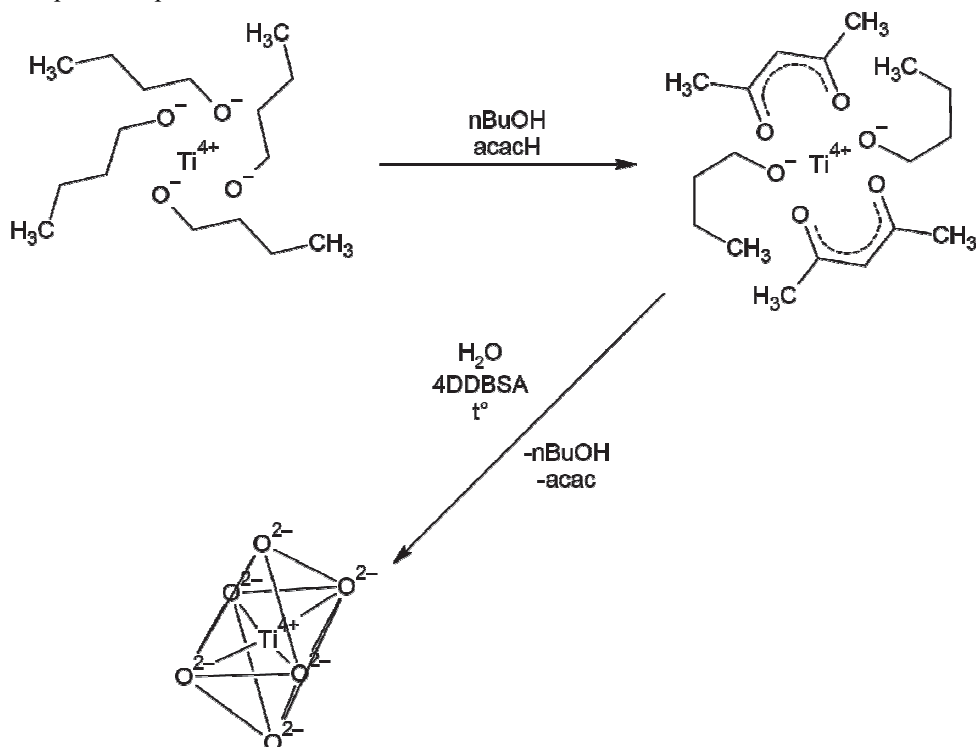


Fig. 2.1. TiO₂ synthesis procedure schematic.

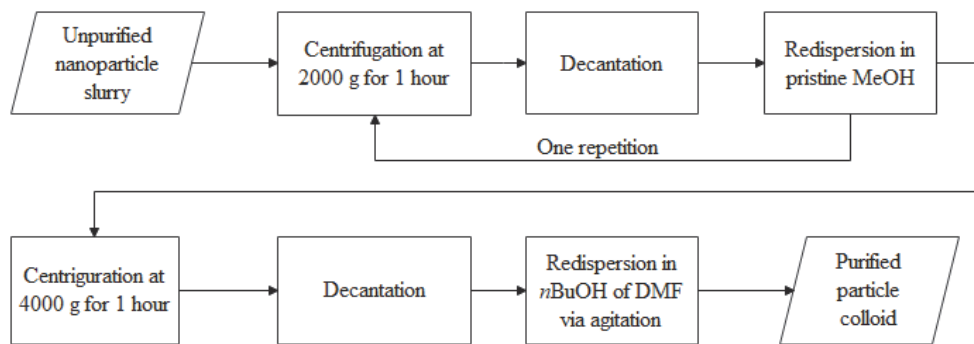


Fig. 2.2. Nanoparticle purification procedure.

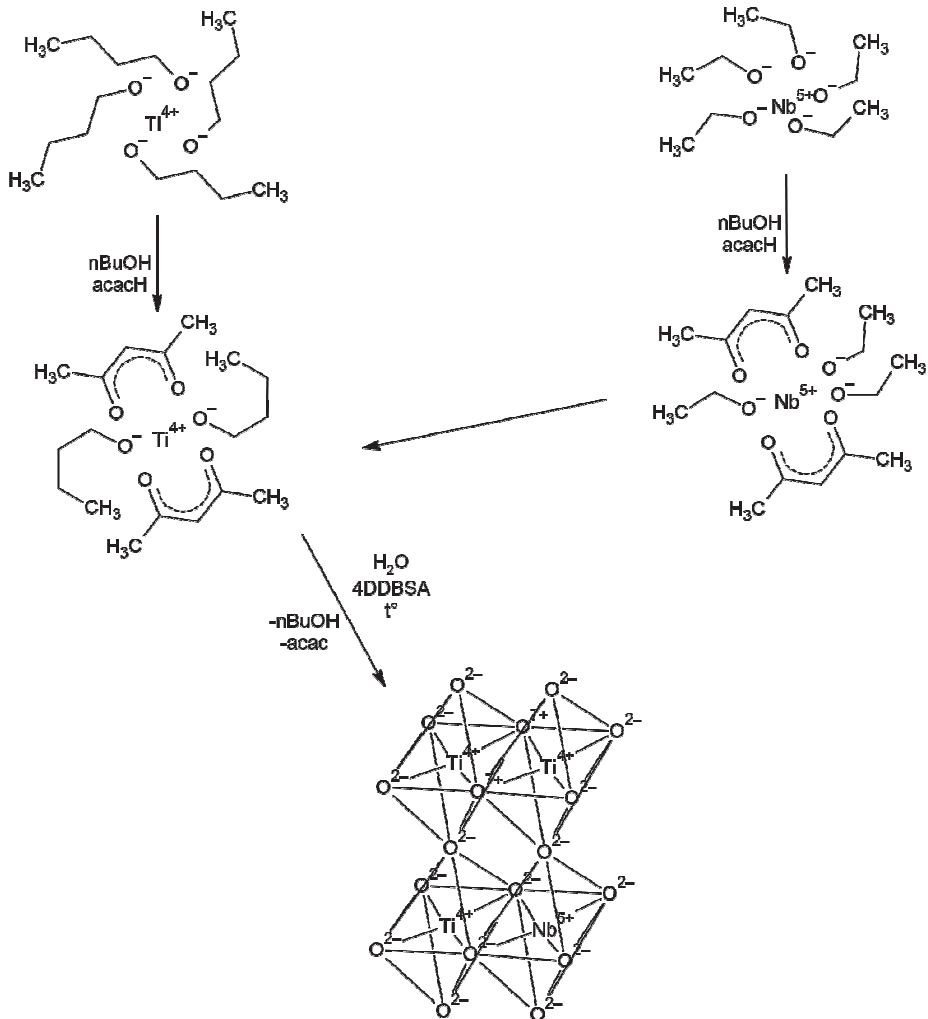


Fig. 2.3. Synthesis route for Nb⁵⁺ doped TiO₂ nanoparticles.

2.3 Coating preparation

Coatings on ITO electrodes were prepared with the usage of spin-coating. Spin-coating is a procedure, in which, a drop of the coating solution is placed in the center of the substrate. The substrate is then spun slowly at first, to spread the solution evenly on the substrate. Lastly, the substrate is spun rapidly, forcing the excessive solution off radially and drying the substrate, creating a thin film.

In our case, a nanoparticle suspension in *n*BuOH (100 g/L) was used to coat an ITO glass substrate, that was plasma treated prior to coating. The substrate was dropped on the substrate, left for 30 seconds, and then spun for 1000 rpm for 30 seconds, producing the thin film. Lastly, the samples were then dried at 150 °C for 1 hour and heat-treated at 400 °C for 1 hour. To get distinct electrodes, a line in the ITO coating was etched with a 9N HCl water solution for 10 min.

2.4 Scientific equipment used for the characterization of the materials and their photochromic performance

The research equipment used throughout the thesis is shown in Table 5. All the data processing was done using Origin 2019 software.

Table 5.

Scientific equipment used in the research

Research method	Equipment used	Parameters
X-ray diffraction	PANalytical X'Pert PRO, <i>Malvern Panalytical</i> , (Riga, Latvia)	Cu K α x-ray source
Scanning electron microscopy	Helios 5 UX, <i>ThermoFischer Scientific</i> , (Riga, Latvia)	Accelerating voltage 2 kV Magnification between 10 000 to 20 000 times
Transmission electron microscopy	Tecnai G2 F20, <i>FEL</i> , (Riga, Latvia)	Magnification between 25 000 to 450 000 times
X-ray photoelectron spectroscopy	XR-4, <i>Thermo VG Scientific</i> , x-ray source and SES100, <i>Scienta</i> , analyzer (Tartu, Estonia)	Mg K α x-ray source. Spectra analyzed using CasaXPS software
Raman spectroscopy	inVia, <i>Renishaw</i> , (Riga, Latvia)	Variable range, 532 nm laser
UV-vis Spectroscopy	UV2000, <i>OceanOptics</i> , (Riga, Latvia) Genesys 10S, <i>ThermoFischer Scientific</i> , (Riga, Latvia)	UV2000: 400-1050 nm range, 5 accumulations 200 ms acquisition time; Genesys 10S: 400-1100 nm range, 1 nm step, medium acquisition speed.
Diffuse reflectance spectroscopy	SolidSpec UV3700, <i>Shimadzu</i> , (Riga, Latvia)	300-1650 nm range, 1 nm step, slow acquisition speed
Rietveld refinement	Profex software	-
Electron paramagnetic resonance	EMX-plus, <i>Bruker</i> , (Riga, Latvia)	X-band frequency 9.86 GHz, power 20 mW, sweep width 400 G centered at 3540 G, receiver modulation frequency 100 kHz with an amplitude of 5.00 G and receiver gain 1×10^4
UV light source	Mercury vapor UV lamp, UVA-LED, and a Triple UVA-LED array (Riga, Latvia)	Mercury lamp (125 W) UVA-LED (1 mW) UVA-LED array (8 mW)
Electrical resistance measurements	B2987A, <i>Keysight technologies</i> , (Riga, Latvia)	Bias voltage 15.0 V

Photocurrent measurements	6514, <i>Keithley Instruments</i> , electrometer with 5444B, <i>Pico Technology</i> , oscilloscope (Riga, Latvia)	No bias voltage, oscilloscope acquisition rate 1000 reads/s
---------------------------	---	---

2.5 X-ray diffraction

To determine the crystalline structure of all the nanoparticles studied, the colloids were first heated at 120 °C to obtain dried nanoparticles. This resulted in large agglomerates of nanoparticles. To avoid any anisotropy of the nanoparticles stemming from orientation, these agglomerates were ground to a fine powder using a mortar and pestle. This resulted in a slightly yellowish powder. The powder XRD patterns were then determined using a PANalytical X'Pert PRO XRD diffractometer using Cu K α radiation with a wavelength of 0.15406 nm. The obtained XRD diffractograms were compared with databases to identify the crystalline phase as well as between different samples in terms of the diffraction angle for different diffraction peaks. As the x-ray radiation has a wavelength comparable to the distance between the crystalline lattices in a crystal, these lattices act as a diffraction grating. This means that even slight changes in the lattice plane distance can result in shifts in the diffraction peaks.³¹⁹ Furthermore, the size of the nanoparticles will also have an effect on the diffraction peaks, with small nanoparticles (<50 nm) resulting in a increase in the FWHM of the diffraction peak.³²⁰

2.6 Rietveld refinement

To obtain more information from the obtained powder XRD patterns, Rietveld refinement was carried out using *Profex* software, based on the BGMN simulation tool.³²¹ This method is based on work published between 1967 and 1969 by Prof. Hugo Rietveld, and simulated XRD patterns based on crystallographic information. These simulated patterns are then compared to the experimental XRD patterns and the differences are analysed.³²² This allows to obtain detailed information about the crystalline structure of a material, such as the unit cell parameters, nanoparticle size, anisotropy and lattice strain.³²³

2.7 Raman spectroscopy

Dried powder samples for Raman Spectroscopy were prepared the same way as in the XRD samples. The Raman spectra for these samples were recorded using the *Renishaw inVia* micro-Raman spectrometer. For excitation of the sample, a green laser with a wavelength of 532 nm was used. For the photochromic gel, the sample was prepared in a test cell with a quartz top window to minimize the interference from the cell. The obtained Raman spectra have a lot of information about the crystalline lattice of the sample. This is because Raman spectroscopy uses the inelastic scattering resulting in Stokes Raman scattering.^{324,325} Raman spectroscopy is very sensitive to lattice distortions, allowing one to see even slight distortion as noticeable changes in the Raman spectra, similarly to XRD.

2.8 Scanning and transmission electron microscopy

To characterize the synthesized nanoparticles, transmission electron microscopy was used to obtain micrographs of the synthesized nanoparticles. To do this, the pristine TiO₂ nanoparticle colloid was diluted 1:20 with IPA. However, the Nb-doped nanoparticle colloids could not be diluted in the same way as this caused the nanoparticles to agglomerate and sediment. To avoid this, the Nb-doped TiO₂ nanoparticle colloids were diluted 1:20 with *n*-BuOH. Using the colloids, the nanoparticles were suspended on Cu grids using evaporation from IPA or *n*-BuOH. The micrographs were obtained using a *FEI Tecnai G2 F20* high resolution TEM, at different magnifications. This allowed to obtain micrographs with sufficient resolution so that the crystalline planes of the individual nanoparticle would be visible. The data obtained from these micrographs was statistically analyzed to determine the mean nanoparticle size as well as the size distribution of the nanoparticles throughout out the samples studied.

To determine the thickness of the TiO₂ layer used for the study of photoaccumulated electrons, the sample was broken, and SEM micrographs were taken with the sample at a 90° angle with respect to the focal plane of the microscope. The SEM used was a *ThermoFischer Scientific Helios 5 UX* using an accelerating voltage of 2 kV and a magnification of between 10 kx and 20 kx.

2.9 Selected Area Electron Diffraction

Usage of TEM also allowed SAED pictures to be taken for the samples. This technique uses electrons instead of X-rays to obtain diffraction data and can easily discern between amorphous, polycrystalline and monocrystalline samples (Fig. 2.4). This was used to probe the crystalline structure of the samples on a much smaller scale, when compared to XRD and was used to further confirm the highly crystalline nature of the synthesized nanoparticles.

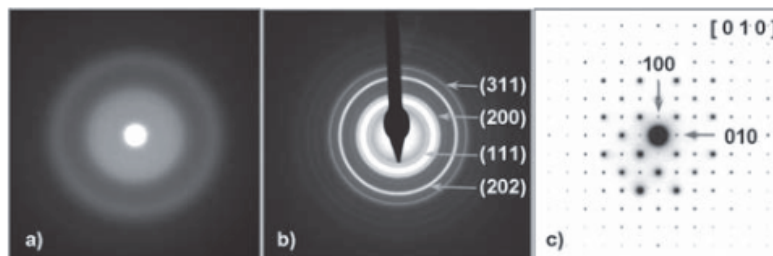


Fig. 2.4. A) SAED pattern of an amorphous sample, B) pattern of a polycrystalline sample; C) diffraction pattern of a single crystal.³²⁶

2.10 Diffuse reflectance spectroscopy

To determine the optical band gap of the nanoparticles, diffuse reflectance spectroscopy was used. For this, spectra of the dried powdered samples was recorded using a *Shimadzu UV3700* UV-Vis-NIR spectrometer equipped with an integrating sphere in the range of 300-1600 nm. The sphere was a crucial part of the setup, as it allowed to gather all the diffusely reflected light from the sample. In a similar way, DRS data was acquired for colloidal samples, suspended in a UV-quartz cuvette. This cuvette was attached to the integrating sphere were the

sample holder normal is located and a white background was used to cover the remaining 3 sides of the cuvette to avoid any light from scattering to the outside of the setup. This was done at set time intervals between of which the sample in the cuvette was irradiated using a triple UVA-LED setup with a light irradiance of 47 mW/cm². In all cases BaSO₄ was used as a reference material, that has high reflectivity throughout the studied wavelength range. The obtained reflectance data was then converted to absorption using equation (50) and (51) as per Kubelka-Munk theory, that describes diffuse reflectance in terms of attenuation due to absorption and scattering.³²⁷

$$\frac{K}{S} = \frac{(1 - R'_{\infty})^2}{2R'_{\infty}} = F(R'_{\infty}) \quad (50)$$

$$R'_{\infty} = \frac{R_{\infty \text{ sample}}}{R_{\infty \text{ standard}}} \quad (51)$$

Where:

- K – absorption coefficient;
- S – scattering coefficient;
- R'_{∞} - reflection of an infinitely scattering sample (in essence no light passes through);
- $F(R'_{\infty})$ - Kubelka-Munk function.

To calculate the band gap of the synthesized powders, the graphs were converted from a Kubelka-Munk plot to a Tauc plot for an indirect allowed transition that is typical for anatase TiO₂ (see Fig. 2.5). From this a linear fit was made for the linear part of the curve and extrapolated to the x-axis. This value corresponds to the optical band gap of the sample.³²⁸

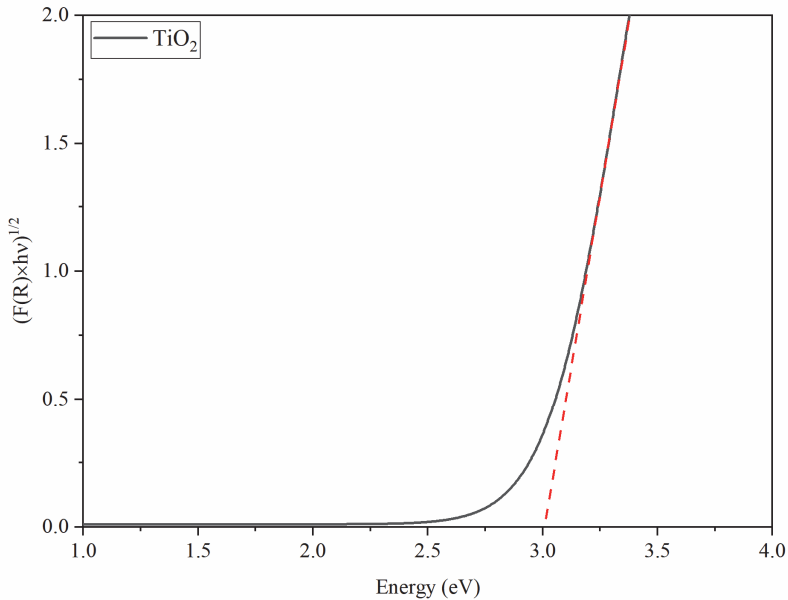


Fig. 2.5 Tauc plot of a TiO₂ sample³²⁸

2.11 X-ray photoelectron spectroscopy

To study the chemical composition of the samples XPS was used. For this, the samples were again dried to obtain powders. However, here, before the samples were examined with XPS, the surface of the nanoparticles was cleaned from the remaining organic ligands. This was done by preparing a highly acidic water solution consisting of concentrated sulfuric acid and DI water at a volume ratio of 1:1. Nanoparticles were dispersed in such a solution at a concentration of 50 g/L and irradiated with UVA light for 24 h to promote photocatalysis. After this time the samples were centrifuged and washed several times with water, to remove the remaining sulfuric acid. Finally, the samples were dried at 120 °C for 2 hours and ground using a mortar and pestle. The XPS spectra was recorded using a *Thermo VG Scientific XR-4 Mg K α* x-ray source and a *Scienta SES100* analyzer. Spectra was analyzed using CasaXPS software.

XPS allowed to obtain data not only on the chemical composition of the samples, but also about the chemical state of the constituents.³²⁹ This is because with changes in the chemical state of the ions, the electron structure of the ions also changes.

2.12 Electron paramagnetic resonance spectroscopy

Electron paramagnetic resonance was used as a non-destructive technique in order to probe the stationary field dependent Zeeman splitting. This gives insights into the structure of paramagnetic materials and their ions that have un-paired electrons.³³⁰ In short, an unpaired electron in an external magnetic field can have two energy states in which it can reside, derived from the possible spin moment values M_z , which can be either $+1/2$ or $-1/2$. Energy gap between these states increased with the increase in the external magnetic field strength. When applying electromagnetic radiation, if the energy gap between the states becomes equal to the radiation photon energy, absorption can occur. This results in a sharp signal in the EPR spectrometer, that is usually expressed as the first derivative in the spectra.³³¹ To obtain the spectra, the sample colloids were transferred to a quartz capillary sealed with cirtoseal. The spectra were obtained for samples in an un-irradiated state as well as after several UVA irradiation intervals using a *Bruker EMX-plus* EPR spectrometer using an X-band resonance frequency of 9.86 GHz. To avoid any additional signals stemming from the capillary or solvent, both an empty capillary and a capillary tube filled with pure solvent were also irradiated and the spectra obtained. The microwave power was set to 20 mW and the magnetic field had a sweep width of 400 G centered at 3540 G with an amplitude of 5.00 G and a receiver gain of 1×10^4 .

2.13 Thermogravimetry

To determine the amount of organic adsorbates on the surface of the nanoparticles (surfactant, remaining acac ligands as well as adsorbed water) a simple thermogravimetric experiment was done. The samples were heat treated at 500 °C for 1 hour to fully remove any organic adsorbates as well as water from the surface. The weight of the samples before and after the heat treatment was recorded. This gave the actual amount of TiO₂ present, in the nanoparticles and was expressed according to equation (52).

$$w\%_{TiO_2} = \frac{m_{TiO_2 \text{ before heat treatment}} - m_{TiO_2 \text{ after heat treatment}}}{m_{TiO_2 \text{ before heat treatment}}} * 100\% \quad (52)$$

2.14 Electric resistance measurements for the determination of photoinduced charge carriers.

Electrical measurements were done using a Keysight B2917 electrometer/high-resistance meter as well as a Kethley 6517B electrometer/high-resistance meter. Since the resistance was substantially high ($> 200 \text{ M}\Omega$), a bias voltage of 15 V was used. The electrical schematic of the two circuits (LED light array and the sample resistance measurement) can be seen in Fig. 2.6 left, while a schematical representation of the LEDs and the TiO_2 thin film sample can be seen in Fig. 2.6 right. The sample was kept in an electrically shielded test chamber to avoid any interference from outside electrical signals.

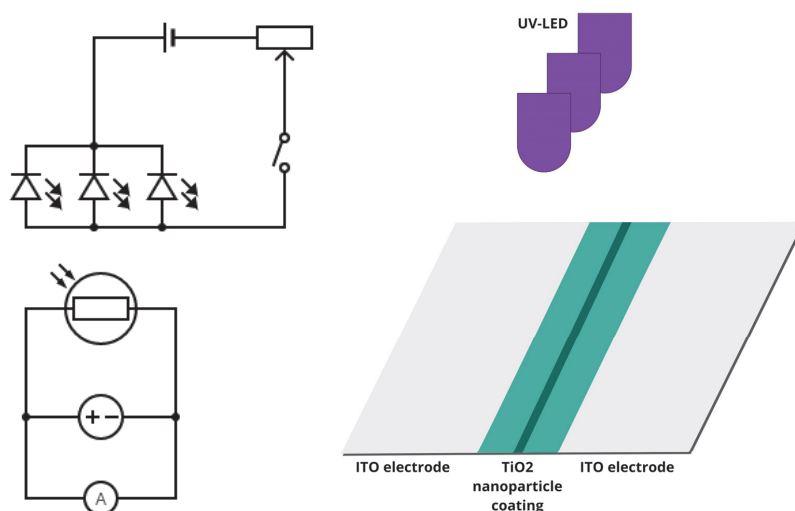


Fig. 2.6 Left) electrical schematic of the sensing and UV irradiation circuits; Right) schematical representation of the UV-LEDs and the gas sensor.

For the charge accumulation measurements, the samples were first tested purely in ambient air by switching the UV-LED array on and off. After this initial testing, the material was subjected to ethanol vapor and after some time, the test chamber was ventilated to evacuate the ethanol vapor. To obtain the necessary ethanol vapor concentration (as well as other solvent vapor concentration), an amount of ethanol (or solvent) was injected into the closed test chamber. This amount was calculated, using the equation (53).

$$V_{solvent} = \frac{C \times V_{gas \text{ chamber}} \times M_{gas}}{24.5 \times 10^9 \times \rho} \quad (53)$$

The resulting change in electrical resistance was expressed as the response S which is a relationship between the initial resistance and resistance when the sensor was exposed to the detectable vapors and calculated according to equation (54).

$$\begin{cases} S = R_0/R; \text{ if } R_0 > R \\ S = R/R_0; \text{ if } R > R_0 \end{cases} \quad (54)$$

2.15 Determination of Photochromic properties and charge carrier concentration using UV-Vis spectroscopy

The photochromic properties of the examined pristine nanoparticle colloids in different hole scavenging solvents were studied using an *OceanOptics* UV2000 spectrometer at a wavelength range of 300-1000 nm in a dark room to avoid any stray light. The colloids were transferred to a UV-quartz fluorescence cuvette (with all 4 sides being clear) with a small stir bar inside. To avoid any air of getting into the cuvette, it was capped with an LD-PE cap with an inlet for bubbling air through the colloid as well as an outlet what passed through a silicon oil bubbler to avoid any air of getting into the system. The spectra of the colloids were taken with the respective solvent acting as the baseline sample. Splitgraphs were taken to record the real time change in transmittance. For UVA irradiation, a single UVA-LED was used with a peak wavelength of 365 nm at a distance of 1 cm. Irradiation was done at a 90° angle with respect to the optical path of the light beam used for spectral measurements to avoid interference. These samples were irradiated until fully photodarkened. For recovery, the UVA-LED was turned off and air was bubbled through the system using a peristaltic pump at a rate of 0.8 mL/min. Throughout these experiments a magnetic stirrer was used to ensure a homogeneous colloid. The spectra were used to compare the photochromic properties at different points during the experiment. The kinetics were determined by calculating the relative transmittance change T/T_0 . The observed kinetic processes had a non-linear nature (Fig. 2.7) and could be classified in different stages (I)-(IV). During stage (I) any adsorbed water or oxygen is first subjected to photocatalysis. At this stage the resulting photochromic expression is slow. The coloring speed increases over time. During stage (II), the transmittance change rate can be considered as constant and constitutes the majority of the change in transmittance. In stage (III) the absorption has reach such a degree, that the non-linear correlation between absorbance and transmittance results in an apparent slow-down in transmittance change. This is also partly due to saturation of the nanoparticles with photodoping induced defects and photoaccumulated electrons and an equilibrium forming between the formation of new defects and the internal hole scavenging of the newly formed defects. For recovery air is bubbled through the colloid either at a constant speed or a set volume of air was injected and the subsequent change in transmittance was recorded. the colloid goes through the oxidation of the Ti^{3+} and the filling of oxygen vacancies (here aggregated into simply stage IV). To compare the kinetics of the different samples the change in transmittance during stages (I)-(III), the rate was calculated as the 1st order time derivative of the relative transmittance change. This then was examined in terms of the maximum and average transmittance change rates. A high maximum change rate and a low average change rate means that the photochromism is very rapid and sudden. A lower maximum change rate and a higher average change rate means that the photochromism is more gradual.

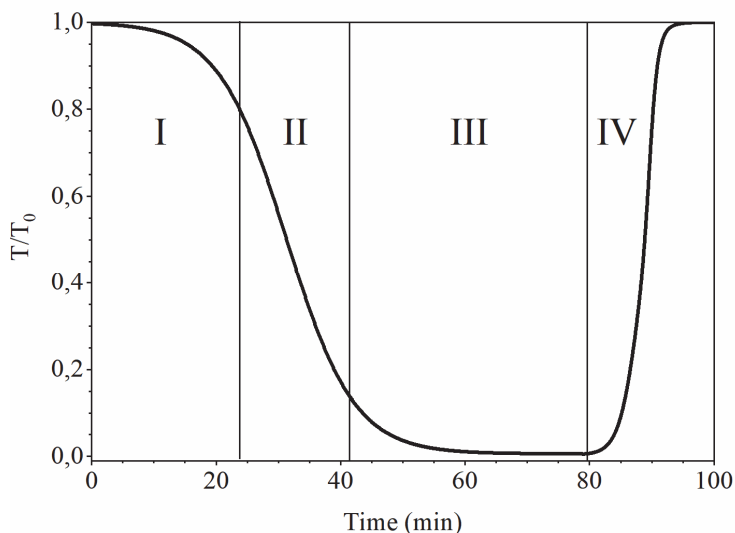


Fig. 2.7. The different stages of photochromism for TiO₂ nanoparticle colloids at 900 nm.

Experiments to determine the photochromic properties of the Nb-doped TiO₂ nanoparticle colloids as well as the photochromic gels were carried out using a *ThermoScientific Genesys 10S* UV-Vis-NIR spectrometer at a wavelength range of 300-1100 nm. Here, since the spectrometers geometry does not allow for simultaneous irradiation and spectra acquisition, UVA irradiation was done intermittently with taking the spectra. The cuvettes were the same as the ones used with the other spectrometer (UV-quartz fluorescence cuvettes equipped with air inlet and outlet). To fully seal the cuvette, the cap was attached to the cuvette using epoxy resin and Parafilm™. In these tests, for UV irradiation a triple UVA-LED array equipped with a heatsink and fan was used at a distance of 2 cm. Schematic of this is shown in Figure 2.8. Here the obtained spectra was used also to calculate the change in transmittance. For recovery experiments, air was injected using a syringe and a syringe pump for precise air injection. There were two recovery experiments carried out – dynamic and steady state. In the dynamic experiment, the fully irradiated samples were subjected to intermittent air injection and spectral acquisition. This was done to study how fast do the nanoparticle colloids recover their transmittance when exposed to an almost continuous flow of an electron scavenger (the oxygen in the air). In the steady state experiment, the fully irradiated samples were exposed to just 5.0 mL of air in the same way as in the dynamic experiment. However, after that, the sample was left to recover on its own, with recombination and electron scavenging processes happening naturally. There were also steady state experiments carried out without the initial injection of air. The transmittance change and change rate was calculated the same way as in the previously described photochromic experiments.

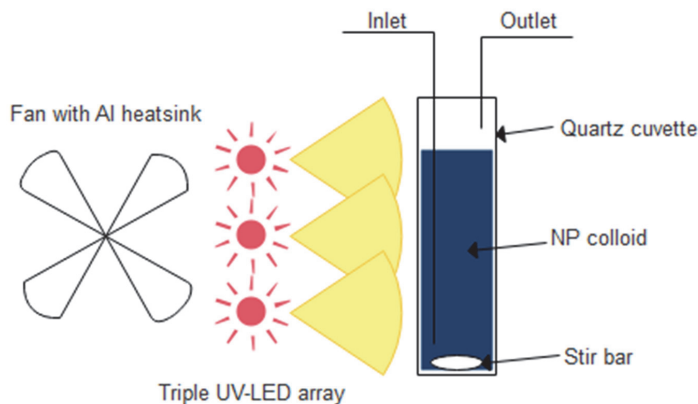


Fig. 2.8. Experimental setup for the determination of photochromic performance. Distance between UV-LEDs and the cuvette – 2.5 cm. LED output power – 15 mW/cm².

To determine the number of accumulated electrons during photodarkening for both pristine TiO₂ colloids in different hole scavengers as well as Nb-doped TiO₂ nanoparticle colloids, the samples were diluted to a concentration of 2 g/L and irradiated to saturation. To ensure saturation, the samples were irradiated for 24 h. These samples were also used to determine the maximum transmittance change, that shows the difference in absorptivity between the different samples. These photodarkened colloids were then titrated with a 10 mM iron (III) acetylacetonate solution in the same solvent as the colloids. To determine the equilibrium point the colloid absorbance spectra was monitored and was deemed to be the point at which the spectra in the NIR wavelength range no longer decreased. The expended volume of the titrant was then used to calculate the number of accumulated electrons.

The photochromic performance of the TiO₂/PEGDA gels was determined using the *ThermoScientific Genesys 10S* UV-Vis-NIR spectrometer at a wavelength range of 300-1100 nm. For these samples, the reference used was air. The gel mixture was injected between two borosilicate glass slides separated by a 700 μm thick PDMS spacer (Sylgard 184, prepared with a PDMS:hardener ratio of 5:1). To minimize any air ingress the perimeter of the sample cells was sealed with epoxy resin. For photochromic property determination, the samples were irradiated with a triple UVA-LED array at a distance of 2.5 cm and after every 5 min, the transmittance spectra was recorded. For recovery, the samples were left to recover in darkness with intermittent spectra acquisition.

2.16 Photochromic gel preparation

To prepare photochromic gels, colloids with a high TiO₂ nanoparticle content were produced (15 vol% with regard to pure TiO₂ nanoparticles, without taking into account the surfactants) in DMF. These were then diluted to get the necessary TiO₂ content. For the formation of the gel network, PEGDA with an average molecular weight of 250 g/mol was employed. The nanoparticle gel network was stabilized by DMF. Finally, a hole scavenger (EtOH) was added to the composition to promote the photodoping process. The compositions studied are shown in Table 6. To promote crosslinking and gel formation in the gels, they still

need to be UV irradiated. As such, the crosslinking occurs during the first 5 minutes of UV irradiation.

Table 6.

Photochromic gel sample composition

Sample ID	TiO₂ content (vol%)	EtOH content (vol%)	PEGDA content (vol%)	DMF content (vol%)
TPD-1	1	-	20	79
TPD-2	2	-	20	78
TPD-3	3	-	20	77
TPD-4	4	-	20	76
TPD-5	5	-	20	75
TPD-6	1	10	20	69
TPD-7	2	10	20	68
TPD-8	3	10	20	67
TPD-9	4	10	20	66
TPD-10	5	10	20	65
TPD-11	1	20	20	59
TPD-12	2	20	20	58
TPD-13	3	20	20	57
TPD-14	4	20	20	56
TPD-15	5	20	20	55
TPD-16	1	30	20	49
TPD-17	2	30	20	48
TPD-18	3	30	20	47
TPD-19	4	30	20	46
TPD-20	5	30	20	45
TPD-21	2	40	20	38
TPD-22	2	50	20	28
TPD-23	2	60	20	18
TPD-24	2	65	20	13

3 RESULTS AND DISCUSSIONS

In this part, we will be discussing the photochromic properties of both TiO₂ in colloids and gels. The influence of Nb⁵⁺ dopant on the photochromic properties will be examined. Different ways of determining charge carrier concentration will be examined. Most of the information discussed here is also published in scientific journals in full length research articles.

3.1 Photochromic properties of titanium dioxide

The synthesized nanoparticles were crystalline according to both TEM and XRD (Fig. 3.1.A&B) with a mean size of 3.6±0.5 nm according to TEM. The nanoparticles were comprised of the anatase TiO₂ crystalline phase, as indicated by XRD (JCPDS 21-1272) and Raman spectroscopy (Fig. 3.1.C). No amorphous or secondary crystalline phases were detected. The Raman bands visible were located at 148 cm⁻¹ (main E_g band), 198 cm⁻¹ (secondary E_g band), 398 cm⁻¹ (B_{1g} band), 515 cm⁻¹ (A_{1g} band) and 638 cm⁻¹ (additional E_g band). These values were red-shifted when compared to the values found in literature of 144 cm⁻¹, 197 cm⁻¹, 399 cm⁻¹, 513 cm⁻¹ and 639 cm⁻¹, respectively.³³² This is caused by the phonon confinement characteristic of ultrafine nanoparticles.³³³ The XPS spectra of Ti 2p and O 1s (Fig. 3.1.D&E) indicate a fully oxidized TiO₂ material. The Ti 2p peaks show only Ti⁴⁺ signals at 464.6 eV and 458.9 eV while the O 1s spectra shows a O²⁻ signal at 529.7 eV and an additional signal at 531.2 eV usually attributed surface oxygen and hydroxyl groups.³³⁴

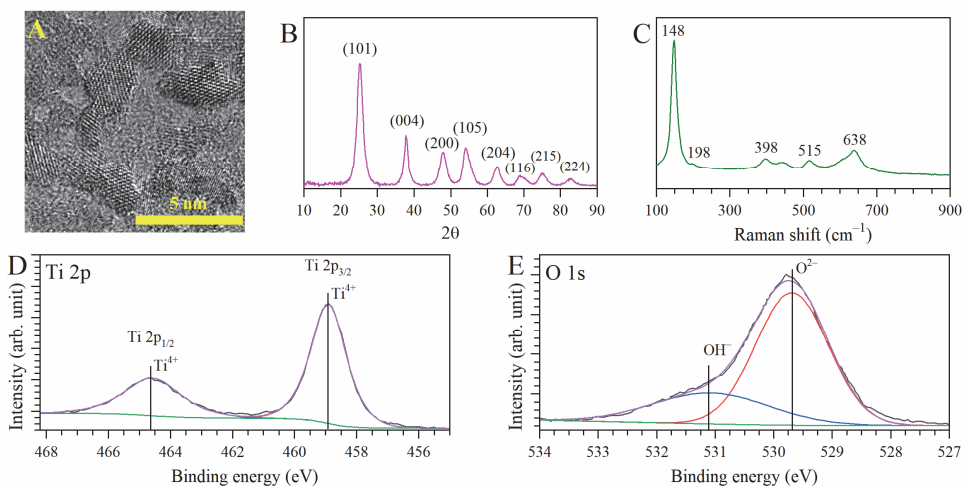


Fig. 3.1. A) TEM micrograph of the TiO₂ nanoparticles; B) XRD diffractogram of the nanoparticles; C) Raman spectra of the nanoparticles; D&E) Ti 2p and O 1s high resolution XPS spectra for the nanoparticles.

The photochromic properties of TiO₂ nanoparticles were studied in different hole scavenger solvents. The main category of hole scavengers studied was different alcohols, as they are capable of easily adsorbing onto the surface of the nanoparticles and partake in the electron donation i.e. hole scavenging.¹⁴⁹ The alcohols studied were ethanol, *n*-propanol, *i*-propanol, *n*-butanol, *n*-pentanol, *n*-hexanol as well as mixtures of ethanol with MEOA, DEOA and TEOA.

The nanoparticle concentration was 100 g/L while the amount of MEOA, DEOA and TEOA was 50 mol% of the amount of TiO₂ present in the colloid. Methanol was not studied because the nanoparticle suspensions in methanol were opaque due to low nanoparticle stability and agglomeration. All the samples showed photodarkening when the colloids were irradiated with UVA (365 nm) light. Furthermore, all the samples that were in pure solvents, were capable of photodarkening to almost complete absorbance, leaving a small transparency window between 400-550 nm. They photodarkened within 60-180 min (Fig. 3.2).

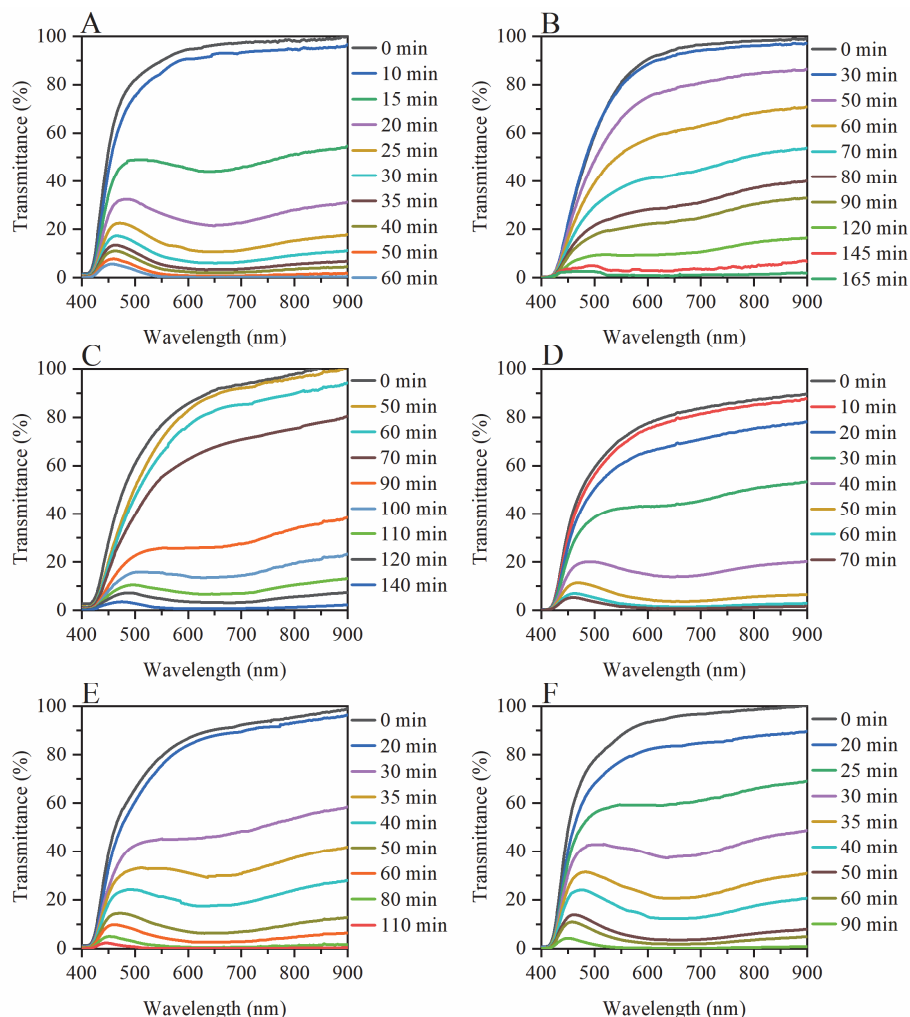


Fig. 3.2. Transmittance spectra in the 400-900 nm part of the spectra during UV irradiation (25 mW/cm²) for TiO₂ NPs in different solvents. **A)** Ethanol; **B)** *n*-Propanol; **C)** *i*-Propanol; **D)** *n*-Butanol; **E)** *n*-Pentanol; **F)** *n*-Hexanol.

To further modulate the photochromic properties of the TiO₂ nanoparticles, the ethanolamines were added to the colloids in ethanol. Specifically, MEOA, DEOA and TEOA was added at a concentration of 50 mol% with respect to TiO₂. This was done because ethanolamine possess several different hole scavenging functional groups. Not mentioning

hydroxyl groups, present also in alcohols, they contain also amino groups. The amino groups can be photooxidized to NO_2^- or NO_3^- with oxygen scavenging happening under neutral or alkaline conditions.³³⁵ This can be favorable, taking into account that photochromism of TiO_2 is accompanied by V_O formation, that would mean potential oxygen expulsion. This expelled oxygen than can be used for oxidation of the amino groups. The addition of the ethanol amines decreased the initial transmittance of the nanoparticle colloids, when compared to the transmittance of the colloid in pure ethanol (Fig. 3.3). The reason for this was additional absorption caused by the adsorbed ethanolamines. During photodarkening, the amino groups can oxidize, but then can reduce back to the amino group by scavenging the photoinduced electrons. The absorption in the photodarkened state was much lower in the NIR range (700-900 nm) when compared to colloids in pure alcohols due to the electron scavenging of the nitrogroups of the photooxidized ethanolamines. However, since visible light photodarkening still occurs means that Ti^{3+} and V_O formation still happens. The time necessary for photodarkening to saturation was similar to colloids in pure alcohol without the additives.

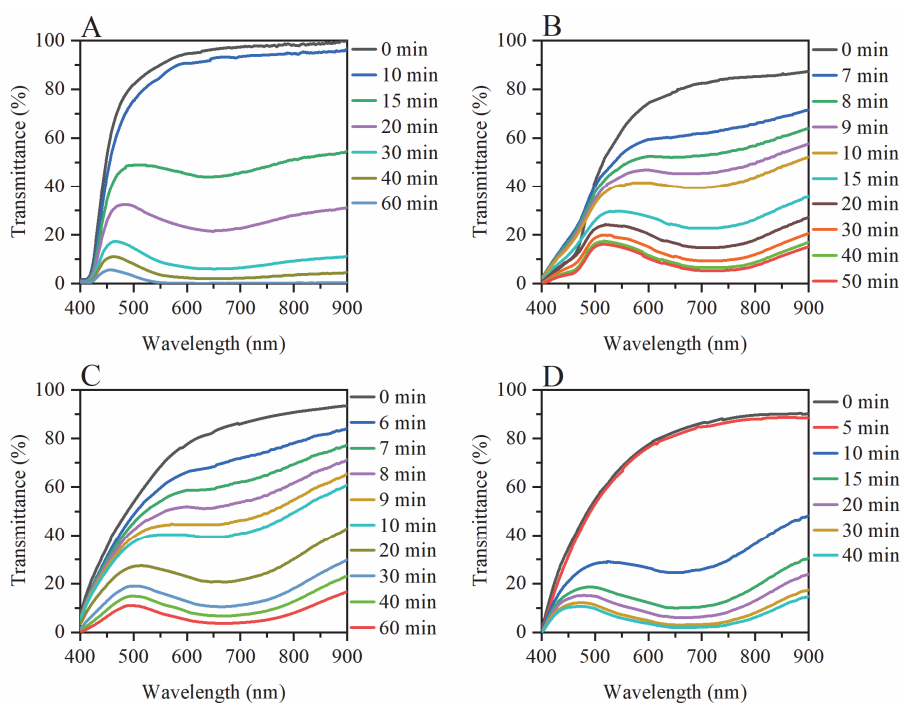


Fig. 3.3. Transmittance spectra in the 400-900 nm part of the spectra during UV irradiation (25 mW/cm^2) for TiO_2 NPs in ethanol and with different hole scavenger additions. **A)** Pure ethanol; **B)** 50 mol% of MEOA; **C)** 50 mol% DEOA; **D)** 50 mol% TEOA.

The calculated photodarkening rates for the different solvents are shown in (Figure 3.4). The transmittance change rate at different wavelengths was different. This was because different defects are responsible for photochromism at different wavelength. At 450 nm, the main absorbance stems for the additional intra band gap levels introduced by the oxygen vacancies V_O . At 600 nm the main absorbance comes from the Ti^{3+} defects, bringing acceptor levels near the CB minimum.¹⁴⁶ At higher wavelength (900 nm) the absorbance comes from

plasmon resonance due to the photoaccumulated electrons.¹ From the studied colloids it was seen that the highest transmittance change rate was observed at 600 nm with the change rate at 900 nm being quite similar. The high change rate at 600 nm when compared to 450 nm was because, as per defect equation (23), the formation of one V_O defect is accompanied by two Ti^{3+} defects. The transmittance change rate at 600 nm is twice that of the change rate at 450 nm, because of this relationship between the Ti^{3+} and V_O vacancy formation, since Ti^{3+} introduces acceptor levels at 1.25 eV below the conduction band³³⁶ while V_O introduces donor levels between 0.75 eV and 1.18 eV below the conduction band.³³⁷ The highest transmittance change rate was observed for colloids in ethanol and *n*-butanol with rates of -0.039 min^{-1} , -0.137 min^{-1} and -0.120 min^{-1} for colloids in ethanol and -0.028 min^{-1} , -0.055 min^{-1} and -0.070 min^{-1} for colloids in *n*-butanol at the wavelengths of 450 nm, 600 nm and 900 nm, respectively.

The addition of the ethanolamines to the ethanol colloid, caused changes in the transmittance change rates. Out of the three ethanolamines studied only TEOA increased the transmittance change rate at all wavelengths to values of -0.077 min^{-1} , -0.198 min^{-1} and -0.122 min^{-1} at the wavelengths of 450 nm, 600 nm and 900 nm, respectively. This can be attributed to the higher amount of hydroxyl groups in the TEOA molecule (3 groups per molecule of TEOA) as well as the presence of the nitrogen atom that had an additional electron pair and could scavenge an additional hole.³³⁶ No effects on the transmittance change at 900 nm was visible. This is because, unlike DEOA and MEOA, TEOAs nitrogen atom is sterically protected.³³⁵ Consequently, it cannot oxidize that easily to a nitro group, that could the scavenge the accumulated electrons. The same cannot be said about DEOA and MEOA additions. Here, oxidation can occur and hence, electron scavenging NO_2^- or NO_3^- groups can be obtained resulting in lower change rate values at 900 nm.

The hole scavenger is the most important part for the photodarkening of the samples. The hole scavenging capability is determined by such factors as the redox potential of the hole scavenger³³⁶ as well as the adsorption/desorption rates of the hole scavenger and its oxidation products. Another important factor is the stability of the radical species generated via hole scavenging. The main sites for radical generation are the surface Ti^{4+} sites with an adjacent oxygen that allows to adsorption and dissociation of the hydroxyl group of the hole scavenger.¹⁴⁹ For fast hole scavenging, the adsorbed scavenger after electron donation should desorb as quickly as possible. As such, photodarkening here could be considered desorption limited. Such photooxidation products (hole scavenging products) as acetone (in the case of *i*-propanol) would remain on the surface longer, than acetaldehyde (photooxidation product of ethanol) given that acetone in radical form would be more stable due to its branched structure when compared to the linear structure of the other alcohols studied.³³⁸ This would explain the decreased photodarkening rate for colloids in *i*-propanol. Another factor determining the absorption of alcohol molecules on the surface of TiO_2 is the molecular weight of the solvent with lower molecular weight alcohols having a better adsorption coverage).³³⁹ This, combined with a low radical stability explains the high photodarkening rate of the colloids in ethanol.

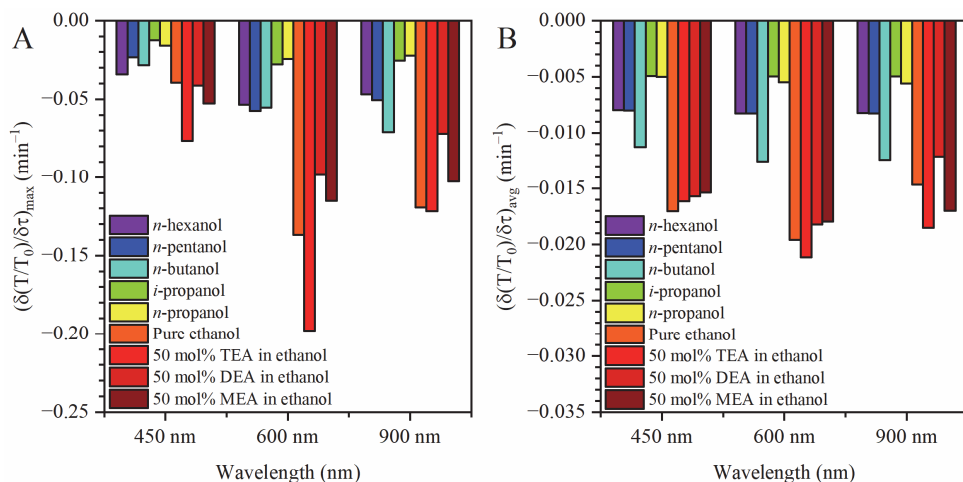


Fig. 3.4. A) Maximum transmittance change rate and **B)** average transmittance change rate for TiO₂ nanoparticle colloids in different hole scavenging media.

As the Ti³⁺ and V_O defects are unstable in the presence of oxygen all the photodarkened samples were able to recover their transmittance, when air was bubbled through the samples. When bubbling the air at a constant rate of 0.8 mL/min, the samples recovered with between 8.0 to 40.0 mL of air bubbled through them (Fig. 3.5). Here, ethanol, *n*-propanol and *i*-propanol needed the most amount of air (40.0 mL) to recover their transmittance, with the *n*-pentanol and *n*-hexanol requiring 28.0 mL of air for recovery. *n*-Butanol required the least amount with just 8.0 mL. It was also observed that these samples also did not recovery linearly with air bubbling, but there was an initial period during which, the recovery was negligible. This is because transmittance and absorbance have a logarithmic correlation. At a low transmittance, the same change in absorbance results in a smaller decrease in transmittance, than when the transmittance is high (absorbance is low). After this, the transmittance recovery happened relatively rapidly for each sample. At the end, the recovery once again slowed down, this time due to the low amount of remaining defects that need to be oxidized and their oxidation being the limiting step.

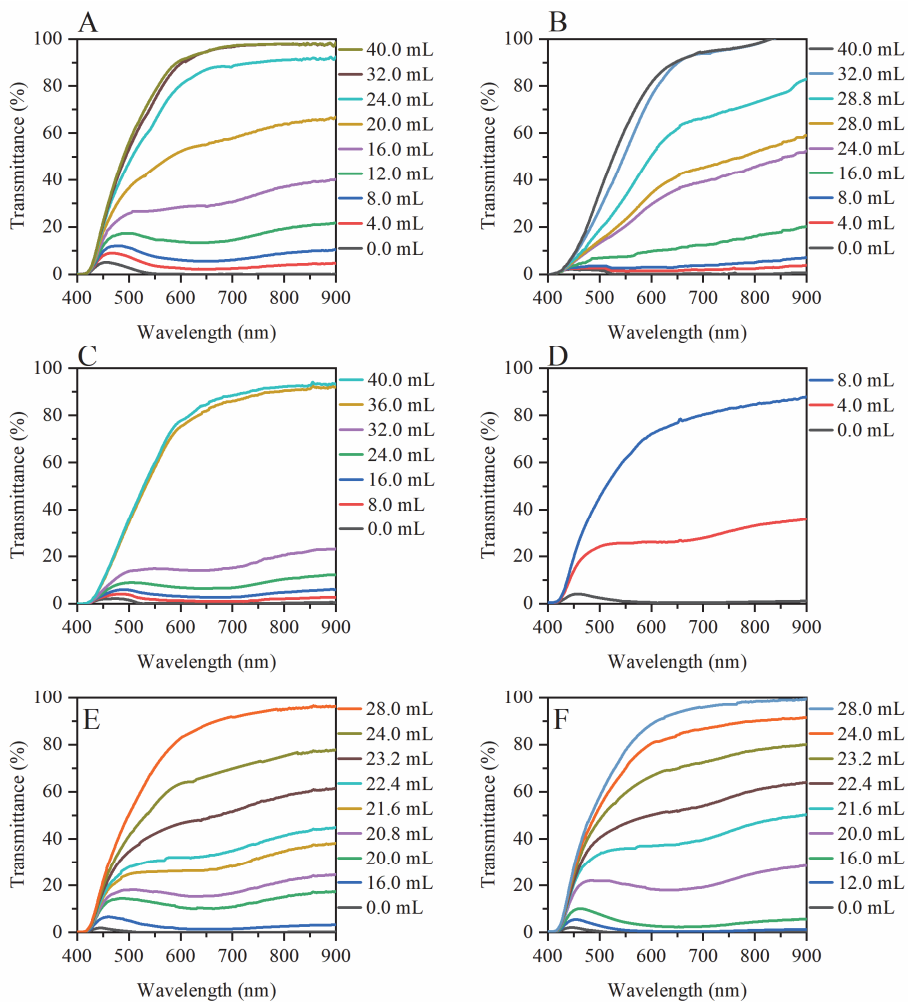


Fig. 3.5. Transmittance spectra in the 400-900 nm part of the spectra during recovery with air injection for TiO₂ NPs in different solvents. **A)** Ethanol; **B)** *n*-Propanol; **C)** *i*-Propanol; **D)** *n*-Butanol; **E)** *n*-Pentanol; **F)** *n*-Hexanol.

The colloids in the ethanol/ethanolamine mixture needed a smaller amount of air to recover the transmittance (Fig. 3.6). Even if we consider that the ethanol/ethanolamine colloids did not photodarken to the same extent as the colloid in pure ethanol, the reduction in the air requirement was between 6.7-13 times when compared to the colloid in ethanol. The smallest amount of oxygen for decoloration was for the colloid with MEOA. The colloid with DEOA exhibited 6.7 times decrease, while the colloid with TEOA exhibited an 8 times reduction in the amount of air required when compared to the colloid in ethanol.

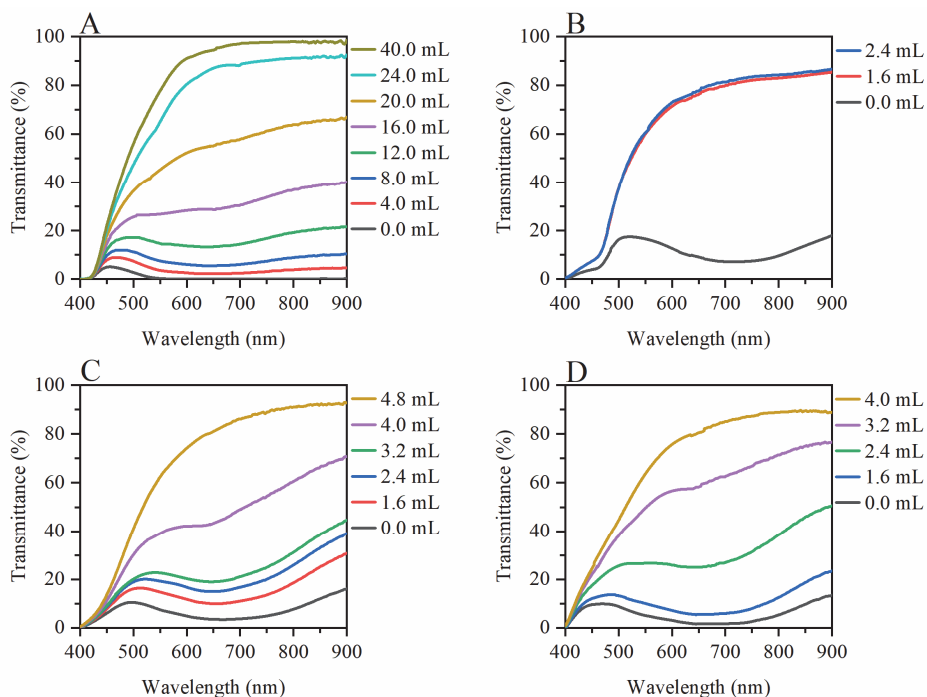


Fig. 3.6. Transmittance spectra in the 400-900 nm part of the spectra during recovery with air injection for TiO₂ NPs in ethanol and with different hole scavenger additions. **A)** Pure ethanol; **B)** 50 mol% of MEOA; **C)** 50 mol% DEOA; **D)** 50 mol% TEOA.

Since the air bubbling speed was kept constant throughout the recovery experiments, the amounts of required air for recovery can easily be converted to recovery rates (Fig. 3.7). The recovery is assumed to be dependent mainly by oxygen solubility. This assumption correlates nearly with the observed recovery rates as the oxygen solubility increases in the following sequence ethanol < *i*-propanol < *n*-propanol < *n*-butanol following that a slight decrease for *n*-pentanol and *n*-hexanol.³⁴⁰ By comparing the recovery rates at different wavelengths, it can be seen that the annihilation rate of Ti³⁺ defects was higher than compared to V_O or the delocalized electrons. The V_O show the slowest recovery mainly because for each of these defects to be annihilated, two Ti³⁺ defects of delocalized electrons must be quenched. This means that the recovery rate at 600 nm (Ti³⁺ defects) and delocalized electrons (900 nm) should be roughly double of the recovery rate at 450 nm (V_O defects). This is what is also observed, with the average recovery rate, for example, for ethanol being 0.004 min⁻¹ at 450 nm and 0.016 min⁻¹ and 0.014 min⁻¹ at 600 nm and 900 nm respectively.

Addition of ethanolamines increases the rate of recovery several times. All of the ethanolamines increased the recovery rate at least 2 times, with TEOA increasing both the maximum and average recovery rates 6 and 7.2 times, respectively. The increase in recovery stemming from the addition of ethanolamines can be attributed to the fact that amino groups can be oxidized to nitro groups, that can act as electrons scavengers.³⁴¹ Another possibility is the electron donor nature of the amino groups. These could potentially donate electrons to the TiO₂ nanoparticles, while remaining adsorbed on the TiO₂ surface. This would also explain the reduced photodarkening rate and transmittance change during UV irradiation. UV is turned off

and air is introduced into the system, the nitrogen of the amino group could take back its donated electron, thus aiding the recovery.³⁴²

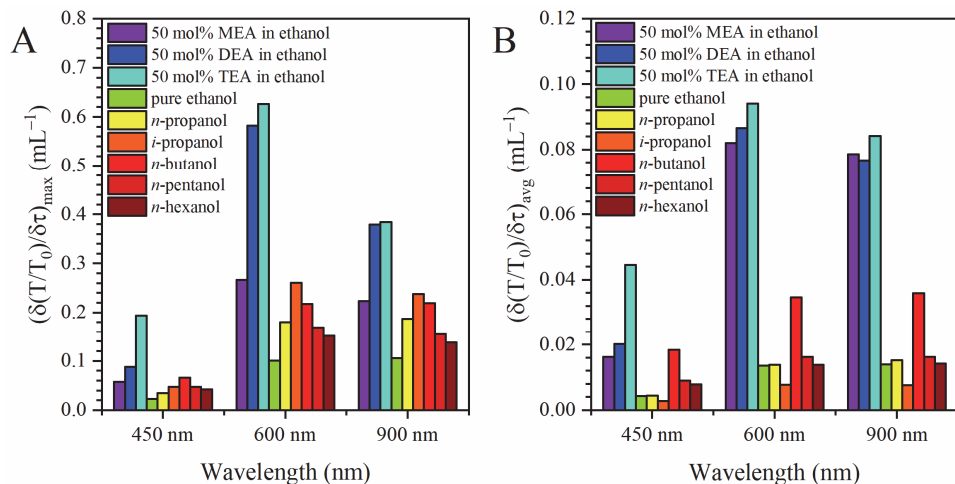


Fig. 3.7 A) Maximum recovery rate and **B)** average recovery rate for TiO₂ nanoparticle colloids in different hole scavenging media.

The photodarkening was accompanied by electron accumulation. This was responsible for absorption in the NIR wavelength range. These photoaccumulated electrons can be scavenged by Fe(acac)₃. This can be used to determine the amount of these electrons via spectrometric titration with a Fe(acac)₃ solution. These photoaccumulated electron values are similar, showing that, this property of photodoping is inherent to the nanoparticles themselves, with only a slight influence stemming from the hole scavenging medium, with the charge carrier concentration increasing from 2.01×10^{20} – 2.60×10^{20} in the row *n*-propanol < ethanol < *n*-hexanol < *n*-pentanol < *i*-propanol < *n*-butanol (Table 7). These values are similar to values previously reported in literature³⁴³ and are similar to values reported for other doped TiO₂ samples, such as carbon doped TiO₂.³⁴⁴ This shows that photodoping can be used to modify the amount of charge carriers in the material, similarly to conventional doping.

Table 7.

Charge carrier concentration for colloids in different solvents

Solvent	Electron carrier concentration (cm ⁻³)
Ethanol	$(2.10 \pm 0.168) \times 10^{20}$
<i>n</i> -propanol	$(2.01 \pm 0.168) \times 10^{20}$
<i>i</i> -propanol	$(2.52 \pm 0.168) \times 10^{20}$
<i>n</i> -butanol	$(2.60 \pm 0.168) \times 10^{20}$
<i>n</i> -pentanol	$(2.26 \pm 0.168) \times 10^{20}$
<i>n</i> -hexanol	$(2.18 \pm 0.168) \times 10^{20}$

This research shows that the hole scavenging medium has a profound effect on the photodarkening kinetics of TiO₂ nanoparticles while there is small influence on total number

of accumulated electrons in TiO₂ material. The recovery of the transmittance was observed when bubbling air through the colloids. Colloids in solvents with a higher oxygen solubility shown higher recovery rate. Furthermore, the addition of ethanol amines changes the photodarkening kinetics of the nanoparticle colloids while dramatically increasing the recovery rate of the colloid.

The type of point defect formed in TiO₂ during UV irradiation was determined using EPR spectroscopy. The EPR spectra were taken for TiO₂ colloid in *n*-BuOH. Prior to UV irradiation, the un-doped TiO₂ nanoparticles exhibited three EPR peaks at *g*-values of 2.0238, 2.0098 and 2.0036 (Fig. 3.8.A). These are attributable to signal coming from Ti⁴⁺ and O²⁻.³⁴⁵ During UV irradiation these three signals are replaced by a new and much more intense signal at a *g*-value of 1.957 with a line width $\Delta H=12.9$ G. This signal is attributed to Ti³⁺.³⁴⁶ This signal increased in intensity with irradiation time, reaching a maximum after 60 min of irradiation (Fig. 3.8.B). The amount of Ti³⁺ corresponding to this signal was calculated by with the help of an internal standard (Bruker ER 4119HS-2100) with a known spin concentration. The maximum Ti³⁺ concentration was determined to be 3.01×10^{-3} % or 1.812×10^{21} spins/mol after 60 min irradiation. This shows that the main defect in the photodoped TiO₂ is Ti³⁺. However, similarly as has been shown before, the vast majority of the photoaccumulated electrons populate the conduction band and only a small amount (0.34%) of these electrons have taken part in the formation of Ti³⁺.

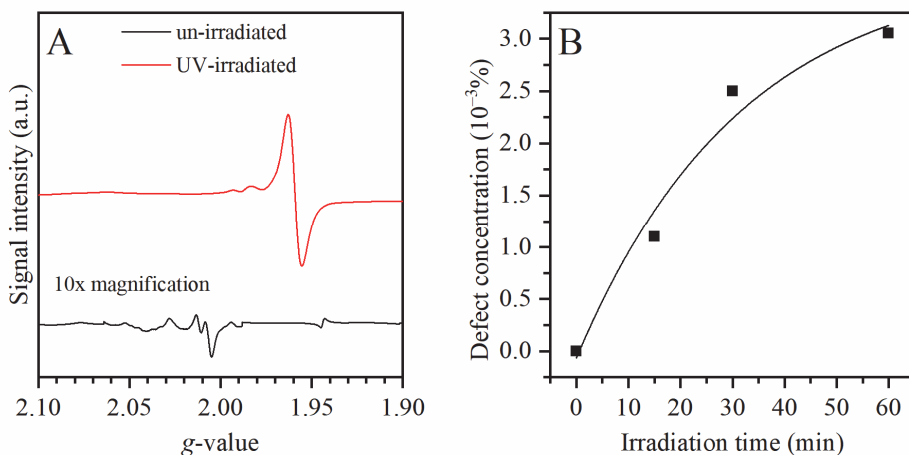


Fig. 3.8. **A)** EPR spectra for the un-doped TiO₂ nanoparticle colloid at different UV irradiation times; **B)** Ti³⁺ defect concentrations as a function of irradiation time.

3.2 The electrical properties of titanium dioxide thin films under UV illumination and in the presence of hole scavenger vapors

As the TiO₂ nanoparticles were capable of accumulating electrons in the conduction band when undergoing photodoping, this would imply that there would be a change in their electrical resistance under photodoping conditions. To measure the resistance of the nanoparticles, thin films of TiO₂ nanoparticles were prepared via spin-coating on ITO electrodes. The electrodes were prepared by etching a 140 nm ITO layer with HCl. This produced a 200 μm wide gap

between the ITO electrodes that was filled with the TiO₂ nanoparticles. This resulted in a TiO₂ thin film with a thickness of 130 nm (Fig. 3.9).

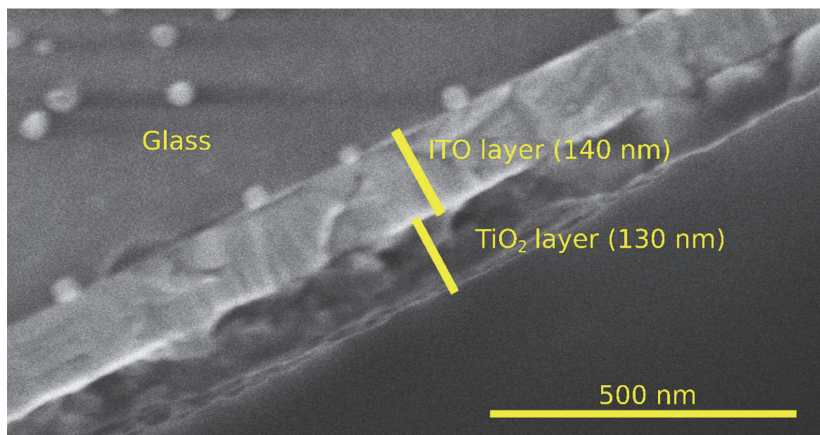


Fig. 3.9. SEM micrographs of the TiO₂ thin film (to the right size is empty space).

This sample, when irradiated with UV light (365 nm) exhibited a slight decrease in its resistance from the original $1.5 \times 10^9 \Omega$ to $1.1 \times 10^9 \Omega$. This resulted in a change in response of $S = 1.36$ (Fig. 3.10.A). This slight decrease in resistance can be attributed to the photoconductivity of the TiO₂ upon UV illumination.³⁴⁷ As the electron-hole pairs are generated in the TiO₂ material, the holes are scavenged by the adsorbed water species, allowing the electrons to accumulate in the conduction band. This leads to an increase in the conductivity observed in the experiments. The illuminated TiO₂ film also can interact with the oxygen in the air, leading to electron scavenging. Since there is an abundance of both oxygen and water in the surrounding air, when the UV light is turned off, the adsorbed water species and oxygen are replenished, and the excess charge carriers are scavenged.

The opposite reaction is observed when the sample is exposed to ethanol vapor at a concentration of 1000 ppm in the dark. This resulted in an increase in the resistance of the sample from $1.5 \times 10^9 \Omega$ to $1.17 \times 10^{10} \Omega$ with a response of $S = 7.8$ (Fig. 3.10.B). This increase can be attributed to the ethanol absorption on the sample film.³⁴⁸ The absorption increased the barrier height between the nanoparticles, which in turn decreased the change of electron tunneling between the adjacent nanoparticles.³⁴⁹ When the sample was exposed to ethanol vapor and under UV irradiation, the response was the complete opposite than the response in the dark. The samples resistance dropped from the initial $1.1 \times 10^9 \Omega$ all the way to $7.8 \times 10^6 \Omega$ resulting in a response of $S = 141$ (Fig. 3.10.C).

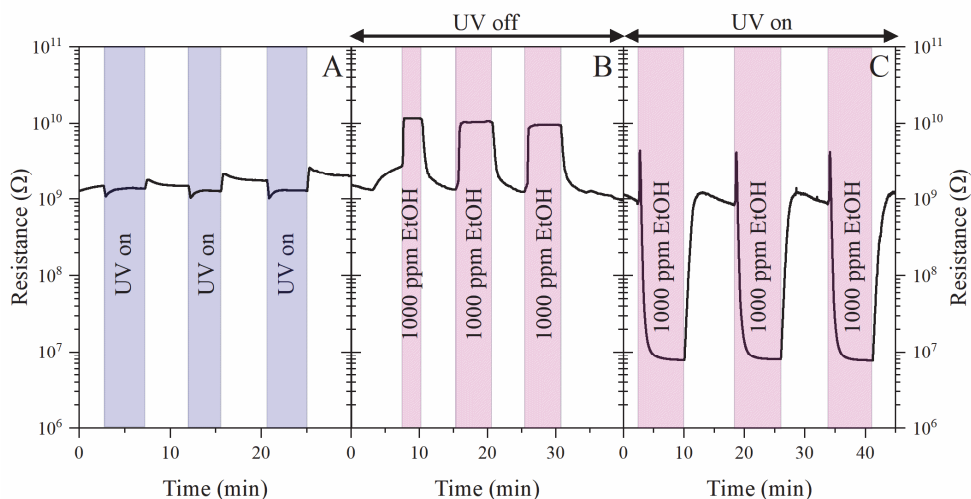


Fig. 3.10. **A)** Change in resistance when switching UV light on and off without solvent gas at a flux density of 46 mW/cm^2 ; **B)** Change in resistance when adding EtOH (1000 ppm) and ventilating the chamber without UV light; **C)** Change in resistance when adding EtOH (1000 ppm) and ventilating the chamber while irradiating with UV light.

The dramatic decrease in resistance under UV and 1000 ppm EtOH can be attributed to the hole scavenging nature of ethanol seen when the nanoparticles were dispersed in the solvent. As the electron-hole pairs are generated under UV light, ethanol, that adsorbs on the surface of the nanoparticle thin film, scavenges the holes, leaving behind the electrons. When the test chamber was vented and the ethanol vapors were removed from the air in the chamber, the oxygen present in the air scavenged the accumulated electrons, allowing the samples electrical resistance to return to its original value. To test these claims, several other tests were done. To test whether oxygen is indeed necessary for the recovery of the sample's resistance, the sample was exposed to ethanol vapor in a purely N_2 atmosphere (Fig. 3.11.A). With no oxygen in the chamber but UV light on, the resistance gradually increased. This was due to the fact, that, under UV light irradiation in air, the sample still has an accumulation of charge carriers present, because both oxygen and water vapor can scavenger the charges (oxygen – electrons and water vapor – holes). In pure N_2 , this can only happen because of already adsorbed species on the film surface. When these have scavenged their respective charge carriers and desorbed, an equilibrium forms, that diminishes the amount of charge carriers, increasing the resistance of the sample. When ethanol vapor is injected into the test chamber, there is a resistance change from $4.54 \times 10^9 \Omega$ to $4.54 \times 10^5 \Omega$, resulting in a resistance change of $S = 10\,000$. Furthermore, even when the ethanol vapor was flushed out and replaced with N_2 , the resistance recovered very slowly, reaching a value of $1.31 \times 10^6 \Omega$ after 100 minutes possibly due to thermal relaxation of the electrons. The phenomenon of a persistently low resistance has been observed previously in other works and has been themed persistent photoconductivity.³⁵⁰ For comparison, under normal operating conditions, the sample recovered its resistance in just 3 minutes. This shows that oxygen can also be used to measure the amount of photoaccumulated charge carriers.

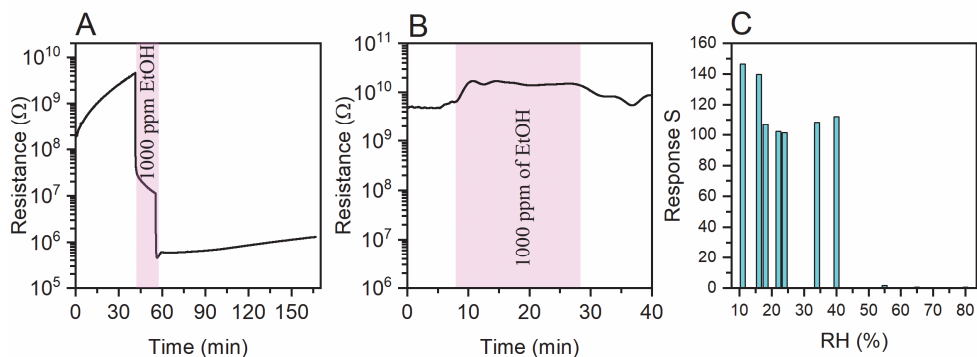


Fig. 3.11. **A)** Resistance change when the samples resistance was measured in a N_2 atmosphere while irradiating with a UV LED with a light intensity of 46 mW/cm^2 ; **B)** The resistance changes of the sample during irradiation with a 10 W commercial visible LED light, when adding EtOH to the chamber; **C)** The response S of the sample at different relative humidity when irradiating with a UV LED with a light intensity of 33 mW/cm^2 and exposed to 1000 ppm EtOH.

To test whether or not the TiO_2 nanoparticles thin film sample changes its resistance only under UV light irradiation an experiment was carried out by swapping the UV LED array with a 10 W commercial white LED light (cut off wavelength 410 nm) at a distance of 5 cm from the sample. When the sensor sample was exposed to the same ethanol vapor concentration as before (1000 ppm), only a marginal increase in the resistance of the sample was seen (Fig. 3.11.B), similar to that seen when the sensor was exposed to ethanol vapor in the dark. This acts as a confirmation of the theory, for electron accumulation, UV light is necessary. When looking at the samples charge accumulation abilities in different humidity (Fig. 3.11.C), it can be observed, that there are limitations to the environments in which this sample can accumulate electrons. At low RH of 10-16 %, the change in resistance is the highest, reaching a response of 140-146 at a reduced UV light intensity (33 mW/cm^2 when compared to the previous 46 mW/cm^2). This is mainly due to the fact, that such low RH values consequently cause part of the adsorbed water molecules to desorb from the surface for equilibrium with the surrounding air, exposing more of the hole scavenging sites, thus increasing the change in transmittance. The response drops to 101-112 when exposed to RH of 18-40 %. These RH values are a lot more common in the ambient environment, especially in countries with a milder climate, showing that photoelectrons can accumulate in an ambient environment. However, above $RH = 40 \%$, the change in resistance drops to just 1.6 and lower, when exposed to the same amount of EtOH and UV. This could be attributed to the formation of a mono-layer of liquid water on the surface of the sample thin film. As this layer is more conductive than the semiconductor material itself, it would then provide a charge screening effect and electric conductivity via Grotthuss proton jumping.³⁵¹ When the sample was again tested at a more moderate humidity of 40%, the sample once again exhibited the same response, indicating stability of the material.

The samples response to ethanol vapor was dependent of the concentration of the vapor and could also be varied by modulating the UV light intensity (Fig. 3.12.A). This indicates that

substantial amounts of ethanol vapor are necessary to saturate the sample with photoaccumulated electrons. As the change in resistance is UV light intensity dependent, this would mean that the hole scavenging rate could be considered the limiting step of the photoaccumulation process. At a low irradiation intensity (15 mW/cm²) the response i.e., the change in resistance increased from 1.6-75 in a linear manner, when the ethanol vapor concentration was varied from 100-1000 ppm. When the ethanol vapor concentration was decreased to just 50 ppm, no noticeable change in resistance was observed, indicating an insufficient amount for photoelectron accumulation. When the UV light intensity was increased to 33 mW/cm², the response also increased from 2.8 to 138 in the ethanol vapor range of 100-1000 ppm. Furthermore, at this light intensity the sample also exhibited a very low response (1.34) to 50 ppm of ethanol vapor. This indicated that at such a light intensity, enough photoelectrons are excited for hole scavenging to happen and hence photoaccumulation and resistance change. A further increase in the UV light intensity to 47 mW/cm² resulted in the further increased in the response to 37 at an ethanol vapor concentration of 100 ppm to 170 when the ethanol concentration increased to 1000 ppm. Also, at this light intensity, the sample also showed a response of 18.4 to ethanol vapor at 50 ppm ethanol and 18 at an ethanol vapor concentration of just 25 ppm. It can be observed, that at this UV light intensity, the response is no longer linear, but shows that saturation starts to occur. This is due to the fact, that the hole scavenging rate with ethanol absorption becomes the rate limiting factors.

The TiO₂ thin film sample exhibited a resistance change response to not only ethanol vapor, but also hole scavengers in general. When exposing the sample to different solvent vapors – both polar and non-polar – solvents (Fig. 3.12.B) the photoinduced electron accumulation was different. The samples showed a high photoaccumulated electron concentration towards alcohol vapor and a comparatively low electron photoaccumulation when exposed to acetone vapor. A very slight change in resistance was observed when the sample was exposed to *n*-hexane vapors. Potential photoaccumulated hole accumulation could be seen when exposing the sample to toluene vapors or due to purely absorption into the sample, increasing resistance. The change in resistance due to photoaccumulated charge carriers was similar as it was when the TiO₂ nanoparticles were dispersed in the corresponding hole scavenger solvent. These results also confirm that to successfully scavenge the photogenerated holes, the analyte gas molecules should contain hydroxyl groups as these can adsorb onto the TiO₂ surface.¹⁴⁹ The low affinity towards acetone can be explained by the fact, that aldehydes can also act as hole scavengers, but very mild one. Furthermore, acetone has a tautomeric enol form, that has a hydroxyl group and is present in very small quantities in acetone.³³⁸ As toluene and *n*-hexane lacks this groups, then this pathway is not available for these solvents.

The resistance change response to alcohol falls in the order *n*-butanol > *n*-hexanol > *n*-propanol > methanol > ethanol > *i*-propanol > *n*-pentanol > acetone. The different response towards various alcohols is complex. Butanol is known for its effective photogenerated hole scavenging properties from TiO₂.¹⁴⁶ It has been shown that the hole scavenging process on the surface result is alkoxy radicals.³³⁸ The alkoxy radical stability increases with an increase in the branching and size in the carbon backbone.³³⁸ A secondary alcohol, such as *i*-propanol, and heavier alcohols, such as *n*-pentanol and *n*-hexanol, produce more stable radicals. The photogenerated holes oxidize alcohols to aldehydes and, in the case of *i*-propanol and acetone are stable on the TiO₂ surface at 300 K.³⁵² The stable adsorbates do not desorb and limit adsorption of additional hole scavenging alcohols, resulting in a lower photoaccumulated

electron concentration. Furthermore, depending on the complexity of the alcohol, the reaction rate varies, resulting in a varied resistance response of the material.

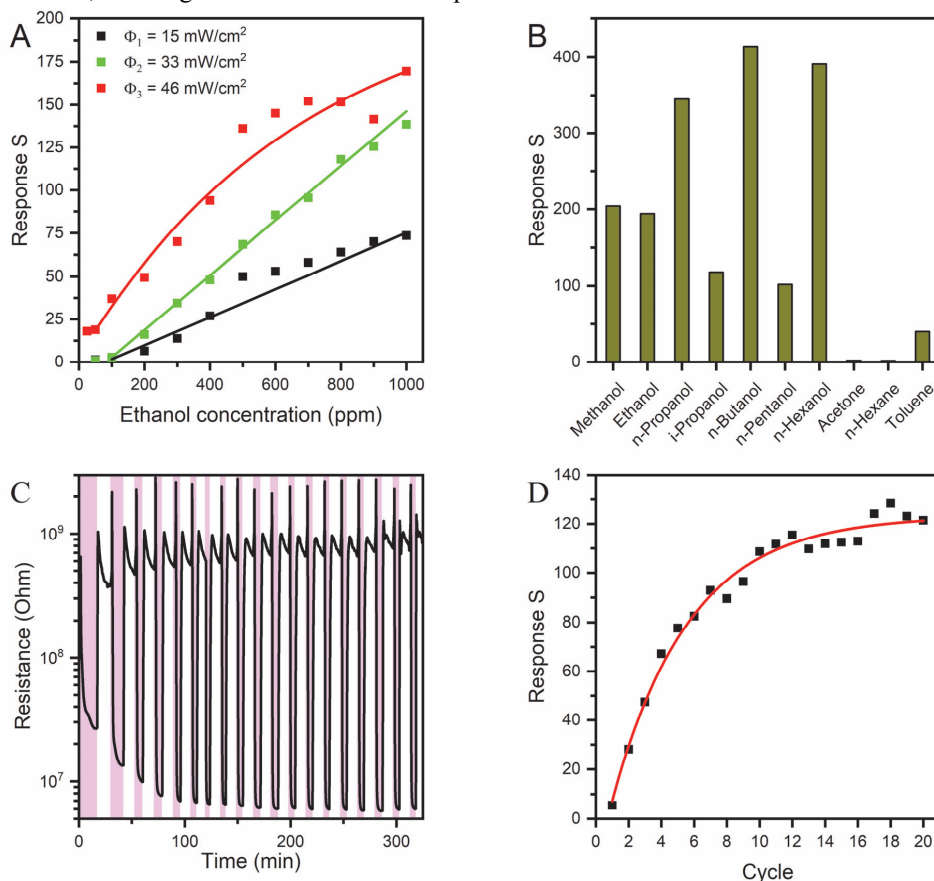


Fig. 3.12. A) Response S while changing the EtOH vapor concentration and while irradiating the sensor with different intensity UV light; B) Response S when exposing the sample to different solvents at a concentration of 1000 ppm and while irradiating the sample with UV light at an intensity of 46 mW/cm²; C) Resistance during repeated exposure of the sample to 1000 ppm of ethanol (exposure to ethanol is shown as pink) in the presence of UV light (33 mW/cm²); D) Response S during the repeated exposure.

Lastly, the repeatability of the photoaccumulated charge carrier concentration was looked at during multiple repeated exposure/recovery cycles (Fig. 3.12.C). It was observed that during the first 10 exposure/recovery cycles the resistance change increased and reached a minimum resistance of $6.2 \times 10^6 \Omega$ when exposed to 1000 ppm of ethanol vapor. The recovered resistance stayed roughly the same at $1 \times 10^9 \Omega$. After those first 10 cycles, the exposure and recovery resistance values varied very little, and the response showed an average value of 116.4 ± 5.7 (Fig. 3.12.D). This shows good stability of the results after the initial cycles while also showing that some of the photoaccumulated electrons remain and reached an equilibrium after these first 10 cycles. Furthermore, the initial increase in the response can be attributed to the gradual removal of adsorbed water molecules, that opens up additional sites for ethanol adsorption. This in turn increases the hole scavenging rate and subsequently the change in resistance.

3.3 Photoelectron accumulation in titanium dioxide films under UV irradiation while submersed in a hole scavenger

Since the TiO₂ nanoparticles exhibited electron accumulation in thin film form when exposed to hole scavenger vapor, the next possibility would be to see how the thin film exhibits photoelectron accumulation when immersed in a hole scavenger. This was realized by using a thicker TiO₂ thin film with a thickness of 1075 nm (Fig. 3.14.A and schematic of the device Fig. 3.13) with an area of 4.5 cm², that was immersed in *n*-butanol. As resistance measurements for the film itself would result in measuring the resistance of the solvent, current generation was looked at as to evaluate the amount of photoaccumulated electrons between the thin film and a counter electrode at different supplementary resistances. As a counter electrode a Pt wire was used. Furthermore, the generated current depending on the UVA irradiation time was examined. The system during irradiation and the generated charge was then recorded.



Fig. 3.13. Photoelectron device schematic

The sample could generate 1.35 μA of continuous current and 2.6 μA of peak current (Fig. 3.14.B&C). The continuous current was reduced when resistance was added to the circuit, while the potential increased inversely proportional to the current. This was because adding resistance decreased the number of electrons flowing through the external circuit, thus allowing for a larger potential difference to build up. The maximum power generated from the sample was 0.023 $\mu\text{W}/\text{cm}^2$. This has the potential of being used to power different low-power consumption sensors, as an alternative to solar cells.

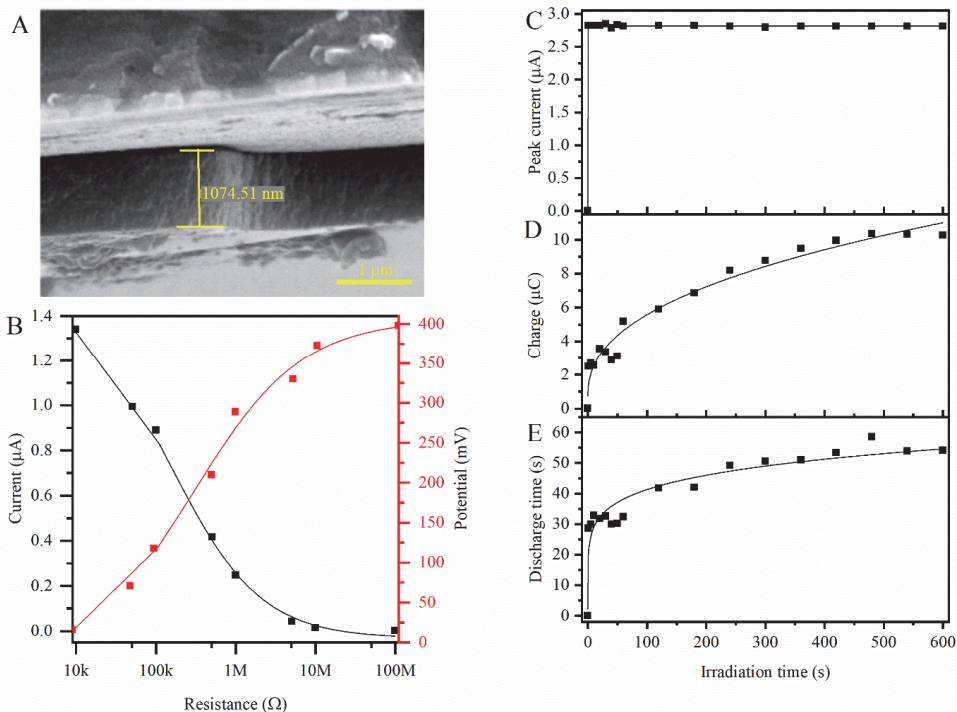


Fig. 3.14 A) SEM micrographs of the used thin film; B) Current and Potential graphs for continuous measurements; C-E) electric properties of the film as a function of irradiation (charging) time.

Under open circuit conditions, a charge could be built up on the thin film in the form of photoexcited electrons, that accumulated in the conduction band of the TiO_2 , with no noticeable change in color. While the peak current, that could be reached was independent of irradiation time (reaching the maximum after just 1 second), the discharge time and subsequently the accumulated charge gradually increased, reaching saturation after 5 minutes of irradiation. This showed that with an irradiation time of 5 min it was possible to saturate the sample with photoaccumulated electrons. The maximum amount of charge that was scavenged this way from the sample was just $10.2 \mu\text{C}$ that corresponds to approx. and 6.4×10^{13} electrons from the sample. When converted to charge carrier concentration, this equates to an electron concentration of $1.17 \times 10^{17} \text{ cm}^{-3}$, which is several orders of magnitude lower than what was obtained from the spectrometric titration results ($2.6 \times 10^{20} \text{ cm}^{-3}$). This could be because in thin film form, the lower layers of the film don't really interact with the hole scavenger, meaning that the upper layer of the thin film experiences electron photoaccumulation. Nevertheless, these results also show that the photoaccumulated charge carrier concentration can also be studied using charging when immersed in a hole scavenger not only when exposed to its vapors.

3.4 The influence of Nb⁵⁺ dopant on photochromic response of titanium dioxide

Niobium Nb⁵⁺ as the dopant was chosen because of its small size difference with regards to Ti⁴⁺ (Nb⁵⁺ (78 pm) and Ti⁴⁺ (75 pm)) as well as its electron acceptor nature. The other candidates such as V⁵⁺ or Ta⁵⁺ were found to either cause persistent visible light absorption or a reduced photochromic effect. The Nb⁵⁺ dopant content was varied from 1 to 20 at%. As seen from the Raman, XRD and SAED results, all of the synthesized nanoparticles with a nominal Nb⁵⁺ content from 1 at% to 20 at% were composed solely of anatase (JCPDS 21-1272).³⁵³ This shows that doping with Nb⁵⁺ did not promote the creation of any secondary phases. Raman spectra showed bands at 152, 402, 516 and 642 cm⁻¹ (see Fig. 3.15). The bands at 152 and 642 cm⁻¹ are attributed to the E_g mode of anatase, while the bands at 402 cm⁻¹ and 516 cm⁻¹ correspond to B_{1g} and A_{1g}+B_{1g} modes, respectively.³⁵⁴ Doping with Nb⁵⁺ caused the shift of the 152 cm⁻¹, 402 cm⁻¹ and 642 cm⁻¹ bands from 152 cm⁻¹ to 150 cm⁻¹, 402 cm⁻¹ to 388 cm⁻¹ and 642 cm⁻¹ to 639 cm⁻¹ respectively. The 152 cm⁻¹ band also increased in width due to the formation of Nb-O-Ti bonds²⁵⁹ and deformation of the Ti sublattice and the stretching of the Ti-O bonds.³³³ The 642 cm⁻¹ also increased in intensity and red-shifted due to the formation Nb-O bonds. The shift of the B_{1g} mode peak at 402 cm⁻¹ with increasing Nb⁵⁺ content is another confirmation as successful Nb⁵⁺ incorporation in the TiO₂ crystalline lattice, as this mode stems from the Ti-O bond stretching.³⁵⁵

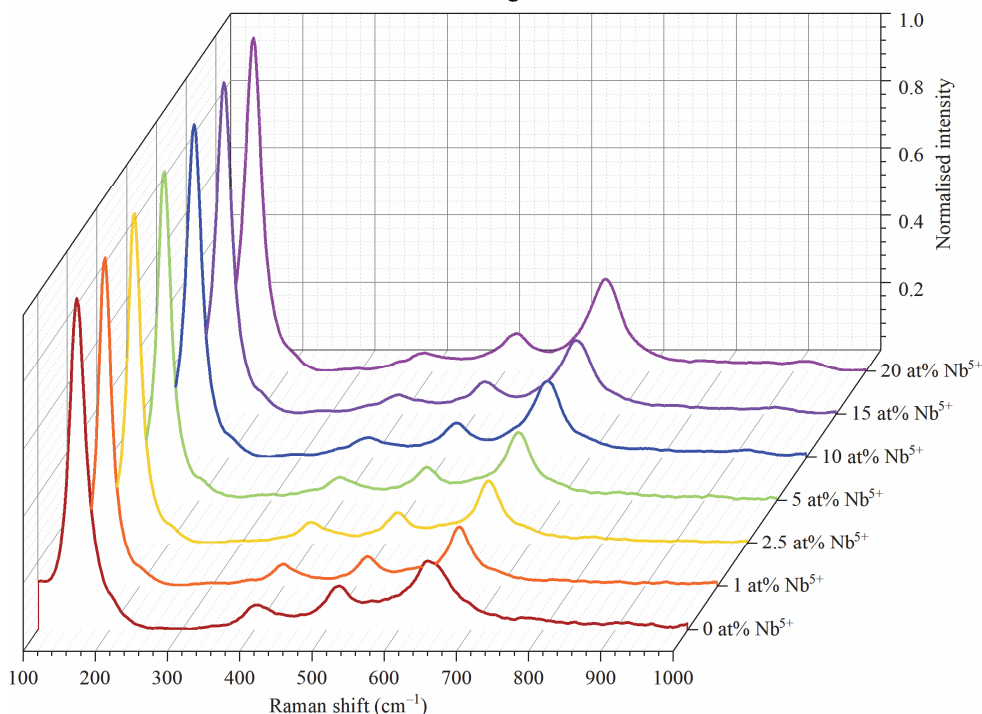


Fig. 3.15. Raman spectroscopy results for un-doped and Nb⁵⁺ doped TiO₂ nanoparticles.

The XRD results (Fig. 3.16.A) showed diffraction peak shifts, with increasing Nb⁵⁺ dopant. The main anatase peak of (101) showed a shift of 2θ values from 25.305 to 25.188, which is

indicative of increased lattice spacing.³³³ This is an indication, that Ti^{4+} cations with of 0.75 Å size where substituted with slightly larger Nb^{5+} cations with a size of 0.78 Å.²⁵⁶ Another observation is the shift of some higher index plane peaks, such as (211) and (220). This stems from the increase in lattice spacing, that corresponds to the index planes in question.

The Rietveld refinement results (Fig. 3.16.B-D) showed, that doping with the larger Nb^{5+} cations caused an increase in both crystalline lattice parameters from 3.791 ± 0.001 Å to 3.807 ± 0.001 Å for parameter a and from 9.506 ± 0.002 Å to 9.554 ± 0.001 Å for parameter c respectively, when comparing the un-doped TiO_2 NCs and the sample with 20% Nb^{5+} content. Subsequently, the unit cell volume increased from 136.618 Å³ to 138.493 Å³. According to the Rietveld refinement, the nanoparticle size increased from 4.3 nm for the un-doped TiO_2 sample to 8.6 nm for the Nb^{5+} doped TiO_2 nanoparticles with a nominal dopant content of 20 at%.

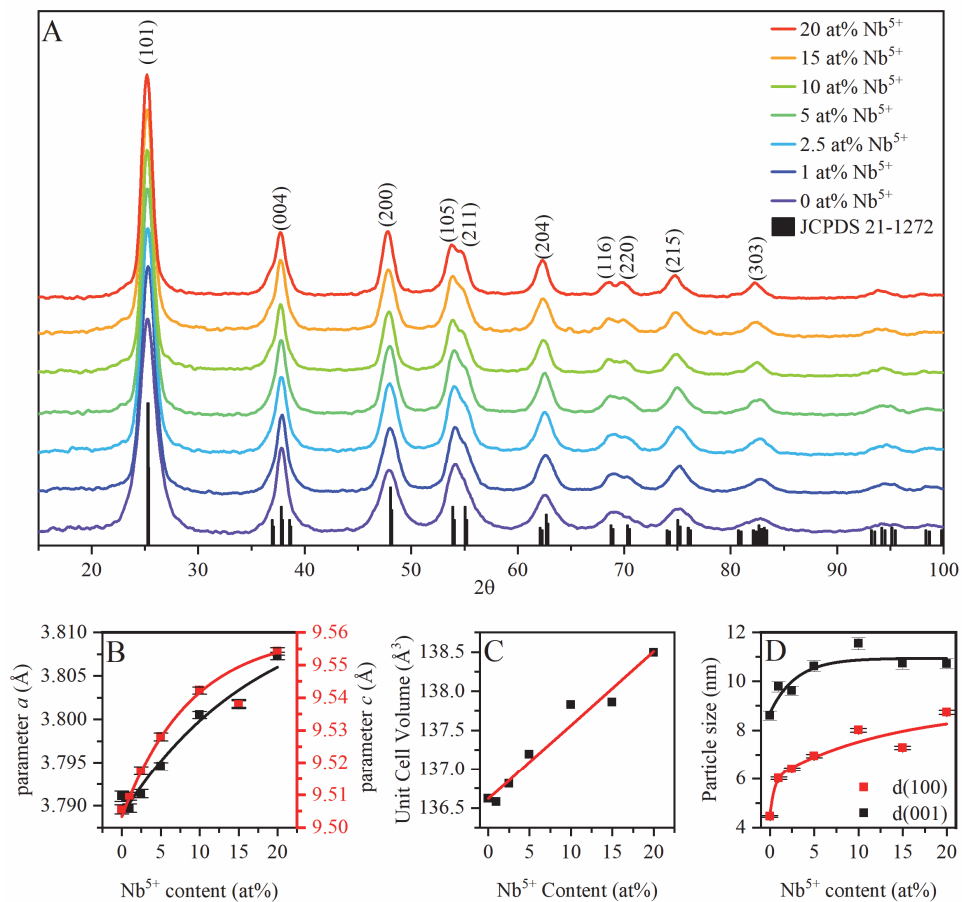


Fig. 3.16. A) XRD of the samples with different Nb^{5+} content; B,C,D) Rietveld refinement results.

The nanoparticle size grows in both (100) and (001) directions (Fig. 3.16.D) with the growth along the (100) direction being more pronounced than along the (001) direction. This indicated that the nanoparticle shape changed from oblong to a rounder shape (aspect ratio changed from 1.34:1 to 1.26:1). Furthermore, a diminishing influence on the nanoparticle size was observed

stemming from fact that as more and more large Nb^{5+} cations replace the smaller Ti^{4+} the crystalline lattice will distort less, as it was already distorted previously. These results were corroborated with the TEM micrographs of the nanoparticles (Fig. 3.17 A-G). The TEM micrographs showed that the nanoparticles were monocrystalline and without any signs of either being amorphous or having a core-shell structure. The nanoparticles were uniformly sized, with no large agglomerates present. Another conformation the crystalline nature of the nanoparticles stems from the SAED diffractograms (see Fig. 3.17.H-I). The coaxial ring patterns are indicative of polycrystalline samples. This is because the electron beam hits a multitude of nanoparticles, showing polycrystalline diffraction rings instead of discrete monocrystalline diffraction patterns. The rings themselves corresponded to the same diffraction peaks from XRD diffractograms and correspond to the (101), (004), (200), (105), (204), (220) and (215) planes.³⁵⁶

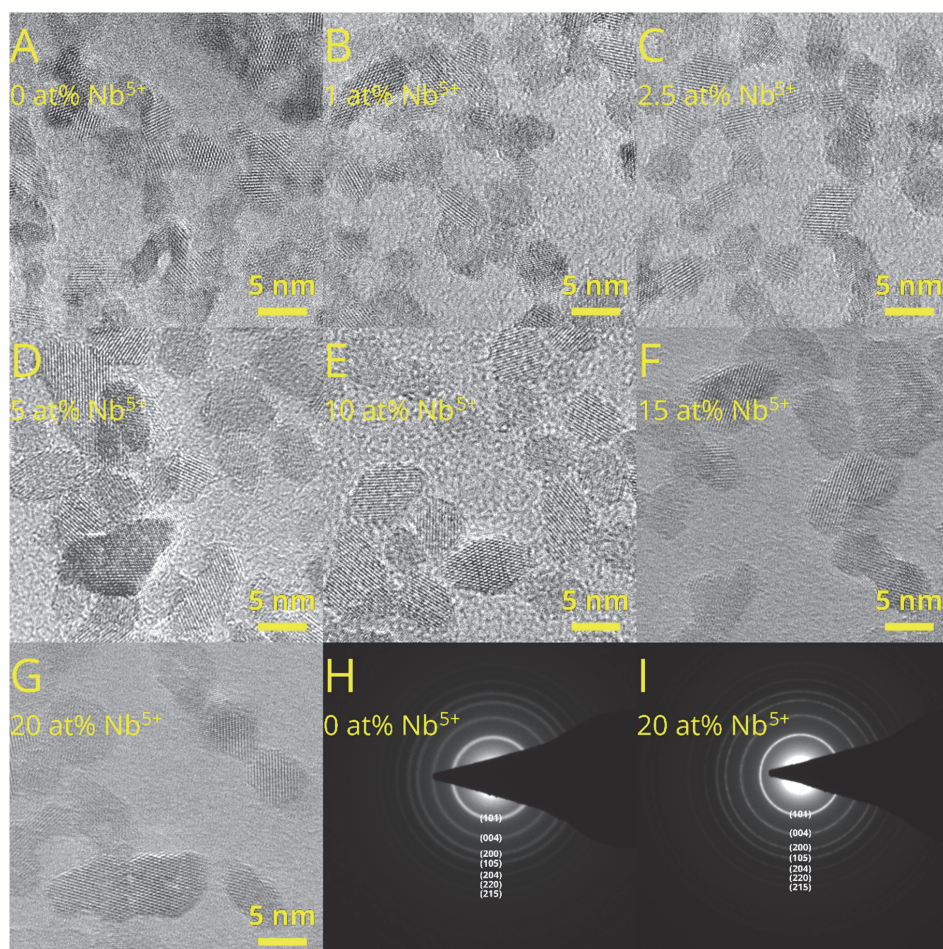


Fig. 3.17. A-G) High resolution TEM images of the synthesized nanoparticles with different Nb content; H and I) Selected Area Electron Diffraction Pattern for pure TiO_2 and TiO_2 with 20 at% Nb^{5+} .

From the TEM micrographs, 100 measurements of the nanoparticle sizes were taken using ImageJ software. These measurements were then used to calculate the mean $d(50)$ size of the nanoparticles as a function of Nb^{5+} content (Fig. 3.18). The nanoparticle size increases logarithmically from 3.6 ± 0.5 nm for the un-doped samples to 6.7 ± 1.0 nm for the samples with a Nb^{5+} content of 20 at%. These results match the tendency of the results obtained from the Rietveld refinement for the crystallite size along the (100) plane. The difference in the sizes between the TEM and Rietveld refinement results can be attributed to the fact, that Rietveld refinement shows crystallite size, while TEM gives information on the actual nanoparticle size.

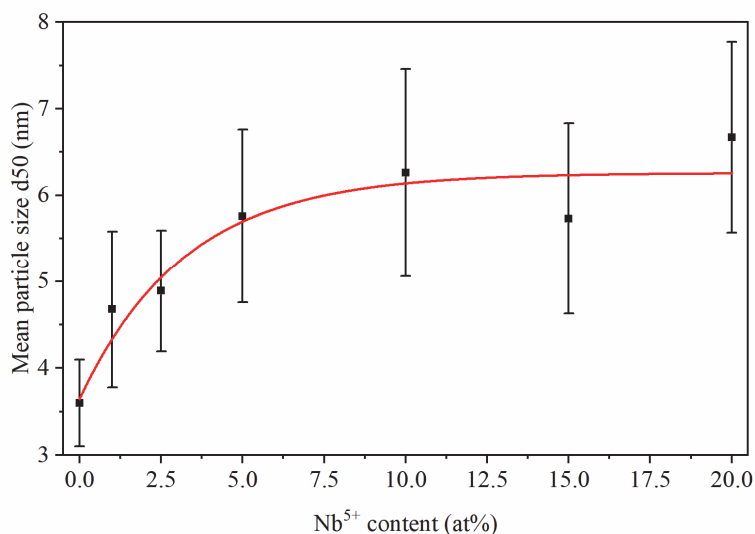


Fig. 3.18. Nanoparticle size d_{50} (nm) plotted against Nb^{5+} content. The red line indicates a exponential fit for reference.

The overview of XPS spectra of all the doped TiO_2 samples (Fig. 3.19.A) showed the presence of O, Ti and Nb with no additional stray elements present. The In 3d and C 1s signals stem from the sample holder and organic contamination, respectively. The binding energy of the Ti 2p 3/2 peak at 458.5 eV and 2p 1/2 peak at 464.2 eV indicates fully oxidized TiO_2 , with a homogeneous Ti^{4+} oxidation state (Fig. 3.19.D), while the Nb 3d peaks at slightly above 207 eV and 209.9 eV indicates fully oxidized Nb^{5+} with no indication of other Nb oxidation states (Fig. 3.19.C). The O 1s peak consists of two overlapping peaks at 530 eV and 531 eV (Fig. 3.19.B). The main peak at 530 eV corresponds to lattice oxygen in the bulk oxide. The broad and weak peak at 531 eV is usually attributed to surface hydroxide groups. According to this data it was determined that the samples, in their un-irradiated state do not contain any Ti^{3+} or V_O . This is contrary to other authors.¹⁵⁵ The difference can be attributed to the different synthesis methods used. As the doped nanoparticles are synthesized using a solvothermal treatment, the increased pressure could retard V_O formation. Using the ratio of Ti 2p and Nb 3d peaks, the Nb^{5+} content was calculated as a function of nominal dopant content (Fig. 3.19.E). These calculated values were in good agreement with the theoretical Nb^{5+} content, resulting in a very high doping efficiency (99-100 %). This can be attributed to the minor size difference between both cations of Ti and Nb.

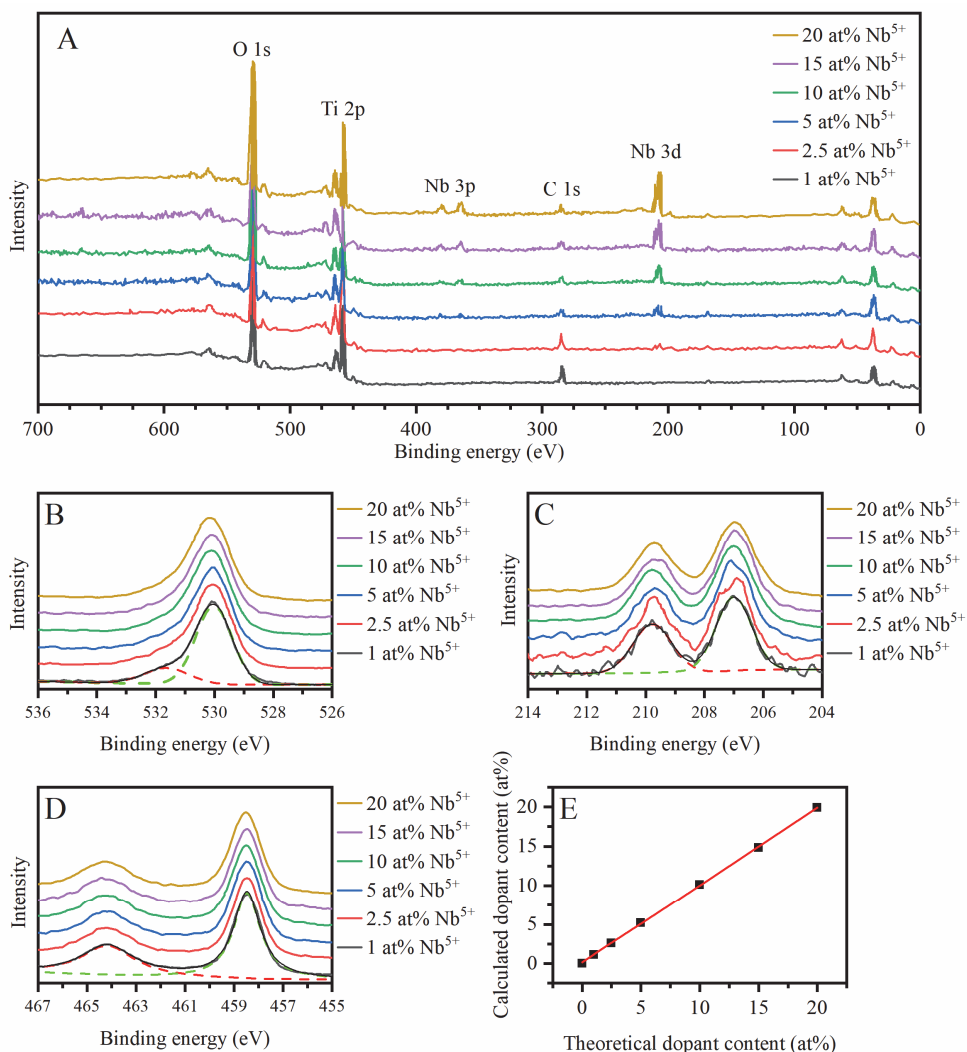


Fig. 3.19. A) Overview XPS spectra of the Nb⁵⁺ doped TiO₂ samples; B,C,D) high-resolution XPS spectra of O 1s, Nb 3d and Ti 2p binding energy regions respectively; E) calculated dopant content vs theoretical dopant content.

The influence of Nb⁵⁺ doping on the optical properties of the nanoparticles was studied using diffuse reflectance spectroscopy and Kubelka-Munk spectra showed that the samples exhibit no native absorption in the NIR spectra, in the wavelength range of 700-1600 nm (Fig. 3.20.A). This shows that the nanoparticles have no noticeable SPR absorption which could be caused by doping induced electron accumulation. The doping leads to a gradual decrease in the optical band gap of the nanoparticles (Fig. 3.20.B) from 3.13 eV for the un-doped TiO₂ nanoparticles to 2.98 eV for the Nb⁵⁺ doped TiO₂ with a nominal dopant content of 20 at%. The narrowing of the band gap was due to the introduction of lattice point defects as well as electron acceptor levels near the conduction band edge from the interaction of the Ti 3d states with the

Nb⁵⁺ 4d states.³⁵⁷ Furthermore this decrease was linear with the increase in the nominal dopant content.

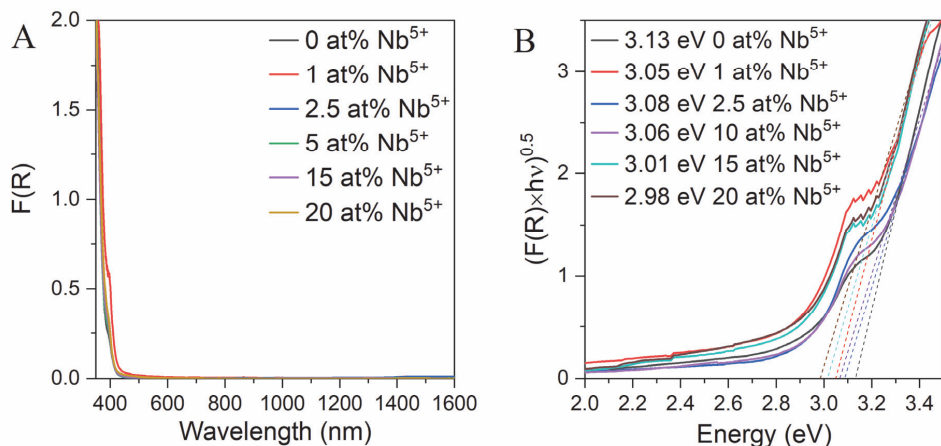
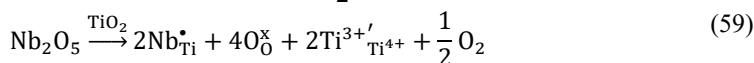
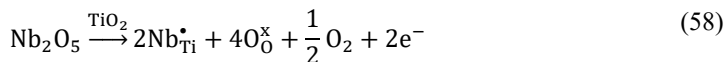
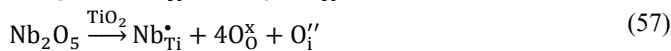
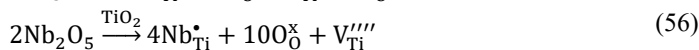
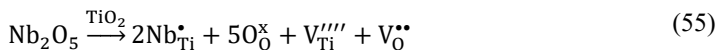


Fig. 3.20. **A)** Kubelka-Munk plots for samples with different amounts of Nb⁵⁺; **B)** Optical band gap dependence on Nb⁵⁺ dopant content.

Furthermore, the nanoparticles when dispersed in *n*-butanol showed a change in their optical band gap when they were irradiated with UV light (Fig. 3.21). Here, the observed optical band gap was smaller compared to the band gap of the nanoparticles in the dry state, because of the surface acac ligands.³⁵⁸ Examining the band gap of the un-doped TiO₂ colloid and the Nb⁵⁺ doped TiO₂ nanoparticle colloid (dopant content 20 at%) difference in the band gap change could be seen. The un-doped TiO₂ colloid exhibited an apparent increase in the nanoparticle optical band gap from 2.87 eV initially to 2.94 eV after the colloid was irradiated with UVA light for 35 min. This widening of the band gap can be attributed to the Moss-Burstein effect.³⁵⁹ The Nb⁵⁺ doped TiO₂ nanoparticle colloid exhibited the opposite behaviour, with the optical band gap apparently decreasing. This can stem from additional photoinduced defects in combination with the Nb⁵⁺ presence, similarly to the narrowing of the band gap of the nanoparticles in the dry state. In accordance with known defect chemistry, Nb⁵⁺ doping likely produces several different types of point defects (equations 55-59):



The oxygen vacancies create new donor levels between 0.75 eV and 1.18 eV below the conduction band,³³⁷ the Ti⁴⁺ vacancy introduces an acceptor level 1.15 eV above valence band edge,²⁴⁴ and the Ti³⁺ creates shallow donor levels slightly below conduction band minimum.³³⁷

These point defects can contribute to the apparent narrowing of the band-gap. The observed shrinking of the band gap is in sharp contrast with the work published by Trizio et al., where the TiO₂ doping by Nb⁵⁺ causes the band gap widening due to Moss-Burstein effect without any UV irradiation.³⁵⁹ The differences between the present study and the study reported by Trizio et al. can be related to different compensation mechanism for excess charge introduced by donor Nb⁵⁺ dopant. The Moss-Burstein effect is widely observed when the excess positive charge is compensated by delocalized electron in conduction band forming degenerated semiconductor as per equation (58). As the delocalized electrons are occupying the first levels in the conduction band, the higher energy is needed to excite electrons from lowest occupied level in valence band to unoccupied level in conduction band. In the present work the excess charge from Nb⁵⁺ is most likely compensated by means of other point defect such as Ti interstitials or Ti vacancies as per equations (55)-(57).

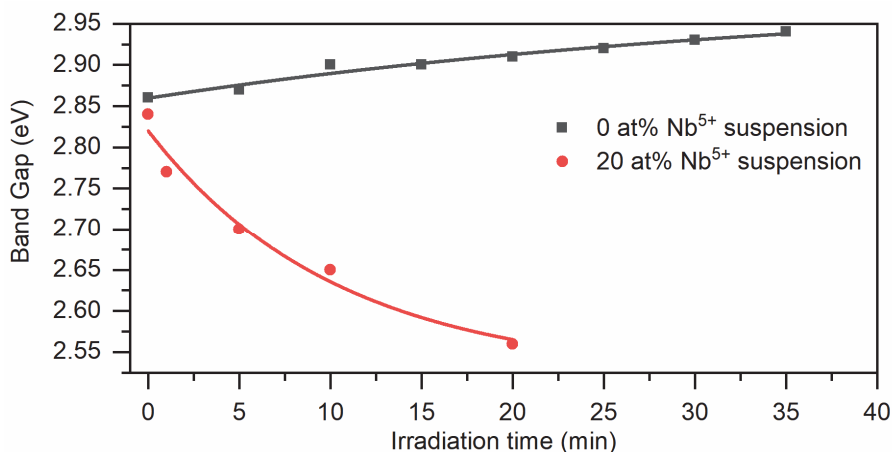


Fig. 3.21. Nanoparticle colloid optical band gap change during UV irradiation.

The Nb⁵⁺ doping resulted in a very strong increase in the photochromic response of the TiO₂ nanoparticles. Under identical irradiation conditions, when comparing colloids of un-doped TiO₂ nanoparticles and nanoparticles with a Nb⁵⁺ content of 20 at% at a concentration of 100 g/L, it was observed that the Nb-doped nanoparticle colloid photodarkened visibly already after 30 seconds and after 120 seconds had almost 0% transmittance (Fig. 3.22). For comparison, the un-doped TiO₂ nanoparticle colloid did not photodarken at all during the same 120 second time frame and needed an additional 1080 seconds (18 min for a total of 20 min) to photodarken to the same extent as the Nb-doped TiO₂ nanoparticle colloid.

One drawback of the doping of TiO₂ with Nb⁵⁺ is that the initial transmittance starts to decrease across the whole studied spectral range of 400-1100 nm. This can be a result of multiple factors. Firstly, Nb-doping, as shown in the previous section, resulted in an increase in the average nanoparticle size. However, even the largest nanoparticles had an average size well below 10 nm and thus should not cause scattering. Another possibility is the appearance of additional acceptor levels in the band-gap of TiO₂ stemming from Nb⁵⁺ doping. This can cause the observed absorption to become visible also in unirradiated samples and would also scale with the doping concentration. Lastly, lowered transmittance could be explained by agglomeration. Confirmation of this can be seen in the colloids while in long term storage, as

the sample with the highest Nb^{5+} content of 20 at% contained sedimented nanoparticles and exhibited a visible haze after 1-2 months. In contrast, the un-doped TiO_2 colloids as well as Nb^{5+} doped TiO_2 nanoparticle colloids with a low (≤ 5 at%) remained stable for over a year.

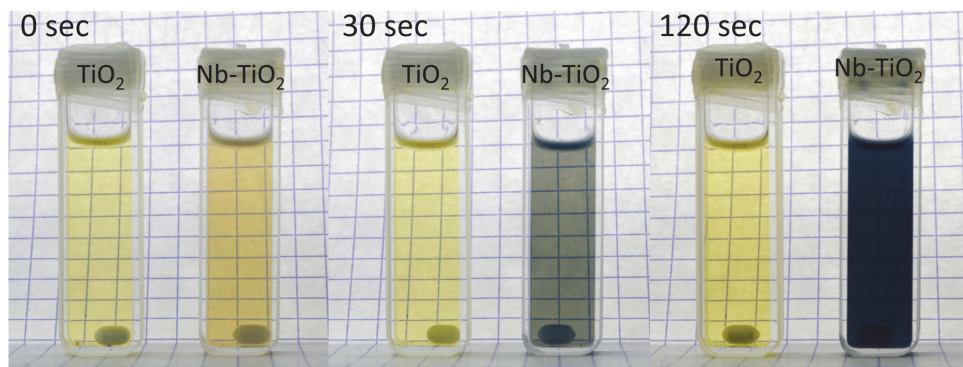


Fig. 3.22. Photographs of undoped TiO_2 and Nb-doped TiO_2 (20 at%) colloids in *n*-butanol, irradiated 0, 30 and 120 seconds showing the strong increase in the photodarkening rate caused by Nb-doping.

The transmittance change demonstrated here from 400-1100 nm (Fig. 3.23.A) shows a more rapid change in transmittance, that shown previously in chapter 3.1. This is because here, the UVA light source had a higher power output of 47 mW/cm^2 as compared to the 25 mW/cm^2 used in the previous photochromic experiments. We can see that the time necessary for photodarkening to reach (almost) total absorbance, was reduced from 60 min to 20 min when comparing un-doped TiO_2 colloids irradiated with different light intensities. Note, some samples needed up to 5 min of irradiation to get rid of the absorbed oxygen (ramp up time). After this, the samples showed a gradual decrease in the transmittance of the sample with a uniform decrease across the wavelength range of 400-1100 nm. Doping with Nb^{5+} caused a dramatic decrease in the ramp up time with transmittance already starting to decrease after the 1st minute (Fig. 3.23.B). This could be explained with lower recombination rate of photogenerated charge carriers which led to the intensified ox-red processes on surface. Furthermore, the absolute transmittance change was much higher in the NIR range than the visible range. With only 1 at% of Nb^{5+} present, the sample achieved a total NIR light blocking within 10 minutes, twice as fast as the un-doped TiO_2 nanoparticle colloid, while simultaneously still allowing a low amount of visible light to pass through the sample. The higher absolute transmittance change in the NIR range, means that a higher amount of the photogenerated electrons are delocalized and partake in surface plasmon resonance absorption. The transmittance change was further sped up when the amount of Nb^{5+} was increased up to a maximum amount studied of 20 at%. Samples with a Nb^{5+} content of 10 at% and higher exhibited total blocking of NIR light at 1000 nm after just 2 minute of irradiation and achieving total blocking of the entire studied NIR range of 700-1100 nm in 3-5 minutes, depending on the Nb^{5+} content (Fig. 3.23.E-G). The maximum change rate for photodarkening (Fig. 3.23.C&F) was similar for both the un-doped and 1% Nb-doped TiO_2 colloids, while the average change rate was 2.25 times higher. A high average change rate combined with a relatively low maximum change rate means, that the change is more gradual, while a high maximum change

rate and a low average change rate means that the transmittance change happens very rapidly, but with a long initiation and/or saturation period. The maximum transmittance change increased with increasing dopant content and reached value of 1 for the 20% Nb-doped TiO₂ colloid at 1000 nm. Since the time step here was 1 minute, this means that the colloid was capable of fully blocking out NIR light after just 1 minute of UVA irradiation.

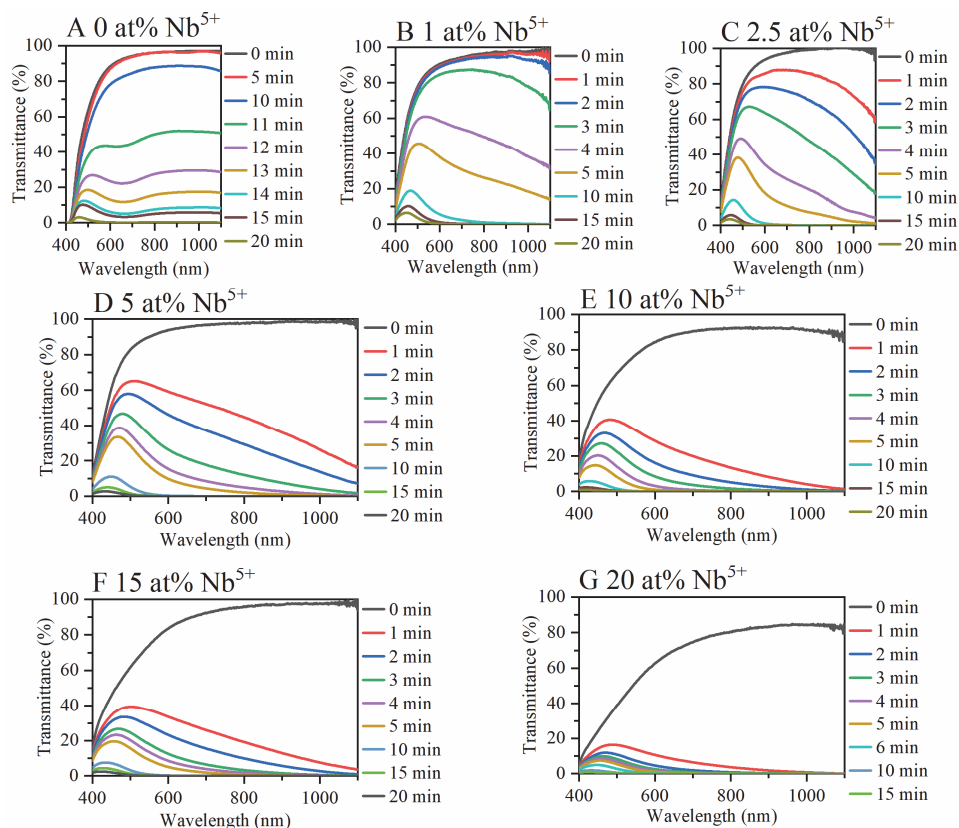


Fig. 3.23. UV-Vis transmittance spectra for un-doped and Nb-doped TiO₂ nanoparticle colloids during UV irradiation.

To determine the influence of Nb⁵⁺ doping on total transmittance change of the TiO₂ nanoparticles in the infrared and visible range the colloids were diluted to a smaller nanoparticle concentration (2 g/L) to avoid saturation of the spectrometer. The un-doped TiO₂ colloid (Fig. 3.24.A) was almost fully transparent in the unirradiated state in the wavelength range of 400-1100 nm, apart from a slight absorption between 400-450 nm. After saturation was achieved (the samples were irradiated for 24 hours to make sure that the particles are fully photodarkened) the transmittance dropped to 23% at 700 nm (the midpoint between visible and NIR wavelengths). In the photodarkened state, the transmittance gradually decreased between 400-700 nm and was constant between 700-1100 nm. Before irradiation the Nb⁵⁺ doped TiO₂ nanoparticle colloids did not exhibit decreases in transmittance when compared to the un-doped TiO₂ colloid (Fig. 3.24.B-G). The photodarkened state of these colloids with a nanoparticle Nb⁵⁺ dopant content of 1-5 at% had a slight decrease in the absorption between 400-550 nm,

while in the NIR range (700-1100 nm) the colloids showed higher absorption. Higher Nb^{5+} doping resulted in a decrease also in the transmittance at shorter wavelengths of 400-550 nm. The added absorption intensity due to Nb^{5+} doping lead to total blocking (<2% transmittance) in the NIR range for samples of 700-1100 nm when the Nb^{5+} content was high (10-20 at%). This showed that, even at this dilution, the nanoparticle colloids were capable of total light blocking in the NIR wavelength range. This also was evident when looking at the absolute transmittance change (Fig. 3.24.H). For comparison the un-doped TiO_2 colloids had an absolute transmittance change ranging from only 30% at 400 nm to 76% at 800-1100 nm. Samples with a low Nb^{5+} dopant content (1-5 at%) had an absolute transmittance change that was slightly lower than the un-doped TiO_2 colloid in the visible wavelength range, while having a higher transmittance change in the NIR wavelength range with values between 24% at 400 nm to 98% at 1000 nm. The samples with higher Nb^{5+} dopant content (10-20 at%) had a higher absolute transmittance change in both visible and NIR ranging from 38% at 400 nm to 99% at 1000 nm and reached full saturation at this dilution.

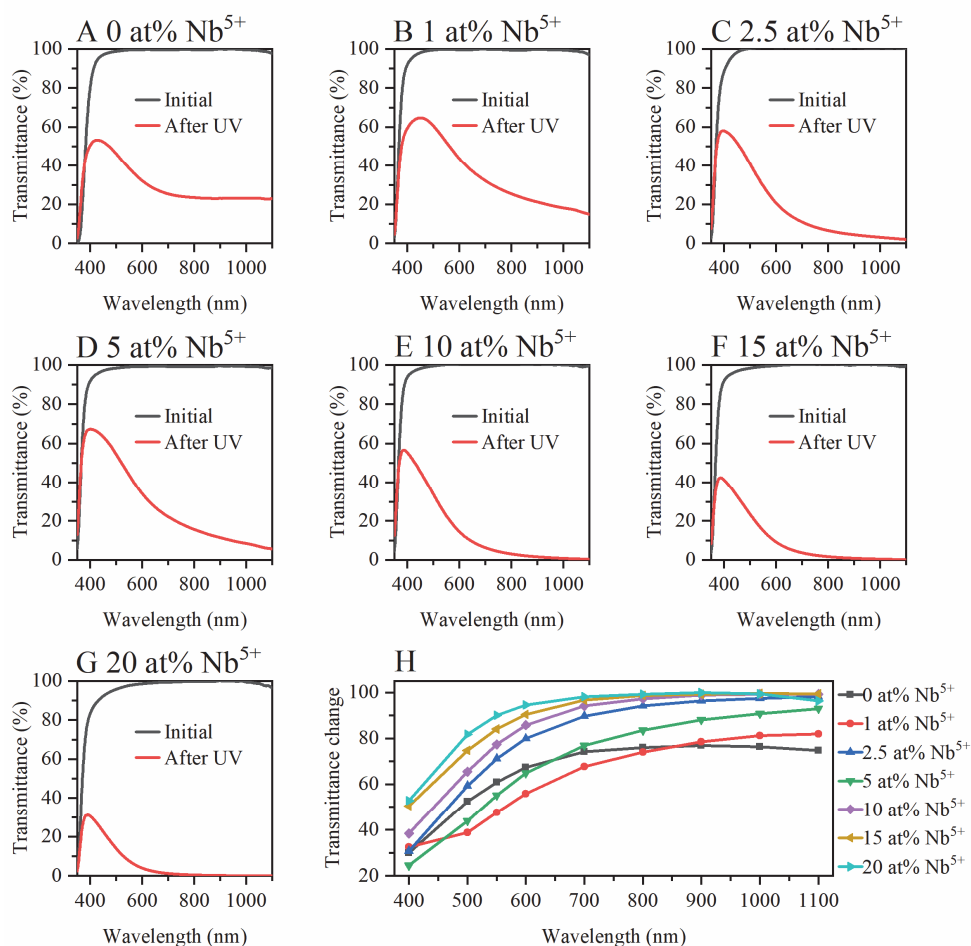


Fig. 3.24. A-G) Vis-NIR transmittance spectra of the diluted Nb-doped TiO_2 samples before and after 24h UV irradiation; H) Absolute transmittance change for samples with different Nb-content at 550 nm.

Doping with Nb^{5+} resulted in an increase in the absorption within the NIR range because of the increase in the amount of photoaccumulated electrons. This was evident also when determining the accumulated charge carrier concentration. The calculated values ranged from $1.74 \times 10^{20} \text{ cm}^{-3}$ to $4.03 \times 10^{20} \text{ cm}^{-3}$ with the Nb^{5+} content increasing from 0 at% to 20 at% (Table 8). Charge carrier concentrations of this magnitude have previously been reported for nanoparticles when they have been doped electrochemically.³⁶⁰

Table 8.

Photoaccumulated electron concentration of the samples with different Nb^{5+} content

Nb^{5+} content (at%)	Photoaccumulated electron concentration (cm^{-3})
0	$(1.74 \pm 0.168) \times 10^{20}$
1	$(1.94 \pm 0.168) \times 10^{20}$
2.5	$(2.11 \pm 0.168) \times 10^{20}$
5	$(2.53 \pm 0.168) \times 10^{20}$
10	$(3.32 \pm 0.168) \times 10^{20}$
15	$(3.80 \pm 0.168) \times 10^{20}$
20	$(4.03 \pm 0.168) \times 10^{20}$

Nb^{5+} doping has a profound influence on the photodarkening properties of TiO_2 nanoparticles, not only in terms of photodarkening speed but also the absorption intensity. The reason for this is that Nb^{5+} introduces excess positive charge that increases electron accumulation as well as the secondary defects introduced into the anatase TiO_2 crystalline lattice to compensate the electrical charge imbalance caused by substituting Ti^{4+} with Nb^{5+} , such as e' , V_{Ti}'''' or O_i'' . During photodarkening of un-doped TiO_2 all the electrons, that are localized, reduce Ti^{4+} to Ti^{3+} and in this way, generate $V_{\text{O}}^{\bullet\bullet}$. When Nb^{5+} is present in the TiO_2 lattice, it is favored by the excited electrons and reduces Nb^{5+} to Nb^{4+} . This also causes the secondary defects to change to preserve charge neutrality.

Further, the recovery was studied for two different recovery experiments were done here. In the first experiment (dynamic), the photodarkened colloids (3 mL) with a nanoparticle content of 100 g/L were gradually exposed to an increasing amount of air (up to 20 mL) and the subsequent transmittance recovery was recorded. The second kind were steady state experiments, where a set amount (5 mL) of air was first bubbled through the photodarkened colloid (UV-irradiated for 30 min). After this, the colloids were allowed to recover on their own.

As for the Nb^{5+} doped samples (Fig. 3.25.B-G), we can see a gradual decrease in the achieved recovery with increasing Nb^{5+} content. Samples that had a Nb^{5+} content of 5 at% and higher requiring more than 20.0 mL of air, which was 6.7 times the volume of the colloid. The sample with 20 at% Nb^{5+} recovered to only 17% at 500 nm and recovered 0-3% in the whole NIR range, indicating that they still possessed many accumulated electrons. For the samples with a low amount of Nb^{5+} (0-2.5 at%), the recovery also proved to be a challenge. The un-doped TiO_2 colloid had a slight decrease in transmittance within the visible range. This has been attributed to remanent secondary defects within the subsurface of the nanoparticles, that recover more slowly and hence require a longer time to fully recover. The Nb^{5+} doped TiO_2 colloid with a nominal dopant content of 1 at% exhibited this decrease between the initial and

recovered stated the most, with a difference of 10% throughout the measured wavelength range. This contrasts with the 2.5 at% sample, that recovered just within 1-2% of its initial transmittance. This shows that the remnant defects within the nanoparticles could be called quasi-permanent, recovering in a larger time scale, than within the dynamic experiment. The transmittance change rate during dynamic recovery (Fig. 3.25.D&G) was highest for the un-doped TiO₂ colloid, reaching a maximum change rate up to 0.502 mL⁻¹ and average up to 9.46×10^{-2} mL⁻¹ at the NIR wavelength range with the recovery rate highly dependent on the wavelength in the visible range. These values dropped gradually with increasing Nb⁵⁺ doping content and dropped by more than an order of magnitude in the NIR range for both maximum and average recovery rate, to 1.38×10^{-3} mL⁻¹ and 2.65×10^{-4} mL⁻¹ at 1000 nm respectively when the nanoparticle Nb⁵⁺ dopant content reached 20 at%.

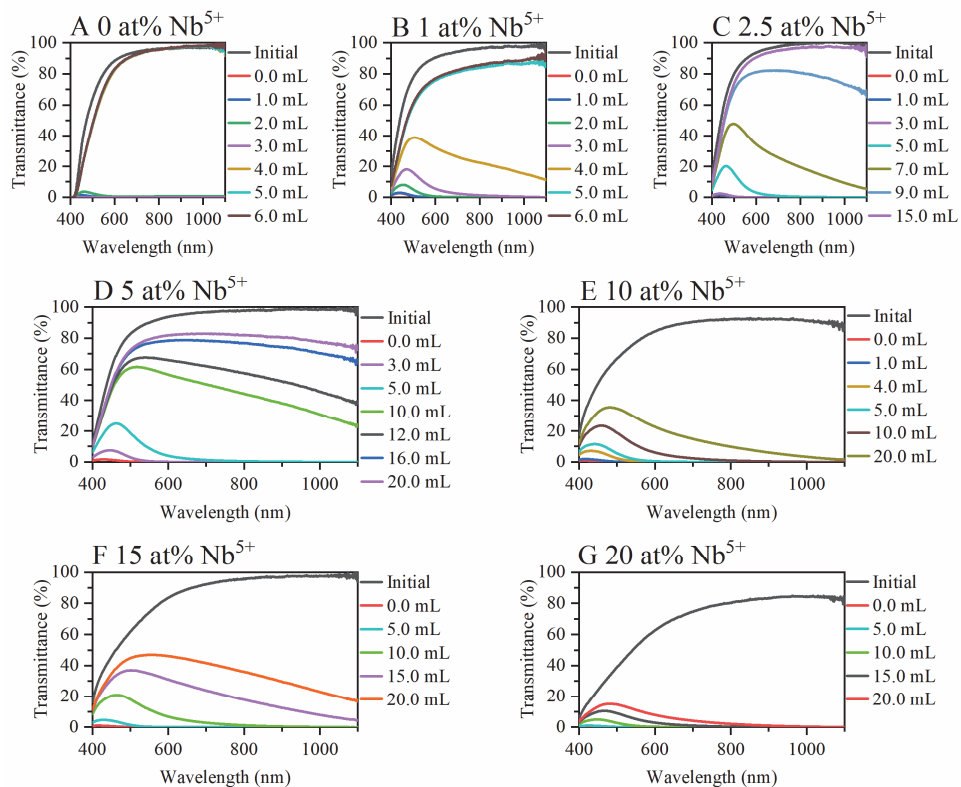


Fig. 3.25. UV-Vis transmittance spectra for un-doped and Nb-doped TiO₂ nanoparticle colloids during dynamic recovery.

A similar picture is seen when looking at the steady state recovery rates (Fig. 3.26.A&B). Here, the un-doped TiO₂ sample after 5 mL of air, recovered relatively rapidly, in only 25 min. This is largely due to the fact, that 5 mL is very close to the amount of air necessary to achieve recovery in the dynamic experiment. In both the visible (550 nm) and NIR (1000 nm) ranges, the un-doped TiO₂ nanoparticle colloid showed a similar recovery, owing to the easily quenchable nature of the Ti³⁺ and V_O[•] defects. All the Nb⁵⁺ samples on the other hand required at least 3 times the amount of time to recover (1 at% Nb⁵⁺ sample required 76 min to recover

in the NIR range). This time was exponentially longer for the 15 at% and 20 at% sample colloids around 35 hours to recovered in the visible range and even longer (40-48 hours) to recover in the NIR range. This can be attributed to multiple effects. First, the slow initial recovery can be attributed to the correlation of transmittance and absorbance at low transmission values. In this regime, large changes in absorbance result in only marginal changes transmittance. The second effect taking place is due to the more stable Nb⁴⁺-V_O-Ti⁴⁺ complex defect. The relative transmittance change was derivated by time, resulting the relative transmittance change rate for not only the photodarkening (Fig. 3.26.C&F), but also the dynamic (Fig. 3.26.D,G) and steady-state recovery rates (Fig. 3.26.E,H). The steady-state recovery rates had a much wider spread depending on the Nb⁵⁺ content. The difference between the un-doped and 20 at% Nb⁵⁺ doped TiO₂ colloids was more than 2 orders of magnitude (359 times) at 700 nm for the maximum recovery rate and similar difference also for the average recovery rate. As a higher stability of the defects leads to an increased formation rate and a decreased annihilation rate, this theory correlates neatly with the observed results.

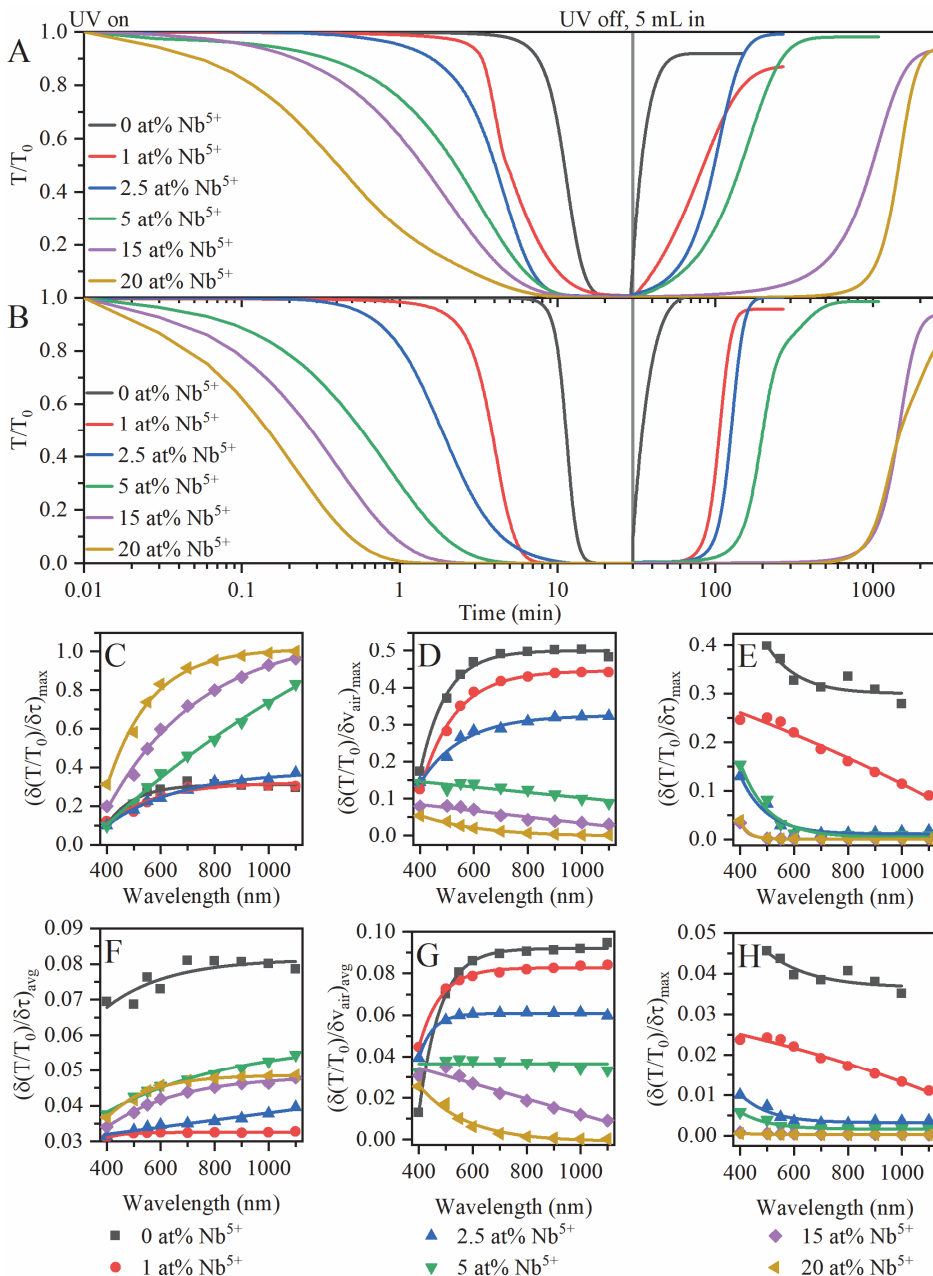


Fig. 3.26. T/T_0 plots of the transmittance change during UV irradiation and subsequent steady state recovery at **A)** 550 nm; **B)** 1000 nm; C,D,E) maximum relative transmittance change rate for photodarkening (C); dynamic recovery (D) and steady-state recovery (E); F,G,H) average relative transmittance change rate of photodarkening (F); dynamic recovery (G); steady-state recovery (H).

The optical response to UV in hole scavenging media can be observed for multiple cycles indicating stability of photochromic effect in synthesized nanoparticles (Fig. 3.27). The figure shows response/recovery cycles for the sample with 1 at% Nb. After the first cycle, there is a

slight difference between the initial and recovered transmittance. However, each subsequent cycle recovers fully to the transmittance of the previous cycle. Although some remanent $\text{Nb}^{4+}\text{-V}_\text{O}\text{-Ti}^{4+}$ defect complexes may be present in the material, there is no gradual decrease in the recovered transmittance. Hence, it is certain that the recovery can be observed also for other compositions with higher Nb dopant concentration, but the complete experiments were not conducted due to long recovery periods.

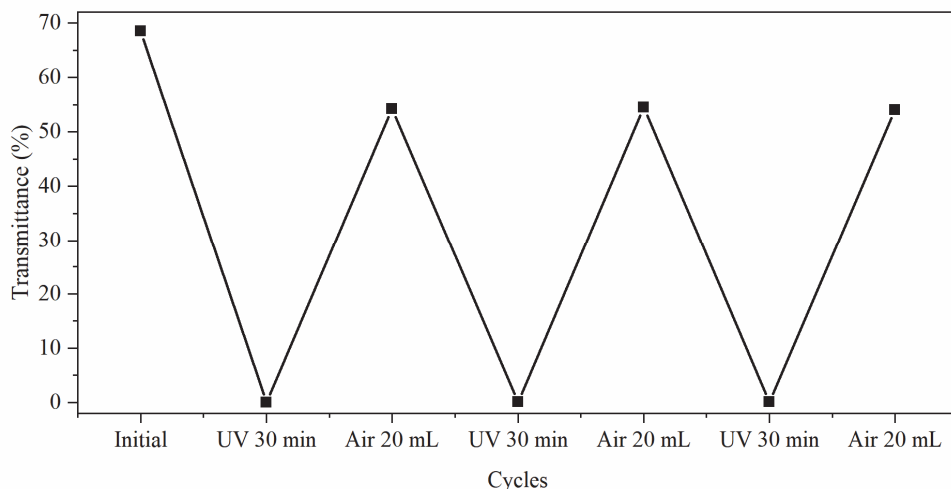


Fig. 3.27 Repeatability testing done when cycling between UV irradiation and recovery with air injection for the sample with 1% Nb at a wavelength of 550 nm.

To make the Nb^{5+} doped TiO_2 nanoparticle colloids more suitable for practical applications, the recovery rate needs to be increased. Taking inspiration from the previous research on TiO_2 colloids in different solvents, one possibility for the increase in the recovery can be the usage of an ethanolamine additive. For that purpose, the colloids of 20 at% Nb^{5+} doped TiO_2 nanoparticles were modified with varying amounts of TEOA (25, 50 and 100 mol% with respect to the amount of TiO_2 present, Fig. 3.28). The steady-state recovery rate for colloids containing 25 mol% TEOA in both wavelength ranges recovered 7.42 times faster - in 330 min. It is worth noting, that the recovery in case of TEOA addition was observed with no air injection. If air would additionally be injected, this in further increase the recovery rate, similarly as was overserved for the un-doped TiO_2 colloids.

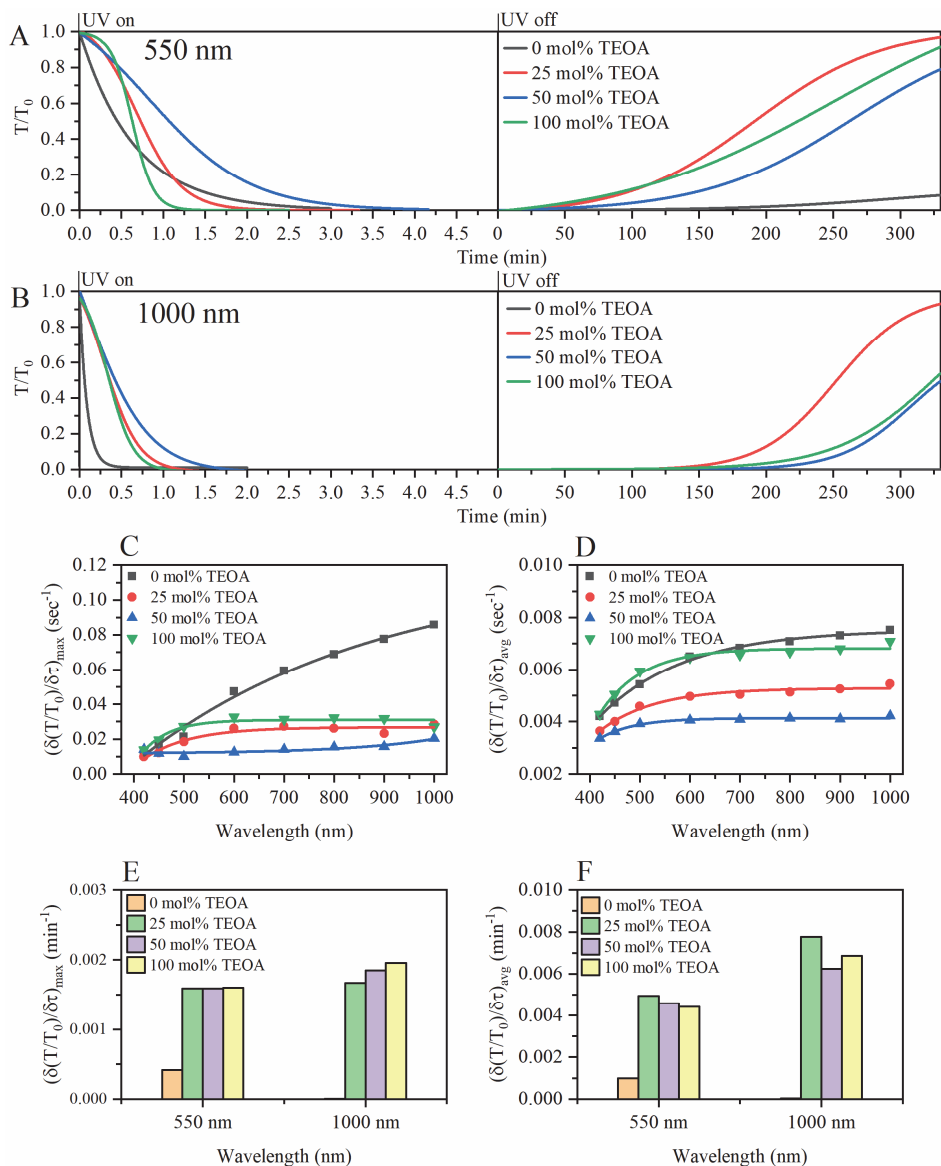


Fig. 3.28. T/T_0 plots during UV irradiation and airless recovery for the colloid of 20% Nb-doped TiO₂ with the addition of triethanolamine (different mol% relative to the amount of TiO₂ for **A**) 550 nm; **B**) 1000 nm; **C**) maximum photodarkening rate and **D**) average photodarkening rate for Nb⁵⁺-doped TiO₂ colloid without and with 25, 50 and 100 mol% TEA additive; **E**) maximum recovery rate of the colloids without air injection at 550 and 1000 nm; **F**) average recovery rate of the colloids without air injection at 550 and 1000 nm.

As mentioned previously, the dramatic increase in the photodarkening rate of the Nb⁵⁺-doped TiO₂ colloids when compared to pristine TiO₂ stems from the formation of the complex point defect Nb⁴⁺-V_O-Ti⁴⁺. The evidence for this can be gathered from EPR experiments. EPR spectroscopy was done for the Nb⁵⁺ doped TiO₂ colloid sample with the highest Nb content of 20 at% (Fig. 3.29). Before UV irradiation, we observe the same three

signals as for the un-doped TiO₂ colloid. However, there is no evidence of a Ti³⁺ signal either during or after UV irradiation. Instead, a new spectral feature with a g-value of 1.977 and ΔH = 4 G was detected, and its intensity was seen to increase with irradiation time. This signal can be attributed to Nb⁴⁺ to be precise, the defect model of Nb⁴⁺-V_O-Ti⁴⁺.³⁶¹ Although the Nb⁴⁺ signal cannot be seen in EPR at temperatures above 77 K, because of the complex defect configuration, detection of the signal was permitted above 77 K at room temperature. The results indicate that the Nb⁵⁺ doped TiO₂ contain different point defects responsible for photochromism when compared to un-doped TiO₂. When calculating the number of defects, it was observed that the number of defects reached saturation already after 30 min, instead of the 60 min for un-doped TiO₂. This observation is in agreement with our UV-Vis spectroscopy results that show a higher photodarkening rate for samples doped with Nb⁵⁺.

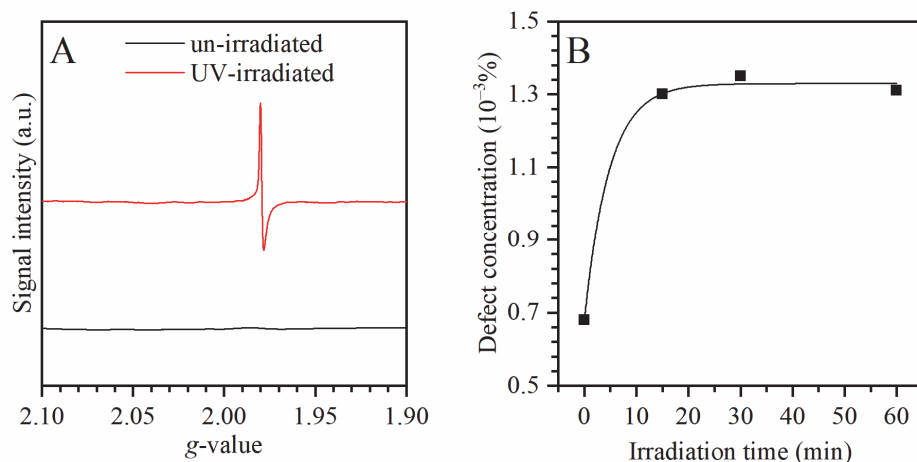


Fig. 3.29. A) EPR spectra for the 20 at% Nb⁵⁺ doped TiO₂ nanoparticle colloid before and after UV irradiation; B) the relevant defect concentrations as a function of irradiation time.

3.5 Photochromic TiO₂ polymer gels

The TiO₂ nanoparticles suspended in a hole scavenging media is a potent material for photochromic applications. However, for most real-life applications, colloids are not usable as they are prone to leakage from most closed systems and can evaporate, causing a pressure increase, that can potentially ruin the closed system. Thin films, however, have a much lower absorptivity, cause to achieve the equivalent absorption to the colloids, a film with a thickness of at least 8 μm is necessary. Films that thick are difficult to produce. Furthermore, when films are this thick, the hole scavenger can only interact with the upper layer of the films. Thus, photodoping happens only on the top layer, and basically makes thin film usage impossible. The middle ground for to combine the potential of colloids with the stability of thin films, would be gels as these would allow to produce closed systems, that are much less prone to evaporation and leakage, while allowing hole scavenging to happen throughout the hole gel volume. The gels presented here are transparent in the undarkened state, while absorbing almost all the light in the photodarkened state. These gels also have a performance, comparable to the colloid samples discussed earlier.

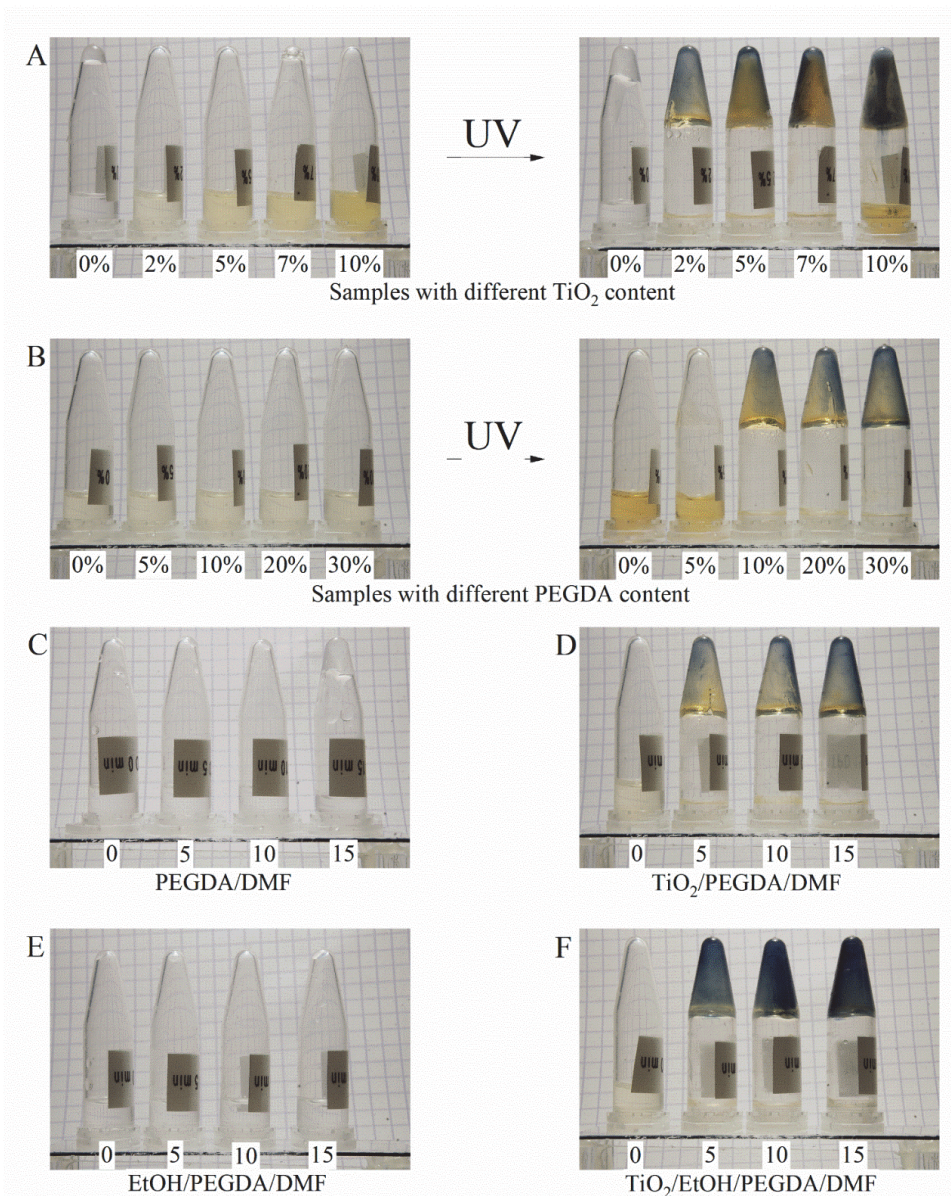


Fig. 3.30 **A)** Photographs of samples with different content of TiO_2 before and after UV irradiation (PEGDA content 20 vol%/ EtOH content 20 vol%); **B)** Photographs of samples with different PEGDA content before and after UV irradiation (TiO_2 content 2 vol% / EtOH content 20 vol%); **C)** PEGDA 20 vol%/DMF solutions after (0, 5, 10 and 15 min) UV irradiation; **D)** TiO_2 2 vol%/ PEGDA 20 vol%/DMF solutions after (0, 5, 10 and 15 min) UV irradiation; **E)** EtOH 20 vol%/ PEGDA 20 vol%/DMF solutions after (0, 5, 10 and 15 min) UV irradiation; **F)** TiO_2 2 vol%/ EtOH 20 vol%/ PEGDA 20 vol%/ DMF solutions after (0, 5, 10 and 15 min) UV irradiation.

The gels form by photocrosslinking the PEGDA polymer with the help of the TiO_2 nanoparticles (Fig. 3.31.A). TiO_2 acts as a photoinitiator for the crosslinking process, resulting

in the polymerization of PEGDA via the vinyl terminal groups. To keep the gels stable and transparent, DMF was necessary. A large variety of gel compositions were made under this study and an approximation of a compositional diagram can be made (Fig. 3.31.B). We can see, that if the PEGDA content is below 5 vol%, gel formation is not expected. This, however, is not quite the case as, if the TiO₂ content is above 17 vol%, the samples were gels, even without PEGDA. Sadly, these gels have hardly any photochromic activity, as DMF is not known to be a hole scavenger and as such, the photodoping effect is severely diminished.

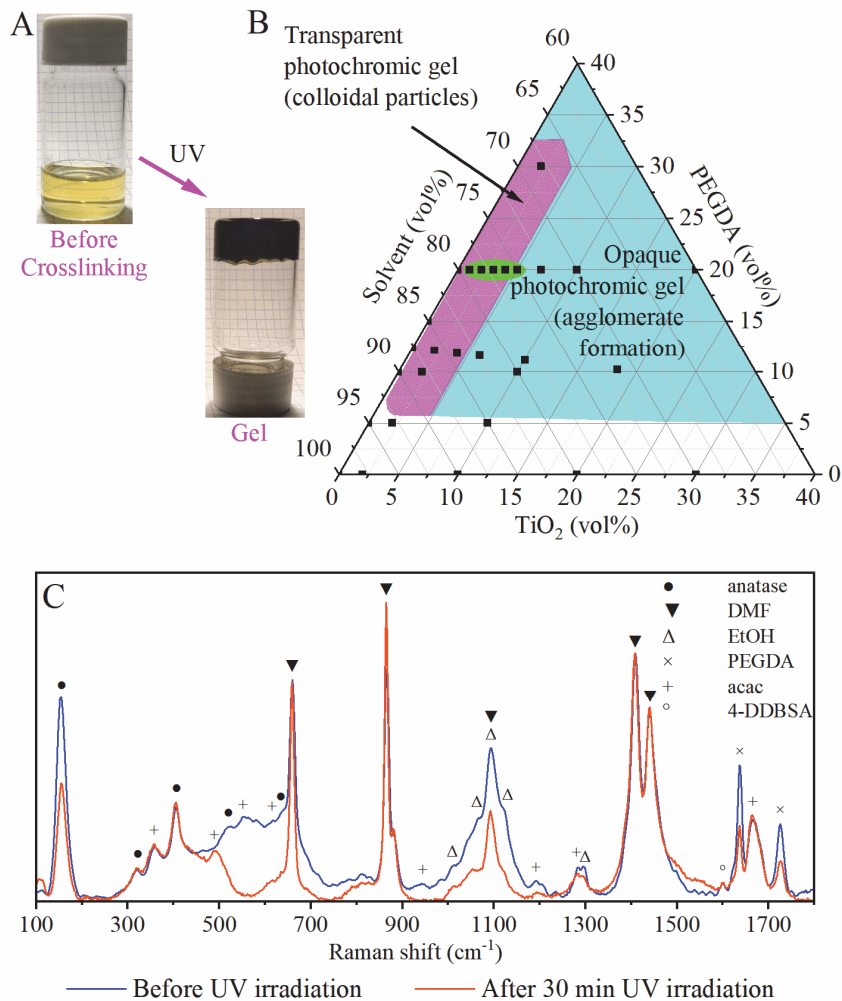


Fig. 3.31. **A)** Photograph of a TiO₂ / PEGDA gel composition (3 vol% TiO₂ and 20 vol% EtOH) before and after UV irradiation; **B)** Ternary diagram displaying the compositional range where the transparent and opaque gels are obtained (white region indicates no gel formation). Green circle indicates the region of compositions studied further; **C)** Raman spectra of a TiO₂ / PEGDA gel (2 vol% TiO₂ and 20 vol% EtOH) before and after UV treatment (photochromism and crosslinking).

If the TiO₂ content of the gels is sufficiently low (below 0.25 vol%), no gelation or very minor gelation can be observed. To obtain gels that are crosslinked throughout the hole sample volume, at least 0.5 vol% of TiO₂ are necessary. In the TiO₂ content region of 0.5-4.5 vol%, the gels are transparent after crosslinking, and can be used in photochromic applications. However, if the TiO₂ content is increased above this amount, the crosslinked gels were no longer transparent, but opaque, indicating, that scattering is occurring.

One of the samples was looked at before and after crosslinking with UV irradiation (Fig. 3.31.C). It is worth noting that photodoping also took place during the crosslinking cycle. As such several of the Raman bands decreased in intensity. The loss in the intensity of the Raman bands at 517 and 638 cm⁻¹ can be attributed to a loss in Ti-O bonds indicating the presence of oxygen vacancies^{332,362}. Oxygen vacancies are forming to compensate the Ti³⁺ which are forming due to electron accumulation and reduction of Ti⁴⁺. Similarly, the decrease in the Raman band at 148 cm⁻¹ that is attributed to Ti-Ti sublattice vibrations, indicates distortions caused by Ti³⁺ formation³⁶². The other constituents of the gel experienced changes, except for DMF. The DMF bands at 660, 866, 1400 and 1440 cm⁻¹ retained their intensity after irradiation and the band at 866 cm⁻¹ was used to normalize the spectra for comparison. Peaks at 493, 553, 580, 616 and 939 cm⁻¹ were no longer visible after irradiation. The peak at 553 cm⁻¹ corresponds to acac out-of-plane ring deformations, while the peaks at 616 cm⁻¹ and 939 cm⁻¹ correspond to C-CH₂-C bending and C-C stretching respectively³⁶³. The band that increase in intensity is at 493 cm⁻¹ and is attributed to acac in plane ring deformations³⁶⁴. This indicates, that acac undergoes chemical reactions with TiO₂ photodoping byproducts via Knoevenagel condensation³⁶⁵. The byproducts being aldehydes from the oxidation of ethanol. The fact, that the amount of ethanol decreases is indicated by the decrease in the 1100 cm⁻¹ band intensity³⁶⁶. To determine the crosslinking factor (how much of the C=C bonds from PEGDA were crosslinked), the Raman band at 1638 cm⁻¹ was looked at as it correspond to C=C bond stretching³⁶⁷, that were only present in PEGDA before crosslinking³⁶⁸. As such, the intensity of this band decreases with crosslinking (Fig. 3.32). This bands intensity decreased, with irradiation time, resulting in a crosslinking factor of 52%.

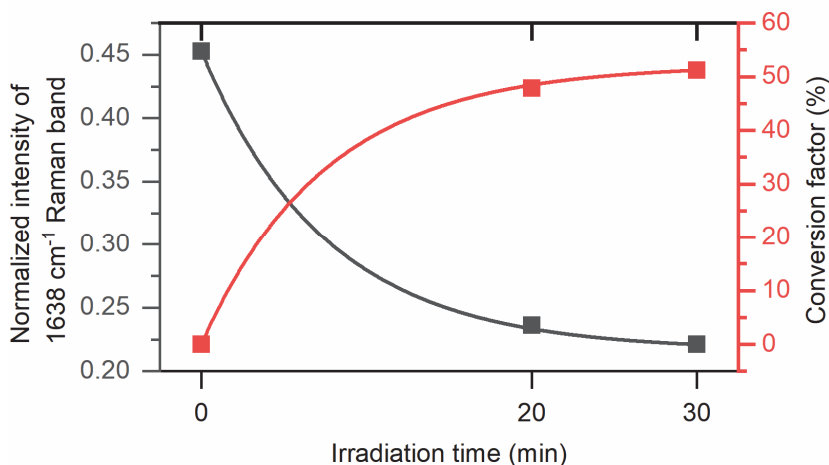


Fig. 3.32. 1638 cm⁻¹ Raman band intensity decrease, and the resulting crosslinking factor change during UV irradiation.

The samples photodarkened when irradiated with UV light (Fig. 3.33.A) and recovered when the UV light was turned off. All the samples were capable of light absorption in a wide range of wavelengths, similarly to colloids (Fig. 3.33.B). The samples darkened within the time span of 30-120 min, with recovery slowly taking place in the time span of 120-480 min, depending on the composition (Fig. 3.33.C). The transmittance change as well as the kinetics were dependent of the wavelength. This is due to the fact, that the change in transmittance at different wavelengths depends on different mechanisms as explained in chapter 3.1.

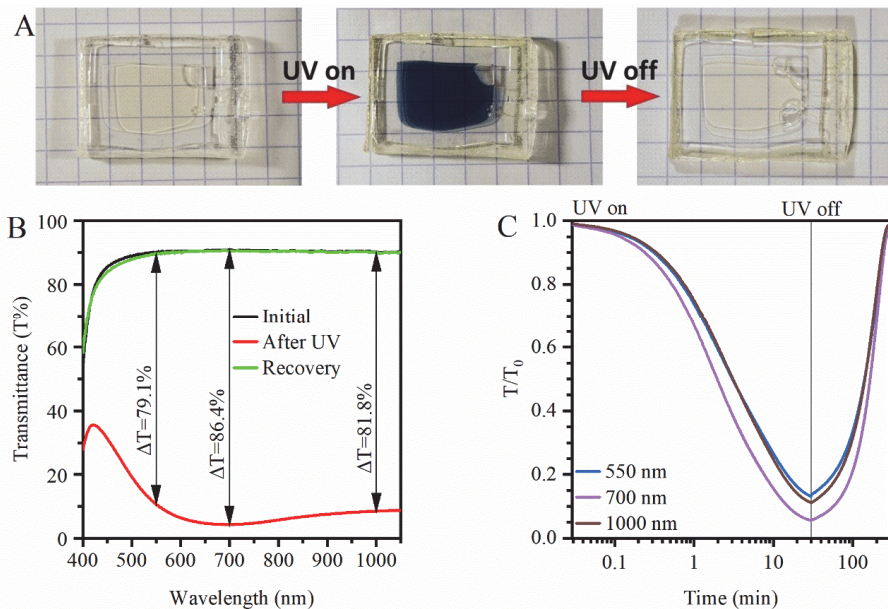


Fig. 3.33. **A)** Photographs of photochromic gel sample in PDMS cell before UV irradiation (left), after 30 min UV irradiation (middle) and after 5 hours of recovery (right). The sample consisted of 3 vol% TiO_2 / 20 vol% EtOH / 20 vol% PEGDA / DMF; **B)** Spectra of a sample before UV, after UV irradiation and after recovery (3 vol% TiO_2 / 30 vol% EtOH / 20 vol% PEGDA / DMF); **C)** Relative transmittance change during UV irradiation and recovery of the same sample.

The transmittance change between the initial and photodarkened states was dependent on the TiO_2 content as well as on the amount of EtOH present in the gels. The highest amount of variation in the transmittance change was for samples without EtOH. Here, the transmittance change varied from 11.2% for sample with 1 vol% of TiO_2 at 400 nm to 89.8% for the sample with 5 vol% TiO_2 at 700 nm (Fig. 3.34.A).

The transmittance change dependence on the TiO_2 content was linear for low to medium TiO_2 contents (1-3 vol%), while for higher TiO_2 contents (4-5 vol%), the transmittance change was decreased. This can be explained by several reasons. First, the diminishing returns can be explained by the correlations between absorbance and transmittance. This correlation is logarithmic, meaning that, when the absorbance is low, small changes in absorbance lead to large changes in transmittance. Subsequently, when the absorbance is high, even large changes in absorbance can lead to relatively small changes in transmittance. Another possibility is that

this is mainly due to saturation. This is also the reason why Lambert's law can only be applied only for low concentrations.

When EtOH was added to the samples, an increase in the transmittance change was observed with a maximum transmittance change seen at 700 nm (Fig. 3.34.B-D). The increase in the absolute transmittance change is due to the nature of ethanol being a very potent hole scavenger, as was seen previously. This, in turn, allowed for a greater number of electrons to accumulate in the nanoparticles, both as delocalized electrons in the conduction band as well as in the form of Ti^{3+} defects. The presence of EtOH gradually increased the transmittance change, with samples with a lower TiO_2 content (1-3 vol%) benefiting more than samples with a higher TiO_2 content (4-5 vol%). This is again due to saturation. However, the presence of EtOH (30 vol%) allowed low TiO_2 content (1-2 vol%) samples to achieve a transmittance change of over 80%.

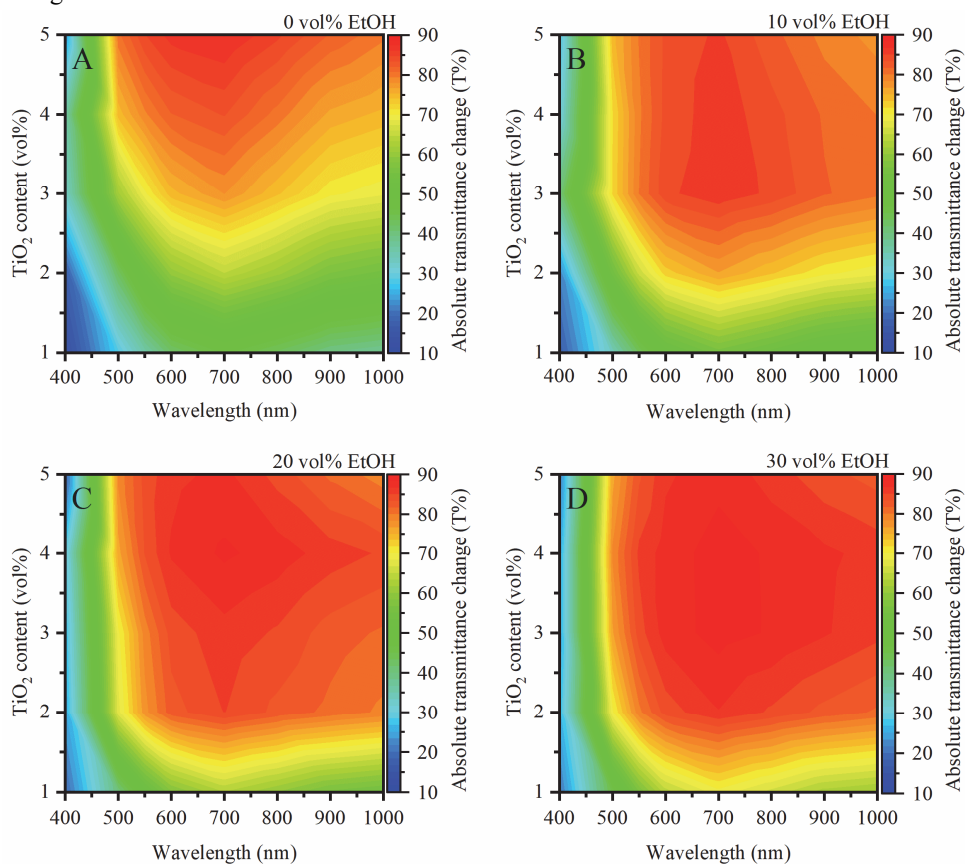


Fig. 3.34. Absolute transmittance change of the samples with different TiO_2 contents and at different wavelengths for samples with a EtOH content of **A)** 0 vol%; **B)** 10 vol%; **C)** 20 vol%; **D)** 30 vol%.

The increase in absolute transmittance change also is indicative of a metastable system, as recovery takes place all the time, just very slowly. Without ethanol, the photodarkening and recovery reach an equilibrium at a lower absorption. Ethanol, acting as a catalyst, shifts this equilibrium towards a higher absorption. Evidence for this can also be seen in the transmittance

change rate. Without ethanol (Fig. 3.35.A) the samples photodarkened very slowly, requiring 120 min to reach saturation. This resulted in change rates of as low as $-1.6 \times 10^{-2} \text{ min}^{-1}$ for 1 vol% TiO₂ sample at 400 nm to as high as -0.93 min^{-1} for 5 vol% TiO₂ samples at 400 nm. Here, the large apparent photodarkening rate of the sample with 5 vol% of TiO₂ was the result of multiple simultaneous processes. First was the photodarkening taking place similarly to the rest of the samples. However, another process that took place, was the agglomeration of the nanoparticles. This leads to scattering, that further decreased the transmittance of the gel samples. Evidence for this was the fact, that the high photodarkening rate was mainly seen for shorter wavelengths (400-550 nm) that a susceptible to scattering from smaller agglomerates, than longer wavelengths as per Mie scattering theory. For all other samples, the photodarkening rate was the highest at 700 nm.

When ethanol was added to the composition, the result was a general increase in the photodarkening rate, that was also evident from the fact, that the samples needed to only be irradiated for 30 min instead of 120 min for saturation. Further irradiation didn't result in any noticeable increase in absorption. The photodarkening rate increased the most when the ethanol content was increased from 0-10 vol% (Fig. 3.35.B). This resulted in on average a 408% increase in the photodarkening rate irrespective of wavelength. Samples with a low TiO₂ content of 1-2 vol% exhibited a slightly higher increase (362% on average) when compared to samples with a higher TiO₂ content of 3-4 vol% (248% on average). The sample with a TiO₂ content of 5 vol% exhibited a very slight increase in the photodarkening rate of just 29% on average, mainly due to the already high photodarkening rate. This comparatively negligible photodarkening rate increase, when compared to the rest of the samples, shows that scattering effects, taking place due to agglomeration, are the main causes for the high photodarkening rate. When the ethanol content was increased further the results were a lot less pronounced. An increase in the photodarkening rate of just 6% on average was observed when the ethanol content was increased from 10 vol% to 20 vol% (Fig. 3.35.C), with a further 10% on average observed when the ethanol content was increased by an addition 10 vol% to 30 vol% in total (Fig. 3.35.D). Here again, the highest 29% increase was for samples with a low TiO₂ content of 1-2 vol%, while the photodarkening rate increased by just 2% on average for higher TiO₂ content samples. With the maximum amount of ethanol this resulted in photodarkening rates ranging from $-7.9 \times 10^{-2} \text{ min}^{-1}$ to $-5.2 \times 10^{-1} \text{ min}^{-1}$, that was a total increase of 465% on average for samples with a low TiO₂ content of 1-2 vol%. The diminishing returns for subsequent increases in ethanol show, that with even 10 vol%, have almost all of the possible adsorption sites covered, i.e. the nanoparticle surface is almost saturated with ethanol and during photodarkening, the TiO₂ nanoparticles give out holes (the ethanol scavenges the holes) at almost the maximum rate, that is limited by the processes of ethanol adsorption, electron migration and subsequent aldehyde desorption.

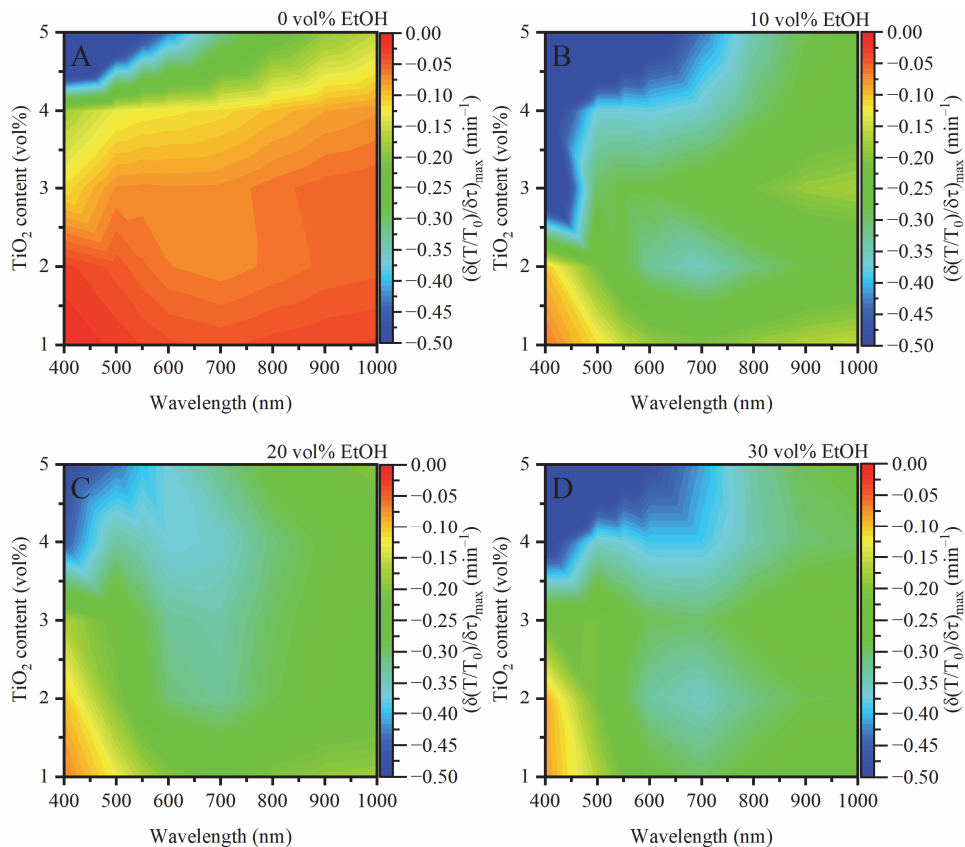


Fig. 3.35. Photodarkening kinetics of the samples with different TiO₂ contents and at different wavelengths for samples with a EtOH content of **A)** 0 vol%; **B)** 10 vol%; **C)** 20 vol%; **D)** 30 vol%.

The samples recovered when the UV light was turned off. The recovery was much slower, with an average recovery rate in the order of magnitude of from $2.4 \times 10^{-5} \text{ min}^{-1}$ to $2.2 \times 10^{-3} \text{ min}^{-1}$, with the highest recovery rate for the 3 vol% TiO₂ sample at the NIR range (Fig. 3.36.A). The slowest recovery was for the sample with the highest TiO₂ of 5 vol%. This is due to the fact, that, the more photodoped TiO₂ is present in the sample, the more recovery needs to take place. In this case, the recovery is done through the photoreduction of the oxidized species, present in the gel. The photoreduction takes place because the nanoparticles have a large accumulation of electrons. These electrons are then capable of reducing organic species in the gel, that have previously been oxidized.

When 10 vol% of ethanol is added to the samples, the recovery rate increases by 90.3% on average (Fig. 3.36.B). Here, the highest increase in recovery rate is seen again for samples with a low TiO₂ of 1-2 vol%, with an increase of 139%. The sample with the lowest TiO₂ content studied of just 1 vol% exhibited an increase in the recovery rate of 204% on average, increasing the recovery rate from $1.2 \times 10^{-3} \text{ min}^{-1}$ to $3.8 \times 10^{-3} \text{ min}^{-1}$ at 550 nm and from $1.4 \times 10^{-3} \text{ min}^{-1}$ to $4.2 \times 10^{-3} \text{ min}^{-1}$ at 1000 nm. All the rest of the samples showed a much lower increase in the recovery rate of just 62% on average. A further increase in the ethanol content of 10 vol%

(20 vol% in total Fig. 3.36.C) resulted in a further 43% increase in the recovery rate, with a lot more even increase across the studied samples. The highest recovery rate was observed for the samples with a low TiO₂ content (1-2 vol%) with values of $4.2 \times 10^{-3} \text{ min}^{-1}$ at 550 nm and $4.9 \times 10^{-3} \text{ min}^{-1}$ at 1000 nm for the sample with a TiO₂ content of 1 vol% and $3.4 \times 10^{-3} \text{ min}^{-1}$ at 550 nm and $3.3 \times 10^{-3} \text{ min}^{-1}$ at 1000 nm for the sample with a TiO₂ content of 2 vol%. Further increasing the ethanol content to 30 vol% (Fig. 3.36.D) lead to an average increase of 33% across all the samples with the highest increase observed for the samples with a high TiO₂ content. The highest overall increase was observed for the samples with a TiO₂ content of 2 and 3 vol%, with the 3 vol% sample reaching a recovery rate of $5.6 \times 10^{-3} \text{ min}^{-1}$ at 550 nm and $4.4 \times 10^{-3} \text{ min}^{-1}$ at 1000 nm.

The gradual increase in the recovery rate with ethanol addition was due to the nature of the oxidation products. When ethanol is present in the gels, during hole scavenging, the by products are acetaldehyde or even acetic acid. With the photodoped TiO₂ nanoparticles, acetaldehyde can be photoreduced back to ethanol with the interaction with the accumulated electrons. This is done easier than the photoreduction of the other potential photooxidation products possible, such as oxidation products of acetylacetonate, PEGDA or DMF. This is also of note, because the photooxidation of these molecules can be accompanied by the cleavage of bonds, resulting in an irreversible oxidation reaction. Acetylacetonate can be oxidized to acetic acid and formic acid via Baeyer-Villiger oxidation.³⁶⁹ PEGDA has multiple fragments in its molecule, that are prone to possible oxidation reactions such as the carboxy fragments at the ends as well as ethylene glycol fragments in the middle of the molecule.³⁷⁰ DMF is susceptible to oxidation, with the help of hydroxyl groups, that could easily be introduced into the system from the TiO₂ surface.³⁷¹ This oxidation is also accompanied by the cleavage of a C-N bond, resulting in demethylation of the DMF molecule. On the flip side, acetaldehyde, could be photoreduced back to ethanol as it has been shown that aldehydes can be reduced with the help of TiO₂ under UV irradiation, acting as electron scavengers.³⁷²⁻³⁷⁴

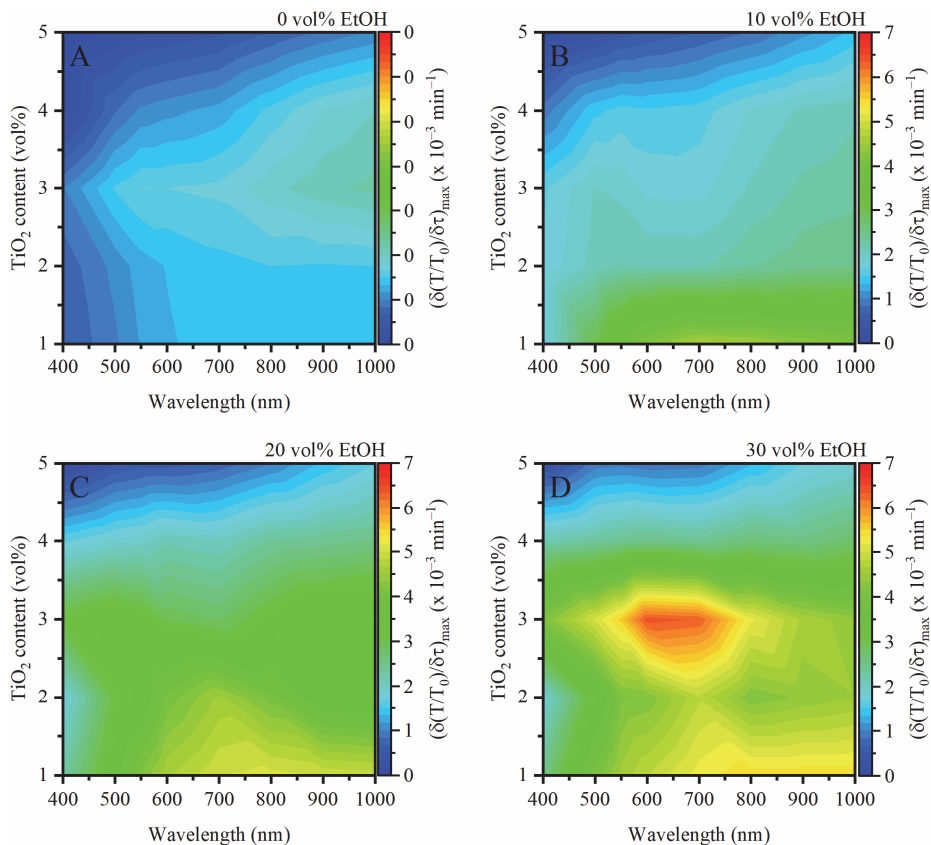


Fig. 3.36. Recovery kinetics of the samples with different TiO₂ contents and at different wavelengths for samples with a EtOH content of **A)** 0 vol%; **B)** 10 vol%; **C)** 20 vol%; **D)** 30 vol%.

For samples without ethanol (Fig. 3.37.A), with a TiO₂ content above 1 vol%, the recovery is incomplete, especially in the shorter wavelength range. The sample with 2 vol% TiO₂ showed a recovery effectiveness of 86.6% at 400 nm, that gradually increased with increasing wavelength, and at 600 nm reached full recovery of 99.2%. The sample with 3 vol% TiO₂ recovered only 24.2% at 400 nm with a gradual increase in recovery up to 97% at 1000 nm. The samples with a higher TiO₂ (4-5 vol%) did not recover with the 4 vol% sample recovering to just 92.5% at 1000 nm and the 5 vol% sample recovering to just 81.5% at 1000 nm. The reason for this limited recovery, is that without a dedicated hole scavenger, the gels themselves start to degrade during the photodarkening process and as such, scattering starts to occur. This is indicated by the recovery efficiency being higher at longer wavelengths when comparing to shorter ones.

When 10 vol% of ethanol is introduced into the samples (Fig. 3.37.B), the recovery shows a noticeable increase across all the samples. The 2 vol% TiO₂ sample now recovers fully even at 400 nm with a recovery effectiveness between 97.8% and 100%. Samples with a higher TiO₂ content samples exhibit an increase in recovery effectiveness of 9% on average in the NIR wavelength range of 700-1100 nm and 20% on average in the visible range (400-600 nm) when

compared to the samples without ethanol. The highest increase in the recovery effectiveness was observed for the sample with 4 vol% TiO₂ with an increase in recovery effectiveness of 30% at 550 nm. This drastic increase in the recovery effectiveness of the samples with the introduction of ethanol even at 10 vol%, shows that when a dedicated hole scavenger is present in the system, the rest of the constituents are spared from the photooxidation happening when photodarkening occurs. This allows for the stability to be kept and scattering caused by agglomeration – avoided.

An increase in the ethanol content to 20 vol% (Fig. 3.37.C) resulted in a very slight (~1%) increase in the recovery effectiveness overall when compared to samples with 10 vol% ethanol, with a more noticeable increase in the recovery of the 3 vol% TiO₂ sample at 400 nm (from 31.8% to 40.6%). When the ethanol content was increased to 30 vol% (Fig. 3.37.D), there was a more noticeable increase in the recovery effectiveness, with the mayor increase being for the sample with 3 vol% TiO₂. This sample exhibited an increased in recovery effectiveness of 49.3% at 400 nm and 7.7% at 550 nm, bringing its total recovery effectiveness up to 89.9% at 400 nm and full recovery (98+ %) at the wavelength range of 600-1100 nm. The samples with a high TiO₂ content of 4-5 vol% exhibited an overall increase in the recovery effectiveness of 30.4% and 18.6% in the visible range (400-600 nm) and 9.3% and 14.4% in the NIR range for the samples with 4 vol% and 5 vol% TiO₂ respectively.

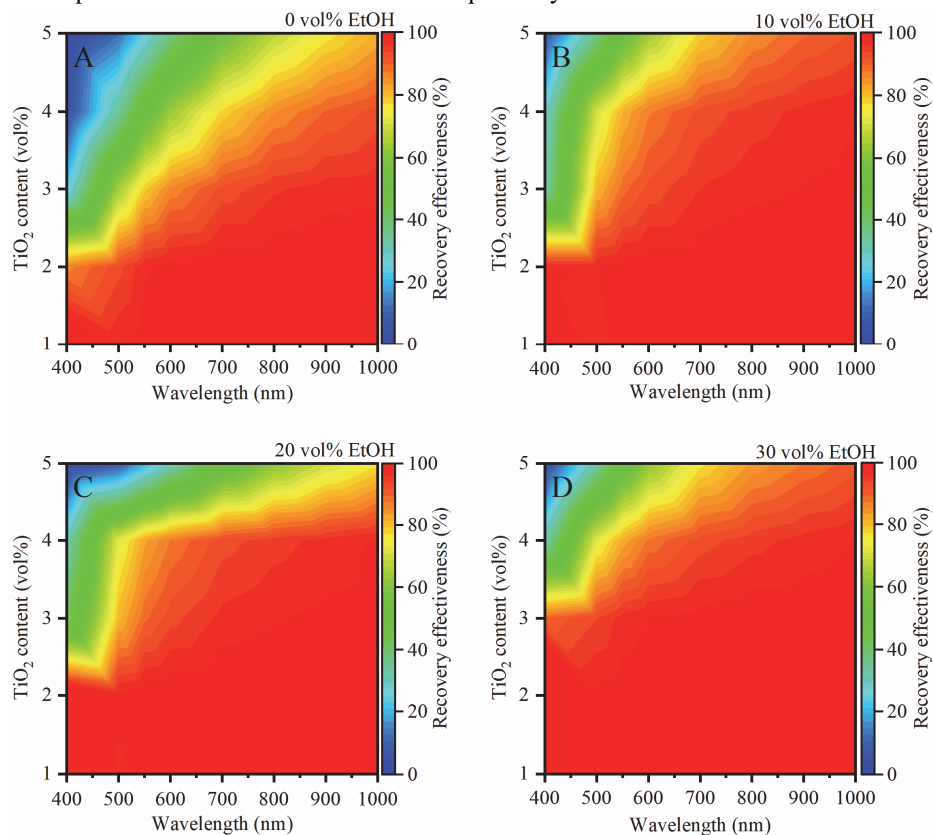


Fig. 3.37. Recovery effectiveness (%) of the samples with different TiO₂ contents and at different wavelengths for samples with a EtOH content of **A)** 0 vol%; **B)** 10 vol%; **C)** 20 vol%; **D)** 30 vol%.

The fact, that, even with 30 vol% of ethanol, the samples with a high TiO₂ content (>3 vol%) did not recover fully would suggest, that there is need to continue to increase the amount of ethanol. After all, only at 30 vol% ethanol content did the sample with 3 vol% TiO₂ start to exhibit a full recovery. The amount of ethanol usable in the composition is not unlimited. When experimenting with higher ethanol contents for samples with a TiO₂ content of 2 vol% (Fig. 3.38.A) it can be seen that the upper limit for the ethanol content is between 40-50 vol%. Already at 40 vol% the sample exhibited a slight decrease in the recovery of between 0-2% in the visible wavelength range. At 50 vol%, the sample exhibited a more pronounced decrease in the recovery effectiveness of the gel, with a decrease in recovery of between 2.8-6.8% in the visible range. In both cases the recovery in the NIR wavelength range, was unchanged. However, when the ethanol content was increased above 50 vol% (to 60 vol%), the samples recovery drastically decreased, do to just 5.9% on average, with an average recovery of just 1.4% in the visible range. When the ethanol content was increased even further, the recovery effectiveness further decreased, to just 2.8% on average across the whole studied wavelength range. This in essence meant that the gel system is no longer stable. The reason for this is the fact, that, ethanol replaces DMF in the composition. With an increase in the ethanol content, the DMF content is reduced proportionally. As DMF is the stabilizer in the system, it is needed at least a minimum amount, to keep the gel/nanoparticle network stable. From these observations, it can be concluded, that a minimum nanoparticle to DMF volume ration of 1:10 should be used, to keep the gel transparent.

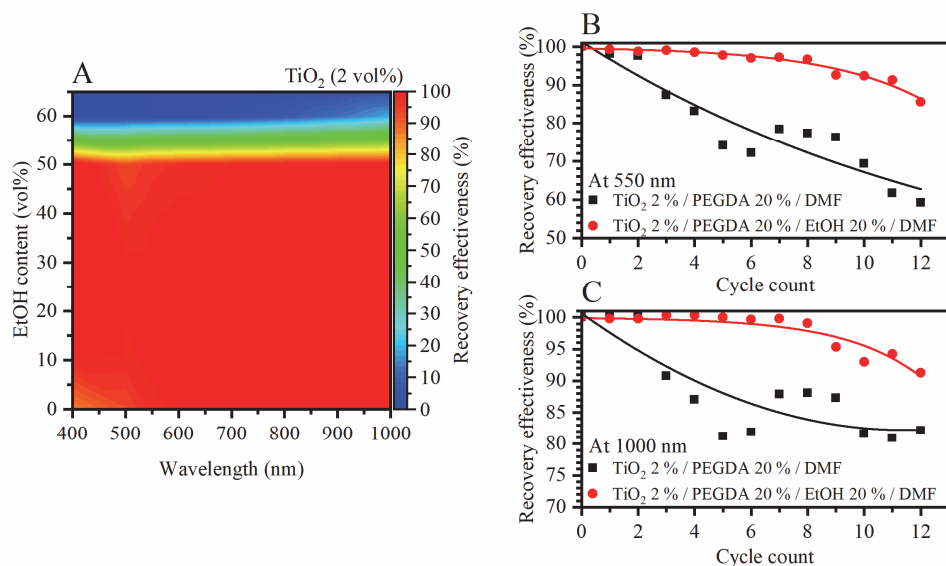


Fig. 3.38. A) Recovery effectiveness of samples with a TiO₂ content of 2 vol% and different amounts of ethanol at different wavelengths; **B)** transmittance recovery during subsequent UV irradiation/recovery cycles at 550 nm for samples with and without EtOH; **C)** transmittance recovery during subsequent UV irradiation/recovery cycles at 1000 nm for samples with and without EtOH.

Lastly, we investigate the cycling stability of the photochromic gels. The stability was tested for 12 photodarkening-recovery cycles by repeatedly irradiating samples with a TiO₂ content of 2 vol% (samples without EtOH 120 min, samples with 20 vol% EtOH 30 min) and allowing them to recover. The recovery in visible and NIR ranges was different with gels being stable for longer in the NIR range when compared to the visible. In the visible range (Fig. 3.38.B) the transmittance recovery in response to UV gradually decreases cycle over cycle, with the sample with 20 vol% EtOH decreasing from 99% on the 1st to 92% on the 10th and sample without EtOH decreasing from 98% on the 1st to just 69% on the 10th. This resulted in a recovery effectiveness decrease of 7% and 29% for samples with and without EtOH, respectively. In the NIR region (Fig. 3.38.C) the samples showed a much better recovery from cycle to cycle, especially with the 20 vol% EtOH addition with the transmittance recovery decreasing from an initial 100% on the 1st to 93% on the 10th cycle. The sample without EtOH showed a recovery efficiency decrease of 18% over 10 cycles, from 100% on the 1st to 82% on the 10th. The difference between the visible and NIR ranges stems from the fact, that shorter wavelengths are more susceptible to the scattering caused by agglomeration and scatter on smaller size agglomerates as per Mie theory^{375,376}. This can also be explained by the fact, that the Ti³⁺ and oxygen vacancy defects, created under the TiO₂ QD surface are stable and recover slowly because point defects migrate slower than electrons. Also, it is worth pointing out, that for both vis and NIR spectral ranges, the recovered transmittance for the sample with 20 vol% EtOH after each cycle was fairly constant and only started no noticeably drop after 8 cycles (at 550 nm 91% on the 1st and 88% on the 8th and at 1000 nm 90% on the 1st and 89% after the 8th) as opposed to the sample without ethanol, that had a drop in the recovered transmittance after just 3 cycles (at 550 nm from 91% on the 1st 90% on the 3rd and 70% after the 8th and at 1000 nm 90% on the 1st and 3rd and 79% after the 8th). This shows that the addition of EtOH had a positive impact not only on the photodarkening intensity and rate as well as the recovery effectiveness and rate, but also on the stability of the system. This also is due to the fact, that EtOH, acting as the hole scavenger, allows the rest of the constituents (DMF and crosslinked PEGDA) to remain untouched, thus making the gel more stable. Also, it photooxidation products can be photoreduced on photodoped TiO₂ QDs to facilitate better recovery.

3.6 Conclusions

1. Titanium dioxide has been found to exhibit photochromism in a variety of different hole scavenging solvents, such as primary and secondary alcohols. The highest photochromic response has been found to be for primary alcohols, with colloids in ethanol having the highest photochromic response. This is due to the unstable nature of the ethanol oxidation products, allowing for rapid adsorption/hole scavenging/desorption to happen of the nanoparticle surface.
2. The addition of ethanolamines increased the recovery, allowing the colloids to recover their transmittance in a fraction of the time, when compared to colloids without ethanolamines. However, this also had a negative effect on the photodarkening of titanium dioxide. This is because ethanolamines can oxidize to nitrocompounds, that can in turn scavenge the photoaccumulated electrons during photodarkening.
3. The change in charge carrier concentration can be measured as a change in electrical resistivity for nanoparticle thin films that are too thin to measure their change in transmittance spectroscopically. This resistivity change was observed when the thin films were exposed to hole scavenger vapors similarly to particles suspended in hole scavengers. This has the potential of being used for alcohol vapor gas sensing.
4. The electron photoaccumulation can be used for electricity generation and its photostorage by the usage of a photoelectric device. Thin films can be charged in 5 min allowing to obtain a power output of $0.0203 \mu\text{W}/\text{cm}^2$. This shows that the photochromic effect can be also used further, not only for light modulation but also to supply power to low-powered sensors in remote locations.
5. Successful doping of titanium dioxide with niobium was prepared by subsequent solvothermal treatment, which resulted in high doping efficiency of 99-100 % up to a dopant amount of 20 at%. No secondary phase formation was seen with distortions of the anatase crystalline lattice being observed by the introduction of the slightly larger Nb^{5+} cations. This resulted in a decrease in the optical band gap, which can be attributed by the formation of acceptor defect near the conduction band minimum.
6. The Nb^{5+} doped titanium dioxide exhibited a strong increase in the photochromic kinetics. The Nb^{5+} defects allowed for rapid photochromism, with 20 at% of niobium resulting in an order of magnitude increase in the photochromism speed photodarkening in just 1 minute, comparing to 20 minutes required for the un-doped nanoparticles, at the same conditions. Due to the nature of the Nb^{5+} traps, this also resulted in an increased recovery time, requiring almost 2 days to recover, comparing to just 30 minutes for the un-doped nanoparticle colloids. The main type of defects in these nanoparticles were $\text{Nb}^{4+}\text{-V}_\text{O}\text{-Ti}^{4+}$ while without Nb^{5+} , the main defects were Ti^{3+} .
7. The un-doped titanium dioxide was successfully incorporated into transparent polymeric gels comprised of polyethylene glycol diacrylate and *N,N*-dimethylformamide. The transparency was retained because of the stabilizing properties of *N,N*-dimethylformamide. The amount of titanium dioxide had to be kept between 1-4 vol% to retain transparency and at least 10 vol% of polyethylene glycol diacrylate was needed to produce a gel.
8. The partial substitution of *N,N*-dimethylformamide with ethanol, allowed for a dramatic increase in both the photodarkening and recovery speed. This also resulted in an increase of the stability of the prepared gel, due to ethanol taking over the role as the main hole

scavenger, thus protecting the remaining constituents from oxidation. This allowed the gel to remain transparent in its undarkened state for longer, withstanding 8 photodarkening/recovery cycles, without noticeable degradation.

3.7 Secinājumi

1. Titāna dioksīdam tika novērots fotohromais efekts dažādos caurumu ķērājos. Salīdzinot primāros un sekundāros spirtus, noskaidrots, ka augstākā fotohromā aktivitāte ir novērojama etanolā un citos primāros spirtos. Augstā fotohromā aktivitāte etanolā ir skaidrojama ar nestabilajiem etanola oksidācijas produktiem, kas ļauj strauji adsorbēties uz nanodaļiņu virsmas, saķert caurumu un desorbēties no nanodaļiņu virsmas.
2. Etanolamīnu pievienošana nanodaļiņu koloīdiem paātrināja atkrāsošanos, vienlaikus arī palēninot aptumšošanos. Tas saistīts ar etanolamīnu fotooksidācijas produktiem, kas satur nitro grupas un ir elektronu akceptori. Tas ļauj šiem produktiem saistīt elektronus.
3. Izmaiņa lādiņnesēju koncentrācijā plānām kārtiņām var tikt izmērīta, nosakot elektriskās pretestības izmaiņas kārtiņām, kas ir pārāk plānas, lai to fotohromās īpašības noteiktu spektroskopiski. Izmaiņas pretestībā tika konstatētas, kad plānā kārtiņa tika pakļauta caurumu ķērāju tvaikiem analogi to daļiņu suspensijām caurumu ķērājos un var tikt izmantota arī šo vielu tvaiku detektēšanai.
4. Elektronu akumulēšanas var tikt izmantota elektrības uzkrāšanai fotoelektriskās šūnās. Šāda šūna var tikt uzlādēta 5 min un spēj ģenerēt $0,0203 \mu\text{W}/\text{cm}^2$. Šādas šūnas var izmantot ne tikai gaismas modulācijai, bet arī mazas jaudas sensoru darbināšanai.
5. Titāna dioksīda nanodaļiņas tika veiksmīgi dopētas ar niobija katjoniem, pēc sintēzes veicot nanodaļiņu solvotermālo apstrādi. Tas ļāva iegūt dopētas titāna dioksīda nanodaļiņas ar augstu dopēšanas efektivitāti (99–100 %), ļaujot aizstāt līdz pat 20 at% titāna ar niobiju. Netika konstatētas sekundārās fāzes. Niobija dopēšana anatāza kristāliskajā režģī radīja elementāršūnas parametru palielināšanos, pateicoties lielāka katjona (Nb^{5+}) ievietošanai anatāze kristālrežģī, aizvietojojot Ti^{4+} katjonus. Tas arī izraisīja optiskās aizliegtās zonas samazināšanos, pateicoties akceptora līmeņu izveidošanai nedaudz zem vadāmības zonas minimuma.
6. Nb^{5+} ievietošana titāna dioksīda režģī radīja vārienīgu fotohromo īpašību uzlabošanos. Nb^{5+} defekti paātrina fotokrāsošanos, pie 20 at% satura ļaujot pilnībā nokrāsoties nanodaļiņu koloīdam vienas minūtes laikā. Tādos pašos apstākļos nedopētu nanodaļiņu koloīds nokrāsojās 20 minūšu laikā. Ņemot vērā Nb^{5+} slazdu dabu, ievērojami tika paildzināts atkrāsošanās laiks. Ar 20 at% Nb^{5+} koloīds atkrāsājās divu dienu laikā, savukārt nedopēto nanodaļiņu koloīds atkrāsājās 30 minūšu laikā. Nb^{5+} dopētajās nanodaļiņās galvenie defekti bija Nb^{4+} -V_o- Ti^{4+} un netika veidots Ti^{3+} . Nedopēto nanodaļiņu gadījumā galvenie defekti ir Ti^{3+} .
7. Nedopētās nanodaļiņas tika veiksmīgi integrētas fotohromos gēlos, kas tika izveidoti no polietilēnglikola diakrilāta un *N,N*-dimetilformamīda. Gēlu caurspīdīgums tika saglabāts *N,N*-dimetilformamīda stabilizējošo īpašību dēļ. Lai iegūtu caurspīdīgu gēlu, titāna dioksīda nanodaļiņu saturs nevar pārsniegt 4 tilpuma%. Lai iegūtu gēlu, nepieciešamais polietilēnglikola diakrilāta saturs ir vismaz 10 tilpuma%.
8. Daļēji aizstājot *N,N*-dimetilformamīdu ar etanolu, bija iespējams ievērojami paātrināt gan fotokrāsošanās, gan atkrāsošanās ātrumu. Etanola pievienošana uzlaboja arī šo gēlu stabilitāti, etanolam kļūstot par galveno caurumu ķērāju, tādējādi pasargājot pārējās gēla sastāvdaļas no oksidācijas. Tas ļāva gēlam saglabāt tā caurspīdīgumu neaptumšotā stāvoklī astoņus nokrāsošanās/atkrāsošanās ciklus bez redzamas degradācijas.

4 REFERENCES

- 1 D. T. Gillaspie, R. C. Tenent and A. C. Dillon, Metal-oxide films for electrochromic applications: Present technology and future directions, *J. Mater. Chem.*, 2010, **20**, 9585–9592.
- 2 C. G. Granqvist, P. C. Lansåker, N. R. Mlyuka, G. A. Niklasson and E. Avendaño, Progress in chromogenics: New results for electrochromic and thermochromic materials and devices, *Sol. Energy Mater. Sol. Cells*, 2009, **93**, 2032–2039.
- 3 P. Talvenmaa, in *Intelligent Textiles and Clothing*, Elsevier, 2006, pp. 193–205.
- 4 A. J. Moulson, Transition Metal Oxides, *Concise Encycl. Adv. Ceram. Mater.*, 1991, **12**, 497–499.
- 5 Y. Yao, Q. Zhao, W. Wei, Z. Chen, Y. Zhu, P. Zhang, Z. Zhang and Y. Gao, WO₃ quantum-dots electrochromism, *Nano Energy*, 2020, **68**, 104350.
- 6 J. Kim, G. K. Ong, Y. Wang, G. Leblanc, T. E. Williams, T. M. Mattox, B. A. Helms and D. J. Milliron, Nanocomposite Architecture for Rapid, Spectrally-Selective Electrochromic Modulation of Solar Transmittance, *Nano Lett.*, 2015, **15**, 5574–5579.
- 7 W. Zhang, H. Li, E. Hopmann and A. Y. Elezzabi, Nanostructured inorganic electrochromic materials for light applications, *Nanophotonics*, 2020, **10**, 825–850.
- 8 A. V. Shchegolkov, S. H. Jang, A. V. Shchegolkov, Y. V. Rodionov, A. O. Sukhova and M. S. Lipkin, A brief overview of electrochromic materials and related devices: A nanostructured materials perspective, *Nanomaterials*, , DOI:10.3390/nano11092376.
- 9 R. J. Mortimer, D. R. Rosseinsky and P. M. S. Monk, *Electrochromic Materials and Devices*, Wiley-VCH Verlag GmbH & Co. KGaA, Weinheim, Germany, 2013.
- 10 K. Madasamy, D. Velayutham, V. Suryanarayanan, M. Kathiresan and K. C. Ho, Viologen-based electrochromic materials and devices, *J. Mater. Chem. C*, 2019, **7**, 4622–4637.
- 11 J. H. Day, Thermochromism of inorganic compounds, *Chem. Rev.*, 1968, **68**, 649–657.
- 12 M. Li, S. Magdassi, Y. Gao and Y. Long, Hydrothermal Synthesis of VO₂ Polymorphs: Advantages, Challenges and Prospects for the Application of Energy Efficient Smart Windows, *Small*, 2017, **13**, 1–25.
- 13 Y. Gao, H. Luo, Z. Zhang, L. Kang, Z. Chen, J. Du, M. Kanehira and C. Cao, Nanoceramic VO₂ thermochromic smart glass: A review on progress in solution processing, *Nano Energy*, 2012, **1**, 221–246.
- 14 M. Aburas, V. Soebarto, T. Williamson, R. Liang, H. Eborndorff-Heidepriem and Y. Wu, Thermochromic smart window technologies for building application: A review, *Appl. Energy*, 2019, **255**, 113522.
- 15 J. Guo, K. Fu, Z. Zhang, L. Yang, Y. C. Huang, C. I. Huang, L. Zhu and D. Chen, Reversible thermochromism via hydrogen-bonded cocrystals of polydiacetylene and melamine, *Polymer (Guildf.)*, 2016, **105**, 440–448.
- 16 A. Chanakul, N. Traiphol and R. Traiphol, Controlling the reversible thermochromism of polydiacetylene/zinc oxide nanocomposites by varying alkyl chain length, *J. Colloid Interface Sci.*, 2013, **389**, 106–114.
- 17 M. Visková and M. Pechová, Study of adaptive thermochromic camouflage for combat uniform, *Text. Res. J.*, 2020, **90**, 2070–2084.
- 18 S. Kingchok, P. Nontasorn, K. Laohasurayotin, N. Traiphol and R. Traiphol, Reversible thermochromic polydiacetylene/zinc-aluminium layered double hydroxides nanocomposites for smart paints and colorimetric sensors: The crucial role of zinc ions, *Colloids Surfaces A Physicochem. Eng. Asp.*, 2021, **610**, 125733.
- 19 J. Pitchaimani, S. Karthikeyan, N. Lakshminarasimhan, S. P. Anthony, D. Moon and V. Madhu, Reversible Thermochromism of Nickel(II) Complexes and Single-Crystal-to-Single-Crystal Transformation, *ACS Omega*, 2019, **4**, 13756–13761.
- 20 A. Mirzaei, J. H. Kim, H. W. Kim and S. S. Kim, Gasochromic WO₃ nanostructures for the detection of hydrogen gas: An overview, *Appl. Sci.*, , DOI:10.3390/app9091775.

- 21 V. Wittwer, M. Datz, J. Ell, A. Georg, W. Graf and G. Walze, Gasochromic windows, *Sol. Energy Mater. Sol. Cells*, 2004, **84**, 305–314.
- 22 C. W. Hu, Y. Yamada and K. Yoshimura, A new type of gasochromic material: conducting polymers with catalytic nanoparticles, *Chem. Commun.*, 2017, **53**, 3242–3245.
- 23 M. C. Rezende, A generalized reversal model for the solvatochromism of merocyanines, *J. Phys. Org. Chem.*, 2016, **29**, 460–467.
- 24 X. L. Guan, T. M. Jia, D. H. Zhang, Y. Zhang, H. C. Ma, D. D. Lu, S. J. Lai and Z. Q. Lei, A new solvatochromic linear π -conjugated dye based on phenylene-(poly)ethynylene as supersensitive low-level water detector in organic solvents, *Dye. Pigment.*, 2017, **136**, 873–880.
- 25 Z. Z. Lu, R. Zhang, Y. Z. Li, Z. J. Guo and H. G. Zheng, Solvatochromic behavior of a nanotubular metal-organic framework for sensing small molecules, *J. Am. Chem. Soc.*, 2011, **133**, 4172–4174.
- 26 T. He and J. N. Yao, Photochromism in transition-metal oxides, *Res. Chem. Intermed.*, 2004, **30**, 459–488.
- 27 U. Joost, A. Šutka, M. Oja, K. Smits, N. Döbelin, A. Loot, M. Järvekülg, M. Hirsimäki, M. Valden and E. Nömmiste, Reversible Photodoping of TiO₂ Nanoparticles for Photochromic Applications, *Chem. Mater.*, 2018, **30**, 8968–8974.
- 28 Y. Badour, V. Jubera, I. Andron, C. Frayret and M. Gaudon, Photochromism in inorganic crystallised compounds, *Opt. Mater. X*, 2021, **12**, 100110.
- 29 H. Nakai and K. Isobe, Photochromism of organometallic compounds with structural rearrangement, *Coord. Chem. Rev.*, 2010, **254**, 2652–2662.
- 30 Y. Kobayashi, Y. Mishima, K. Mutoh and J. Abe, Highly durable photochromic radical complexes having no steric protections of radicals, *Chem. Commun.*, 2017, **53**, 4315–4318.
- 31 Y. Oka and N. Tamaoki, Structure of silver(I) complex prepared from azobenzonaphthalenophane, photochemical coordination change of silver(I) and silver(i)-induced acceleration of Z-E thermal isomerization of azobenzene unit, *Inorg. Chem.*, 2010, **49**, 4765–4767.
- 32 C. G. Granqvist, Electrochromic devices, *J. Eur. Ceram. Soc.*, 2005, **25**, 2907–2912.
- 33 C. M. Lampert, Chromogenic smart materials, *Mater. Today*, 2004, **7**, 28–35.
- 34 L. M. N. Assis, R. Leones, J. Kanicki, A. Pawlicka and M. M. Silva, Prussian blue for electrochromic devices, *J. Electroanal. Chem.*, 2016, **777**, 33–39.
- 35 M. Qiu, F. Zhou, P. Sun, X. Chen, C. Zhao and W. Mai, Unveiling the electrochromic mechanism of Prussian Blue by electronic transition analysis, *Nano Energy*, 2020, **78**, 105148.
- 36 K. C. Ho, Cycling and at-rest stabilities of a complementary electrochromic device based on tungsten oxide and Prussian blue thin films, *Electrochim. Acta*, 1999, **44**, 3227–3235.
- 37 O. C. Nwamba, E. Echeverria, D. N. McIlroy, J. M. Shreeve and D. E. Aston, Electrochemical stability and capacitance of in-situ synthesized Prussian blue on thermally-activated graphite, *SN Appl. Sci.*, 2019, **1**, 1–16.
- 38 D. R. Rosseinsky and P. M. S. Monk, Solid-state conductivities of CPQ. [1,1'-bis(p-cyanophenyl)-4,4'-bipyridilium] salts, redox-state mixtures and a new intervalence adduct, *J. Chem. Soc., Faraday Trans.*, 1994, **90**, 1127–1131.
- 39 K. W. Shah, S. X. Wang, D. X. Y. Soo and J. Xu, Viologen-based electrochromic materials: From small molecules, polymers and composites to their applications, *Polymers (Basel)*, , DOI:10.3390/polym11111839.
- 40 Y. Alesanco, A. Viñuales, J. Palenzuela, I. Odriozola, G. Cabañero, J. Rodriguez and R. Tena-Zaera, Multicolor Electrochromics: Rainbow-Like Devices, *ACS Appl. Mater. Interfaces*, 2016, **8**, 14795–14801.
- 41 F. Chen, Y. Ren, J. Guo and F. Yan, Thermo- and electro-dual responsive poly(ionic liquid) electrolyte based smart windows, *Chem. Commun.*, 2017, **53**, 1595–1598.

- 42 S. Y. Kao, H. C. Lu, C. W. Kung, H. W. Chen, T. H. Chang and K. C. Ho, Thermally Cured Dual Functional Viologen-Based All-in-One Electrochromic Devices with Panchromatic Modulation, *ACS Appl. Mater. Interfaces*, 2016, **8**, 4175–4184.
- 43 T. Jarosz, K. Gebka, A. Stolarczyk and W. Domagala, Transparent to black electrochromism-The ‘holy grail’ of organic optoelectronics, *Polymers (Basel)*, 2019, **11**, 1–18.
- 44 A. L. Dyer, E. J. Thompson and J. R. Reynolds, Completing the color palette with spray-processable polymer electrochromics, *ACS Appl. Mater. Interfaces*, 2011, **3**, 1787–1795.
- 45 K. Perera, Z. Yi, L. You, Z. Ke and J. Mei, Conjugated electrochromic polymers with amide-containing side chains enabling aqueous electrolyte compatibility, *Polym. Chem.*, 2020, **11**, 508–516.
- 46 J. Tarver, J. E. Yoo and Y.-L. Loo, Comprehensive Nanoscience and Technology, *Compr. Nanosci. Technol.*, 2011, 413–446.
- 47 C. G. Granqvist, *Handbook of Inorganic electrochromic materials*, Elsevier, Amsterdam, 1995.
- 48 Y. Wang, E. L. Runnerstrom and D. J. Milliron, Switchable Materials for Smart Windows, *Annu. Rev. Chem. Biomol. Eng.*, 2016, **7**, 283–304.
- 49 C. G. Granqvist, Oxide electrochromics: An introduction to devices and materials, *Sol. Energy Mater. Sol. Cells*, 2012, **99**, 1–13.
- 50 R. R. Kharade, K. R. Patil, P. S. Patil and P. N. Bhosale, Novel microwave assisted sol-gel synthesis (MW-SGS) and electrochromic performance of petal like h-WO₃ thin films, *Mater. Res. Bull.*, 2012, **47**, 1787–1793.
- 51 A. Karupphasamy, Electrochromism in surface modified crystalline WO₃ thin films grown by reactive DC magnetron sputtering, *Appl. Surf. Sci.*, 2013, **282**, 77–83.
- 52 C. G. Granqvist, A. Azens, A. Hjelm, L. Kullman, G. A. Niklasson, D. Rönnow, M. Strømme Mattsson, M. Veszeli and G. Vaivars, Recent advances in electrochromics for smart windows applications, *Sol. Energy*, 1998, **63**, 199–216.
- 53 P. G. Dickens and M. S. Whittingham, The tungsten bronzes and related compounds, *Q. Rev. Chem. Soc.*, 1968, **22**, 30–44.
- 54 S. Heo, J. Kim, G. K. Ong and D. J. Milliron, Template-Free Mesoporous Electrochromic Films on Flexible Substrates from Tungsten Oxide Nanorods, *Nano Lett.*, 2017, **17**, 5756–5761.
- 55 F. Lin, J. Cheng, C. Engrakul, A. C. Dillon, D. Nordlund, R. G. Moore, T. C. Weng, S. K. R. Williams and R. M. Richards, In situ crystallization of high performing WO₃-based electrochromic materials and the importance for durability and switching kinetics, *J. Mater. Chem.*, 2012, **22**, 16817–16823.
- 56 B. W. Faughnan and R. S. Crandall, Optical properties of mixed-oxide WO₃/MoO₃ electrochromic films, *Appl. Phys. Lett.*, 1977, **31**, 834–836.
- 57 F. S. Manciu, Y. Yun, W. G. Durrer, J. Howard, U. Schmidt and C. V. Ramana, Comparative microscopic and spectroscopic analysis of temperature-dependent growth of WO₃ and W_{0.95}Ti_{0.05}O₃ thin films, *J. Mater. Sci.*, 2012, **47**, 6593–6600.
- 58 H. MATSUOKA, S. HASHIMOTO and H. KAGECHIKA, Lifetime of electrochromism of amorphous WO₃-TiO₂ thin films., *J. Surf. Finish. Soc. Japan*, 1991, **42**, 246–252.
- 59 S. Hashimoto and H. Matsuoka, Prolonged Lifetime of Electrochromism, *Surf. Interface Anal.*, 1992, **19**, 464–468.
- 60 T. Guillemot, N. Schneider, N. Loones, F. Javier Ramos and J. Rousset, Electrochromic nickel oxide thin films by a simple solution process: Influence of post-treatments on growth and properties, *Thin Solid Films*, 2018, **661**, 143–149.
- 61 P. W. Chen, C. Te Chang, T. F. Ko, S. C. Hsu, K. D. Li and J. Y. Wu, Fast response of complementary electrochromic device based on WO₃/NiO electrodes, *Sci. Rep.*, 2020, **10**, 1–12.
- 62 Q. Liu, Q. Chen, Q. Zhang, Y. Xiao, X. Zhong, G. Dong, M. P. Delplancke-Ogletree, H. Terryn, K. Baert, F. Reniers and X. Diao, In situ electrochromic efficiency of a nickel

- oxide thin film: Origin of electrochemical process and electrochromic degradation, *J. Mater. Chem. C*, 2018, **6**, 646–653.
- 63 F. Lin, D. Nordlund, T. C. Weng, R. G. Moore, D. T. Gillaspie, A. C. Dillon, R. M. Richards and C. Engtrakul, Hole doping in Al-containing nickel oxide materials to improve electrochromic performance, *ACS Appl. Mater. Interfaces*, 2013, **5**, 301–309.
- 64 H. Peng, X. Sun, W. Weng and X. Fang, Flexible Electronic Devices Based on Polymers, *Polym. Mater. Energy Electron. Appl.*, 2017, 325–354.
- 65 P. Chandrasekhar, B. J. Zay, C. Cai, Y. Chai and D. Lawrence, Matched-dual-polymer electrochromic lenses, using new cathodically coloring conducting polymers, with exceptional performance and incorporated into automated sunglasses, *J. Appl. Polym. Sci.*, 2014, **131**, 1–21.
- 66 S. A. Kahani and F. Abdevali, Mechanochemical synthesis and characterization of a nickel(II) complex as a reversible thermochromic nanostructure, *RSC Adv.*, 2016, **6**, 5116–5122.
- 67 RCS, Vanadium, <https://www.rsc.org/periodic-table/element/23/vanadium>, (accessed 27 March 2022).
- 68 M. Arnesano, G. Pandarese, M. Martarelli, F. Naspì, K. L. Gurunatha, C. Sol, M. Portnoi, F. V. Ramirez, I. P. Parkin, I. Papakonstantinou and G. M. Revel, Optimization of the thermochromic glazing design for curtain wall buildings based on experimental measurements and dynamic simulation, *Sol. Energy*, 2021, **216**, 14–25.
- 69 Y. Wang, E. L. Runnerstrom and D. J. Milliron, Switchable Materials for Smart Windows, *Annu. Rev. Chem. Biomol. Eng.*, 2016, **7**, 283–304.
- 70 M. Salamati, P. Mathur, G. Kamyabjou and K. Taghizade, Daylight performance analysis of TiO₂@W-VO₂ thermochromic smart glazing in office buildings, *Build. Environ.*, 2020, **186**, 107351.
- 71 Y. Cui, Y. Ke, C. Liu, Z. Chen, N. Wang, L. Zhang, Y. Zhou, S. Wang, Y. Gao and Y. Long, Thermochromic VO₂ for Energy-Efficient Smart Windows, *Joule*, 2018, **2**, 1707–1746.
- 72 A. Seeboth and D. Löttsch, *Thermochromic and Thermotropic Materials*, CRC Press, 2013.
- 73 U. El-Ayaan, F. Murata and Y. Fukuda, Thermochromism and solvatochromism in solution, *Monatshfte fur Chemie*, 2001, **132**, 1279–1294.
- 74 H.-L. (Cindy) Kao, M. Mohan, C. Schmandt, J. A. Paradiso and K. Vega, in *Proceedings of the 2016 CHI Conference Extended Abstracts on Human Factors in Computing Systems*, ACM, New York, NY, USA, 2016, vol. 07-12-May-, pp. 3703–3706.
- 75 S. Wang, T. Jiang, Y. Meng, R. Yang, G. Tan and Y. Long, Scalable thermochromic smart windows with passive radiative cooling regulation, *Science (80-.)*, 2021, **374**, 1501–1504.
- 76 W. L. Jang, Y. M. Lu, Y. R. Lu, C. L. Chen, C. L. Dong, W. C. Chou, J. L. Chen, T. S. Chan, J. F. Lee, C. W. Pao and W. S. Hwang, Effects of oxygen partial pressure on structural and gasochromic properties of sputtered VO_x thin films, *Thin Solid Films*, 2013, **544**, 448–451.
- 77 G. Shim, S. Y. Lee, S. S. Kalanur and H. Seo, Eye-readable gasochromic and electrical detectability of hydrogenated Pd-TiO₂ to gaseous fluorine species, *Appl. Surf. Sci.*, 2018, **462**, 791–798.
- 78 M. A. Hosseini and M. Ranjbar, Plasmonic Au-MoO₃ Colloidal Nanoparticles by Reduction of HAuCl₄ by Blue MoO_x Nanosheets and Observation of the Gasochromic Property, *Plasmonics*, 2018, **13**, 1897–1906.
- 79 C. C. Chang, J. Y. Luo, T. K. Chen, K. W. Yeh, T. W. Huang, C. H. Hsu, W. H. Chao, C. T. Ke, P. C. Hsu, M. J. Wang and M. K. Wu, Pulsed laser deposition of (MoO₃)_{1-x}(V₂O₅)_x thin films: Preparation, characterization and gasochromic studies, *Thin Solid Films*, 2010, **519**, 1552–1557.
- 80 M. Imani, A. I. zad and A. Tadjarodi, H₂S gasochromic effect of mixed ammonium salts

- of phosphomolybdate nanoparticles synthesized by microwave assisted technique, *Sensors Actuators, B Chem.*, 2016, **237**, 715–723.
- 81 J. Domaradzki, D. Kaczmarek, D. Wojcieszak and M. Mazur, Investigations of reversible optical transmission in gasochromic (Ti-V-Ta)_x thin film for gas sensing applications, *Sensors Actuators, B Chem.*, 2014, **201**, 420–425.
- 82 S. S. Fomanyuk, G. Y. Kolbasov, V. Y. Chernii and I. N. Tretyakova, Gasochromic A,B–Ni(OH)₂ films for the determination of CO and chlorine content, *Sensors Actuators, B Chem.*, 2017, **244**, 717–726.
- 83 B. Orel, U. Opara Krašovec, N. Grošelj, M. Kosec, G. Dražič and R. Reisfeld, Gasochromic behavior of sol-gel derived Pd doped peroxopolytungstic acid (W-PTA) nano-composite films, *J. Sol-Gel Sci. Technol.*, 1999, **14**, 291–308.
- 84 T. Hakoda, H. Igarashi, Y. Isozumi, S. Yamamoto, H. Aritani and M. Yoshikawa, Gasochromic property of dehydrogenation-catalyst loaded tungsten trioxide, *J. Phys. Chem. Solids*, 2013, **74**, 200–204.
- 85 C. Peter, K. Schmitt, M. Apitz and J. Woellenstein, Metallo-porphyrin zinc as gas sensitive material for colorimetric gas sensors on planar optical waveguides, *Microsyst. Technol.*, 2012, **18**, 925–930.
- 86 Z. Wang, X. Yuan, S. Cong, Z. Chen, Q. Li, F. Geng and Z. Zhao, Color-Changing Microfiber-Based Multifunctional Window Screen for Capture and Visualized Monitoring of NH₃, *ACS Appl. Mater. Interfaces*, 2018, **10**, 15065–15072.
- 87 J. E. Benson, H. W. Kohn and M. Boudart, On the Reduction of Tungsten Trioxide Accelerated by Platinum and Water, *J. Catal.*, 1966, **5**, 307–313.
- 88 H. Shen, H. Li, Z. Yang and C. Li, Magic of hydrogen spillover: Understanding and application, *Green Energy Environ.*, DOI:10.1016/j.gee.2022.01.013.
- 89 C. W. Hu, Y. Yamada, K. Yoshimura, A. Takahashi, H. Watanabe, K. Tajima and T. Kawamoto, High contrast gasochromism of wet processable thin film with chromic and catalytic nanoparticles, *J. Mater. Chem. C*, 2018, **6**, 4760–4764.
- 90 W. Feng, L. Zou, G. Gao, G. Wu, J. Shen and W. Li, Gasochromic smart window: Optical and thermal properties, energy simulation and feasibility analysis, *Sol. Energy Mater. Sol. Cells*, 2016, **144**, 316–323.
- 91 J. Domaradzki, K. Baniewicz, M. Mazur, D. Wojcieszak and D. Kaczmarek, Characterization and properties of multicomponent oxide thin films with gasochromic effect, 2013, **8902**, 890223.
- 92 Y. A. Lee, S. S. Kalanur, G. Shim, J. Park and H. Seo, Highly sensitive gasochromic H₂ sensing by nano-columnar WO₃-Pd films with surface moisture, *Sensors Actuators, B Chem.*, 2017, **238**, 111–119.
- 93 K. Dimroth, C. Reichardt, T. Siepmann and F. Bohlmann, Über Pyridinium-N-phenolbetaine und ihre Verwendung zur Charakterisierung der Polarität von Lösungsmitteln, *Justus Liebigs Ann. Chem.*, 1963, **661**, 1–37.
- 94 F. Effenberger and F. Würthner, 5-Dimethylamino-5'-nitro-2, 2'-bithiophene—a New Dye with Pronounced Positive Solvatochromism, *Angew. Chemie Int. Ed. English*, 1993, **32**, 719–721.
- 95 C. Reichardt, Solvatochromic dyes as solvent polarity indicators, *Chem. Rev.*, 1994, **94**, 2319–2358.
- 96 R. Letrun and M. Koch, Ultrafast Excited-State Dynamics of Donor–Acceptor Biaryls: Comparison between Pyridinium and Pirylium Phenolates, *J. ...*, 2013, **117**, 13112–13126.
- 97 C. E. A. de Melo, C. R. Nicoleti, L. G. Nandi, F. S. S. Schneider, R. da S. Oliboni, G. F. Caramori and V. G. Machado, Solvatochromism of new substituted 4-[(E)-(4-nitrophenyl)diazenyl]phenolate dyes, *J. Mol. Liq.*, 2020, **301**, 112330.
- 98 G. Bourhill, J.-L. Bredas, L. Cheng, S. R. Marder, F. Meyers, J. W. Perry and B. G. Tiemann, Experimental Demonstration of the Dependence of the First Hyperpolarizability of Donor-Acceptor-Substituted Polyenes on the Ground-State

- Polarization and Bond Length Alternation, *J. Am. Chem. Soc.*, 1994, **116**, 2619–2620.
- 99 L. W. Lee, H. Y. Chi, Y. C. Kao, T. H. Hung, D. S. Chiou, G. H. Lee, S. M. Peng, D. Y. Kang, C. M. Wang and K. L. Lu, Zinc(II)–Organic Framework Films with Thermochromic and Solvatochromic Applications, *Chem. - A Eur. J.*, 2020, **26**, 4204–4208.
- 100 A. Pramanik, S. Biswas and P. Kumbhakar, *Solvatochromism in highly luminescent environmental friendly carbon quantum dots for sensing applications: Conversion of bio-waste into bio-asset*, Elsevier B.V, 2018, vol. 191.
- 101 L. Ascherl, E. W. Evans, M. Hennemann, D. Di Nuzzo, A. G. Hufnagel, M. Beetz, R. H. Friend, T. Clark, T. Bein and F. Auras, Solvatochromic covalent organic frameworks, *Nat. Commun.*, 2018, **9**, 1–8.
- 102 Y. M. Zhang, X. Wang, W. Zhang, W. Li, X. Fang, B. Yang, M. Li and S. X. A. Zhang, A single-molecule multicolor electrochromic device generated through medium engineering, *Light Sci. Appl.*, DOI:10.1038/lsa.2015.22.
- 103 J. Zhai, X. Xie and E. Bakker, Solvatochromic Dyes as pH-Independent Indicators for Ionophore Nanosphere-Based Complexometric Titrations, *Anal. Chem.*, 2015, **87**, 12318–12323.
- 104 H. Ramlow, K. L. Andrade and A. P. S. Immich, Smart textiles: an overview of recent progress on chromic textiles, *J. Text. Inst.*, 2021, **112**, 152–171.
- 105 M. Trigo-López, A. Muñoz, A. Mendía, S. Ibeas, F. Serna, F. C. García and J. M. García, Palladium-containing polymers as hybrid sensory materials (water-soluble polymers, films and smart textiles) for the colorimetric detection of cyanide in aqueous and gas phases, *Sensors Actuators, B Chem.*, 2018, **255**, 2750–2755.
- 106 R. Pardo, M. Zayat and D. Levy, Photochromic organic-inorganic hybrid materials, *Chem. Soc. Rev.*, 2011, **40**, 672–687.
- 107 J. Han and J. Ben Meng, Progress in synthesis, photochromism and photomagnetism of biindenylidenedione derivatives, *J. Photochem. Photobiol. C Photochem. Rev.*, 2009, **10**, 141–147.
- 108 Y. Yokoyama and M. Kose, Reversible control of properties of materials by thermally irreversible photochromism, *J. Photochem. Photobiol. A Chem.*, 2004, **166**, 9–18.
- 109 M. Morimoto, S. Kobatake and M. Irie, Polymorphism of 1,2-bis(2-methyl-5-p-methoxyphenyl-3-thienyl)perfluorocyclopentene and photochromic reactivity of the single crystals, *Chem. - A Eur. J.*, 2003, **9**, 621–627.
- 110 K. Amimoto and T. Kawato, Photochromism of organic compounds in the crystal state, *J. Photochem. Photobiol. C Photochem. Rev.*, 2005, **6**, 207–226.
- 111 E. Hadjoudis, T. Dziembowska and Z. Rozwadowski, Photoactivation of the thermochromic solid di-anil of 2-hydroxy-5-methyl-isophthalaldehyde in β -cyclodextrin, *J. Photochem. Photobiol. A Chem.*, 1999, **128**, 97–99.
- 112 H. J. Hoffmann, *The Use of Silver Salts for Photochromic Glasses*, Elsevier B.V., Revised Ed., 2003.
- 113 J. Li, J. Liu and W. Lu, Photochromism and hydrochromism of three complexes based on a new viologen 1-(4-carboxybutyl)-4,4'-bipyridinium ligand, *Inorganica Chim. Acta*, 2020, **512**, 119921.
- 114 A. Mukhopadhyay and J. N. Moorthy, Phenomenon to functions: Photochromism of diarylpyrans, spectrokinetic properties and functional materials, *J. Photochem. Photobiol. C Photochem. Rev.*, 2016, **29**, 73–106.
- 115 M. Biancardo, R. Argazzi and C. A. Bignozzi, A Solid State Photochromic Device Based on Nanocrystalline TiO₂ Functionalized with Electron Donor-Acceptor Species, *Inorg. Chem.*, 2005, **44**, 9619–9621.
- 116 H. Miyazaki, T. Matsuura and T. Ota, Nickel oxide-based photochromic composite films, 2016, 1175–1177.
- 117 Y. A. Yang, Y. Ma, J. N. Yao and B. H. Loo, Simulation of the sublimation process in the preparation of photochromic WO₃ film by laser microprobe mass spectrometry, *J.*

- Non. Cryst. Solids*, 2000, **272**, 71–74.
- 118 N. Xu, M. Sun, Y. W. Cao, J. N. Yao and E. G. Wang, Influence of pH on structure and photochromic behavior of nanocrystalline WO₃ films, *Appl. Surf. Sci.*, 2000, **157**, 81–84.
- 119 H. Ikake, W. Hashimoto, T. Obara, K. Kurita and S. Yano, Photochromic Properties and Microstructures of Poly (tetramethylene oxide)/Tungsten Trioxide Hybrid Materials, *Kobunshi Ronbunshu*, 2000, **57**, 376–382.
- 120 S. Li, I. N. Germanenko and M. S. El-Shall, Nanoparticles from the Vapor Phase: Synthesis and Characterization of Si, Ge, MoO₃, and WO₃ Nanocrystals, *J. Clust. Sci.*, 1999, **10**, 533–547.
- 121 L. Su, Q. Dai and Z. Lu, Spectroelectrochemical and photoelectrochemical studies of electrodeposited tungsten trioxide films, *Spectrochim. Acta - Part A Mol. Biomol. Spectrosc.*, 1999, **55**, 2179–2185.
- 122 B. H. Loo, J. N. Yao, C. H. D., K. Hashimoto and A. Fujishima, A Raman microprobe study of the electrochromic and photochromic thin films of molybdenum trioxide and tungsten trioxide, *Appl. Surf. Sci.*, 1994, 175–181.
- 123 S. K. Deb, Optical and photoelectric properties and colour centres in thin films of tungsten oxide, *Philos. Mag.*, 1973, **27**, 801–822.
- 124 K. Ajito, L. A. Nagahara, D. A. Tryk, K. Hashimoto and A. Fujishima, Study of the photochromic properties of amorphous MoO₃ films using raman microscopy, *J. Phys. Chem.*, 1995, **99**, 16383–16388.
- 125 J. N. Yao, Y. A. Yang and B. H. Loo, Enhancement of photochromism and electrochromism in MoO₃/Au and MoO₃/Pt thin films, *J. Phys. Chem. B*, 1998, **102**, 1856–1860.
- 126 N. Li, Y. Li, Y. Zhou, W. Li, S. Ji, H. Yao, X. Cao and P. Jin, Interfacial-charge-transfer-induced photochromism of MoO₃@TiO₂ crystalline-core amorphous-shell nanorods, *Sol. Energy Mater. Sol. Cells*, 2017, **160**, 116–125.
- 127 H. Miyazaki, T. Matsuura and T. Ota, Vanadium oxide-based photochromic composite film, *RSC Adv.*, 2017, **7**, 2388–2391.
- 128 L. Pan, Y. Wang, X. J. Wang, H. Y. Qu, J. P. Zhao, Y. Li and A. Gavriluk, Hydrogen photochromism in Nb₂O₅ powders, *Phys. Chem. Chem. Phys.*, 2014, **16**, 20828–20833.
- 129 D. K. Diop, L. Simonot, J. Martínez-García, M. Hébert, Y. Lefkir, G. Abadias, P. Guérin, D. Babonneau and N. Destouches, Spectral and Color Changes of Ag/TiO₂ Photochromic Films Deposited on Diffusing Paper and Transparent Flexible Plastic Substrates, *Appl. Spectrosc.*, 2017, **71**, 1271–1279.
- 130 C. Alcober, F. Alvarez, S. A. Bilmes and R. J. Candal, Photochromic W-TiO₂ membranes, *J. Mater. Sci. Lett.*, 2002, **21**, 501–504.
- 131 S. Prabhu, L. Cindrella, O. J. Kwon and K. Mohanraju, Photoelectrochemical, photocatalytic and photochromic performance of rGO-TiO₂-WO₃ composites, *Mater. Chem. Phys.*, 2019, **224**, 217–228.
- 132 C. Renz, Lichtreaktionen der Oxyde des Titans, Cers und der Erdsäuren, *Helv. Chim. Acta*, 1921, **4**, 961–968.
- 133 S. Wang, S. V. Kershaw, G. Li and M. K. H. Leung, The self-assembly synthesis of tungsten oxide quantum dots with enhanced optical properties, *J. Mater. Chem. C*, 2015, **3**, 3280–3285.
- 134 Nickel, <https://www.cdc.gov/niosh/topics/nickel/default.html>, (accessed 28 December 2021).
- 135 X. Lu, G. Wang, S. Xie, J. Shi, W. Li, Y. Tong and Y. Li, Efficient photocatalytic hydrogen evolution over hydrogenated ZnO nanorod arrays, *Chem. Commun.*, 2012, **48**, 7717–7719.
- 136 H. Fu, T. Xu, S. Zhu and Y. Zhu, Photocorrosion Inhibition and Enhancement of Photocatalytic Activity for ZnO via Hybridization with C 60, *Environ. Sci. Technol.*, 2008, **42**, 8064–8069.

- 137 M. Ali and M. Winterer, ZnO nanocrystals: Surprisingly ‘alive’, *Chem. Mater.*, 2010, **22**, 85–91.
- 138 I. Andron, L. Marichez, V. Jubera, C. Labrugère, M. Duttine, C. Frayret and M. Gaudon, Photochromic Behavior of ZnO/MoO₃ Interfaces, *ACS Appl. Mater. Interfaces*, 2020, **12**, 46972–46980.
- 139 O. F. Schirmer, V. Wittwer, G. Baur and G. Brandt, Dependence of WO₃ Electrochromic Absorption on Crystallinity, *J. Electrochem. Soc.*, 1977, **124**, 749–753.
- 140 S. Wang, W. Fan, Z. Liu, A. Yu and X. Jiang, Advances on tungsten oxide based photochromic materials: Strategies to improve their photochromic properties, *J. Mater. Chem. C*, 2018, **6**, 191–212.
- 141 Y. A. Yang, Y. W. Cao, P. Chen, B. H. Loo and J. N. Yao, Visible-light photochromism in electrolytically pretreated WO₃ thin films, *J. Phys. Chem. Solids*, 1998, **59**, 1667–1670.
- 142 J. N. Yao, K. Hashimoto and A. Fujishima, Photochromism induced in an electrolytically pretreated MoO₃ thin film by visible light, *Nature*, 1992, **355**, 624–626.
- 143 X. Dong, Y. Wei, J. Gao, X. Liu, L. Zhang, Y. Tong and Y. Lu, Efficient charge transfer over Cu-doped hexagonal WO₃ nanocomposites for rapid photochromic response, *J. Photochem. Photobiol. A Chem.*, 2021, **425**, 113716.
- 144 A. Zukuls, R. Eglitis, T. Kaāmbre, R. Ignatans, K. Šmits, K. Rubenis, D. Začs and A. Šutka, Permanent photodoping of plasmonic gallium-ZnO nanocrystals, *Nanoscale*, 2020, **12**, 6624–6629.
- 145 J. J. Carey and K. P. McKenna, Screening Doping Strategies to Mitigate Electron Trapping at Anatase TiO₂ Surfaces, *J. Phys. Chem. C*, 2019, **123**, 22358–22367.
- 146 U. Joost, A. Šutka, M. Oja, K. Smits, N. Döbelin, A. Loot, M. Järvekülg, M. Hirsimäki, M. Valden and E. Nömmiste, Reversible Photodoping of TiO₂ Nanoparticles for Photochromic Applications, *Chem. Mater.*, 2018, **30**, 8968–8974.
- 147 C. Z. Wen, H. B. Jiang, S. Z. Qiao, H. G. Yang and G. Q. (Max) Lu, Synthesis of high-reactive facets dominated anatase TiO₂, *J. Mater. Chem.*, 2011, **21**, 7052.
- 148 H. Zhang, R. Shi, A. Xie, J. Li, L. Chen, P. Chen, S. Li, F. Huang and Y. Shen, Novel TiO₂/PEGDA hybrid hydrogel prepared in situ on tumor cells for effective photodynamic therapy, *ACS Appl. Mater. Interfaces*, 2013, **5**, 12317–12322.
- 149 C. Di Valentini and D. Fittipaldi, Hole scavenging by organic adsorbates on the TiO₂ surface: A DFT model study, *J. Phys. Chem. Lett.*, 2013, **4**, 1901–1906.
- 150 N. Serpone, D. Lawless, R. Khairutdinov and E. Pelizzetti, Subnanosecond Relaxation Dynamics in TiO₂ Colloidal Sols, *J. Phys. Chem.*, 1995, **99**, 16655–16661.
- 151 T. Tachikawa, Y. Takai, S. Tojo, M. Fujitsuka and T. Majima, Probing the surface adsorption and photocatalytic degradation of catechols on TiO₂ by solid-state NMR spectroscopy, *Langmuir*, 2006, **22**, 893–896.
- 152 I. Nakamura, N. Negishi, S. Kutsuna, T. Ihara, S. Sugihara and K. Takeuchi, Role of oxygen vacancy in the plasma-treated TiO₂ photocatalyst with visible light activity for NO removal, *J. Mol. Catal. A Chem.*, 2000, **161**, 205–212.
- 153 N. Serpone, D. Lawless and R. Khairutdinov, Size effects on the photophysical properties of colloidal anatase TiO₂ particles: Size quantization or direct transitions in this indirect semiconductor?, *J. Phys. Chem.*, 1995, **99**, 16646–16654.
- 154 G. Liu, F. Li, D.-W. Wang, D.-M. Tang, C. Liu, X. Ma, G. Q. Lu and H.-M. Cheng, Electron field emission of a nitrogen-doped TiO₂ nanotube array, *Nanotechnology*, 2008, **19**, 025606.
- 155 L. De Trizio, R. Buonsanti, A. M. Schimpf, A. Llordes, D. R. Gamelin, R. Simonutti and D. J. Milliron, Nb-Doped Colloidal TiO₂ Nanocrystals with Tunable Infrared Absorption, *Chem. Mater.*, 2013, **25**, 3383–3390.
- 156 D. A. Panayotov, S. P. Burrows and J. R. Morris, Infrared Spectroscopic Studies of Conduction Band and Trapped Electrons in UV-Photoexcited, H-Atom n-Doped, and Thermally Reduced TiO₂, *J. Phys. Chem. C*, 2012, **116**, 4535–4544.

- 157 E. Burstein, Anomalous Optical Absorption Limit in InSb, *Phys. Rev.*, 1954, **93**, 632–633.
- 158 S. Gahlawat, J. Singh, A. K. Yadav and P. P. Ingole, Exploring Burstein-Moss type effects in nickel doped hematite dendrite nanostructures for enhanced photoelectrochemical water splitting, *Phys. Chem. Chem. Phys.*, 2019, **21**, 20463–20477.
- 159 P.-A. Blanche, in *Optical Holography-Materials, Theory and Applications*, Elsevier Inc., 2020, pp. 41–60.
- 160 V. A. Barachevsky, Negative photochromism in organic systems, *Rev. J. Chem.*, 2017, **7**, 334–371.
- 161 Z. Gao, L. Liu, Z. Tian, Z. Feng, B. Jiang and W. Wang, Fast-Response Flexible Photochromic Gels for Self-Erasing Rewritable Media and Colorimetric Oxygen Indicator Applications, *ACS Appl. Mater. Interfaces*, DOI:10.1016/j.jbiomech.2005.02.020.
- 162 M. Irie, *Diarylethenes for Memories and Switches*, 2000, vol. 100.
- 163 W. Jeong, M. I. Khazi, D. H. Park, Y. S. Jung and J. M. Kim, Full Color Light Responsive Diarylethene Inks for Reusable Paper, *Adv. Funct. Mater.*, 2016, **26**, 5230–5238.
- 164 P. Nyamukamba, O. Okoh, H. Mungondori, R. Taziwa and S. Zinya, in *Titanium Dioxide - Material for a Sustainable Environment*, InTech, 2018.
- 165 T. Hachisu, K. Shi, T. Yokoshima, A. Sugiyama, S. Kuroiwa, T. Osaka, N. Nakajima and M. Yoshino, Preparation of anatase phase titanium dioxide film by non-aqueous electrodeposition, *Electrochem. commun.*, 2016, **65**, 5–8.
- 166 T. Cottineau, L. Brohan, M. Pregelj, P. Cevc, M. Richard-Plouet and D. Arçon, Evidence of interfacial charge transfer upon UV-light irradiation in novel titanium oxide gel, *Adv. Funct. Mater.*, 2008, **18**, 2602–2610.
- 167 P. Szymanski and M. A. El-Sayed, Some recent developments in photoelectrochemical water splitting using nanostructured TiO₂: a short review, *Theor. Chem. Acc.*, 2012, **131**, 1202.
- 168 H. Dürr, in *Photochromism*, Elsevier, 2003, pp. 1–14.
- 169 J. G. Li and T. Ishigaki, Brookite → rutile phase transformation of tio₂ studied with monodispersed particles, *Acta Mater.*, 2004, **52**, 5143–5150.
- 170 D. A. H. Hanaor and C. C. Sorrell, Review of the anatase to rutile phase transformation, *J. Mater. Sci.*, 2011, **46**, 855–874.
- 171 G. Odling and N. Robertson, Why is anatase a better photocatalyst than rutile? the importance of free hydroxyl radicals, *ChemSusChem*, 2015, **8**, 1838–1840.
- 172 D. Reyes-Coronado, G. Rodríguez-Gattorno, M. E. Espinosa-Pesqueira, C. Cab, R. de Coss and G. Oskam, Phase-pure TiO₂ nanoparticles: anatase, brookite and rutile., *Nanotechnology*, 2008, **19**, 145605.
- 173 T. A. Kandiell, L. Robben, A. Alkaim and D. Bahnemann, Brookite versus anatase TiO₂ photocatalysts: Phase transformations and photocatalytic activities, *Photochem. Photobiol. Sci.*, 2013, **12**, 602–609.
- 174 V. Aravindan, Y. S. Lee, R. Yazami and S. Madhavi, TiO₂ polymorphs in ‘rocking-chair’ Li-ion batteries, *Mater. Today*, 2015, **18**, 345–351.
- 175 R. S. Dubey, S. R. Jadar and A. B. Bhorde, Synthesis and Characterization of Various Doped TiO₂ Nanocrystals for Dye-Sensitized Solar Cells, *ACS Omega*, 2021, **6**, 3470–3482.
- 176 J. Li and D. Xu, Tetragonal faceted-nanorods of anatase TiO₂ single crystals with a large percentage of active {100} facets, *Chem. Commun.*, 2010, **46**, 2301–2303.
- 177 F. Amano, T. Yasumoto, O. O. Prieto-Mahaney, S. Uchida, T. Shibayama and B. Ohtani, Photocatalytic activity of octahedral single-crystalline mesoparticles of anatase titanium(iv) oxide, *Chem. Commun.*, 2009, 2311–2313.
- 178 H. E. Prakasam, K. Shankar, M. Paulose, O. K. Varghese and C. A. Grimes, A new benchmark for TiO₂ nanotube array growth by anodization, *J. Phys. Chem. C*, 2007, **111**, 7235–7241.

- 179 J. Lu, P. Zhang, A. Li, F. Su, T. Wang, Y. Liu and J. Gong, Mesoporous anatase TiO₂ nanocaps with plasmonic metal decoration for highly active visible-light photocatalysis, *Chem. Commun.*, 2013, **49**, 5817–5819.
- 180 Y. Li, P. Zhang, D. Wan, C. Xue, J. Zhao and G. Shao, Direct evidence of 2D/1D heterojunction enhancement on photocatalytic activity through assembling MoS₂ nanosheets onto super-long TiO₂ nanofibers, *Appl. Surf. Sci.*, 2020, **504**, 144361.
- 181 J. I. L. Chen, G. Von Freymann, V. Kitaev and G. A. Ozin, Effect of disorder on the optically amplified photocatalytic efficiency of titania inverse opals, *J. Am. Chem. Soc.*, 2007, **129**, 1196–1202.
- 182 Z. Sun, J. H. Kim, Y. Zhao, F. Bijarbooneh, V. Malgras, Y. Lee, Y. Kang and S. X. Dou, Rational Design of 3D Dendritic TiO₂ Nanostructures with Favorable Architectures, *J. Am. Chem. Soc.*, 2011, **133**, 19314–19317.
- 183 M. S. Waghmode, A. B. Gunjal, J. A. Mulla, N. N. Patil and N. N. Nawani, Studies on the titanium dioxide nanoparticles: biosynthesis, applications and remediation, *SN Appl. Sci.*, DOI:10.1007/s42452-019-0337-3.
- 184 S. H. Feng and G. H. Li, in *Modern Inorganic Synthetic Chemistry: Second Edition*, 2017, pp. 73–104.
- 185 A. H. Mamaghani, F. Haghghat and C. S. Lee, Hydrothermal/solvothermal synthesis and treatment of TiO₂ for photocatalytic degradation of air pollutants: Preparation, characterization, properties, and performance, *Chemosphere*, 2019, **219**, 804–825.
- 186 O. Malik, F. J. D. La Hidalga-Wade and R. R. Amador, in *Pyrolysis*, InTech, 2017.
- 187 S. C. Jung, S. J. Kim, N. Imaishi and Y. I. Cho, Effect of TiO₂ thin film thickness and specific surface area by low-pressure metal-organic chemical vapor deposition on photocatalytic activities, *Appl. Catal. B Environ.*, 2005, **55**, 253–257.
- 188 Q. Zhang, 1993.
- 189 J. D. Wright and N. A. J. M. Sommerdijk, *Sol-Gel Materials: Chemistry and Applications*, Taylor & Francis, 2003.
- 190 A. k. Bandyopadhyay, *Nano Materials*, New age International Publishers, New Dehli, 2008.
- 191 T. N. Ravishankar, M. D. O. Vaz and S. R. Teixeira, The effects of surfactant in the sol-gel synthesis of CuO/TiO₂ nanocomposites on its photocatalytic activities under UV-visible and visible light illuminations, *New J. Chem.*, 2020, **44**, 1888–1904.
- 192 D. Dastan and N. B. Chaure, Influence of Surfactants on TiO₂ Nanoparticles Grown by Sol-Gel Technique, *Int. J. Mater. Mech. Manuf.*, 2014, 21–24.
- 193 C. M. Sorensen and A. Chakrabarti, The sol to gel transition in irreversible particulate systems, *Soft Matter*, 2011, **7**, 2284–2296.
- 194 C. J. Brinker and G. W. Scherer, *Sol-Gel Science: The physics and chemistry of sol-gel processing*, Academic Press, INC., 1990.
- 195 P. Alphonse, A. Varghese and C. Tendero, Stable hydrosols for TiO₂ coatings, *J. Sol-Gel Sci. Technol.*, 2010, **56**, 250–263.
- 196 R. Eglitis and G. Mežinskis, *Photocatalytically active cotton fabrics produced with anatase synthesized using a low-temperature sol-gel process*, 2018, vol. 762.
- 197 Y. Hu and C. Yuan, Low-temperature preparation of photocatalytic TiO₂ thin films from anatase sols, *J. Cryst. Growth*, 2005, **274**, 563–568.
- 198 M. J. Uddin, F. Cesano, F. Bonino, S. Bordiga, G. Spoto, D. Scarano and a. Zecchina, Photoactive TiO₂ films on cellulose fibres: synthesis and characterization, *J. Photochem. Photobiol. A Chem.*, 2007, **189**, 286–294.
- 199 O. Galkina, Swedish University of Agricultural Sciences, 2015.
- 200 K. Shimizu, H. Imai, H. Hirashima and K. Tsukuma, Low-temperature synthesis of anatase thin films on glass and organic substrates by direct deposition from aqueous solutions, *Thin Solid Films*, 1999, **351**, 220–224.
- 201 P. Dulian, J. Zajic and W. Zukowski, Effect of titanium source and sol-gel TiO₂ thin film formation parameters on its morphology and photocatalytic activity, *Mater. Sci. Pol.*,

- 2021, **38**, 424–433.
- 202 P. Vivo, A. Ojanperä, J. H. Smått, S. Sandén, S. G. Hashmi, K. Kaunisto, P. Ihalainen, M. T. Masood, R. Österbacka, P. D. Lund and H. Lemmetyinen, Influence of TiO₂ compact layer precursor on the performance of perovskite solar cells, *Org. Electron.*, 2017, **41**, 287–293.
- 203 W. A. Daoud and J. H. Xin, Nucleation and Growth of Anatase Crystallites on Cotton Fabrics at Low Temperatures, *J. Am. Ceram. Soc.*, 2004, **87**, 953–955.
- 204 S. I. Mogal, M. Mishra, V. G. Gandhi and R. J. Tayade, Metal doped titanium dioxide: Synthesis and effect of metal ions on physico-chemical and photocatalytic properties, *Mater. Sci. Forum*, 2013, **734**, 364–378.
- 205 N. D. Mohd Said, M. Z. Sahdan, N. Nayan, H. Saim, F. Adriyanto, A. S. Bakri and M. Morsin, Difference in structural and chemical properties of sol-gel spin coated Al doped TiO₂, y doped TiO₂ and Gd doped TiO₂ based on trivalent dopants, *RSC Adv.*, 2018, **8**, 29686–29697.
- 206 L. Wang, Z. Yuan and T. A. Egerton, Comparison of nano-particulate TiO₂ prepared from titanium tetrachloride and titanium tetraisopropoxide, *Mater. Chem. Phys.*, 2012, **133**, 304–310.
- 207 C. Zhou, J. Ouyang and B. Yang, Retarded hydrolysis-condensing reactivity of tetrabutyl titanate by acetylacetone and the application in dye-sensitized solar cells, *Mater. Res. Bull.*, 2013, **48**, 4351–4356.
- 208 V. O. Kotsyubynsky, I. F. Myronyuk, L. I. Myronyuk, V. L. Chelyadyn, M. H. Mizilevska, A. B. Hrubciak, O. K. Tadeush and F. M. Nizamutdinov, The effect of pH on the nucleation of titania by hydrolysis of TiCl₄: Der Einfluss des pH-Werts auf die Keimbildung von Titandioxid bei der Hydrolyse von TiCl₄, *Materwiss. Werksttech.*, 2016, **47**, 288–294.
- 209 C. Leyva-Porras, A. Toxqui-Teran, O. Vega-Becerra, M. Miki-Yoshida, M. Rojas-Villalobos, M. García-Guaderrama and J. A. Aguilar-Martínez, Low-temperature synthesis and characterization of anatase TiO₂ nanoparticles by an acid assisted sol-gel method, *J. Alloys Compd.*, 2015, **647**, 627–636.
- 210 R. J. Tayade, R. G. Kulkarni and R. V. Jasra, Photocatalytic degradation of aqueous nitrobenzene by nanocrystalline TiO₂, *Ind. Eng. Chem. Res.*, 2006, **45**, 922–927.
- 211 S. Songara, M. K. Patra, M. Manoth, L. Saini, V. Gupta, G. S. Gowd, S. R. Vadera and N. Kumar, Synthesis and studies on photochromic properties of vanadium doped TiO₂ nanoparticles, *J. Photochem. Photobiol. A Chem.*, 2010, **209**, 68–73.
- 212 V. M. Ramakrishnan, M. Natarajan, A. Santhanam, V. Asokan and D. Velauthapillai, Size controlled synthesis of TiO₂ nanoparticles by modified solvothermal method towards effective photo catalytic and photovoltaic applications, *Mater. Res. Bull.*, 2018, **97**, 351–360.
- 213 L. Zhu, K. Liu, H. Li, Y. Sun and M. Qiu, Solvothermal synthesis of mesoporous TiO₂ microspheres and their excellent photocatalytic performance under simulated sunlight irradiation, *Solid State Sci.*, 2013, **20**, 8–14.
- 214 H. F. Mehnane, C. Wang, K. K. Kondamareddy, W. Yu, W. Sun, H. Liu, S. Bai, W. Liu, S. Guo and X. Z. Zhao, Hydrothermal synthesis of TiO₂ nanoparticles doped with trace amounts of strontium, and their application as working electrodes for dye sensitized solar cells: tunable electrical properties & enhanced photo-conversion performance, *RSC Adv.*, 2017, **7**, 2358–2364.
- 215 S. Shen, J. Chen, M. Wang, X. Sheng, X. Chen, X. Feng and S. S. Mao, Titanium dioxide nanostructures for photoelectrochemical applications, *Prog. Mater. Sci.*, 2018, **98**, 299–385.
- 216 N. Sethaya, P. Chindaprasirt and K. Pimraksa, Preparation of zeolite nanocrystals via hydrothermal and solvothermal synthesis using of rice husk ash and metakaolin, *Mater. Sci. Forum*, 2016, **872**, 242–247.
- 217 L. Ndlwana, N. Raleie, K. M. Dimpe, H. F. Ogutu, E. O. Oseghe, M. M. Motsa, T. A.

- M. Msagati and B. B. Mamba, Sustainable hydrothermal and solvothermal synthesis of advanced carbon materials in multidimensional applications: A review, *Materials (Basel)*, , DOI:10.3390/ma14175094.
- 218 W. R. W. Ahmad, M. H. Mamat, A. S. Zoolfakar, Z. Khusaimi and M. Rusop, A review on hematite α -Fe₂O₃ focusing on nanostructures, synthesis methods and applications, *Proc. - 14th IEEE Student Conf. Res. Dev. Adv. Technol. Humanit. SCORED 2016*, 2017, 1–7.
- 219 T. Aguilar, I. Carrillo-Berdugo, R. Gómez-Villarejo, J. J. Gallardo, P. Martínez-Merino, J. C. Piñero, R. Alcántara, C. Fernández-Lorenzo and J. Navas, A solvothermal synthesis of TiO₂ nanoparticles in a non-polar medium to prepare highly stable nanofluids with improved thermal properties, *Nanomaterials*, , DOI:10.3390/nano8100816.
- 220 N. Liu, X. Chen, J. Zhang and J. W. Schwank, A review on TiO₂-based nanotubes synthesized via hydrothermal method: Formation mechanism, structure modification, and photocatalytic applications, *Catal. Today*, 2014, **225**, 34–51.
- 221 J. Huang, H. Liu, Z. Li, J. Zhong, T. Wang, J. Li and M. Li, Photocatalytic activity of TiO₂ prepared by different solvents through a solvothermal approach, *Solid State Sci.*, 2019, **98**, 106024.
- 222 L. Cano-Casanova, A. Amorós-Pérez, M. Á. Lillo-Ródenas and M. del C. Román-Martínez, Effect of the preparation method (sol-gel or hydrothermal) and conditions on the TiO₂ properties and activity for propene oxidation, *Materials (Basel)*, , DOI:10.3390/ma11112227.
- 223 A. Kashyap, N. K. Singh, M. Soni and A. Soni, in *Chemical Solution Synthesis for Materials Design and Thin Film Device Applications*, Elsevier, 2021, pp. 79–117.
- 224 J. Yu, G. Wang, B. Cheng and M. Zhou, Effects of hydrothermal temperature and time on the photocatalytic activity and microstructures of bimodal mesoporous TiO₂ powders, *Appl. Catal. B Environ.*, 2007, **69**, 171–180.
- 225 R. Khan, S. Javed and M. Islam, Hierarchical Nanostructures of Titanium Dioxide: Synthesis and Applications, *Titan. Dioxide - Mater. a Sustain. Environ.*, 2018, 3–40.
- 226 A. H. Mamaghani, F. Haghighat and C. S. Lee, Systematic variation of preparation time, temperature, and pressure in hydrothermal synthesis of macro-/mesoporous TiO₂ for photocatalytic air treatment, *J. Photochem. Photobiol. A Chem.*, 2019, **378**, 156–170.
- 227 N. Rausch and E. P. Bulte, Thin TiO₂ Films Prepared by Low Pressure Chemical Vapor Deposition, *J. Electrochem. Soc.*, 1993, **140**, 145–149.
- 228 M. Malekshahi Byranvand, A. Nemati Kharat, L. Fatholahi and Z. Malekshahi Beiranvand, A Review on Synthesis of Nano-TiO₂ via Different Methods, *J. Nanostructures*, 2013, **3**, 1–9.
- 229 P. S. Shinde and C. H. Bhosale, Properties of chemical vapour deposited nanocrystalline TiO₂ thin films and their use in dye-sensitized solar cells, *J. Anal. Appl. Pyrolysis*, 2008, **82**, 83–88.
- 230 Q. Zhang and C. Li, Pure anatase phase titanium dioxide films prepared by mist chemical vapor deposition, *Nanomaterials*, , DOI:10.3390/nano8100827.
- 231 A. M. Alotaibi, S. Sathasivam, B. A. D. Williamson, A. Kafizas, C. Sotelo-Vazquez, A. Taylor, D. O. Scanlon and I. P. Parkin, Chemical Vapor Deposition of Photocatalytically Active Pure Brookite TiO₂ Thin Films, *Chem. Mater.*, 2018, **30**, 1353–1361.
- 232 A. Ito, T. Sato and T. Goto, Transparent anatase and rutile TiO₂ films grown by laser chemical vapor deposition, *Thin Solid Films*, 2014, **551**, 37–41.
- 233 M. Aghaee, J. Verheyen, A. A. E. Stevens, W. M. M. Kessels and M. Creatore, TiO₂ thin film patterns prepared by chemical vapor deposition and atomic layer deposition using an atmospheric pressure microplasma printer, *Plasma Process. Polym.*, 2019, **16**, 1–14.
- 234 A. Möllmann, D. Gedamu, P. Vivo, R. Frohnhoven, D. Stadler, T. Fischer, I. Ka, M. Steinhörst, R. Nechache, F. Rosei, S. G. Cloutier, T. Kirchartz and S. Mathur, Highly Compact TiO₂ Films by Spray Pyrolysis and Application in Perovskite Solar Cells, *Adv. Eng. Mater.*, 2019, **21**, 1–8.

- 235 I. Dundar, M. Krichevskaya, A. Katerski and I. O. Acik, TiO₂ thin films by ultrasonic spray pyrolysis as photocatalytic material for air purification, *R. Soc. Open Sci.*, , DOI:10.1098/rsos.181578.
- 236 S. M. N. Khatami, 2014.
- 237 C. Falcony, M. A. Aguilar-Frutis and M. García-Hipólito, Spray pyrolysis technique; High-K dielectric films and luminescent materials: A review, *Micromachines*, 2018, **9**, 1–33.
- 238 M. Okuya, N. A. Prokudina, K. Mushika and S. Kaneko, TiO₂ thin films synthesized by the spray pyrolysis deposition (SPD) technique, *J. Eur. Ceram. Soc.*, 1999, **19**, 903–906.
- 239 Z. Chen, I. Dünder, I. Oja Acik and A. Mere, TiO₂ thin films by ultrasonic spray pyrolysis, *IOP Conf. Ser. Mater. Sci. Eng.*, , DOI:10.1088/1757-899X/503/1/012006.
- 240 D. Chantarawong, K. Onlaor, T. Thiwawong and B. Tunhoo, TiO₂ Nanoparticles Thin Film Prepared by Electrostatic Spray Deposition Technique for Humidity-Sensing Device, *Adv. Mater. Res.*, 2015, **1131**, 153–156.
- 241 V. Likodimos, C. Han, M. Pelaez, A. G. Kontos, G. Liu, D. Zhu, S. Liao, A. A. de la Cruz, K. O’Shea, P. S. M. Dunlop, J. A. Byrne, D. D. Dionysiou and P. Falaras, Anion-Doped TiO₂ Nanocatalysts for Water Purification under Visible Light, *Ind. Eng. Chem. Res.*, 2013, **52**, 13957–13964.
- 242 L. E. Smart and E. A. Moore, *Solid State Chemistry*, CRC Press, 4th Editio., 2012.
- 243 C. Colbeau-Justin, M. Kunst and D. Huguenin, Structural influence on charge-carrier lifetimes in TiO₂ powders studied by microwave absorption, *J. Mater. Sci.*, 2003, **38**, 2429–2437.
- 244 M. K. Nowotny, L. R. Sheppard, T. Bak and J. Nowotny, Defect chemistry of titanium dioxide. Application of defect engineering in processing of TiO₂-based photocatalysts, *J. Phys. Chem. C*, 2008, **112**, 5275–5300.
- 245 F. A. Kröger and H. J. Vink, Relations between the Concentrations of Imperfections in Crystalline Solids, *Solid State Phys. - Adv. Res. Appl.*, 1956, **3**, 307–435.
- 246 H. Su, Y. T. Huang, Y. H. Chang, P. Zhai, N. Y. Hau, P. C. H. Cheung, W. T. Yeh, T. C. Wei and S. P. Feng, The Synthesis of Nb-doped TiO₂ Nanoparticles for Improved-Performance Dye Sensitized Solar Cells, *Electrochim. Acta*, 2015, **182**, 230–237.
- 247 D. Bauer, A. J. Roberts, N. Matsumi and J. A. Darr, Nano-sized Mo- and Nb-doped TiO₂ as anode materials for high energy and high power hybrid Li-ion capacitors, *Nanotechnology*, , DOI:10.1088/1361-6528/aa69df.
- 248 S. Singh, V. Sharma and K. Sachdev, Investigation of effect of doping concentration in Nb-doped TiO₂ thin films for TCO applications, *J. Mater. Sci.*, 2017, **52**, 11580–11591.
- 249 O. R. de la Fuente, in *Modern Technologies for Creating the Thin-film Systems and Coatings*, InTech, 2017, vol. 2, p. 64.
- 250 R. S. Hyam, J. Lee, E. Cho, J. Khim and H. Lee, Effect of annealing environments on self-organized TiO₂ nanotubes for efficient photocatalytic applications, *J. Nanosci. Nanotechnol.*, 2012, **12**, 8908–8912.
- 251 W. Choi, A. Termin and M. R. Hoffmann, The role of metal ion dopants in quantum-sized TiO₂-n: Correlation between photoreactivity and charge carrier recombination dynamics, *J. Phys. Chem.*, 1994, **98**, 13669–13679.
- 252 C. M. Teh and A. R. Mohamed, Roles of titanium dioxide and ion-doped titanium dioxide on photocatalytic degradation of organic pollutants (phenolic compounds and dyes) in aqueous solutions: A review, *J. Alloys Compd.*, 2011, **509**, 1648–1660.
- 253 A. Khlyustova, N. Sirotkin, T. Kusova, A. Kraev, V. Titov and A. Agafonov, Doped TiO₂: the effect of doping elements on photocatalytic activity , *Mater. Adv.*, 2020, **1**, 1193–1201.
- 254 J. Li, X. Xu, X. Liu, C. Yu, D. Yan, Z. Sun and L. Pan, Sn doped TiO₂ nanotube with oxygen vacancy for highly efficient visible light photocatalysis, *J. Alloys Compd.*, 2016, **679**, 454–462.
- 255 J. W. Pan, C. Li, Y. F. Zhao, R. X. Liu, Y. Y. Gong, L. Y. Niu, X. J. Liu and B. Q. Chi,

- Electronic properties of TiO₂ doped with Sc, Y, La, Zr, Hf, V, Nb and Ta, *Chem. Phys. Lett.*, 2015, **628**, 43–48.
- 256 S. Parthasarathy and V. Parthasarathi, A statistical study on the measurability of Bijvoet differences in crystals with type-I and type-II degree of centrosymmetry, *Acta Crystallogr. Sect. A*, 1976, **32**, 768–771.
- 257 H. Abdelouhab Reddam, R. Elmail, S. C. Lloria, G. Monrós Tomás, Z. A. Reddam and F. Coloma-Pascual, Synthesis of Fe, Mn and Cu modified TiO₂ photocatalysts for photodegradation of Orange II, *Bol. la Soc. Esp. Ceram. y Vidr.*, 2020, **59**, 138–148.
- 258 S. Kohtani, A. Kawashima and H. Miyabe, Reactivity of trapped and accumulated electrons in titanium dioxide photocatalysis, *Catalysts*, , DOI:10.3390/catal7100303.
- 259 H. Su, Y. T. Huang, Y. H. Chang, P. Zhai, N. Y. Hau, P. C. H. Cheung, W. T. Yeh, T. C. Wei and S. P. Feng, The Synthesis of Nb-doped TiO₂ Nanoparticles for Improved-Performance Dye Sensitized Solar Cells, *Electrochim. Acta*, 2015, **182**, 230–237.
- 260 S. Sathasivam, D. S. Bhachu, Y. Lu, N. Chadwick, S. A. Althabaiti, A. O. Alyoubi, S. N. Basahel, C. J. Carmalt and I. P. Parkin, Tungsten doped TiO₂ with enhanced photocatalytic and optoelectrical properties via aerosol assisted chemical vapor deposition, *Sci. Rep.*, 2015, **5**, 1–10.
- 261 V. Kumaravel, S. Rhatigan, S. Mathew, M. C. Michel, J. Bartlett, M. Nolan, S. J. Hinder, A. Gascó, C. Ruiz-Palomar, D. Hermosilla and S. C. Pillai, Mo doped TiO₂: Impact on oxygen vacancies, anatase phase stability and photocatalytic activity, *JPhys Mater.*, , DOI:10.1088/2515-7639/ab749c.
- 262 L. Kong, C. Wang, H. Zheng, X. Zhang and Y. Liu, Defect-Induced Yellow Color in Nb-Doped TiO₂ and Its Impact on Visible-Light Photocatalysis, *J. Phys. Chem. C*, 2015, **119**, 16623–16632.
- 263 T. Nikolay, L. Larina, O. Shevaleevskiy and B. T. Ahn, Electronic structure study of lightly Nb-doped TiO₂ electrode for dye-sensitized solar cells, *Energy Environ. Sci.*, 2011, **4**, 1480–1486.
- 264 G. M. Carroll, A. M. Schimpf, E. Y. Tsui and D. R. Gamelin, Redox Potentials of Colloidal n-Type ZnO Nanocrystals: Effects of Confinement, Electron Density, and Fermi-Level Pinning by Aldehyde Hydrogenation, *J. Am. Chem. Soc.*, 2015, **137**, 11163–11169.
- 265 M. Ghini, N. Curreli, A. Camellini, M. Wang, A. Asaithambi and I. Kriegel, Photodoping of metal oxide nanocrystals for multi-charge accumulation and light-driven energy storage, *Nanoscale*, 2021, **13**, 8773–8783.
- 266 O. Zandi, A. Agrawal, A. B. Shearer, L. C. Reimnitz, C. J. Dahlman, C. M. Staller and D. J. Milliron, Impacts of surface depletion on the plasmonic properties of doped semiconductor nanocrystals, *Nat. Mater.*, 2018, **17**, 710–717.
- 267 A. J. Morfa, B. I. MacDonald, J. Subbiah and J. J. Jasieniak, Understanding the chemical origin of improved thin-film device performance from photodoped ZnO nanoparticles, *Sol. Energy Mater. Sol. Cells*, 2014, **124**, 211–216.
- 268 P. P. Filippatos, N. Kelaidis, M. Vasilopoulou, D. Davazoglou, N. N. Lathiotakis and A. Chroneos, Defect processes in F and Cl doped anatase TiO₂, *Sci. Rep.*, 2019, **9**, 1–10.
- 269 V. Štengl and T. M. Grygar, The simplest way to iodine-doped anatase for photocatalysts activated by visible light, *Int. J. Photoenergy*, , DOI:10.1155/2011/685935.
- 270 A. McGuinness, J. Baltrusaitis and R. Nessler, Synthesis and Characterization of Chlorine and Bromine Doped TiO₂ Nanoparticles for Photocatalytic Methanol Production , *Microsc. Microanal.*, 2011, **17**, 1704–1705.
- 271 P. P. Filippatos, A. Soutlati, N. Kelaidis, C. Petaroudis, A. A. Alivisatou, C. Drivas, S. Kennou, E. Agapaki, G. Charalampidis, A. R. bin M. Yusoff, N. N. Lathiotakis, A. G. Coutsolelos, D. Davazoglou, M. Vasilopoulou and A. Chroneos, Preparation of hydrogen, fluorine and chlorine doped and co-doped titanium dioxide photocatalysts: a theoretical and experimental approach, *Sci. Rep.*, 2021, **11**, 1–12.
- 272 S. K. Joung, T. Amemiya, M. Murabayashi and K. Itoh, Chlorine-Doped Visible Light

- Driven TiO₂ Photocatalysts: Property Changes due to Preparation Condition, 2003, **269**, 2001.
- 273 A. M. Czoska, S. Livraghi, M. Chiesa, E. Giamello, S. Agnoli, G. Granozzi, E. Finazzi, C. Di Valentiny and G. Pacchioni, The nature of defects in fluorine-doped TiO₂, *J. Phys. Chem. C*, 2008, **112**, 8951–8956.
- 274 L. Hua, Z. Yin and S. Cao, Recent advances in synthesis and applications of carbon-doped TiO₂ nanomaterials, *Catalysts*, 2020, **10**, 1–16.
- 275 S. Varnagiris, A. Medvids, M. Lelis, D. Milcius and A. Antuzevics, Black carbon-doped TiO₂ films: Synthesis, characterization and photocatalysis, *J. Photochem. Photobiol. A Chem.*, 2019, **382**, 111941.
- 276 Y. A. Shaban, A. A. El Maradny and R. K. Al Farawati, Photocatalytic reduction of nitrate in seawater using C/TiO₂ nanoparticles, *J. Photochem. Photobiol. A Chem.*, 2016, **328**, 114–121.
- 277 Y. Nakano, T. Morikawa, T. Ohwaki and Y. Taga, Electrical characterization of band gap states in C-doped TiO₂ films, *Appl. Phys. Lett.*, 2005, **87**, 19–22.
- 278 Y. A. Shaban and S. U. M. Khan, Visible light active carbon modified n-TiO₂ for efficient hydrogen production by photoelectrochemical splitting of water, *Int. J. Hydrogen Energy*, 2008, **33**, 1118–1126.
- 279 G. Wu, T. Nishikawa, B. Ohtani and A. Chen, Synthesis and characterization of carbon-doped TiO₂ nanostructures with enhanced visible light response, *Chem. Mater.*, 2007, **19**, 4530–4537.
- 280 Y. Nakano, T. Morikawa, T. Ohwaki and Y. Taga, Deep-level optical spectroscopy investigation of N-doped TiO₂ films, *Appl. Phys. Lett.*, 2005, **86**, 1–3.
- 281 D. Nassoko, Y. F. Li, H. Wang, J. L. Li, Y. Z. Li and Y. Yu, Nitrogen-doped TiO₂ nanoparticles by using EDTA as nitrogen source and soft template: Simple preparation, mesoporous structure, and photocatalytic activity under visible light, *J. Alloys Compd.*, 2012, **540**, 228–235.
- 282 S. A. Bakar, G. Byzinski and C. Ribeiro, Synergistic effect on the photocatalytic activity of N-doped TiO₂ nanorods synthesised by novel route with exposed (110) facet, *J. Alloys Compd.*, 2016, **666**, 38–49.
- 283 C. Trapalis, N. Todorova, T. Giannakopoulou, G. Romanos, T. Vaimakis and J. Yu, Preparation of fluorine-doped TiO₂ photocatalysts with controlled crystalline structure, *Int. J. Photoenergy*, , DOI:10.1155/2008/534038.
- 284 M. V. Dozzi, C. D’Andrea, B. Ohtani, G. Valentini and E. Selli, Fluorine-doped TiO₂ materials: Photocatalytic activity vs time-resolved photoluminescence, *J. Phys. Chem. C*, 2013, **117**, 25586–25595.
- 285 S. Tojo, T. Tachikawa, M. Fujitsuka and T. Majima, Iodine-doped TiO₂ photocatalysts: Correlation between band structure and mechanism, *J. Phys. Chem. C*, 2008, **112**, 14948–14954.
- 286 W. Zhang, N. Luo, S. Huang, N. L. Wu and M. Wei, Sulfur-Doped Anatase TiO₂ as an Anode for High-Performance Sodium-Ion Batteries, *ACS Appl. Energy Mater.*, 2019, **2**, 3791–3797.
- 287 S. Cravanzola, F. Cesano, F. Gaziano and D. Scarano, Sulfur-doped TiO₂: Structure and surface properties, *Catalysts*, , DOI:10.3390/catal7070214.
- 288 L. G. Devi and R. Kavitha, Enhanced photocatalytic activity of sulfur doped TiO₂ for the decomposition of phenol: A new insight into the bulk and surface modification, *Mater. Chem. Phys.*, 2014, **143**, 1300–1308.
- 289 J. C. A. Boeyens, The periodic electronegativity table, *Zeitschrift fur Naturforsch. - Sect. B J. Chem. Sci.*, 2008, **63**, 199–209.
- 290 K. Naoi, Y. Ohko and T. Tsuma, TiO₂ Films Loaded with Silver Nanoparticles: Control of Multicolor Photochromic Behavior, *J. Am. Chem. Soc.*, 2004, **126**, 3664–3668.
- 291 R. Del Angel, J. C. Durán-Álvarez and R. Zanella, TiO₂-Low Band Gap Semiconductor Heterostructures for Water Treatment Using Sunlight-Driven Photocatalysis, *Titan.*

- Dioxide - Mater. a Sustain. Environ.*, , DOI:10.5772/intechopen.76501.
- 292 L. Guo, Z. Yang, K. Marcus, Z. Li, B. Luo, L. Zhou, X. Wang, Y. Du and Y. Yang, MoS₂/TiO₂ heterostructures as nonmetal plasmonic photocatalysts for highly efficient hydrogen evolution, *Energy Environ. Sci.*, 2018, **11**, 106–114.
- 293 W. Avansi, A. C. Catto, L. F. Da Silva, T. Fiorido, S. Bernardini, V. R. Mastelaro, K. Aguir and R. Arenal, One-Dimensional V₂O₅/TiO₂ Heterostructures for Chemiresistive Ozone Sensors, *ACS Appl. Nano Mater.*, 2019, **2**, 4756–4764.
- 294 G. Zhang, Y. Tan, Z. Sun and S. Zheng, Synthesis of BiOCl/TiO₂ heterostructure composites and their enhanced photocatalytic activity, *J. Environ. Chem. Eng.*, 2017, **5**, 1196–1204.
- 295 N. Helaïli, Y. Bessekhouad, A. Bouguelia and M. Trari, Visible light degradation of Orange II using xCu_yO_z/TiO₂ heterojunctions, *J. Hazard. Mater.*, 2009, **168**, 484–492.
- 296 Q. L. Yang, Y. W. Fang, Y. B. Song, S. S. Jia, Y. L. Lu, D. K. Yu and M. L. Fu, Preparation of Cu₂O/TiO₂ Heterostructure with High Visible-Light Photocatalytic Activity, *Adv. Mater. Res.*, 2014, **1073–1076**, 47–51.
- 297 M. Sakar, R. Mithun Prakash and D. Trong-On, Insights into the tio₂-based photocatalytic systems and their mechanisms, *Catalysts*, , DOI:10.3390/catal9080680.
- 298 Y. Yan, Z. Zeng, M. Huang and P. Chen, Van der waals heterojunctions for catalysis, *Mater. Today Adv.*, 2020, **6**, 100059.
- 299 M. Murdoch, G. I. N. Waterhouse, M. A. Nadeem, J. B. Metson, M. A. Keane, R. F. Howe, J. Llorca and H. Idriss, The effect of gold loading and particle size on photocatalytic hydrogen production from ethanol over Au/TiO₂ nanoparticles, *Nat. Chem.*, 2011, **3**, 489–492.
- 300 U. Siemon, D. Bahnemann, J. J. Testa, D. Rodríguez, M. I. Litter and N. Bruno, Heterogeneous photocatalytic reactions comparing TiO₂ and Pt/TiO₂, *J. Photochem. Photobiol. A Chem.*, 2002, **148**, 247–255.
- 301 V. Kavitha, P. S. Ramesh and D. Geetha, Synthesis of Cu loaded TiO₂ nanoparticles for the improved photocatalytic degradation of Rhodamine B, *Int. J. Nanosci.*, 2016, **15**, 1–8.
- 302 A. L. Linsebigler, G. Lu and J. T. Yates, Photocatalysis on TiO₂ Surfaces: Principles, Mechanisms, and Selected Results, *Chem. Rev.*, 1995, **95**, 735–758.
- 303 F. Wu, X. Hu, J. Fan, E. Liu, T. Sun, L. Kang, W. Hou, C. Zhu and H. Liu, Photocatalytic Activity of Ag/TiO₂ Nanotube Arrays Enhanced by Surface Plasmon Resonance and Application in Hydrogen Evolution by Water Splitting, *Plasmonics*, 2013, **8**, 501–508.
- 304 Y. Ohko, T. Tatsuma, T. Fujii, K. Naoi, C. Niwa, Y. Kubota and A. Fujishima, Multicolour photochromism of TiO₂ films loaded with silver nanoparticles, *Nat. Mater.*, 2003, **2**, 29–31.
- 305 A. H. Mamaghani, F. Haghightat and C. S. Lee, Hydrothermal/solvothermal synthesis and treatment of TiO₂ for photocatalytic degradation of air pollutants: Preparation, characterization, properties, and performance, *Chemosphere*, 2019, **219**, 804–825.
- 306 S. K. Wallace and K. P. McKenna, Facet-dependent electron trapping in TiO₂ nanocrystals, *J. Phys. Chem. C*, 2015, **119**, 1913–1920.
- 307 Z. Xiong, Z. Lei, Y. Li, L. Dong, Y. Zhao and J. Zhang, A review on modification of facet-engineered TiO₂ for photocatalytic CO₂ reduction, *J. Photochem. Photobiol. C Photochem. Rev.*, 2018, **36**, 24–47.
- 308 G. Liu, H. G. Yang, X. Wang, L. Cheng, H. Lu, L. Wang, G. Q. Lu and H. M. Cheng, Enhanced photoactivity of oxygen-deficient anatase TiO₂ sheets with dominant {001} facets, *J. Phys. Chem. C*, 2009, **113**, 21784–21788.
- 309 K. Wang, P. Chen, W. Nie, Y. Xu and Y. Zhou, Improved photocatalytic reduction of Cr(VI) by molybdenum disulfide modified with conjugated polyvinyl alcohol, *Chem. Eng. J.*, 2019, **359**, 1205–1214.
- 310 N. Serpone, I. Texier, A. V. Emeline, P. Pichat, H. Hidaka and J. Zhao, Post-irradiation effect and reductive dechlorination of chlorophenols at oxygen-free TiO₂/water

- interfaces in the presence of prominent hole scavengers, *J. Photochem. Photobiol. A Chem.*, 2000, **136**, 145–155.
- 311 I. A. Shkrob, M. C. Sauer and D. Gosztola, Efficient, rapid photooxidation of chemisorbed polyhydroxyl alcohols and carbohydrates by TiO₂ nanoparticles in an aqueous solution, *J. Phys. Chem. B*, 2004, **108**, 12512–12517.
- 312 P. N. Uyen Thi, U. Male and D. S. Huh, Fabrication of photo-responsive moth eye-like patterned poly(vinyl alcohol) films selectively containing TiO₂ nanoparticles in the microdome, *Polymer (Guildf.)*, 2018, **144**, 103–110.
- 313 H. Miyazaki, T. Matsuura and T. Ota, TiO₂ nano-particles based photochromic composite films, *Compos. Commun.*, 2018, **10**, 136–139.
- 314 L. M. F. Tandy, J. J. P. Bueno, Y. M. Vong, I. Z. Torres, L. L. Rojas, C. J. R. Torres, H. M. Gutiérrez and M. L. M. López, Reversible photochromic effect in the TiO₂—polymer hybrid system, *J. Sol-Gel Sci. Technol.*, 2017, **82**, 51–58.
- 315 M. Hočevár and U. Opara Krašovec, A photochromic single glass pane, *Sol. Energy Mater. Sol. Cells*, 2018, **186**, 111–114.
- 316 S. Glass, B. Trinklein, B. Abel and A. Schulze, TiO₂ as photosensitizer and photoinitiator for synthesis of photoactive TiO₂-PEGDA hydrogel without organic photoinitiator, *Front. Chem.*, 2018, **6**, 1–9.
- 317 E. Scolan and C. Sanchez, Synthesis and Characterization of Surface-Protected Nanocrystalline Titania Particles, *Chem. Mater.*, 1998, **10**, 3217–3223.
- 318 A. S. Attar, M. S. Ghamsari, F. Hajiesmaeilbaigi and S. Mirdamadi, Modifier ligands effects on the synthesized TiO₂ nanocrystals, *J. Mater. Sci.*, 2008, **43**, 1723–1729.
- 319 R. E. Morris and P. S. Wheatley, Diffraction techniques applied to zeolites, *Stud. Surf. Sci. Catal.*, 2007, **168**, 375–401.
- 320 C. F. Holder and R. E. Schaak, Tutorial on Powder X-ray Diffraction for Characterizing Nanoscale Materials, *ACS Nano*, 2019, **13**, 7359–7365.
- 321 N. Doebelin and R. Kleeberg, Profex: A graphical user interface for the Rietveld refinement program BGMN, *J. Appl. Crystallogr.*, 2015, **48**, 1573–1580.
- 322 V. Grant, *The Rietveld Method*, Oxford University Press, Oxford, 1993.
- 323 J. P. R. De Villiers and L. Lu, XRD analysis and evaluation of iron ores and sinters, *Iron Ore Mineral. Process. Environ. Sustain.*, 2015, 85–100.
- 324 A. R. Barron and P. M. V. Raja, Raman Spectroscopy, [https://chem.libretexts.org/Bookshelves/Analytical_Chemistry/Book%3A_Physical_Methods_in_Chemistry_and_Nano_Science_\(Barron\)/04%3A_Chemical_Speciation/4.03%3A_Raman_Spectroscopy](https://chem.libretexts.org/Bookshelves/Analytical_Chemistry/Book%3A_Physical_Methods_in_Chemistry_and_Nano_Science_(Barron)/04%3A_Chemical_Speciation/4.03%3A_Raman_Spectroscopy).
- 325 Renishaw, What is Raman Spectroscopy?, www.nanophoton.net/raman/raman-spectroscopy.html.
- 326 B. Marczewska and K. Marczewski, First glass electrode and its creators F. haber and Z. klemensiewicz - on 100th anniversary, *Zeitschrift fur Phys. Chemie*, 2010, **224**, 795–799.
- 327 J. Torrent and V. Barrón, Diffuse Reflectance Spectroscopy, 2015, 367–385.
- 328 P. Makuła, M. Pacia and W. Macyk, How To Correctly Determine the Band Gap Energy of Modified Semiconductor Photocatalysts Based on UV-Vis Spectra, *J. Phys. Chem. Lett.*, 2018, **9**, 6814–6817.
- 329 F. A. Stevie and C. L. Donley, Introduction to x-ray photoelectron spectroscopy, *J. Vac. Sci. Technol. A*, 2020, **38**, 063204.
- 330 P. Pietrzyk, T. Mazur and Z. Sojka, in *Local Structural Characterisation*, ed. D. W. Bruce, John Wiley & Sons, Ltd, 1st Editio., 2014, pp. 225–299.
- 331 B. Principles, ELECTRON-SPIN RESONANCE SPECTROSCOPY, 2005, **3**, 426–437.
- 332 H. C. Choi, Y. M. Jung and S. Bin Kim, Size effects in the Raman spectra of TiO₂ nanoparticles, *Vib. Spectrosc.*, 2005, **37**, 33–38.
- 333 W. F. Zhang, Y. L. He, M. S. Zhang, Z. Yin and Q. Chen, Raman scattering study on anatase TiO₂ nanocrystals, *J. Phys. D. Appl. Phys.*, 2000, **33**, 912–916.

- 334 T. Cottre, M. Fingerle, M. Kranz, T. Mayer, B. Kaiser and W. Jaegermann, Interaction of Water with Atomic Layer Deposited Titanium Dioxide on p-Si Photocathode: Modeling of Photoelectrochemical Interfaces in Ultrahigh Vacuum with Cryo-Photoelectron Spectroscopy, *Adv. Mater. Interfaces*, , DOI:10.1002/admi.202002257.
- 335 M. Klare, J. Scheen, K. Vogelsang, H. Jacobs and J. A. C. Broekaert, Degradation of short-chain alkyl- and alkanolamines by TiO₂- and Pt/TiO₂-assisted photocatalysis, *Chemosphere*, 2000, **41**, 353–362.
- 336 J. Garcia-Amoros, U. Banin, M. Baroncini and Y. Ben-Shahar, *Photoactive Semiconductor Nanocrystal Quantum Dots*, Springer International Publishing, Cham, 2017.
- 337 X. Pan, M.-Q. Yang, X. Fu, N. Zhang and Y.-J. Xu, Defective TiO₂ with oxygen vacancies: synthesis, properties and photocatalytic applications, *Nanoscale*, 2013, **5**, 3601.
- 338 P. Y. Bruice, *Organic chemistry*, Pearson Education, Santa Barbara, 8th editio., 2016.
- 339 Y. Suda, T. Morimoto and M. Nagao, Adsorption of Alcohols on Titanium Dioxide (Rutile) Surface, *Langmuir*, 1987, **3**, 99–104.
- 340 R. Battino, *Oxygen and ozone*, Pergamon Press, 1981, vol. 7.
- 341 A. Rahimi Niaraki, M. R. Saraee, F. Kazemi and B. Kaboudin, Chemoselective photocatalytic oxidation of alcohols to aldehydes and ketones by nitromethane on titanium dioxide under violet 400 nm LED light irradiation, *Org. Biomol. Chem.*, 2020, **18**, 2326–2330.
- 342 Y. Pellegrin and F. Odobel, Les donneurs d'électron sacrificiels pour la production de combustible solaire, *Comptes Rendus Chim.*, 2017, **20**, 283–295.
- 343 C. Han, M. Y. Qi, Z. R. Tang, J. Gong and Y. J. Xu, Gold nanorods-based hybrids with tailored structures for photoredox catalysis: fundamental science, materials design and applications, *Nano Today*, 2019, **27**, 48–72.
- 344 C. S. Enache, J. Schoonman and R. V. A. N. D. E. Krol, The Photoresponse of Iron- and Carbon-Doped TiO₂ (Anatase) Photoelectrodes, 2004, **2**, 177–182.
- 345 U. Joost, A. Šutka, M. Oja, K. Smits, N. Döbelin, A. Loot, M. Järvekülg, M. Hirsimäki, M. Valden and E. Nömmiste, Reversible Photodoping of TiO₂ Nanoparticles for Photochromic Applications, *Chem. Mater.*, 2018, **30**, 8968–8974.
- 346 Y. Yan, M. Han, A. Konkin, T. Koppe, D. Wang, T. Andreu, G. Chen, U. Vetter, J. R. Morante and P. Schaaf, Slightly hydrogenated TiO₂ with enhanced photocatalytic performance, *J. Mater. Chem. A*, 2014, **2**, 12708–12716.
- 347 Y. L. Chueh, C. H. Hsieh, M. T. Chang, L. J. Chou, C. S. Lao, J. H. Song, J. Y. Gan and Z. L. Wang, RuO₂ nanowires and RuO₂/TiO₂ core/shell nanowires: From synthesis to mechanical, optical, electrical, and photoconductive properties, *Adv. Mater.*, 2007, **19**, 143–149.
- 348 U. Joost, A. Šutka, M. Visnapuu, A. Tamm, M. Lembinen, M. Antsov, K. Utt, K. Smits, E. Nömmiste and V. Kisand, Colorimetric gas detection by the varying thickness of a thin film of ultrasmall PTSA-coated TiO₂ nanoparticles on a Si substrate, *Beilstein J. Nanotechnol.*, 2017, **8**, 229–236.
- 349 M. Knite, V. Teteris, A. Kiploka and J. Kaupuzs, Polyisoprene-carbon black nanocomposites as tensile strain and pressure sensor materials, *Sensors Actuators, A Phys.*, 2004, **110**, 142–149.
- 350 Y. Li, J. K. Cooper, W. Liu, C. M. Sutter-Fella, M. Amani, J. W. Beeman, A. Javey, J. W. Ager, Y. Liu, F. M. Toma and I. D. Sharp, Defective TiO₂ with high photoconductive gain for efficient and stable planar heterojunction perovskite solar cells, *Nat. Commun.*, 2016, **7**, 1–7.
- 351 K. Maier, A. Helwig, G. Müller, P. Hille and M. Eickhoff, Effect of water vapor and surface morphology on the low temperature response of metal oxide semiconductor gas sensors, *Materials (Basel)*, 2015, **8**, 6570–6588.
- 352 G. Harrison, K. Katsiev, Y. Alsalik, G. Thornton and H. Idriss, Switch in photocatalytic

- reaction selectivity: The effect of oxygen partial pressure on carbon-carbon bond dissociation over hydroxylated TiO₂(1 1 0) surfaces, *J. Catal.*, 2018, **363**, 117–127.
- 353 X. Wei, G. Zhu, J. Fang and J. Chen, Synthesis, Characterization, and Photocatalysis of Well-Dispersible Phase-Pure Anatase TiO₂ Nanoparticles.
- 354 D. Das Mulmi, T. Sekiya, N. Kamiya and S. Kurita, Optical and Electric Properties of Nb-doped Anatase TiO₂ Single Crystal.
- 355 J. Yang, X. Zhang, C. Wang, P. Sun, L. Wang, B. Xia and Y. Liu, Solar photocatalytic activities of porous Nb-doped TiO₂ microspheres prepared by ultrasonic spray pyrolysis, *Solid State Sci.*, 2012, **14**, 139–144.
- 356 N. Yu, Y. Hu, X. Wang, G. Liu, Z. Wang, Z. Liu, Q. Tian, M. Zhu, X. Shi and Z. Chen, Dynamically tuning near-infrared-induced photothermal performances of TiO₂ nanocrystals by Nb doping for imaging-guided photothermal therapy of tumors, *Nanoscale*, 2017, **9**, 9148–9159.
- 357 S. Khan, H. Cho, D. Kim, S. S. Han, K. H. Lee, S. H. Cho, T. Song and H. Choi, Defect engineering toward strong photocatalysis of Nb-doped anatase TiO₂: Computational predictions and experimental verifications, *Appl. Catal. B Environ.*, 2017, **206**, 520–530.
- 358 R. Egiřitis, U. Joost, A. Zukuls, K. Rubenis, R. Ignatāns, L. Avotiņa, L. Baumane, K. Šmits, M. Hirsimäki, T. Käämbre and A. Šutka, Strong, Rapid, and Reversible Photochromic Response of Nb Doped TiO₂ Nanocrystal Colloids in Hole Scavenging Media, *ACS Appl. Mater. Interfaces*, 2020, **12**, 57609–57618.
- 359 B. Bharti, S. Kumar, H. N. Lee and R. Kumar, Formation of oxygen vacancies and Ti³⁺ state in TiO₂ thin film and enhanced optical properties by air plasma treatment, *Sci. Rep.*, 2016, **6**, 1–12.
- 360 C. J. Dahlman, A. Agrawal, C. M. Staller, J. Adair and D. J. Milliron, Anisotropic Origins of Localized Surface Plasmon Resonance in n-Type Anatase TiO₂ Nanocrystals, *Chem. Mater.*, 2019, **31**, 502–511.
- 361 T. R. N. Kutty and M. Avudathai, Sacrificial water photocleavage using Nb-doped TiO₂ fine particles under band gap irradiation, *Int. J. Hydrogen Energy*, 1990, **15**, 621–628.
- 362 X. Pan, M. Q. Yang, X. Fu, N. Zhang and Y. J. Xu, Defective TiO₂ with oxygen vacancies: Synthesis, properties and photocatalytic applications, *Nanoscale*, 2013, **5**, 3601–3614.
- 363 V. Mohaček-Grošev, K. Furić and H. Ivanković, Luminescence and raman spectra of acetylacetone at low temperatures, *J. Phys. Chem. A*, 2007, **111**, 5820–5827.
- 364 S. F. Tayyari and F. Milani-nejad, Vibrational assignment of acetylacetone, *Spectrochim. Acta - Part A Mol. Biomol. Spectrosc.*, 2000, **56**, 2679–2691.
- 365 V. N. Mathi, A. J. Suresh and S. C. Bala, Eco-Friendly One-Pot Synthesis and Characterization of 1, 4-Dihydro Pteidine Derivatives, *Int. J. Pharm. Pharm. Sci.*, 2012, **4**, 2–5.
- 366 Z. Jin, Q. Chu, W. Xu, H. Cai, W. Ji, G. Wang, B. Lin and X. Zhang, All-Fiber Raman Biosensor by Combining Reflection and Transmission Mode, *IEEE Photonics Technol. Lett.*, 2018, **30**, 387–390.
- 367 J. Sung, D. G. Lee, S. Lee, J. Park and H. W. Jung, Crosslinking dynamics and gelation characteristics of photo- and thermally polymerized poly(ethylene glycol) hydrogels, *Materials (Basel)*, , DOI:10.3390/MA13153277.
- 368 E. Gontran, M. Juchaux, C. Deroulers, S. Kruglik, N. Huang, M. Badoual and O. Seksek, Assessment of the ability of poly(l-lysine)–poly(ethylene glycol) (PLL–PEG) hydrogels to support the growth of U87-MG and F98 glioma tumor cells, *J. Appl. Polym. Sci.*, 2018, **135**, 1–11.
- 369 A. E. Gekhman, V. M. Nekipelov, S. G. Sakharov, K. I. Zamaraev and I. I. Moiseev, Mechanism of the oxidation of acetylacetone by hydrogen peroxide, catalyzed by Mo(VI) complexes, *Bull. Acad. Sci. USSR Div. Chem. Sci.*, 1986, **35**, 1126–1130.
- 370 M. B. Browning, S. N. Cereceres, P. T. Luong and E. M. Cosgriff-Hernandez, Determination of the in vivo degradation mechanism of PEGDA hydrogels, *J. Biomed.*

- Mater. Res. - Part A*, 2014, **102**, 4244–4251.
- 371 G. Amato, E. Grasso, V. Longo and P. G. Gervasi, Oxidation of N, N-dimethylformamide and N, N-diethylformamide by human liver microsomes and human recombinant P450s, *Toxicol. Lett.*, 2001, **124**, 11–19.
- 372 C. Joyce-Pruden, J. K. Pross and Y. Li, Photoinduced reduction of aldehydes on titanium dioxide, *J. Org. Chem.*, 1992, **57**, 5087–5091.
- 373 S. Kohtani and H. Miyabe, in *Titanium Dioxide*, ed. J. Brown, Nova Science Publishers, 2014.
- 374 S. Kohtani, E. Yoshioka, K. Saito, A. Kudo and H. Miyabe, Photocatalytic hydrogenation of acetophenone derivatives and diaryl ketones on polycrystalline titanium dioxide, *Catal. Commun.*, 2010, **11**, 1049–1053.
- 375 Y. Hu and W. Pan, Calculation of pore scattering in transparent ceramics, *Solid State Phenom.*, 2018, **281 SSP**, 655–660.
- 376 J. G. J. Peelen and R. Metselaar, Light scattering by pores in polycrystalline materials: Transmission properties of alumina, *J. Appl. Phys.*, 1974, **45**, 216–220.



Raivis Eglītis was born in 1993 in Riga. He received a Bachelor's degree in Chemical Engineering in 2016 and a Master's degree in Material Nanotechnologies in 2018 from Riga Technical University. Since 2016, he has been a research assistant with Riga Technical University. Currently, he is a researcher with the Institute of Materials and Surface Engineering of the Faculty of Materials Science and Applied Chemistry of Riga Technical University. His research interests include spectroscopy as well as the optical properties of materials.